3D MAGNETOTELLURIC AND DCR INVESTIGATIONS AT SELECTED SITES IN UTTARAKHAND

Ph. D. THESIS

by

ANITA DEVI

DEPARTMENT OF EARTH SCIENCES
INDIAN INSTITUTE OF TECHNOLOGY ROORKEE
ROORKEE-247 667 (INDIA)
NOVEMBER, 2019

3D MAGNETOTELLURIC AND DCR INVESTIGATIONS AT SELECTED SITES IN UTTARAKHAND

A THESIS

Submitted in partial fulfilment of the requirements for the award of the degree

of

DOCTOR OF PHILOSOPHY

in

EARTH SCIENCES

by

ANITA DEVI

DEPARTMENT OF EARTH SCIENCES
INDIAN INSTITUTE OF TECHNOLOGY ROORKEE
ROORKEE-247 667 (INDIA)
NOVEMBER, 2019

INDIAN INSTITUTE OF TECHNOLOGY ROORKEE

STUDENT'S DECLARATION

I hereby certify that the work presented in the thesis entitled "**3D MAGNETOTELLURIC AND DCR INVESTIGATIONS AT SELECTED SITES IN UTTARAKHAND**" is my own work carried out during a period from July, 2014 to August, 2019 under the supervision of Dr. M. Israil, Professor, Department of Earth Sciences, Indian Institute of Technology Roorkee, Roorkee.

The matter presented in the thesis has not been submitted for the award of any other degree of this or any other Institute.

Dated: **November 04, 2019** **(ANITA DEVI)**

SUPERVISOR'S DECLARATION

This is to certify that the above mentioned work is carried out under my supervision.

Dated: **November 04, 2019** **(M. Israil)**

Supervisor

The Ph.D. Viva-Voce Examination of **Anita Devi**, Research Scholar, has been held on **November 04, 2019.**

Chairperson, SRC **External Examiner**

This is to certify that the student has made all the corrections in the thesis.

Supervisor **Head of the Department**

Dated: November 04, 2019

ABSTRACT

Electrical resistivity structures at four selected regions were deciphered from 3D inversion of Magnetotelluric (MT), Radio Magnetotelluric (RMT) and Direct Current Resistivity (DCR) data recorded in Uttarakhand, India. Earlier, the recorded MT and DCR data from the regions were interpreted assuming a 2D model of Earth. However, the geological structures, in general, are 3D in nature. Hence, the MT, RMT and DCR data, recorded by our group prior to the onset of this study along with the data recorded during the present work, are analyzed using 3D inversion techniques. The entire data comprises four different case studies, (i) MT data recorded in the Garhwal Himalayan Corridor (GHC) along Roorkee-Gangotri (RG) profile, (ii) MT data recorded in and around MCT zone in Chamoli region, (iii) DCR data recorded near a proposed bridge site in Tehri region and (iv) DCR and RMT data recorded in Saliyar Village near Roorkee.

The first case study is an MT investigation in GHC where MT data were acquired at 39 sites on RG profile. *AP3DMT*, a MATLAB based code developed by our group, was used for 3D inversion of this MT dataset. Before performing this 3D inversion several 3D synthetic inversion experiments, on full impedance tensor data, were carried out to estimate the optimal values of important control parameters affecting the inversion results. The synthetic studies established that the off-profile resistivity structures within 20 km from the profile can be deciphered from profile data. The optimal values of some other inversion parameters (e.g. model grids, smoothing, regularization parameter etc.) were also inferred and then used for 3D inversion of the field data. A 3D geoelectric model was obtained after performing several 3D inversion experiments on RG profile MT data using different components of data independently and jointly. The data types used were vertical magnetic field transfer function (VTF), Phase Tensor (PT), full impedance tensor (Z), VTF + PT and VTF + Z. Based on sensitivities of Z and VTF data and on other related tests, the model obtained from the VTF + Z data was chosen as the final model for detailed interpretation. The robustness of important features in the inverted model were validated through sensitivity tests. The model defines the geometry of DHR beneath the IGP, SH and LH in Garhwal Himalayan region. The model also suggests that DHR is a fault bounded structure. The obtained 3D geoelectrical model reveals some new off-profile resistivity structures which are aligned transverse to the main

Himalayan arc. The off-profile structures are interpreted as conductive ($<$ 10 Ωm) fluid saturated fractured zones bounding the highly resistive ($>$ 1000 Ωm) Delhi-Haridwar Ridge (DHR). The 3D resistivity model explains the thrust tectonics and *flat ramp flat* geometry of Main Himalayan Thrust (MHT). The model was also correlated with other geophysical models and with seismicity of the region. It has been observed that the earthquakes are generally located in the resistive zone of the crust with a few exceptions where they are near or in the conductive zone.

In second case study, MT data recorded at 28 sites in and around MCT zone in Chamoli region of Uttarakhand, India were inverted using the code *AP3DMT*. The dimensionality and directionality analysis of the MT data revealed the dominant 3D nature of the impedance tensor. In first step, the dataset was inverted for 28 sites. However, due to some noisy sites data, 23 MT sites were selected for obtaining the final 3D model. The 23 sites were inverted using the full impedance tensor data. Experiments were done to test the consistency, robustness and stability of the obtained 3D geolectrical model. Experiments were also done to identify the depth of investigation upto which the model is valid. The main highlight of the resistivity model is the presence of two doublets comprising low-high resistivity features. One of the doublet ('AB') is located in MCT zone and Inner Lesser Himalaya and the second one ('CD') in Higher Himalayan region. The low resistivity feature of the doublet represents the fluid saturated fracture zone while the high resistivity feature represents the brittle rigid rocks. The conductive features ('A' and 'C') are related to the change in porosity, fluid content, pore distribution and possibly high heat flow and these can be explained in terms of the fluid saturated sediments adjacent to the resistive rigid rock matrix ('B' and 'D'). The resistivity model supports the role of fluid in triggering the medium and large size earthquakes in the region. The model features were correlated with the velocity model obtained from seismic tomography studies. The resistivity model also explains the high heat flow and the presence of thermal springs in the area.

The third case study was a ERT study where the data were used to characterize the subsurface soil at a bridge foundation site on the banks of Bhagirathi River at Tehri reservoir site, Uttarakhand, India. For this, six Electrical Resistivity Tomography (ERT) profiles were recorded on West and East banks of the river and these profiles were interpreted to determine the electrical resistivity image of the subsurface. The 2D and 3D subsurface resistivity models were obtained after inverting the data using the inversion codes *Res2dinv*

and *AP3DMT-DC* respectively. Based on the 2D and 3D ERT inversions, the resistivity of different lithological units have been defined for the investigated sites. The basement depth has been found on the basis of resistivity variation. The basement depth was found on the basis of resistivity variations. The borehole data and geological inputs were used for lithological correlation and calibration of the resistivity values to the subsurface formation. The Standard Penetration Test (SPT) data (N-values) were correlated with the extracted resistivity values at selected points of the inverted models. The correlation study shows that resistivity is linearly correlated with the N-values. The coefficient of correlation was greater than 0.85, indicating that it is good and consistent. The relationship is site specific but useful for geotechnical investigations in the Himalayan region where undertaking a destructive test is prohibited.

The last case study deals with the ERT and RMT data from Roorkee region which were used to study the effect of groundwater contamination due to untreated sewage irrigation near the Saliyar village, Roorkee. Nine RMT and five ERT profiles were recorded in and around the contaminated zone and one ERT and one RMT profile were recorded in the uncontaminated zone, for comparison. The two datasets were inverted independently as well as jointly using the 3D inversion code *AP3DMT-DC*. Prior to this, a synthetic study was carried out to validate the algorithm capabilities. This study demonstrated that the two methods, ERT and RMT, complement each other and that in the inverted model obtained through joint 3D inversion the resistivity values and geometry of the low and high resistivity features are better resolved than the models obtained through individual inversions. In the present study, the 3D models obtained after inversions of field data were found to be consistent with the published results of 2D inversion. The 3D inverted resistivity model shows an unconfined aquifer of low resistivity which is overlain by a slightly resistive near surface unsaturated soil formation. Moving away from the waste disposal site, an increase in resistivity was observed for the shallow unconfined aquifer. In comparison to the inverted results of an uncontaminated reference site, the inverted results of the contaminated region show a decrease in resistivity of the aquifer layer establishing the influence of contamination. The results of 3D joint inversion of the two datasets were encouraging in terms of accuracy and resolution of the model features and better explains the resistivity variation and geometry of all the features than the models obtained by individual inversions.

LIST OF PUBLICATIONS

Journals

Anita Devi, Mohammad Israil, Rathinam Anbalagan and Pravin K. Gupta, 2017. Subsurface soil characterization using geoelectrical and geotechnical investigations at a bridge site in Uttarakhand Himalayan region, *Journal of Applied Geophysics*, (144): 78–85.

Anita Devi Mohammad Israil, Pravin K. Gupta, S. K. Varshney and Naser Meqbel, 2019. Transverse Tectonics Structures in the Garhwal Himalaya Corridor Inferred from 3D Inversion of Magnetotelluric Profile Data, *Pure And Applied Geophysics*. `https://doi.org/10.1007/s00024-019-02222-3`.

Anita Devi, Mohammad Israil, Arun Singh and Pravin K. Gupta. Three-dimensional resistivity structure in MCT zone around Chamoli region, Garhwal Himalaya and its seismogenic implication, *Under Review*, *Journal of Applied Geophysics*.

Anita Devi, Mohammad Israil, Arun Singh and Pravin K. Gupta, Pritam Yogeshwar, Bulent Tezkan. Imaging of groundwater contamination using 3D joint inversion of DCR and RMT data: A case study from Northern India, Under Review, *Near Surface Geophysics*.

Conference/Workshop

Anita Devi, Mohammad Israil, Arun Singh and Pravin K. Gupta, Pritam Yogeshwar, Bulent Tezkan, 2019. GW Contamination due to untreated sewage irrigation and waste disposal in Saliyar area delineated using 3D joint inversion of RMT and DCR data-A case study, *IGWC*, Roorkee, India.

Mohammad Israil, **Anita Devi**, Pravin K. Gupta, Bulent Tezkan, Pritam Yogeshwar, 2019. 3D inversion of MT data from Garhwal Himalaya, *EMTF*, Haltern am See, Germany.

Anita Devi, Mohammad Israil, Arun Singh, Pravin K. Gupta, 2018. Geothermal inferences drawn from 3D inversion of Magnetotelluric Data recorded from Chamoli region, Uttarakhand, India , *EMIW*, Helsingør, Denmark.

Mohammad Zubair, **Anita Devi**, Mohammad Israil and Pravin K. Gupta, 2018. Electrical resistivity imaging over a buried elongated dipping conductor using Dipole-dipole and quasi null configurations , *EMIW*, Helsingør, Denmark.

Mohammad Israil, Arun Singh, **Anita Devi** and Pravin K. Gupta, 2018. MATLAB based

code for 3D joint inversion of Magnetotelluric and Direct Current Resistivity imaging data , *EMIW*, Helsingør, Denmark.

Mohammad Israil, **Anita Devi**, Arun Singh and Pravin K. Gupta, 2017. 3D Geoelectrical model of Sub-Himalayan Region - A Magnetotelluric study , *SPG*, Jaipur , India.

Anita Devi, Mohammad Israil, Rathinam Anbalagan and Pravin K. Gupta, 2016. Delineation of overburden thickness using resistivity imaging at Dobra bridge site, Uttarakhand, India, *EMIW*, Chiang Mai, Thailand.

Acknowledgements

First and foremost, I would like to thank my supervisor Prof. M. Israil support and encouragement throughout my work at Indian Institute of Technology Roorkee, Roorkee and making the completion of this thesis possible. It has been a privilege and pleasure being his student.

I thank my research committee members, Prof. Anand Joshi, Prof. Pravin. K. Gupta (Retd.), and Prof. G. D. Verma, and honorable chairman of department research committee Prof. Sandeep Singh for always being there to help and provide general guidance, not to mention helping meet all the document deadlines.

I am especially thankful to Prof. Pravin K. Gupta (Retd.), Department of Earth Sciences for his invaluable help and advice from time to time as when needed.

During this research, the department has had three heads; Prof. A. K. Saraf, Prof. D. C. Srivastava and Prof. Sunil Bajpai and I sincerely acknowledge the support they provided by extending every sort of help as and when sought for.

I extend a special note of thanks to all faculty members of the department for their co-operation. I also thank, all the non-teaching staff of the department who have helped me in all possible ways for the official work.

I express my heartily gratitude to Smt. Mamta Gupta and Smt. Shahida as time spent occasionally during tea, dinner was very pleasant.

The financial support provided by Ministry of Human Resources and Development (MHRD), New Delhi to complete the present work is highly acknowledged. I am also thankful to Department of Sicence and Technology, India and Ministry of Earth Sciences, India for providing fund for data acquisition and computation facilities. I also thank Institute Computer Center, IIT Roorkee for providing MATLAB-2013a.

A special thanks to my former and current lab-mates Dr. Rahul Dehiya, Dr. Arun Singh, Pramjeet, Zubair and Dharmendra for all the enlightening discussions we had during these years. I also thank all my other friends from IIT Roorkee, who helped lighten the burden, especially, Anirudh, Nupur, Zia, Meenakshi, Neha and Tina.

A special thanks to my younger brother Jitender Kumar and my sister Nisha for their unconditional love and support during crucial times.

Finally, I express my heartfelt gratitude to my father, Shri Jiwan Singh and mother, Smt. Phulo Devi for their unconditional love, encouragement and blessings. They have been a guiding force all my life and have given me necessary energy and happiness to work hard throughout this research work. I also express my feelings of gratitude to all those who helped me in this course but have not been listed here.

Roorkee (Anita Devi)

November 04, 2019

TABLE OF CONTENTS

LIST OF FIGURES

LIST OF TABLES

List of notation used.

Symbols	*Notations*
ρ	electric resistivity
E	electric field
D	electric displacement current
B	magnetic flux density
H	magnetic field
J or j	current density
D	electric displacement current
q	electric charge
μ	magnetic permeability
ε	electric permittivity
σ	electric conductivity
ω	angular frequency
k	wave number
i	$\sqrt{-1}$
Z	impedance tensor
Φ	phase tensor
$T_x,\ T_y$	vertical magnetic field transfer functions
R	rotation matrix
t	twist angle
S	shear angle
θ	strike
κ	Swift's skew
ν	phase difference
η	phase sensitive skew
Σ	rotational invariant
α	strike direction (angle)
β	skew angle
Φ_{max},Φ_{min}	maximum and minimum of phase tensor ellipse
N_e	total number of internal nodes
N_d	total number of data points
$\mathbf{A_m}$	coefficient matrix
e	nodal electric field vector
s	source vector
ϕ	potential field
I	current
K	geometric factor
$\tilde{\mathbf{m}}$, **m**	model parameter vector
$\mathbf{m_0}$	apriori model
$\tilde{\mathbf{d}}^{obs}$, $\mathbf{d}^{obs}$	observed data
$\tilde{F}$ ($\tilde{\mathbf{m}}$), F (**m**)	forward mapping
$\mathbf{C_d}$,$\mathbf{C_m}$	data and model covariance matrix
φ	penalty function
J	jacobian matrix
g_w	up-weighting factor
δ	skin depth

Chapter 1

INTRODUCTION

1.1 Preamble

The aim of geophysical investigations is to generate three dimensional (3D) geological map of earth interior. By measuring physical fields on or near the earth surface, geophysicists determine the physical properties of subsurface information. The examples of such physical fields are seismic, gravity, magnetic, thermal, electrical, electromagnetic and magnetotelluric.

The characteristics of these fields are governed by the properties of medium in which they propagate as well as the properties of their sources. The highly variable of all the physical properties of the earth materials is electrical resistivity ($10^{-4} < \rho < 10^{8}$) [121]. This large range of the resistivity values of the subsurface formation is an advantage of using resistivity values to determine subsurface structure, composition and inhomogeneities.

Magnetotelluric (MT) method is used to investigate various problems, at different depth scales, in diverse geological environment. MT data comprises natural time varying orthogonal components of electric and magnetic fields measured simultaneously. Its interpretation provides electrical resistivity image of the earth's interior. Electrical resistivity is sensitive to the amount of fluid/water present in pore spaces, to salinity of fluid, to temperature, to the amounts of partial melt, graphite and conducting minerals present in the subsurface formations. The derived electrical resistivity image of the subsurface can be used to decipher the amount and type of fluid distributed in pore spaces, to decipher the geothermal reservoir and to delineate the partial melt and conducting minerals present in the crust. This information can be used to solve various problems related to crustal

structure, fault geometry in depth, earthquake related studies, geothermal, mineral and hydrocarbon exploration [12, 13, 21, 23, 33, 50, 57, 197, 234]. Based on the frequency used in the investigations, MT methods are further classified as Audio- frequency Magnetotelluric (AMT), Broad Band Magnetotelluric (BBMT), Long period Magnetotelluric (LMT), Radio Magnetotelluric (RMT) etc.. In literature BBMT is generally referred as Magnetotelluric (MT) [23, 70]. I will follow the later convention in this thesis.

Direct Current Resistivity (DCR) method uses the concept of four electrode system for measuring the electrical resistivity variation, in near surface formation. Presently, Electrical Resistivity Tomography (ERT) are routinely used for the measurements. In ERT a large number of electrodes are deployed along a predefined profile line with fixed inter-electrode spacing. All the electrodes are connected to the resistivity meter through a multi-core cable. For each measurement, the resistivity meter automatically selects a particular set of four electrodes through a software (*Electre Pro*) designed sequence, preloaded in the system. Each measured apparent resistivity value can be considered as a weighted volume average of true point resistivity of the region sensed by the equipment. DCR methods have variety of application related to near surface investigations e.g. geohydrological, environmental, geotechnical etc. [91, 225, 258].

Present thesis is devoted to 3D MT and DCR investigations at selected sites in Uttarakhand, India. More specifically, I recorded some MT and DCR data and integrated them with the existing MT, Radio Magnetotelluric (RMT), DCR data recorded earlier by IIT Roorkee group from Uttarakhand, India for 3D inversion.

1.2 Brief Review of Literature

The MT and DCR methods have been extensively used in literature for solving various geological problems at shallow, intermediate and deeper depth scales. There is a vast amount of literature available on the MT and DCR investigations. It is difficult to present here a complete review on the subject. I, therefore, restrict my review, relevant to the present work. MT and DCR methodology are discussed in several textbooks [24, 26, 43, 101, 155, 263] written on the subject. Generally, the MT and DCR investigations were carried out independently. I, therefore, review relevant literature on theory and field studies based on MT and DCR methods separately in following sections.

1.2.1 Magnetotelluric Method

As the MT method deals with natural electromagnetic waves, to apply electromagnetic induction to the Earth, few simplified assumptions are considered [36, 100, 202]. Theory of MT is based on Maxwell's equations. For data recording, the horizontal components of electric and magnetic fields are measured simultaneously at the earth's surface. From these measurements, MT transfer functions, the so-called impedance tensor is estimated.

Before modeling and inversion, dimensionality and directionality analysis of impedance tensor is an intermediate step. Dimensionality analysis suggests most appropriate model for given MT dataset for further inversion. Several techniques have been presented and routinely used for this purpose. Some commonly used dimensionality analysis and impedance decomposition techniques are: phase-sensitive skew analysis by Bahr [15, 16], the Mohr circle analysis by Lilley [120], the Groom and Bailey decomposition by Groom and Bailey [75], galvanic tensor decomposition by Chave and Smith [44], rotational invariant analysis by Weaver et al. [250], multi-site and multi-frequency tensor decomposition by McNeice and Jones [141], the phase tensor analysis Caldwell et al. [37] and WAL rotational invariants by Marti et al. [137]. For a review of MT techniques including modeling, dimensional analysis and interpretation one can refer to [43, 143, 163].

Forward modeling is an essential component in the inversion algorithm. The numerical techniques used for 3D MT and DCR forward modeling in MT are: Integral Equation Method (IEM), Finite Element Method (FEM), and Finite Difference Method (FDM) [54, 55, 65, 74, 115, 128, 145, 156, 159, 204, 205, 256, 254]. FDM is perhaps one of the most commonly used approach. In the inversion algorithms a meaningful model was found while fitting the data to an acceptable level. The algorithms developed for MT and DCR data inversion, includes the Occam's inversion [e.g. 47, 53, 210], the Gauss–Newton (*GN*) method [e.g. 81, 189, 190], the Gauss–Newton with the conjugate gradient (*GN-CG*) method [126, 204, 210], the quasi-Newton (*QN*) method [10, 80], and the non-linear conjugate gradient (*NLCG*) method [e.g. 46, 62, 98, 159, 186, 204].

Significant 3D effect in MT profile data has initiated the application of 3D inversion for profile data. Subsequently, 3D inversion of MT profile data were implemented over synthetic case [116, 211] and field data [57, 161, 202, 253]. These studies shows that when the data contains 3D effects, 2D inversion can mislead the interpretation. The ambiguity in the data can be overcome by using 3D inversion where it is not necessary to make an

assumption about the strike direction as recommended in 2D inversion. Such inversion can recover anomalies correctly as demonstrated by Newman et al. [161]. With 3D inversion, structures may be put outside the profile where they belong although their size, shape, depth and location cannot be determined exactly. This is in contrast to 2D inversion where structures are inserted beneath the profiles which could lead to misinterpretation [211]. Station locations need not be projected on the profile line for 3D inversion and hence a 3D model geometry is likely to be more reliable. For more advantages of 3D over 2D inversion readers can refer to Siripunvaraporn [208].

The disadvantage of 3D inversion is the large computational cost in terms of both computation time and memory. In 3D inversion the number of model parameters increases exponentially and are of the order of hundred-thousand to million, hence, the inherent complexities associated with large number of model parameters become more challenging. In spite of these challenges, 3D inversion is being performed for meaningful data interpretation.

Case Studies

MT methods have been used in solving various geological problems in different depth scale. A review of field studies is given below.

In Himalayan region, MT methods were used to study the resistivity structure and geometry of various Himalayan thrusts (Main Frontal Thrust (MFT), Main Boundary Thrust (MBT) and Main Central Thrust (MCT)) along various segments of Himalayan arc [7, 72, 89, 112, 118, 144, 170, 183, 216]. Electrical resistivity variation along and perpendicular to Himalayan arc was correlated with thrust geometry, partial melt, fluid released due to metamorphic dehydration and geothermal regime [112, 118, 144, 183]. In these studies the nature of the high conductivity associated with the Main Himalayan Thrust (MHT) in the Higher Himalaya indicated the presence of metamorphic fluids released due to the under thrusting of Indian plate.

In Eastern Indian Craton, Bhattacharya and Shalivahan [27] and Shalivahan and Bhattacharya [196] conducted MT studies and resolved the boundary between lower crust and upper mantle. The identification of crust-mantle boundary was possible due to the absence of a conducting lower crust. A geothermal study was carried out near the Bakreswar hot spring, in Eastern India by Sinharay et al. [207]. They reported a deep geothermal

reservoir in the northwestern part of the survey area.

In Central India Gokarn et al. [71] studied the archean Bundelkhand craton and observed high resistivity subsurface in the form of layers, mainly observed for the Archean-Proterozoic regions, indicating a northward dipping tectonic fiber immediate north of this craton. Similarly, MT studies were used by Gokarn et al. [70] at 50 stations to delineate the geoelectric structure of a 400 km long granite–greenstone terrain of Dharwar, southern India. The geoelectric model delineated a suture along the Chitradurga–Gadag schist belt, due to the thrusting of the West Dharwar craton beneath its eastern counterpart. Rao et al. [182] conducted MT studies in central India across the Narmada Son lineament (NSL) through 24 sites in a north-south oriented profile. The resistivity structure indicated two deep-seated conductive features, one on the southern flank due to magma intrusion into the crust of the Satpura horst and other on northern side below Dorwa on the Narmada graben caused by the tectonic activity and partially molten magma emplacement. Danda et al. [51] performed broadband and LMT studies along $\sim$ 200 km long east–west profile over the northern side of Cambay rift and observed highly conductive ($\sim$ 1000 S) layer of thick Quaternary and Tertiary sediments within the Cambay rift zone.

In Western India Danda and Rao [50] studied the Kachchh and Cambay rift basins and MT measurements were carried out at 68 stations along four east–west trending profiles across these basins to infer basement configuration and sediment thickness. The study indicated top conductive layers across the Kachchh and Cambay rift basins as the Cenozoic sediments and Deccan traps. Igneous intrusives and a Precambrian Aravalli–Delhi fold belt were also delineated on either side of the Cambay rift basin.

Some recent MT studies carried out in Indian continent are summarized in Table 1.1.

Table 1.1: Recent MT investigations in India.

Study area	Area/ Group	Working group	Profile	Major results with references
Himalaya	GHC, SH	IITR, KUK, CSRI-NGRI	3	Existence of transverse tectonic feature was discussed on the basis of geoelectric strike directions estimated from MT data recorded in Garhwal Himalayan corridor [88]. An updated electrical resistivity model of GHC was presented [216]. Topographic correction based on impedance tensor correction algorithm was presented with examples of corrections applied on Sikkim Himalaya data [114].
IGP	IGP	CSIR-NGRI	1	Thickness of sediments and basement topographic variation were estimated along profile between Hamirpur to Rupadiah [132].
Gujarat	SR, TG, KHH, CH, B-EQ, CB	CSRI-NGRI, IIGM, AU, ISR, GERMI	14	MT investigation in and around hot water spring indicated high conductive thermal influx of mantle exchange of heat to lower crust, resistive Precambrian crust, sediment thickness of north dipping KMF, and new fault [146, 148]. Heat flow values in the Cambay basin filled with fluids were linked with the heat source at deeper levels [149]. Conductive features correlated with the SWF and KMF basement configuration was delineated [22, 150]. Basement fracturing was correlated with heat exchange between the deeper geothermal source and near by hotwater spring [147]. 3D crustal resistivity structure beneath the Wagad aftershock zone of the Bhuj earthquake was delineated [13].
Mahar--ashtra	KW	CSRI- NGRI, OU	9	Processing of culturally noise contaminated data of Koyna-Warna seismic zone was discussed by Borah et al. [30]. Identification of variation of the thickness of Deccan volcanics, nature of the granitic basement and lithospheric electrical structure in the Western Ghat were presented [169, 171]

Table 1.1 contd...

Study area	Area/ Group	Working group	Profile	Major results with reference
Eastern India	, DV PAB, EGMB	IIT(ISM), IITB, UCIL	4	Resistivity structure was used to confirm the southward extension of the EGMB beyond Ongole [42]. Low resistivity features were correlated with the presence of gold, silver, uranium and copper deposits in Singhbhum Mobile Belt [139]. Near surface conductive deposit of gold and sulfide mineralization zone in Proterozoic -Archean greenstone belts of of Eastern India craton were correlated with low resistivity features by Maurya et al. [140].
Central India	NSL, CITZ	CSRI-NGRI	2	Extension of igneous body of large igneous province of Deccan Volcanics in the NSL region was explained on the basis of resistivity model [172]. Conductive to moderately conductive structures were correlated with various shear/faults, granulitic belts and occurrence of lower crustal Earthquake [12, 14]
Dharwar	DC, BRCM	CSRI-NGRI, CIST	3	Evidence for mantle suture and plume--continental interaction, hotspots, the metasomatized fluids inferred by low resistivity near Billigiri Rangan massif and resistivity structure of kimberlite melts zone in Dharwar craton are discussed [131, 177, 176].
South India	CuB	IIGM, CSRI- NGRI, ONGC	1	Dipping resistive crustal layer in the NE parts of Cuddapah basin inferred as E-W compression along eastern margin during the Neoarchaean-Neoproterozoic tectonic convergence between India and east Antarctica was discussed [110].

In table the acronyms used are as follows:- B_EQ: Bhuj Earthquake, BRCM: Billigiri Rangan Charnockitic Massif, CB: Cambay Basin, CH: Chabsar, CITZ: Central India Tectonic zone, CuB: Cuddapah Basin, DV: Dalma Volcanics, DC: Dharwar Craton, EGMB: Eastern Ghat Mobile Belt, GHC: Garhwal Himalayan Corridor, IGP: Indo-Gangetic Plain, KHH: Kachchh, KMF: Kachchh Mainland Fault, KW: Koyna Warrna, NSL: Narmada Son Lineament, PAB: Proterozoic-Archean Greenstone Belt, SC: Singhbhum Craton, SH: Sikkim Himalaya, SR: Saurashtra Region, SWF: South Wagad Fault, TG: Tuwa-Godhra. AU:

Andhra University, CSIR-NGRI: Council of Scientific and Industrial Research-National Geophysical Research Institute, GERMI: Gujarat Energy Research & Management Institute, IIGM: Indian Institute of Geomagnetism Mumbai, ISR: Institute of Seismological Research Gandhinagar, IITB: Indian Institute of Technology Bombay, IITR: Indian Institute of Technology Roorkee, IIT(ISM): IIT (Indian School of Mines) Dhanbad, KUK: Kurukshetra University Kurukshetra, ONGC: Oil and Natural Gas Corporation, OU: Osmania University, UCIL: Union Carbide India Limited.

The INDEPTH (INternational DEep Profiling of Tibet and the Himalaya) is one of the significant multi-national and multi-institutional geophysical project in which MT component was included [17, 220, 237, 238, 251]. Wei et al. [251] shows the presence of high conductivity fluid at the depth 15-20 km in the southern Tibet and at the depth of 30-40 km in the northern Tibet. Bai et al. [17] observed two major channels of high conductivity ($0.1 - 0.3$ Ωm) at a depth of 20-40 km and these channels extend horizontally more than 800 km from the Tibetan plateau into southwest China. Unsworth et al. [238] also observed crustal melting in the Himalaya from northern Tibet. Spratt et al. [220] indicated several conductive structures within the Tibetan crust near the Yarlung-Zangbo suture zone.

Moorkamp et al. [152] studied the crustal and mantle weak zones related to the 2017 Botswana earthquake sequence and seismicity in area. They used the MT data from the publicly available SAMTEX dataset for 81 stations in the vicinity of the hypocenter. The occurrence of earthquake was explained as reactivation in the opposite sense to the original fault movement. They showed that all earthquakes occur above a region of low velocities and relatively high resistivities.

Beka et al. [23] investigated the geothermal potential using crooked profile broadband MT (0.001–1000 s) data collected on Spitsbergen. They inverted full MT impedance tensor data along with the tipper to view the 3D structure and nearby off profile features. The inverted 3D model indicated fractures, localized and regional fault systems and igneous intrusions in near surface region in mesozoic platform cover deposits.

Komori et al. [109] also documented the effect of the hydrothermal alteration on the surface conductivity of rock matrix. Amatyakul et al. [2] studied the shallow geothermal fluid reservoir of Fang geothermal system, Thailand. 33 MT sites were deployed on the southern part of the Fang geothermal area. In the 3D resistivity model a high resistivity feature was interpreted as the crystalline granitic rock, while the intermediate resistivity

feature was associated with the Fang sedimentary basin. The resistivity contrast between the higher and lower resistivities helps revealed the orientations of the major Mae Chan Fault (MCF) and the two local faults in the area. Various other researchers [e.g. 49, 85, 92] also used MT for geothermal studies.

In the central Andes a long-period magnetotelluric (LMT) study was carried out by Unsworth et al. [239] to investigate area in the back arc of the South American subduction zone which is similar to subduction of Indian and Eurasian plate. The geoelectrical structure resolved a broad highly conductive feature in the middle and deeper crust beneath the high plateau. Later, several MT investigations were carried out near the San-Andreas fault zone [e.g. 20, 233, 234]

LMT investigations were carried out near South American continental margins by various authors, the 32 sites MT data was used by Brasse and Soyer [34] from the Southern Chilean Andes, Brasse and Eydam [32] carried out LMT at 28 sites beneath the Bolivian Orocline and study its relation to subduction. Both the studies revealed moderately high conductivities (≈ 0.1 S/m) in the mid and deep crustal depths. Smirnov and Pedersen [212] conducted MT experiments near the Sorgenfrei-Tornquist-Zone (STZ) (northwestern part of the Baltic shield), and observed zones of high conductivity in the lower crust and uppermost mantle.

1.2.2 Direct Current Resistivity Method

DCR method is relatively much simpler and mainly used for shallow subsurface investigations. Field data recording and inversion is much easier in comparison to MT method. For modeling and inversion, numerical techniques like FEM, FDM, etc. are routinely used. However, Several developers have used the IEM for DCR modeling [e.g. 60, 165, 255]. Dey and Morrison [58] developed a 3D FDM algorithm to evaluate the potential for a point current source. Since then various algorithms have been developed. [e.g. 124, 125, 203, 218, 219, 262]. FEM technique for DCR modeling was implemented by various workers [e.g. 28, 77, 188, 260].

Petrick Jr et al. [173] determines the positions of conductive anomalies using the concept of alpha centers. Rijo [185] performed inversion by using data bank of forward solutions for a certain 3D models while inversion based on the Born approximation was used by Li and Oldenburg [119]. Shima [200] used FEM to improve the result obtained using alpha

centre method. Park and Van [166] published the 3D inversion scheme using FDM and least square inversion. Since then various authors have presented inversion algorithms [e.g. 77, 122, 188, 203, 261]. In these algorithms, the forward solutions are generally obtained by FDM or FEM and inversion are based on Gauss–Newton (or its variant) technique. For the 3D case the problem is large hence, explicit computation and storage of the Jacobian (sensitivity) matrix is avoided [e.g. 261]. DCR field studies relevant to the present work are reviewed in the following.

Case Studies

The DCR method have variety of application, mainly related with shallow subsurface investigations. It has been extensively used for hydro-geophysical applications, environmental studies, geotechnical, archaeological studies, etc [1, 48, 52, 56, 63, 225]. Electrical resistivity and seismic refraction, are increasingly being used in combination with the borehole, pressure probe and other geotechnical investigations such as Standard Penetration Test (SPT) [1, 84, 107, 225, 226], for solving near surface geological problems.

Coscia et al. [48] used 3D crosshole ERT for investigated of the hydrogeological properties and responses of a productive aquifer in northeastern Switzerland. Pidlisecky et al. [174] determined the subsurface distribution of saltwater- and freshwater-saturated sediments and the geologic controls on fluid distributions along the coast of Monterey Bay (6.8-km). Di Maio et al. [59] used 2D ERT to define the heterogeneity of aquifer system, complex stratigraphic sequences and groundwater flow systems near the coastal alluvial plain of Sarno River, Italy. They identified two aquifers using integrated 3D hydrogeological-geophysical model.

Chambers et al. [41] investigated dolerite quarry and landfill site using 2D and 3D DCR method. The Wenner array was used along intersecting survey lines. Dolerite sill gave resistive sheet-like feature, while the fault zones were defined by contrasting bedrock resistivities. The 3D resistivity model delineate the position of the boundaries and zone of leachate migration from the landfill. Høyer et al. [86] used six different geophysical methods to estimate the risks for leakage and contamination of groundwater due to landfill in the island of Samsø, Denmark. For this study, DCR survey was carried out around 15 profiles across the landfill. They show very low resistivities in the area at the landfill. The chargeability parameters were also used to verify the source of the low resistivities. Maurya

et al. [138] used the time-domain spectral induced polarization for subsurface imaging of contaminated sites at the Grindsted stream (Denmark), where contaminated groundwater from a factory site discharges to the stream. 2D ERT measurements were carried out around seven parallel profiles. The IP-derived permeability and water conductivity values were correlated and formation factor was estimated.

Ramirez et al. [181] used DCR technique for detection of leaks in underground storage tanks. The investigation of an abandoned mining dump which contains slag material originating from steel production were investigated by Günther et al. [77]. DCR studies were successfully used for the prediction of the location of future rupture surfaces of a slowly moving loess landslide along the River Danube in South Hungary [226, 227].

Jamal and Singh [91] used very low frequency electromagnetic (VLF-EM) and electrical resistivity methods for detection of groundwater bearing fracture zones in hard rock area of Sangod Block, Kota District, Rajasthan. The results of the study showed the presence of fracture zones at a depth range of 10 m to 30 m oriented in the NE-SW and NW-SE direction.

Hasan et al. [83] carried out 2D ERT and self-potential survey to delineate the fracture zones in hard rock and estimated the groundwater reserves within the weathered terrain at Huangbu, China. The integration of ERT and self-potential with joint profile method reveal five fracture zones. The 2D ERT models define the fractured zones by low resistivity and the fresh bedrock by high resistive.

Ogilvy et al. [164] developed Automated Time Lapse Electrical Resistivity Tomography (ALERT) system for the long term monitoring of coastal aquifers. They buried an electrode array, below the dry river bed. The electrical images obtained were interpreted for studying the hydrogeologic features including the interface between seawater and freshwater.

Resistivity prospecting was employed for an archaeological survey to detect the remnants of wall foundations of the ancient city of Europos, northern Greece [236]. Argote-Espino et al. [5] used 3D ERT and identified four anomalous areas of interest at archaeological structures site of Teteles de Ocotitla, Tlaxcala, Mexico. Eissa et al. [63] compared different 2D ERT arrays for detection and characterization of near-surface buried objects near brownfield sites. They showed that the Wenner and dipole-dipole arrays were best for the detection of wall foundation. Whereas, the dipole-dipole arrays were good in delineating the top of the wall foundation. The archaeological excavations confirmed the results obtained using the geophysical method. Negri et al. [157] also carried out a 3D ERT survey to resolve

the interpretation problems in ground-penetrating radar (GPR) survey near the archaeological excavations at Muro Leccese (Lecce), Italy. The archaeological remains were found at about 0.3 m depth. The archaeological site of Sagalassos, Turkey was investigated using ERT methods by De Giorgi and Leucci [52]. They investigated three different areas and resolve the location, depth, size and extent of buried archaeological features. The results shows a deep depression related to clay quarry, a number of tombs and defensive walls.

1.2.3 Joint Inversion of RMT and DCR Data

All inversion techniques are in general associated with ambiguities and non-uniqueness. These problems are solved by using additional information and controls about the expected model. The joint inversion of different datasets, which look to the same subsurface structure, is an effective tool to minimize the problems in individual inversion [153, 195, 199, 246]. If different datasets see the same zone of subsurface structure, then the limitation of one dataset is compensated by the other dataset. Finite data acquired in surveys is usually restricted to the surface of the Earth or the shallow subsurface, often with relatively large spacing between measurement sites, and associated with different degree of noise. In such a situation different models can explain the observed data, creating ambiguity in their interpretation. Applying regularization stabilizes the inversion and creates a model with certain characteristics but does not alleviate the ambiguity problem [167]. Joint inversion approaches reduce the set of acceptable models by combining several geophysical datasets in a single inversion scheme and requiring the resulting model that explain all data simultaneously [246]. The sources of noise and its impact on different data often differ so that adding another method can improve the results more than adding more data of the same type. Consequently joint inversion approaches have gained some attention recently.

Considering the advantages of joint inversion, MT data has been analyzed in combination of other geophysical methods like DCR, seismic. Through a synthetic data Sharma et al. [199] showed that the joint inversion of MT and seismic data yields better layer parameters, than the individual MT or seismic inversions. Manglik and Verma [134] and Manglik et al. [135] delineated sediments below flood basalts by using seismic and MT data and delineated a four-layered crustal structure, of low velocity and resistivity, in the Southern Granulite Terrain, India. Moorkamp et al. [153] presented a synthetic example for joint inversion of MT, gravity and seismic refraction data and demonstrated its usefulness. They demonstrate

that cross-gradient coupling is better approach the direct parameter relationship for the joint inversion of data types, having different physical properties.

Vozoff and Jupp [246] combined MT and Schlumberger soundings and inverted the data sets simultaneously for 1D structures. Other examples of lD joint inversion were presented by Gomez-Trevino and Edwards [73] for CSEM and Schlumberger sounding and by Raiche et al. [180] for coincident loop transient EM with Schlumberger sounding. 2D joint inversion were performed by various workers [e.g. 3, 39, 187]. Seher and Tezkan [195] used RMT and DCR measurements for the characterization of conducting soils. Yogeshwar et al. [258] studied the impact of sewage irrigation and groundwater contamination near Roorkee in north India using the RMT and DCR data. Tezkan et al. [228] used RMT and transient EM for investigation of industrial and domestic waste sites in Germany. Through a synthetic study Singh [203] showed that the 3D joint inversion yields better model, than the individual MT or DCR inversions. Tezkan et al. [228] used the Radio Magnetotelluric (RMT) and transient EM to study the waste deposit site in Cologne (Germany) and was able to resolve only the top of the waste site and the lateral boundary, due to the highly conducting waste deposit. Tezkan et al. [229] also showed that the RMT technique is a powerful tool for waste site exploration.

1.3 Geological Setting of Study Area

The study area is located in Uttarakhand state of Northern India region. This includes south of Himalaya foothills region, Indo-Gangetic Plains (IGP) around Roorkee area and Garhwal Himalayan Corridor (GHC) in Himalayan region. IGP is an alluvial plain formed of sediments deposition by Himalayan rivers. Himalaya originated due to continental-continental collision tectonics between the Indian and Eurasian Plate. The Indian Plate underthrust beneath the Eurasian plate. The total convergence between Asia and India has been estimated to be about 2000-3000 km [151], of which about 200-500 km could have occurred along the Himalaya by repeated overthrusting of the slices of Indian crust on itself [240, 242]. The process of continuous convergence and repeated overthrusting resulted in the creation of a complex system of thrusts faults in Himalayan region.

Geologically, the GHC is divided into four major litho-tectonic units, separated by three major south verging thrusts. Starting from the southernmost part the major Himalayan

thrusts are, the Main Frontal Thrust (MFT), the Main Boundary Thrust (MBT) which hades northwards [105, 106] at 30° to 40° and the Main Central Thrust (MCT). In the study area the MCT is defined as a zone bounded by the Munsiari Thrust in south and the Vaikrita Thrust in north which are also referred as MCT-I and MCT-II, respectively [130, 232, 242]. Viewing from south to north, the Indo-Gangetic Plain (IGP) is the southernmost lithotectonic unit with the peninsular shield in its south followed by the Sub-Himalayan (SH) region in North which rises abruptly above the IGP along MFT. The SH predominantly consists of 5-6 km thick tertiary and quaternary sediments. Further North is the Lesser Himalayan (LH) region, which lies between MBT in South and MCT in North. The LH region is further divided into two zones, the southern zone lying between MBT and the Sri Nagar Thrust (SNT) is the Outer Lesser Himalaya and the northern zone lying between SNT and MCT-I is the Inner Lesser Himalaya. The northernmost unit of the study area is the Higher Himalayan crystallines (HHC) and that has an average elevation of 4500 m. In the main Himalayan arc, the MFT, MBT and MCT generally trends in northwest direction. Besides these thrusts, a number of faults and ridges are also oriented transverse to the main Himalayan arc with strike in NE-SW direction [106]. Northeast trending Delhi-Haridwar Ridge (DHR) into the LH is an example of such a feature [192]. Auden [9] first indicated the rejuvenation of the Aravali Mountain which, he believed, extended northeastward into the Himalaya. Based on the analysis of gravity anomaly Qureshy [178] and Godin and Harris [69] explained the prolongation of Aravali in the NNE-SSW direction and also the existence of across the strike discontinuities in the Indian crust beneath the Himalaya.

Besides these major thrust systems, there exist fractures, faults and folds trend oblique and transverse to the main Himalayan arc [9, 69, 240]. Seeber and Armbruster [194] have postulated a gently dipping thrust plane under the Sindhu-Ganga Plains, the Sub- and Lesser Himalaya. The authors call this plane the detachment surface, which coincides with the upper surface of the subducting Indian lithosphere. The sections of the plate boundary that have not ruptured in the past 100 years are indicated as seismic gaps and are identified as locales of high potential for future great earthquake [102]. Seismological studies have revealed several oblique and transverse features on the basis of alignments of epicenters of major and small earthquakes [105].

Recently, the geological information has been integrated with the aeromagnetic, gravity and seismic data to define the locations and sizes of the ridges in Himalayan region

[68]. Godin and Harris [69] have used gravity data to explain the basement cross-strike discontinuities in the Indian crust beneath the Himalayan orogen. In Garhwal Himalaya, a transverse conducting structure is delineated by analyzing the magneto-variation data [6]. Further, in the Sikkim Himalaya, existence of transverse tectonics structure is explained on the basis of Magnetotelluric studies [133].

The region is known to be seismically active, the seismicity in the region is mainly confined around MCT, an E-W trending Alakananda Fault (AF) and an N-S trending Nandprayag Fault (NF). The Chamoli Earthquake on March 28, 1999 of Mb 6.3 (USGS) occurred on the south of MCT at the Basement Thrust and was succeeded by large number of aftershocks (more than 300). More than 40 of these aftershocks range between magnitude of 6 and 4. Kayal et al. [97] represents the region around AF after the 1999 Chamoli Earthquake with isoseismal VII, with the trend of E-W direction. They describe this region with generation of landslides, ground fissures, and emergence of new springs and drying of some old springs.

The metamorphic pressure and temperature across the MCT increase from 5 kbar and 550°C in the LHS to 14 kbar and 850°C at 3 km above the MCT in the Higher Himalaya [217]. The region contains many known and unknown geothermal systems [76, 179] characterized by tertiary magmatism, metamorphic events, geothermal gradient and quaternary orogenic activity. Thermal springs in MCT zone are confined within 45 km in North-South (30 km to north and 15 km to south) and 10-40 km wide range starting from Alakananda valley and going upto Tons valley in East-West direction. The hot springs of the Alakananda Valley have temperature gradient of $60 \pm 20°C/km$ and the heat flow of $130 \pm 30 mW/m^2$ [76]. The hot springs of central crystallines show high temperatures of 55°C to 94°C. Most of the thermal springs emerge through joints and are controlled by interface of lithological units.

1.4 Scope of Present Work

The objective of this work is to apply 3D inversion methodology to the MT, RMT and DCR data from Uttarakhand region. Part of the dataset for the present investigation were recorded earlier by IIT Roorkee group [89, 144]. Some of the MT and DCR data were also added by me during the present investigation. The entire datasets are integrated and 3D inversion

techniques were implemented on the following four sets of independent data.

(i) MT data recorded on Roorkee-Gangotri profile from Garhwal Himalayan Corridor (GHC).

(ii) MT data recorded from Chamoli Region in seismically active Main Central Thrust (MCT) zone.

(iii) DCR data recorded at a bridge site in Tehri region of GHC.

(iv) DCR and RMT data recorded in IGP from Roorkee area and inverted individually and jointly.

The resulted geoelectrical models from above datasets were then interpreted in terms of geological structure and tectonics at shallow, intermediate and deeper depths.

The above work is systematically presented in this thesis in the form of seven chapters in following manner.

1.5 Thesis Layout

Relevant literature review and geology of study area is discussed in first chapter. The second chapter consists of MT and DCR methodology. Forward and inverse modeling as implemented in the code *AP3DMT-DC* [204] have also been presented in chapter two, with discussions on (i) grid generation and (ii) modeling/ inversion.

Third chapter discusses the results of 3D inversion of MT data recorded along Roorkee-Gangotri (RG) profile in GHC of Uttarakhand, India. The impedance tensor response for the 39 sites in the period range of 0.01 to 1000 s and the vertical magnetic field transfer function (VTF) response at 19 sites in the period range from 1 to 1024 s were used for this purpose. A number of synthetic experiments were performed to determine the reliability of off-profile model features. Through synthetic experiments, effect of resistivity of initial guess model, time period range and MT site density were estimated. The information obtain from synthetic experiments were used to meaningfully interpret the 3D resistivity depth model. Tectonics, geological and seismological aspects of the obtained inverted 3D resistivity models were discussed.

Fourth chapter discusses the 3D inversion of MT data from Chamoli region. MT data were recorded at 28 sites, with varying site density in and around MCT zone in Chamoli were used for this purpose. Inverted model features are consistent with seismological models

available for the region.

In the fifth chapter, 3D inversion of DCR investigations carried out in the Tehri area located in Lesser Himalayan region are presented. The main objective of this investigations was to determine near surface geology at a proposed bridge site. Six ERT profiles were recorded and interpreted using 2D and 3D inversion. Electrical resistivity values were further correlated with SPT data along selected profiles. Linear correlation has been obtained between the resistivity and the N-values for this study.

The sixth chapter is devoted to the joint DCR and RMT investigation in Roorkee region. In this study 3D inversion is performed on DCR and RMT data individually and jointly. The objective of this study was to determine the amount and extent of groundwater contamination due to untreated sewage water irrigation and waste disposal practice. Resistivity depth model obtained by 3D inversion are compared with corresponding 2D resistivity model derived from the same dataset earlier. 3D resistivity model shows a better resolved model of the area which explains amount and extent of groundwater contamination in the region.

Major conclusions of the present study along with the scope of future work are presented in chapter seven.

Chapter 2

METHODOLOGY

2.1 Preamble

The Magnetotelluric (MT) method and Direct Current Resistivity (DCR) methods provide 3 Dimensional (3D) resistivity structure of the subsurface. However, the two methods are governed by different physical principle. MT method uses the principle of EM induction whereas in DCR method electrical current is galvanically injected into the ground. MT methods is generally used for deep investigations whereas DCR method is preferred for shallow investigations. Although the theory of the two methods are different but from numerical computation point, DCR forward problem is similar to solving static divergence correction and is implicitly solved in MT algorithms (as implemented in *AP3DMT-DC*). Thus, initially developed code, *AP3DMT* [204], for 3D MT inversion, has been easily extended for DCR problem and the code is referred as *AP3DMT-DC* [203].

In this chapter, I will discuss the theory of MT and DCR methods. Then, MT transfer functions, dimensionality and directionality in impedance tensor are discussed. Various aspect of forward modeling using Finite Difference Method (FDM) like model discretization, boundary conditions, matrix solver, pre-conditioner and static divergence correction are discussed. Individual and joint inversion theory of MT and DCR data is also presented. Finally, a brief description of the code *AP3DMT-DC*, used for 3D inversion of MT and DCR data, either individually or jointly, is discussed.

2.2 Electromagnetic Theory

MT method is developed on the principle of electromagnetic induction. Theory of MT method is governed by Maxwell's equations defining the relationship between time varying electric and magnetic fields as,

$$\nabla \times \mathbf{E} = -\frac{\partial \mathbf{B}}{\partial t}, \tag{2.2.1}$$

$$\nabla \times \mathbf{H} = \frac{\partial \mathbf{D}}{\partial t} + \mathbf{J}, \tag{2.2.2}$$

$$\nabla \cdot \mathbf{B} = 0, \tag{2.2.3}$$

$$\nabla \cdot \mathbf{D} = q, \tag{2.2.4}$$

where, **E** is the electric field vector (V/m), **B** is the magnetic flux density vector (Wb/m^2), **H** is the magnetic field vector (A/m), **D** is the electric displacement current vector (C/m^2), and **J** is the current density vector (A/m^2).

The eq 2.2.1 is the Faraday's law which indicates that the time varying magnetic flux density induces electric field. The eq 2.2.2 is the modified Ampere's law, relating the current density and the electric displacement. The eq 2.2.3 is the Gauss's law for magnetism and indicates that magnetic monopoles does not exist and eq 2.2.4 is Gauss's law and shows that the electric field is the result of the distribution of electric charge.

In addition, the constitutive relations can be used to eliminate three of these and Maxwell's equations can be expressed using two vector fields only. For linear, isotropic media of electric conductivity, σ, magnetic permeability, μ, and electric permittivity, ε, constitutive relationships can be written as,

$$\mathbf{B} = \mu \mathbf{H}, \tag{2.2.5}$$

$$\mathbf{D} = \varepsilon \mathbf{E}, \tag{2.2.6}$$

$$\mathbf{J} = \sigma \mathbf{E}. \tag{2.2.7}$$

In MT method, the variations of the dielectric permittivity, ε, and the magnetic permeability, μ, for most rocks are very small in comparison to the variations of the

electric conductivity. Therefore, the free-space values for both ε and μ are used as, $\mu = \mu_o = 1.25566 \times 10^{-6}$ H/m and $\varepsilon = \varepsilon_o = 8.85 \times 10^{-12}$ F/m.

Using eq 2.2.5 $-$ 2.2.7 the eq 2.2.1 and 2.2.2 can be rewritten as,

$$\nabla \times \mathbf{E} = -\frac{\partial \mathbf{B}}{\partial t}, \tag{2.2.8}$$

$$\nabla \times \mathbf{B} = \mu_0 \varepsilon \frac{\partial \mathbf{E}}{\partial t} + \mu_0 \sigma \mathbf{E}. \tag{2.2.9}$$

2.2.1 Governing Equation

Combining eq 2.2.8 and eq 2.2.9 through curl operator, vector identity and assuming linear, isotropic medium and $e^{i\omega t}$ time dependence, we get,

$$\nabla \times \nabla \times \mathbf{E} + i\omega\mu\sigma\mathbf{E} = 0, \tag{2.2.10}$$

or

$$\nabla^2 \mathbf{E} = i\omega\mu\sigma\mathbf{E} = k^2\mathbf{E}, \tag{2.2.11}$$

where, $i = \sqrt{-1}$ and k = $\sqrt{i\omega\mu\sigma} = (1+i)\sqrt{\omega\mu\sigma/2}$ is the complex wave number. Alternatively, for magnetic field we get,

$$\nabla \times \rho \nabla \times \mathbf{H} + i\omega\mu\mathbf{H} = 0, \tag{2.2.12}$$

or

$$\nabla^2 \mathbf{H} = i\omega\mu\sigma\mathbf{H} = k^2\mathbf{H}, \tag{2.2.13}$$

where, ρ is the electrical resistivity.

2.2.2 MT transfer functions

The relation between electric field, **E**, and magnetic field, **H**, is given in terms of magnetotelluric impedance tensor (**Z**) by Cantwell [40] as,

$$\mathbf{E}(\omega) = \mathbf{Z}(\omega)\mathbf{H}(\omega), \tag{2.2.14}$$

where, ω is the angular frequency.

In terms of orthogonal components of electric and magnetic fields, eq 2.2.14 can be written as,

$$\begin{pmatrix} E_x(\omega) \\ E_y(\omega) \end{pmatrix} = \begin{pmatrix} Z_{xx} & Z_{xy} \\ Z_{yx} & Z_{yy} \end{pmatrix} \begin{pmatrix} H_x(\omega) \\ H_y(\omega) \end{pmatrix}, \tag{2.2.15}$$

where, **E** and **H** represents electric and magnetic fields along two orthogonal directions (x and y). From the impedance tensor (eq 2.2.15) the apparent resistivity and phase for ij (i,j=x and y) component can be derive as,

$$\rho_{ij} = 0.2T \left| \frac{E_i}{H_j} \right|^2 = 0.2T |Z_{ij}|^2, \tag{2.2.16}$$

$$\phi_{ij} = arctan\left(\frac{Im(Z_{ij})}{Re(Z_{ij})} \right), \tag{2.2.17}$$

where, T is time period.

Next, Vertical Magnetic Transfer function (VTF) or tipper as suggested by Vozoff [245] relates horizontal (H_x and H_y) and vertical magnetic field components (H_z) as,

$$H_z = \begin{pmatrix} T_x & T_y \end{pmatrix} \begin{pmatrix} H_x \\ H_y \end{pmatrix}, \tag{2.2.18}$$

where, T_x and T_y are the vertical magnetic transfer functions. The VTFs are also known as complex induction vectors. When induction vectors are plotted with Wiese convention [252] the vectors point away from conductor. The amplitude and the angle of the real part of the induction vector are computed as,

$$amplitude = \sqrt{Re(T_x)^2 + Re(T_y)^2}, \tag{2.2.19}$$

$$angle = arctan\left(\frac{Re(T_y)}{Re(T_x)} \right) \tag{2.2.20}$$

In Phase tensor method given by Caldwell et al. [37], the term phase tensor, Φ, relates real and imaginary part of **Z** and is defined by the relation,

$$\Phi = \mathbf{X^{-1}Y}, \tag{2.2.21}$$

where, $\mathbf{X}$ and $\mathbf{Y}$ are the real and imaginary parts of the MT impedance $\mathbf{Z} = \mathbf{X} + \mathbf{iY}$.

Written in terms of the real and imaginary components of $\mathbf{Z}$ in a Cartesian coordinate system (x_1, x_2), the phase tensor, Φ, in matrix form is written as [37],

$$\begin{pmatrix} \Phi_{11} & \Phi_{12} \\ \Phi_{21} & \Phi_{22} \end{pmatrix} = \frac{1}{det(\mathbf{X})} \begin{pmatrix} X_{22}Y_{11} - X_{12}Y_{21} & X_{22}Y_{12} - X_{12}Y_{22} \\ X_{11}Y_{21} - X_{21}Y_{11} & X_{11}Y_{22} - X_{21}Y_{12} \end{pmatrix}, \tag{2.2.22}$$

where, $det(\mathbf{X}) = X_{11}X_{22} - X_{21}X_{12}$ is the determinant of $\mathbf{X}$.

2.2.3 Dimensionality and Directionality Analysis

Dimensionality and directionality analysis is an intermediate step performed before modeling and inversion. The objective is to determine the dimensionality(1D, 2D and 3D) and geoelectric strike direction of the structure using impedance tensor which is estimated from recorded time series data.

Theoretically, For 1D resistivity structure the impedance tensor, $\mathbf{Z}$, reduces to scalar impedance and the components of impedance tensor in eq 2.2.15 can be written as,

$$Z_{xx} = Z_{yy} = 0; Z_{xy} = -Z_{yx} = Z. \tag{2.2.23}$$

In the presence of 2D resistivity structure, direction of strike can be estimated by aligning coordinate axis in the direction of strike and perpendicular to the strike direction. The Maxwell's equation is decomposed into two modes of polarization referred as transverse electric (TE-) and transverse magnetic (TM-). The impedance tensor components reduces to,

$$Z_{xx} = Z_{yy} = 0; Z_{xy} \neq Z_{yx}. \tag{2.2.24}$$

If the geoelectrical structure is 3D, all components of impedance tensor are non zero.

Impedance tensor characteristics given above are never truly satisfied in case of real/field data. The impedance tensor for field data is corrupted by the different degree of noise and the conditions in eq 2.2.23 and 2.2.24 are never truly satisfied. Several methods were developed and used for dimensionality analysis of field impedance tensor data. These methods [75, 16, 37, 137] efficiently handle different types of noise and errors in the field and determine most appropriate model dimensionality suitable for the given dataset. The methods used in this

thesis are briefly summarized in the following.

In Groom Bailey tensor Decomposition (GBD) (Groom and Bailey [75]) method the impedance tensor, is decomposed using the distortion parameters geoelectric strike, θ, twist angle, t, shear angle S and regional 2D impedance tensor,Z_{2D}, as,

$$\mathbf{Z} = R(\theta)tSZ_{2D}R^{T}(\theta), \tag{2.2.25}$$

where, $R(\theta)$ is a rotation matrix with angle θ, as geoelectric strike direction. Factorization of eq 2.2.25 enables a separation of determinable distortions in terms of twist and shear angles from the observed impedance tensor. The limiting values used for twist and shear angles is $|60|^{\circ}$ and $|45|^{\circ}$ respectively. The distortion parameters are estimated using a least square method by fitting the observed impedance tensor with the decomposition model.

The Bahr method (Bahr [16]) used four invariant parameters, derived from impedance tensor, to classify the types of the geoelectric dimensionality and distortion types that affect it. These are (i) the Swift's skew, κ, and measure the shift in $\mathbf{Z}$ from the 2D model, (ii) ν is a measure of the phase difference between the impedance tensor components, (iii) η is the phase sensitive skew and (iv) Σ is a measure of two dimensionality. In contrary to GBD method, in Bahr method the phase difference between the impedances of each column of the impedance matrix is minimized. The Phase Sensitive Strike (Bahr strike, θ) is used for the strike analysis. Depending upon the conditions given in Table 2.1 the dimensionality of model can be defined as 1D, 2D, 2D with 3D distortion (3D/2D) and 3D.

Table 2.1: Conditions used to find the dimensionality in Bahr Method [15].

Case	**Bahr Parameter Values**	**Dimensionality/ Distortion Type**
1	$\kappa < 0.1; \Sigma < 0.1$	1D
2	$\kappa < 0.1; \Sigma > 0.1$	2D
3	$\kappa > 0.1; \nu = 0$	3D/1D
4	$\kappa > 0.1; \nu \neq 0; \eta < 0.1$ $\kappa > 0.1; \nu \neq 0; 0.1 < \eta < 0.3$	3D/2D
5	$\kappa > 0.1; \nu \neq 0; \eta > 0.3$	3D

In the phase tensor analysis method, as given by Caldwell et al. [37], the dimensionality analysis is done using the phase tensor (Φ), which is defined as the inverse of the tangent of

the ratio between imaginary and real parts of impedance tensor (eq 2.2.21). The coordinate invariants determined and used for dimensionality analysis are, (i) strike direction (angle),α, (ii) the skew angle, β, a measure of the tensor's asymmetry, (iii) Φ_{max}, the maximum of phase tensor and (iv) Φ_{min}, the minimum of phase tensor value. The phase tensor ellipse is constructed using the, Φ_{max} as the major axis of ellipse, Φ_{min} as the minor axis of ellipse and $\alpha - \beta$ as the orientation of the major axis. For 1D case $\beta = 0$ and $\Phi_{max} = \Phi_{min}$, and ellipse transforms into a circle. In 2D case, $\beta = 0$ or $< 3^{\circ}$ and $\Phi_{max} \neq \Phi_{min}$. The alignment of Φ_{max} is parallel or perpendicular to the strike of the resistivity distribution or the model. The value of $\beta > 3^{\circ}$ indicates 3D feature in the model. A rapid lateral change in direction of the Φ_{min} and Φ_{max} also indicates towards the 3D structure in resistivity model.

WAL invariants method was given by Marti et al. [137] and it consists of seven independent invariants (I_1, I_2, I_3, I_4, I_5, I_6, I_7) and a dependent invariant **Q**. All the seven rotational invariants and the angle defining the orientation of the reference axes are defined from the magnetotelluric impedance tensor. Out of the seven invariants first and second (I_1 and I_2) define the 1D structure when the next four invariants are negligibly small. If the two invariants (I_3 and I_4) are also non negligible, the structure is said to be 2D and strike direction can be recoverable. The dimensionality with small scale galvanic distortions i.e. 3D/1D and 3D/2D structure are given by last three invariants i.e. I_5 to I_7. The non zero value of I_7 shows the 3D structure and strike is not recovered in this case.

Dimensionality analysis suggests most appropriate geoelectrical model suitable for the data. It also determines geoelectric strike direction for 2D structure. This helps in choosing appropriate modeling and inversion scheme for the data.

2.3 MT Forward Modeling Scheme

MT forward modeling computation can be implemented using approaches based on Finite Difference Method (FDM) [58, 122, 125, 127, 214, 215, 218], Finite Element Method (FEM) [28, 45, 77, 184, 188, 260] and integral equations [117, 165, 235, 247]. Each of these techniques has certain advantages e.g., integral equation methods are efficient in case of compact model, finite element is better suited for complex model geometry whereas finite difference (FD) is simpler in concept. Forward modeling computation presented in this thesis is based on FDM scheme.

In the following, I shall briefly discuss the various aspect of numerical computations used in MT forward modeling.

2.3.1 Finite Difference Formulation

The FDM can be used to solve Partial Differential Equations (PDE) for electric, **E**, (eq 2.2.10) or magnetic, **H**, (eq 2.2.12) field components. The eq 2.2.10 is reduced to three scaler PDEs for electric field components as,

$$-\frac{\partial^2 \mathbf{E}_x}{\partial y^2}-\frac{\partial^2 \mathbf{E}_x}{\partial z^2}+\frac{\partial^2 \mathbf{E}_y}{\partial x \partial y}+\frac{\partial^2 \mathbf{E}_z}{\partial x \partial z}+k^2 \mathbf{E}_x=0, \tag{2.3.1}$$

$$-\frac{\partial^2 \mathbf{E}_y}{\partial x^2}-\frac{\partial^2 \mathbf{E}_y}{\partial z^2}+\frac{\partial^2 \mathbf{E}_x}{\partial x \partial y}+\frac{\partial^2 \mathbf{E}_z}{\partial y \partial z}+k^2 \mathbf{E}_y=0, \tag{2.3.2}$$

$$-\frac{\partial^2 \mathbf{E}_z}{\partial x^2}-\frac{\partial^2 \mathbf{E}_z}{\partial y^2}+\frac{\partial^2 \mathbf{E}_x}{\partial x \partial z}+\frac{\partial^2 \mathbf{E}_y}{\partial y \partial z}+k^2 \mathbf{E}_z=0, \tag{2.3.3}$$

where, $k^2 = i\omega\mu_0\sigma$ denotes wavenumber and E_x, E_y and E_z are the components of electric field in x, y and z directions respectively.

The first step is discretization of model domain using appropriate grid lines parallel to co-ordinate axes. The staggered-grid [257], is used for more accurate solution of eq 2.2.10. Fig. 2.1 shows an example of field components in a typical cell in FDM mesh. The electric field components ($\mathbf{E}_x$, $\mathbf{E}_y$ and $\mathbf{E}_z$), are defined on cell edges and the magnetic field components ($\mathbf{H}_x$, $\mathbf{H}_y$ and $\mathbf{H}_z$) are defined on center of the cell faces. After discretization, each cell is assigned a constant conductivity value. To accommodate this change in conductivity at the interface of a cell, volume weighted average of the conductivity is computed and assigned to each interface. The forward problem is solved using appropriate boundary conditions. At the boundary faces the field is assumed to be due to 2D resistivity distributions. To simulate this condition, several sparsely spaced grid lines are added on all side of the model domain. The collection of all the discrete FD equations for all nodes, for a frequency, f, results in a matrix equation represented as,

$$\mathbf{A_m e} = \mathbf{s}, \tag{2.3.4}$$

where, $\mathbf{A_m}$ is a frequency dependent $N_e \times N_e$ sparse symmetric complex matrix with 13

non-zero elements per row; **s** is the N_e dimensional source vector and **e** is the N_e dimensional electric field vector at the internal nodes. The system matrix is transformed to a symmetric form by pre-multiplying it with a diagonal matrix whose elements depend on cell volume [66].

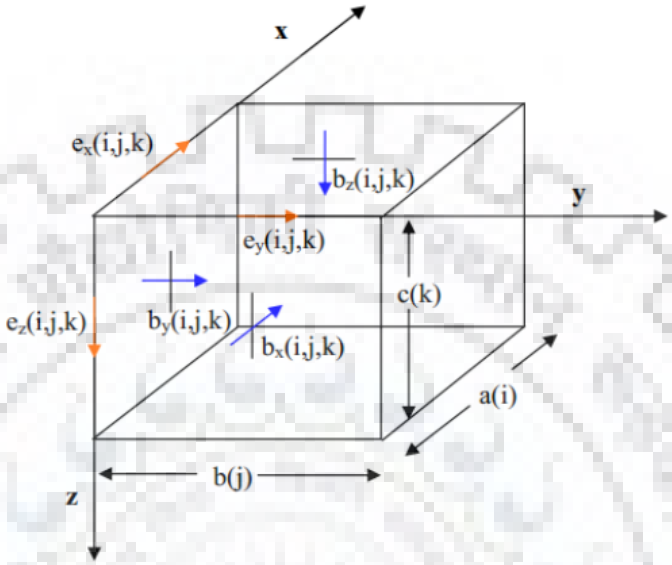

Figure 2.1: Staggered finite difference grid for solving the 3D MT forward problem with electric field components on the cell edges and the magnetic field components on the center of the cell faces [257].

The three components of the electric field are calculated for a current system which flows in N-S (*a* mode polarization) or in E-W (*b* mode polarization) direction [61, 211, 249]. To obtain the same electric field components, however, for another orientation of the current system, we can rotate the model by 90° and form eq 2.3.4 again and solve for **e** [249]. The need for the three electric field components using from two orientations of the current system is based on the fact that the model responses in 3D MT are the full impedance tensor and the VTF. Thus, to construct the full impedance tensor we need both orientations of the current system.

The elements of the right hand side vector, **s** in eq 2.3.4 are the boundary conditions (BCs) values which corresponds to all the outer six faces (north, south, east, west, top and bottom) of the model. At four vertical faces, the BCs are formulated to give 2D solutions of conductivity at these faces and 1D solutions at the edges of these faces. Hence, we need to compute both 1D and 2D solutions and assign the computed values to the grid node at these four vertical faces. For solving the 2D problem at the boundary faces, based on the direction

of current flow, we have to differentiate between the two modes (a and b) of polarization in the 3D modeling. For example, for the E-W direction of the current flows we need to solve the 2D TE- mode problem at the eastern and western boundary faces and the TM- mode problem at the northern and southern boundary faces.

Alternatively, one can use the concept of partitioning of field. In this approach the total electric field, $\mathbf{E}$, is considered as a superposition of primary electric field, $\mathbf{E}_p$, and secondary electric field, $\mathbf{E}_s$, as,

$$\mathbf{E} = \mathbf{E}_p + \mathbf{E}_s. \tag{2.3.5}$$

$\mathbf{E}_p$ is a field simulated for simple background model like half space or layered earth model having conductivity σ_p. If σ_a represents residual conductivity of the medium such that the total conductivity, σ, of medium can be express as,

$$\sigma = \sigma_p + \sigma_a. \tag{2.3.6}$$

Using eq 2.3.5 and 2.3.6, eq 2.2.10 is decomposed into two equations as,

$$\bigtriangledown \times \bigtriangledown \times \mathbf{E}_p + i\omega\mu\sigma_p\mathbf{E}_p = 0, \tag{2.3.7}$$

$$\bigtriangledown \times \bigtriangledown \times \mathbf{E}_s + i\omega\mu\sigma\mathbf{E}_s = -i\omega\mu\sigma_a\mathbf{E}_p. \tag{2.3.8}$$

Now, the forward problem can be solved in two steps. In the first step, eq 2.3.7 is solved to get primary fields, $\mathbf{E}_p$, for background model. Once the primary fields are available, eq 2.3.8 is solved to compute the secondary field, $\mathbf{E}_s$. The total fields are computed from the primary and secondary fields using eq 2.3.5.

2.3.2 Static Divergence Correction

Static divergence correction is applied in periodical manner in MT to overcome the problem of inaccurate solution, when the geometric term $\nabla\times\nabla\times\mathbf{E}$ in eq 2.2.10 dominates over the term $i\omega\mu\sigma\mathbf{E}$ in low conductivity region such as air $\sigma \longrightarrow 0$. It was first proposed by Smith [215]. Mathematically static divergence correction can be derived by taking the divergence of eq. eq 2.2.10 as,

$$\bigtriangledown \cdot (\sigma \mathbf{E}) = 0. \tag{2.3.9}$$

The solution at low frequencies do not satisfy the continuity equation (eq 2.3.9) hence, a correction is made to **E**. This is achieved by adding the gradient of an unknown scaler, ϕ, to $\mathbf{E}^n$ (the solution at the n^{th} iteration of the BiCGSTAB solver [243]). And the scaler, ϕ, is calculated as,

$$\bigtriangledown \cdot \sigma(\bigtriangledown \phi) = -\bigtriangledown \cdot (\sigma \mathbf{E}^n). \tag{2.3.10}$$

The eq 2.3.10, is Poisson-like equation and solved using FD method. The divergence correction is applied after a certain number of BiCGSTAB iterations. The divergence correction improves the convergence and the computational time needed for solution of eq 2.2.10.

The eq 2.3.10 is the governing equation for Direct Current resistivity problems i.e. while solving the divergence correction in MT we are solving the DCR problem.

2.3.3 MT Response Computation

Once the electric field solution, **E**, are computed, the magnetic field, **H**, is computed as $\mathbf{H} = (-i\omega\mu)^{-1}\nabla\times\mathbf{E}$. Computed electric and magnetic fields at nodes are interpolated to the observation sites and from these impedance tensor, **Z**, and vertical magnetic field transfer functions (VTFs) are estimated. In the 3D MT case, the impedance is a 2×2 tensor, which requires two independent electric field solutions computed for two different source polarizations (a and b) [61, 210, 249]. Thus impedance tensor and VTFs can be written as,

$$\begin{pmatrix} E_x^a & E_x^b \\ E_y^a & E_y^b \end{pmatrix} = \begin{pmatrix} Z_{xx} & Z_{xy} \\ Z_{yx} & Z_{yy} \end{pmatrix} \begin{pmatrix} H_x^a & H_x^b \\ H_y^a & H_y^b \end{pmatrix}, \tag{2.3.11}$$

$$\begin{pmatrix} H_z^a & H_z^b \end{pmatrix} = \begin{pmatrix} T_x & T_y \end{pmatrix} \begin{pmatrix} H_x^a & H_x^b \\ H_y^a & H_y^b \end{pmatrix}. \tag{2.3.12}$$

Once impedance tensor and VTFs are computed, other derived responses can be easily

computed.

2.4 Direct Current Resistivity Method

In DCR method, artificially generated electric current is supplied to the subsurface through the pair of electrodes (A and B) and the resulting potential differences are measured using another pair of electrodes (M and N) (Fig. 2.2). The variation in value of measured potential difference provide information about the subsurface resistivity structure.

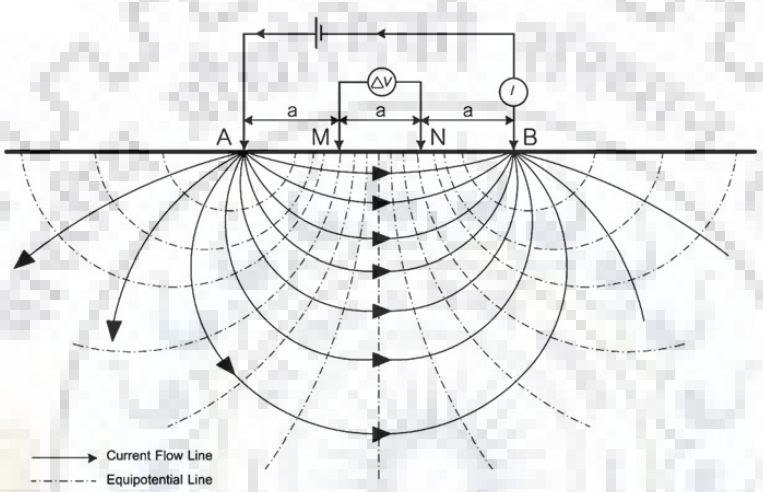

Figure 2.2: Basic setup of DCR method with two current (A and B) and two potential (M and N) electrodes on the surface.

The potential difference, $\Delta\phi$, measured between the electrodes M and N is given as,

$$\Delta\phi = \frac{\rho I}{2\pi}\left[\frac{1}{AM} - \frac{1}{BM} - \frac{1}{AN} + \frac{1}{BN}\right], \tag{2.4.1}$$

where, ρ is the resistivity of the medium, I is the current and AM, BM, AN and BN represent the geometrical distance between the electrodes A and M, B and M, A and N, and B and N, respectively. The electrical resistivity for homogeneous or apparent resistivity for an inhomogeneous earth is then calculated using eq 2.4.1.

2.4.1 Governing Equation

Now let us consider a half space with arbitrary conductivity $\sigma(x,y,z)$ distribution. The electric field, **E**, can be written as,

$$\mathbf{E} = -\nabla\phi, \tag{2.4.2}$$

where, ϕ is the electric potential. For current density, j, and source term, Q, the equation of continuity is defined as,

$$\nabla \cdot j = Q, \tag{2.4.3}$$

with the source term,

$$Q = I\delta(x-x_q)\delta(y-y_q)\delta(z-z_q), \tag{2.4.4}$$

where, I is the current and δ is the Dirac delta function. Using $j = \sigma E$, we get,

$$\nabla \cdot [\sigma(x,y,z)\nabla\phi(x,y,z)] = -I\delta(x-x_q)\delta(y-y_q)\delta(z-z_q). \tag{2.4.5}$$

The eq 2.4.5 is the governing differential equation and relates the potential field to the input current source. The analytical solutions for the above equation are available for selected class of simple models. Hence, for a general 3D conductivity distribution the equation is solved using numerical computation scheme like FDM, FEM etc.. The problem has been introduce as static divergence correction in MT method.

In the present study, the DCR problem is solved using FDM method and using the concept of partitioning of field.

2.4.2 Primary and Secondary Field Formulation

In the vicinity of source or at source, numerical approximations using eq 2.4.5 typically give poor results because of steep gradient of field. The popular approach is to remove the effect of the singular potential by using primary/secondary field formulation [125]. In this approach, the potential ϕ in eq 2.4.5 is considered as the superposition of the primary potential, ϕ_p, and secondary potential, ϕ_s, as,

$$\phi(x,y,z) = \phi_p(x,y,z) + \phi_s(x,y,z). \tag{2.4.6}$$

The primary potential are caused by the current source for simple model like half space or layered model having conductivity σ_p. If σ_a represents residual conductivity of the medium such that the total conductivity, σ, can be written as,

$$\sigma = \sigma_p + \sigma_a. \tag{2.4.7}$$

Using eq 2.4.6 and 2.4.7 the eq 2.4.5 is decomposed into following two equations,

$$\nabla \cdot [\sigma_p(x,y,z)\nabla\phi_p(x,y,z)] = -I\delta(x-x_q)\delta(y-y_q)\delta(z-z_q). \tag{2.4.8}$$

$$\nabla \cdot [\sigma(x,y,z)\nabla\phi_s(x,y,z)] + \nabla \cdot [\sigma_a(x,y,z)\nabla\phi_p(x,y,z)] = 0. \tag{2.4.9}$$

Now, the forward problem is to be solved in two steps. First eq 2.4.8 is solved for primary potentials and later eq 2.4.9 is solved to compute the secondary potentials due to scattered source. Finally, total potentials are computed as superposition of primary and secondary potentials.

Primary Potential

The eq 2.4.8 is solved for primary potential for a background model such that σ_p at the source position is same as σ i.e. zero around the source point. For a uniform half-space and a current source located at $(x_q,\ y_q,\ 0)$, the potential at $(x,\ y,\ z)$ is given as,

$$\phi_p = \frac{I}{2\pi\sigma_p\sqrt{(x-x_q)^2+(y-y_q)^2+z^2}}, \tag{2.4.10}$$

where, while σ_p is the conductivity of the media at the source point [262]. If the background model is layered earth then, the primary potential is assumed to be caused by the current source in a layered earth. For secondary potential eq 2.4.9 is solved numerically.

Secondary Potential

For numerical solution for the model with arbitrarily shaped 3D structures using finite difference method discretization of model is a very crucial step. Dey and Morrison [58] used four nodes between two adjacent electrodes, while Park and Van [166] used only one node. To strike a balance between number of nodes and errors in the calculated potentials Loke and Barker [124] used two nodes. After model discretization, unknown potential are assigned on a normal grid.

The forward problem is solved using the appropriate boundary conditions. The total potential, ϕ, and the normal component of the current density, $j_n = \sigma\partial\phi/\partial n$, must be continuous at boundaries. At the air-earth interface there is no current flow. Hence at air

earth interface,

$$\frac{\partial \phi_s}{\partial n} = 0. \tag{2.4.11}$$

On the outside boundaries, mixed boundary conditions [58] are applied,

$$\frac{\partial \phi_s}{\partial n} + \frac{cos(r,n)}{r}\phi_s = 0, \tag{2.4.12}$$

where, r denotes the radial distance from the source location to the boundary.

After collecting all the discrete FD equations for all nodes and applying BCs, for a current source, f, a matrix equation is formed as,

$$\mathbf{A_m}\phi_s = \mathbf{s}, \tag{2.4.13}$$

where, $\mathbf{A}_m$ is a source independent $N_v \times N_v$ sparse coefficient matrix with seven non-zero elements per row, $\mathbf{s}$ is the N_v dimensional source vector and ϕ_s is the N_v dimensional vector representing secondary potential at the N_v internal nodes. This sparse linear system can be solved either iteratively using BiCGSTAB (incomplete **LU** decomposition as preconditioner) or direct solver. Once the eq 2.4.13 is solved for the secondary potentials these are added to primary potentials and the responses are computed for arbitrary electrode array/geometry.

2.4.3 Response Computation

Once the eq 2.4.13 is solved and secondary potentials are computed, the total nodal potentials are computed as sum of primary and secondary potentials. Since the computed potentials are for a single source, they are superimposed to form the potentials due to a dipole (the simultaneously active current electrodes).

The computation of apparent resistivity from potentials is straight forward. The computed potentials are interpolated to the potential electrode location. The final potential at an electrode is the linear superimposed of potentials due to all the active current electrodes. One these potentials are computed the potential difference are measured for the array used in measurement. From these apparent resistivity can be computed as,

$$\rho_a = K \times \frac{\delta \phi}{I}, \tag{2.4.14}$$

where, K is the geometric factor that depends only on the position of current and potential

electrodes.

2.5 MT and DCR Inversion

The inversion algorithm aims to find a meaningful model $\tilde{\mathbf{m}}$, a M- dimensional model parameter vector, while fitting the data, $\tilde{\mathbf{d}}^{obs}$, of dimension N_d to an acceptable level in a stable manner. This is achived by minimization of the penalty function defined as,

$$\varphi(\tilde{\mathbf{m}}, \tilde{\mathbf{d}}^{obs}) = (\mathbf{d}^{obs} - \tilde{F}(\tilde{\mathbf{m}}))^T \mathbf{C}_\mathbf{d}^{-1} (\mathbf{d}^{obs} - \tilde{F}(\tilde{\mathbf{m}})) + \lambda (\tilde{\mathbf{m}} - \mathbf{m_0})^T \mathbf{C}_\mathbf{m}^{-1} (\tilde{\mathbf{m}} - \mathbf{m_0}), \quad (2.5.1)$$

where, $\tilde{F}(\tilde{\mathbf{m}})$ is the forward mapping, $\mathbf{C_d}$ is the data covariance matrix, $\mathbf{C_m}$ is the model covariance matrix, $\mathbf{m_0}$ is the apriori model and λ is the trade-off parameter. $\mathbf{C_d}$ is generally diagonal hence, it can be eliminated from definition of penalty functional by rescaling of data and forward mapping. Both $\mathbf{m_0}$ and $\mathbf{C_m}$ can also be eliminated from eq 2.5.1 by setting $\mathbf{m} = \mathbf{C}_\mathbf{m}^{-1/2}(\tilde{\mathbf{m}} - \mathbf{m_0})$. This transformation reduces eq 2.5.1 to,

$$\varphi(\mathbf{m}, \mathbf{d}^{obs}) = (\mathbf{d}^{obs} - F(\mathbf{m}))^T (\mathbf{d}^{obs} - F(\mathbf{m})) + \lambda \mathbf{m}^T \mathbf{m}, \quad (2.5.2)$$

where, $F(\mathbf{m}) = \tilde{F}(\mathbf{C}_\mathbf{m}^{1/2}\mathbf{m} + \mathbf{m_0})$. Thus by minimizing eq 2.5.2 in transform domain the model parameters are transformed back into original model parameter, $\tilde{\mathbf{m}} = \mathbf{C}_\mathbf{m}^{1/2}\mathbf{m} + \mathbf{m_0}$ [98]. The eq 2.5.2 can be solved either using the Quasi-linear inversion or the Non-linear Conjugate Gradient (NLCG) inversion technique.

In Quasi-linear Inversion, the penalty functional is first approximated by a Taylor series expansion. The updated model after every iterations is obtained by minimizing the quadratic approximation of penalty functional. In the Gauss Newton (*GN*) method only the first derivative is retained and all the higher order derivatives are discarded. This gives us an approximate solutions as,

$$(\mathbf{J}^T \mathbf{J} + \lambda \mathbf{I}) \delta \mathbf{m}_n = \mathbf{J}^T \mathbf{r} - \lambda \mathbf{m}_n, \quad (2.5.3)$$

where, $\mathbf{m}_n$ are the model parameters at the n^{th} iteration, $\mathbf{J}$ is Jacobian matrix and $\mathbf{r} = \mathbf{d}^{obs} - F(\mathbf{m}_n)$ is the residual. The eq 2.5.3 is solved for $\delta \mathbf{m}_n$ and the new updated model parameter vector is obtained as $\mathbf{m}_{n+1} = \mathbf{m}_n + \delta \mathbf{m}_n$. For stability some form of step length damping is required and λ is used for increment at each step [136, 186]. Alternatively, using the

Occam's approach one can also solve for $\mathbf{m}_{n+1}$ [47, 168] eq 2.5.3 as,

$$(\mathbf{J}^T\mathbf{J}+\lambda\mathbf{I})\mathbf{m}_{n+1} = \mathbf{J}^T\hat{\mathbf{d}}, \tag{2.5.4}$$

where, $\hat{\mathbf{d}} = \mathbf{d}^{obs} - F(\mathbf{m}) + \mathbf{J}\mathbf{m}_n$. In data space [209] the solution of eq 2.5.4 is written as,

$$\mathbf{m}_{n+1} = \mathbf{J}^T\mathbf{b}_n; \qquad (\mathbf{J}\mathbf{J}^T+\lambda\mathbf{I})\mathbf{b}_n = \hat{\mathbf{d}}. \tag{2.5.5}$$

To avoid direct computation of $\mathbf{J}$, eq 2.5.4 and eq 2.5.5 are solved using iterative solvers such as conjugate gradients (*CG*) method. In CG method computation of $\mathbf{J}$ is replaced by the product of matrix and an arbitrary vector such as $(\mathbf{J}^T\mathbf{J}+\lambda\mathbf{I})\mathbf{m}$ is computed at the cost of just two forward problems. The regularization parameter, λ, for *GN* at the n^{th} inversion iteration, is determined as $\lambda = r_{sum}/2^{n-1}$ [158], r_{sum} being the largest row sum of $real(\mathbf{J}^T\mathbf{J})$.

Non-linear conjugate gradient (*NLCG*) method is applied to solve eq 2.5.2 by Kelbert et al. [99], Newman and Boggs [160], Rodi and Mackie [186]. In this approach, the gradient of eq 2.5.2 with respect to the variation in model parameter, $\mathbf{m}$, is computed as,

$$\left.\frac{\partial\varphi}{\partial\mathbf{m}}\right|_{\mathbf{m}_n} = -2\mathbf{J}^T\mathbf{r} + 2\lambda\mathbf{m}_n. \tag{2.5.6}$$

The eq 2.5.6 is then used to a compute new 'conjugate' search direction. The 'line search' is used to minimize the penalty functional along this direction and it requires solving forward problem few times and the gradient is recomputed. Basic computational steps for *NLCG* include solving forward problem for model parameter, $\mathbf{m}_n$, and multiplication of $\mathbf{J}^T$ by the residual, $\mathbf{r}$. The *NLCG* iterations are performed for fixed value of λ (computed on the basis of L-curve) and when misfit stalls i.e. difference between misfits of two previous iterations is less than a predefined threshold, λ is reduced by a predetermined factor (10 in present study).

The schemes for minimizing eq 2.5.2, as discussed above, are expressed in terms of data and model parameter vectors, $\mathbf{d}^{obs}$ and $\mathbf{m}$, forward mapping, $F(\mathbf{m})$, Jacobian, $\mathbf{J}$ (or $\mathbf{J}^T$) and data and model covariance matrices, $\mathbf{C_d}$ and $\mathbf{C_m}$. The NLCG method is implemented in MT and DCR inversion code (*AP3DMT-DC*) used in the present study.

2.6 Brief Description of 3D Inversion Code

The code used for 3D inversion of MT and DCR data is *AP3DMT-DC*, which is an extension of *AP3DMT*, a MATLAB based code developed by our group [203]. This code is made versatile and user friendly by an efficient use of MATLAB's inbuilt functions (subroutines). The accuracy of the code was validated by comparing its results with the corresponding results obtained using the code ModEM [62] for a variety of standard synthetic test models [203, 204]. Since this code is new and not known to the magnetotelluric community, we briefly explain the main features of the code here.

The *AP3DMT-DC* mainly comprises two independent parts; *(i)* the grid generator and I/O control code, for generating essential data and model files and *(ii)* modeling/inversion code. In the following section we briefly explain the salient features of these two parts of the code.

2.6.1 Grid Generator

The grid generator code, is a standalone grid generation program, mainly used for synthetic MT data generation, and it includes a graphic user interface (GUI). Through the GUI, one feeds the necessary input information, like data type and its unit, frequencies, grid type and modeling/inversion control parameters. Also an input model file (*.xls) containing the observation site co-ordinates and the grid and model description is given. Using the inputs from GUI and the input model file, the grid generator code generates four files viz. parameter file, data file, model file, and covariance file (optional).

For the inversion of MT, Radio Magnetotelluric (RMT) and DCR data, the files required are, *(i)* data file; contains information about station and data types, *(ii)* model file; contains information about grid and resistivity at each cell, and *(iii)* parameter file; contains information about basic modeling and inversion parameters.

The parameter file contains the information of forward and inversion control parameters like, the matrix solver (iteration and tolerance), the divergence correction, and regularization parameter etc.. The data file contains information about (i) MT data, like numbers of sites, frequencies, location of sites and data components, and/or for (ii) DCR data, array type and data type (apparent resistivity or resistance) and electrode position. The model file remains same for MT and DCR data, only the model dimension varies. The model file contains

number of grids in each direction, the cell size (distance between two adjacent grids) and the resistivity of each cell. The covariance file provides the desired smoothening details. For MT data, the model grid can be designed by considering the target bodies as cuboids (simple models) or as polyhedron (complex features). For cuboid shaped target bodies, the grids generation is done on the basis of skin depth. First, on the basis of target bodies the model domain is divided into regions and a cell resistivity matrix is constructed. Fine grids are generally preferred near the conductivity contrast with two grid lines are on either side of the interface, spacing equal to δ /4 and then δ /3 and so on. The grid coarseness increases as one moves away from the target model domain. Alternatively, one can also use the manual grids according to one's requirement by giving them in the input(*.xls) file. To represent the complex geological structures, polyhedrons are the best choice. For example, assume a oblique body approximated by a cuboid which encloses the whole target body. Uniform grids of specified size are generated for cuboid region as a staircase model. In other regions of the model, the grids are generated according to the skin depth criteria. The output files are subsequently used by the modeling or inversion code.

The grid generator code has been successfully tested and validated for standard complex MT synthetic models available in literature such as checker board [62], spiral [143] model etc. by Singh [203].

For field MT data the format of the three files remain same but different codes are used to generate field data files. For generating the data file a standalone MATLAB code was used in which inputs are (i) '*.dat' file with station name and location in kilometers and (ii) EDI files, containing MT field data, obtained after processing. Further, in the code we give the details of data type to be used (Impedance, VTF, Phase Tensor), frequency range, field units, data error floor percentage etc.. The code give the data file as output in desired format. For model file generation we can use either the grid generator code as discussed above or for uniform and automatic grids we can use a MATLAB code for a homogeneous half space model in which we provide information about the dimension of model domain, grid spacing in horizontal direction, padding factor for grids outside the model domain, first layer thickness and increasing factor for z- direction, resistivity of half space etc.. The code give us the model and covariance file as output. In the covariance file the value of smoothing in each direction is given for each cell of model file.

For DCR data the format of input and covariance file is same parameters as in case of MT

data. The data file used in *AP3DMT-DC* for DCR data is a '*.dat' file, containing information about, array type used (like Wenner, Schlumberger etc.), the inter electrode spacing for each quadripole (combinations of current and potential electrodes depending upon configuration used), resistivity at each point and corresponding error. The format of *Guess Model* file is same as discussed for MT data. A standalone program is available for generation of guess model file which take the data file as input and one has to provide information like, (i) number of grids required between two electrodes along the profile, (ii) number of grids required between two electrodes perpendicular to the profile, (iii) increasing factor for vertical grids (z direction) and (iv) the padding factor and number of grids to be padded, for horizontal grids, in case of joint inversion (MT, RMT and DCR). The distance of first vertical grid from surface is chosen as one fourth of minimum electrode spacing. And the average of apparent resistivity, available in data files, is taken as the resistivity of homogeneous half-space guess model.

2.6.2 Modeling and Inversion

Modeling and inversion part of the code accept all input files generated earlier, automatically or manually, as mentioned in previous section. The 3D modeling and inversion theory discussed above is implemented in *AP3DMT-DC*.

In *AP3DMT-DC*, the minimization of penalty function can be performed using either Gauss Newton with conjugate gradient method (model space or data space) or the non-linear conjugate gradient (NLCG) method [204]. These algorithms require a small amount of memory usage as only the product vector of Jacobian matrix (or its transpose) with an arbitrary vector is required. The Jacobian computation is further modularized, using the decomposition approach [62]. A coarse grained parallelization over number of frequencies for forward modeling and Jacobian multiplication with a vector is also implemented for efficient computation.

Modular form of this code facilitates easy modifications needed for different forward problems (CSEM, DCR etc.) without affecting other subprograms or modules. The data set, d^{obs}, is generally multi-period, multi-station and multi-component (data type). The starting value of regularization parameter, λ, is chosen using the L curve [142]. The NLCG iterations are performed for a fixed value of λ and if the difference between the misfits of two previous iterations is less than a predefined threshold, λ is reduced by a factor of 10. In

the present work the lower threshold of λ is set as 10^{-8}. For regularization of the objective functional of MT inverse problem, desired model smoothness parameters can be chosen. It is achieved by constructing the model covariance matrix (C_m), using the finite difference approximation to the Laplacian operator (∇^2). Isotropic or anisotropic smoothness can be chosen between 0 and 1, as per the requirement of the data and geological inputs. The updated data and model file is written in '*.dat' file in same format as input file after each iteration. A '*NlcgLogFile.dat*' is also written and updated after each iteration providing the details of updated normalized root mean square (nRMS) and regularization parameter, λ. The inversion process terminates if one of the stopping criteria is fulfilled. These are: (i) data misfit is less than the given threshold value, (ii) a local minimum occurs in case of NLCG, (iii) the data misfit starts increasing, (iv) the data value of regularization parameter, λ, becomes smaller than the given threshold value and (v) iteration number reaches a prescribed maximum value. The nRMS is defined as,

$$nRMS = \sqrt{\frac{1}{N}\sum_{i=1}^{N}\left(\frac{d_i^{obs} - F_i(m)}{\sigma_i}\right)^2}, \tag{2.6.1}$$

where, N is the total number of data points; d_i^{obs} is the i^{th} observed data; $F_i(m)$ is the i^{th} synthetic data and σ_i is the data standard error in i^{th} observed data value.

2.7 Summary

The basic theory of MT and DCR methods including the governing equation are discussed. The modeling algorithms used for each method is presented. For MT modeling, the PDE is solved on a staggered grid using finite difference method. The resultant sparse symmetric matrix is solved using BiCGSTAB with implicit divergence correction (solved iteratively using conjugate gradients). For DCR modeling, PDE is solved on a normal grid using finite difference method and the concept of partitioning of potential field into primary and secondary. The resultant matrix can be used either using direct solver or iterative solver. For minimization of the penalty function, both Quasi-linear and NLCG methods are discussed.

The description of *AP3DMT-DC* code and its two components; the grid generator and modeling/inversion are discussed. The grid generator code creates various I/O files essential for modeling and/or inversion. These files includes data parameter file, model file, data

file and covariance file (optional). For inversion one can choose either GN with conjugate gradient method (model space or data space) or the NLCG method.

In next four chapters the implementation of inversion code *AP3DMT-DC* on some case studies is discussed.

Chapter 3

3D INVERSION OF MT DATA OF ROORKEE GANGOTRI (RG) PROFILE

3.1 Preamble

The first case study was carried out in the Garhwal Himalayan Corridor (GHC) region on Roorkee-Gangotri profile. One of the motivations for this work was to test the hypothesis of oblique and transverse tectonics, proposed by several workers on the basis of limited geological and geophysical studies. We recorded MT data at 40 sites, in three phases. Out of these 40 sites, useful tipper or vertical magnetic field transfer function (VTF) data were available only at 19 sites. Through a synthetic inversion experiment on scattered data over a profile, like our GHC profile, it was demonstrated that MT data can be used to qualitatively infer about the off-profile resistivity structures within about 20 km from the profile. To arrive at the final 3D geoelectrical model for the study area, we conducted several 3D inversion experiments using the full impedance tensor data at 39 sites and the tipper data at 19 sites both independently and jointly. The 3D resistivity model explains the thrust tectonic and *flat ramp flat* geometry of Main Himalayan Thrust (MHT). The inverted model also delineated Delhi-Haridwar Ridge (DHR) as a highly resistive ($>$ 1000 Ωm) feature beneath the low resistive ($<$ 50 Ωm) sediments of Indo-Gangetic Plain (IGP). DHR continues up to Inner Lesser Himalayan region and is bounded by two conductive ($<$ 10 Ωm) fluid saturated fractured zones. These zones are situated off-profile and run nearly parallel to DHR. These new features are confined mainly to the southern zone of the profile and are so oriented that the existences of oblique and transverse tectonic structures in the main Himalayan arc are validated. From the electrical image of DHR and of the associated conducting features, we

inferred that these features are transverse to main Himalayan arc.

3.2 Geology of GHC, the Region of Study

The GHC, study area, is located between 29.50°N to 31.50°N and 77.50°E to 79.00°E, starting from Roorkee in the south and going upto Gangotri in the North, in Uttarakhand Himalaya. In the region there exist many folds and faults, transverse and oblique to the Himalayan tectonic trend. The transverse trend includes three major tectonic thrusts, covering four major lithological units of Northwest Himalaya. The Indian Gangetic Plains (IGP) [231, 241] is the southernmost zone bounded in the north by Main Frontal Thrust (MFT), the youngest active thrust. The next zone lying to the north of IGP is the Sub-Himalaya (SH) which is bounded in the north by Main Boundary Thrust (MBT). Further, to the north of the SH lies the Lesser Himalaya (LH) bounded in the north by Main Central Thrust (MCT). The northernmost region is the Higher Himalaya Crystallines (HHC). Further, at some points MCT gets divided into two thrusts Munsiari thrust and Vaikrita thrust. These two thrust are also known as MCT-I and MCT-II respectively [130, 232, 242] and constitute the MCT zone.

The IGP is a physiography feature of Himalaya, formed by deposition of sediments from the rivers originating in Himalaya. It is, in general, not considered as a tectonic feature. The SH consists of continental molassic sediments of Tertiary age, formed by thrusting and faulting due to the deformation and uplift in the orogenic belt. The rocks of LH are primarily metasedimentary rocks of Early Proterozoic to Lower Cenozoic era. Sheared anticlines and synclines are also seen in LH. The rocks in the Higher Himalaya are composed of crystalline and metamorphic rocks: granites, granulite, gneisses, schists and quartzite. Inverted metamorphism is observed near MCT. It is indicated by the higher grade metamorphic rocks (e.g. highly recrystallized feldspar) lying structurally and topographically above the lower grade metamorphism rocks (e.g. brittle and deformed feldspars) [90]. Thus, the rocks outcropping in the region have age from Pre-Cambrian to Pleistocene and these vary from igneous and sedimentary to metamorphic types.

The prominent amongst the oblique faults and ridges in the region are the Delhi-Hardwar Ridge (DHR) [68, 240] and Mahendragarh-Dehradun Fault (MDF) [18]. The DHR is believed to be located between 76° E and 79° E longitude as a prolongation of the NNE-SSW

trending Aravali Mountain. Its extension towards Garhwal is present in the gravity anomaly model of [178]. The seismicity related to both DHR and MDF is moderate. MDF transcends into MFT as a strike-slip fault and it trends NNE–SSW. MDF gets reactivated as thrust with minor strike-slip component, in the imparted tectonic domain of back thrust [201].

3.3 Description of Data

Broadband MT data were recorded at 40 sites (Fig. 3.1) along Roorkee-Gangotri (RG) profile in GHC in three phases since 2008 [88, 89, 144, 216]. The RG profile passes through major Himalayan thrusts in GHC. The Metronix MT system was used in this survey. It included an ADU-06 data logger, MFS-06 induction coil magnetometers and EFP-06 electrodes. The magnetotelluric processing code, MAPROS [67], was used to transform the recorded time domain data to the four frequency domain complex components of impedance tensor (full impedance tensor). The data was also processed using a robust noise-suppressing code [213, 244] for VTF transfer function. Thus, the stable full impedance tensors were estimated at 39 sites in the period range 0.01-1000 s. In rocky sites in tough Himalayan terrain, the induction coil for vertical magnetic field component couldn't be buried, the estimated VTF data values were noisy at such MT sites. Hence, reliable VTF data were available only at 19 sites in the period range 1-1024 s.

The MT dataset of RG profile was first inverted by Israil et al. [89] and a 2D resistivity model was presented. Subsequently, the 2D model was improved by adding more MT sites and performing fresh dimensionality and directionality analysis and 2D inversion of reprocessed data [88, 144]. Next, to ascertain the need of 3D data inversion, a review of the complete dataset was performed using different decomposition (Bahr, GBD, WAL and Caldwell) methods and a rigorous directionality and dimensionality study were carried out.

3.3.1 Dimensionality and Directionality Analysis

In different lithotectonic domains, the geoelectric strike directions in the region vary with time period. The geoelectric strike was estimated for each region corresponding to the entire frequency band (0.001-1000 s) as one band. The strike direction for IGP and SH in the time period range 2-53 s was found to be $N71^{\circ}W \pm 5^{\circ}$, and $N69^{\circ}W \pm 3^{\circ}$ respectively which is same as the direction of major thrusts of the region. However, for the higher time periods,

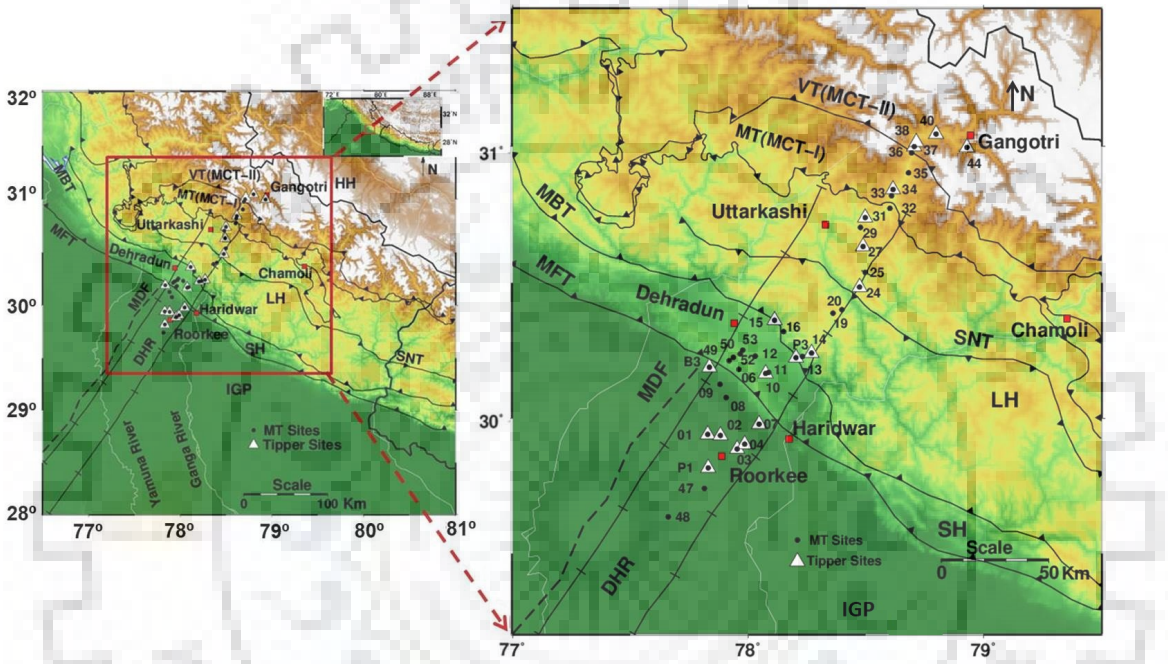

Figure 3.1: Simplified tectonic map of the study area and MT sites locations. MT sites are displayed with black circles, White triangles represent Tipper sites. Acronyms are: DHR is Delhi-Haridwar Ridge; MDF is Mahendaragarh-Dehradun Fault; MBT is Main Boundary Thrust, MFT is Main Frontal Thrust; MT (MCT-I) is Munsiari Thrust; VT (MCT-II) is Vaikrita Thrust, SNT is Srinagar Thrust. IGP is Indian-Gangetic Plain; SH is Sub-Himalaya and LH is Lesser Himalaya (Compiled from [7, 95, 232, 242]). Map was created with gmt software version 5 (`http://gmt.soest.hawaii.edu/`).

Table 3.1: Estimated geoelectric strike by different decomposition schemes: Bahr's Method, Groom-Bailey tensor Decomposition, Caldwell phase tensor analysis method and WAL rotational invariants.

Sites	Region	Period Range (s)	Cadwell Strike (°)	WAL Strike (°)	Bahr Strike (°)	GBD Strike (°)
48, 47, 3 4, 5, 7,10	IGP	2-53	-71.2 ± 5.8(b)	-74 ± 5.1	-71.7 ± 5.3	-72 ± 5.2
11, 12, 13 14, 16	SH	4-53	-69 ± 3.5(c)	-69.7 ± 3.3	-70 ± 4.8	-68 ± 3
15, 18, 19, 20, 25, 27, 31	LH	32-215	-7.8 ± 5(e)	-8.9 ± 4.2	-12 ± 8.2	-6.1 ± 1.4
18, 19, 20, 24 25, 27, 29, 31	LH	0.0023-3	-21 ± 4(a)	-26 ± 3.7	-22.3 ± 4.4	-18.4 ± 2.5
18, 20, 25, 27 29, 31, 32	LH	4-1024	-68.9 ± 5.3(d)	-70 ± 4.8	-71.2 ± 5.6	-70.6 ± 8
33, 34, 35 36, 37, 44	HH	0.0023-1024	-68 ± 2.2(d)	-70.4 ± 4.3	-69.5 ± 3.3	-69 ± 5.1
47, 1, 2, 3, 4 5, 6, 7, 8, 10 11, 12, 14, 16	IGP and SH	13.45-1024	11 ± 3.2(f)	12 ± 3.4	11 ± 2.2	11 ± 3.34

the strike was found to be transverse ($N12°W \pm 2°$) to thrust tectonics. Further, for LH and HH regions, the strike was $N69°W \pm 3°$ which is again in the direction of major thrusts. The results of tensor decomposition are consistent with the regional strike direction of Himalayan region which is NW-SE. The resulting geoelectric strikes in the three Himalayan regions obtained using different decomposition methods are given in Table 3.1

Correlation with Seismicity

In order to study the correlation between the tectonic structures with the geoelectric strike directions, these strike directions were plotted on a simplified tectonic map along with the hypocenters of about 300 earthquakes (Fig. 3.2). The variation in geoelectric strike directions with period and position reveals six dominant strike directions, shown as bold lines in Fig. 3.2. These bold lines are labeled as characters '*a*' to '*f*'. Out of the six strike

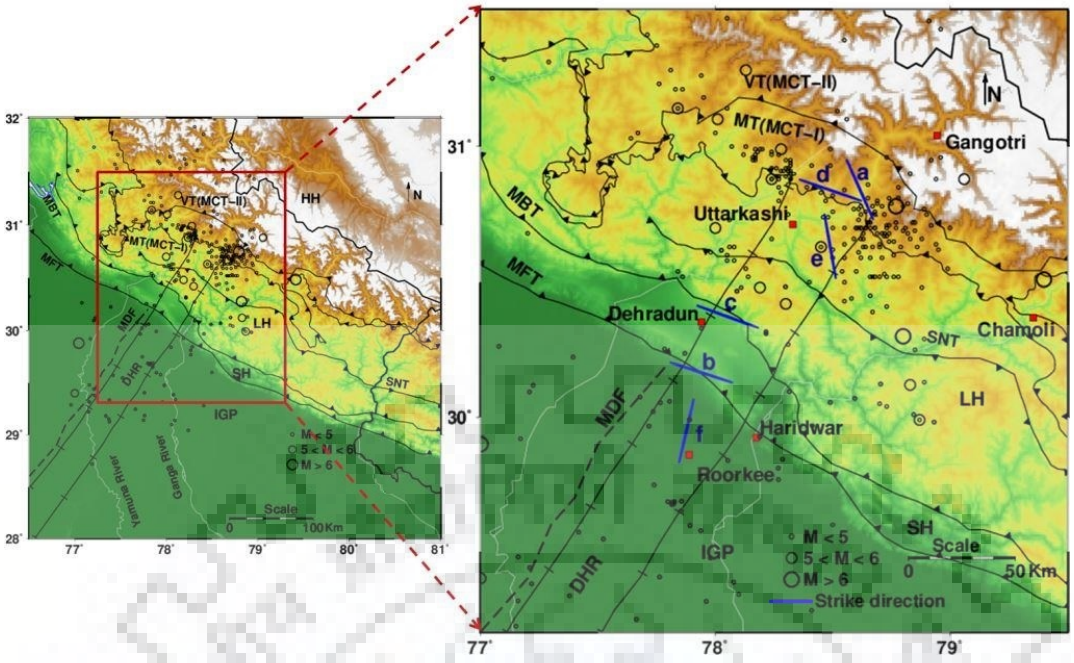

Figure 3.2: Geoelectric strike direction shown by bold lines labeled by characters '*a*' to '*f*' along with locations of epicenters of earthquakes. Acronyms are same as in Fig. 3.1 (Compiled from [7, 95, 232, 242]). Map was created with gmt software version 5 (`http://gmt.soest.hawaii.edu/`).

orientations, three (labeled '*b*', '*c*' and '*d*') are $N72°W \pm 8°$, $N70°W \pm 3°$and $N71°W \pm 6°$. These directions are consistent with the strikes of Himalayan thrusts MCT, MBT and MFT respectively. The fourth strike direction (labeled '*a*') is $N24°W \pm 7°$. It is oblique to the main Himalayan arc and is consistent with the strike of focal plane, NP1, of 19 October, 1991 Uttarkashi Earthquake ($N28°$W) [259]. The fifth strike direction (labeled '*e*') is $N8° \pm 4°$W and is aligned along the near linear distribution of earthquake epicenters in LH. The sixth strike direction (labeled '*f*'), $N12° \pm 3°$E, is aligned nearly transverse to the main Himalayan arc. Such a transverse feature has been indicated earlier in geological [240] and geophysical literature [6] as an extension of Aravali trend into Himalaya, and named as Trans Himalayan Conductor.

The directionality and dimensionality analysis and the known geological strikes of major oblique and transverse tectonic thrusts in the region indicate 3D nature of the region. So, a 3D analysis of the recorded MT data is desired.

3.4 3D Inversion of Profile Data

Several 3D inversion experiments were performed independently or jointly on different components of MT data, i.e. full impedance tensor (Z), Phase Tensor (PT) and tipper or Vertical Magnetic Field transfer function (VTF). For this purpose, the code *AP3DMT* [204] developed in-house and the code ModEM, developed by Egbert and Kelbert [62] were used. Both the codes were run on two systems, a Dell Precision T5610 workstation (with two E5-2600 3.50 GHz Intel Xenon processors and 128 GB RAM with 8 cores) and a HP Z620 workstation (with two E2643 3.30 GHz Intel Xeon processors and 32 GB RAM with 8 cores). Based on various standard synthetic test examples available in literature, it was found that the two codes generate nearly same inverted resistivity models [203] for the same set of control parameters and synthetic data set. In this work results obtained using only *AP3DMT* are presented.

The *AP3DMT* code allows the user to define (i) model covariance matrix ($\mathbf{C_m}$), (ii) the initial values of Marquardt trade-off parameter (λ) and (iii) the decreasing factor for λ while updating the model parameters. Parameters defining smoothing matrix can be chosen between zero and one. In general, a constant smoothing factor of 0.3 is used in x-, y- and z-directions representing an isotropic smoothing. However, if the preferred strike direction is known, then a higher value of smoothing parameter may be assigned in the strike direction leading to an anisotropic smoothing. Some synthetic tests, relevant for present data set from Garhwal Himalayan region, are discussed in 3.4.1.

3.4.1 Numerical Experiments

Preliminary 3D inversion experiments were performed on synthetically generated full impedance tensor data to estimate the optimal values of important parameters affecting the inversion results, such as (a) resistivity of the homogeneous half-space guess model, (b) range and density of time periods and (c) density of sites.

A 100 Ωm half-space model was used for generating the synthetic data for all the experiments. The model was discretized into $66 \times 63 \times 44$ cells (with 10 cells in air). Below the surface, the first grid line was at a distance of 50 m and the spacing of each subsequent grid line increased by a factor of 1.2, extending up to 760 km. Total of 32 cells were padded around the central region, eight in each horizontal direction with increasing width. With

this grid, the dimension of the model domain became $1000 \times 1000 \times 760$ km in x-, y- and z- directions respectively. For all the experiments, a 3% Gaussian error was added to the synthetic data i.e. the full impedance tensor. The isotropic model smoothing with a factor of 0.3 was used for all the inversion tests.

3.4.1.1 Effect of Resistivity of the Homogeneous Half-space Guess Model

To study the effect of resistivity of initial guess model, data were generated for two profiles: profile (i) comprising 21 sites placed diagonally in a straight line, with a 9 km constant site spacing and profile (ii) comprising 39 sites at the actual field locations along RG profile. For each profile four initial half-space guess models of resistivities 1000 Ωm, 500 Ωm, 50 Ωm and 10 Ωm were used. Hence, pairing these two characteristics eight inversions were performed.

The data were computed at 25 periods distributed logarithmically in the time range 0.01-1000 s. The starting and final normalized Root Mean Square (nRMS) error values along with the number of inversion iterations it took for convergence in each case is given in Table 3.2. In Fig. 3.3 the depth slices (x-y plane) of the four inverted 3D models obtained from initial guess model with resistivity greater than 100 Ωm are plotted in columns 'a' to 'd'. Similarly, In Fig. 3.4 the depth slices (x-y plane) of the four inverted 3D models obtained from initial guess model with half-space resistivity less than 100 Ωm are plotted in columns 'a' to 'd'. From Table 3.2 it was observed that the initial nRMS error value and number of iterations are less in case of initial guess model having resistivity 500 Ωm and 50 Ωm as it is closer to true model (100 Ωm).

This experiment further helped in investigating the zone of influence defined as the maximal distance along the strike direction up to which an off-profile resistivity structure can be reasonably resolved. Siripunvaraporn et al. [211], in an earlier study, based on the inversion of full impedance tensor data generated along a straight profile with constant site spacing, found that an off-profile resistivity structure can be sensed up to 1 km. They also found that if the data contain 3D structure, 2D inversion inserts spurious structures in the form of fictitious deep conductive root. The RG profile is neither straight nor recorded at constant site interval. The locations of MT data sites are scattered in a region with a width of about 15 km.

The zone of influence is quantitatively defined as the region whose resistivity lies

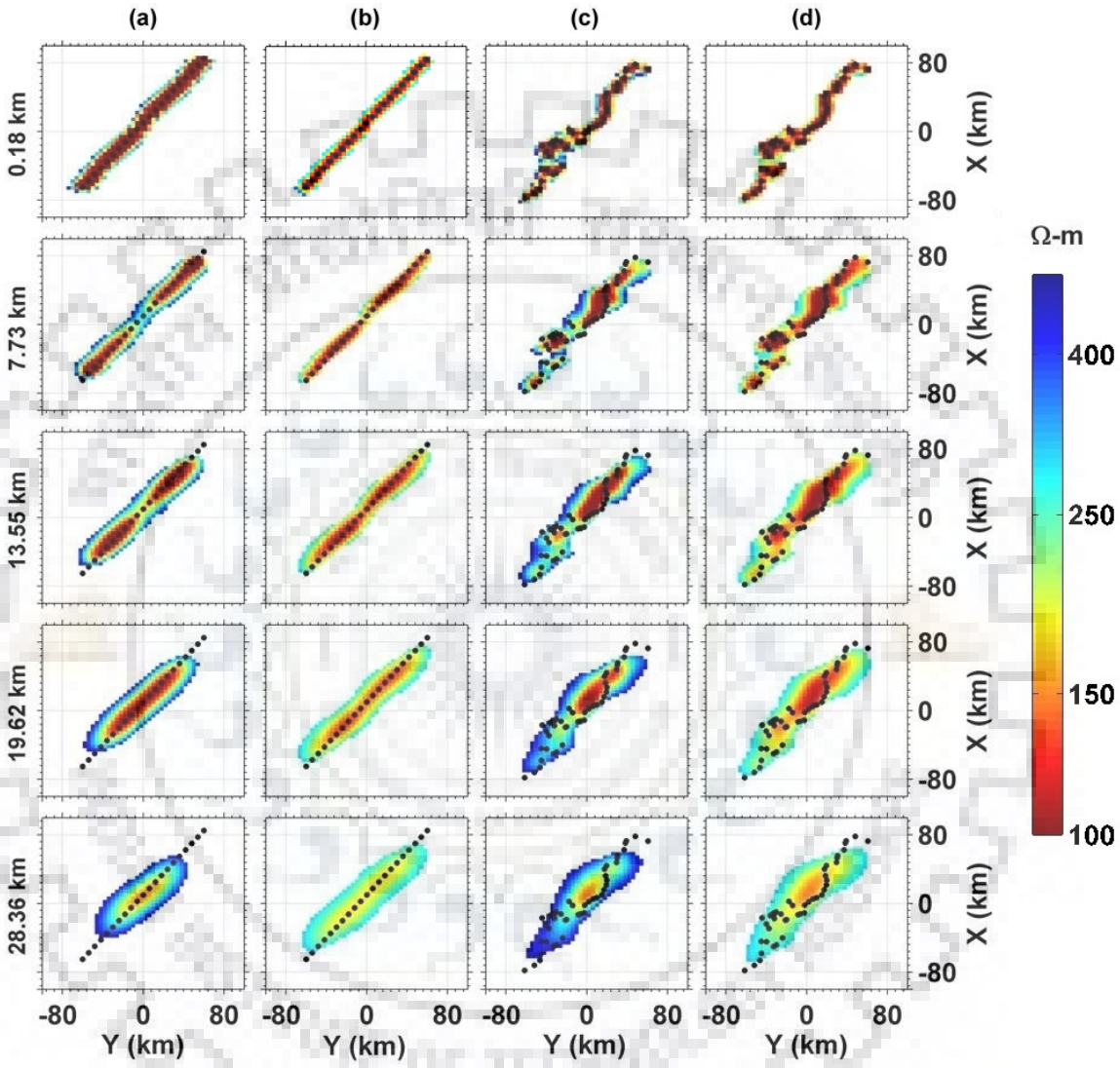

Figure 3.3: Vertical columns showing depth slices of 3D inverted model depicting effect of resistivity of initial guess model for data generated with 100 Ωm as true model and inverted using (a) guess model of 1000 Ωm for profile (i), (b) guess model of 500 Ωm for profile (i), (c) guess model of 1000 Ωm for profile (ii) and (d) guess model of 500 Ωm for profile (ii).

between the true resistivity and a threshold value which may be either the arithmetic or geometric mean of resistivities of initial guess model and true model. The zones of influence for different initial guess model resistivity values along with the arithmetic and geometric mean resistivities are given in Table 3.3. It may be added that the resistivity of inverted model is well resolved when the final resistivity value lies between the true value and threshold value.

Fig. 3.3 and 3.4 shows that within the zone of influence, the resistivity of the inverted model is well resolved for both the initial resistivity values 500 Ωm and 1000 Ωm. The zone of influence is approximately 20 km wide for straight profile and 40 km wide for RG profile. In case of conductive half-space initial models the nRMS error value reaches 1 in few iterations. From Fig. 3.4 it is clear that the zone of influence decreases to a near zero value at depths greater than 13.55 km for 10 Ωm case and at the depth of 20.36 km for 50 Ωm case. This is due to the skin depth effect. It shows that the initial guess model with very low resistivity is unable to resolve the high resistivity features.

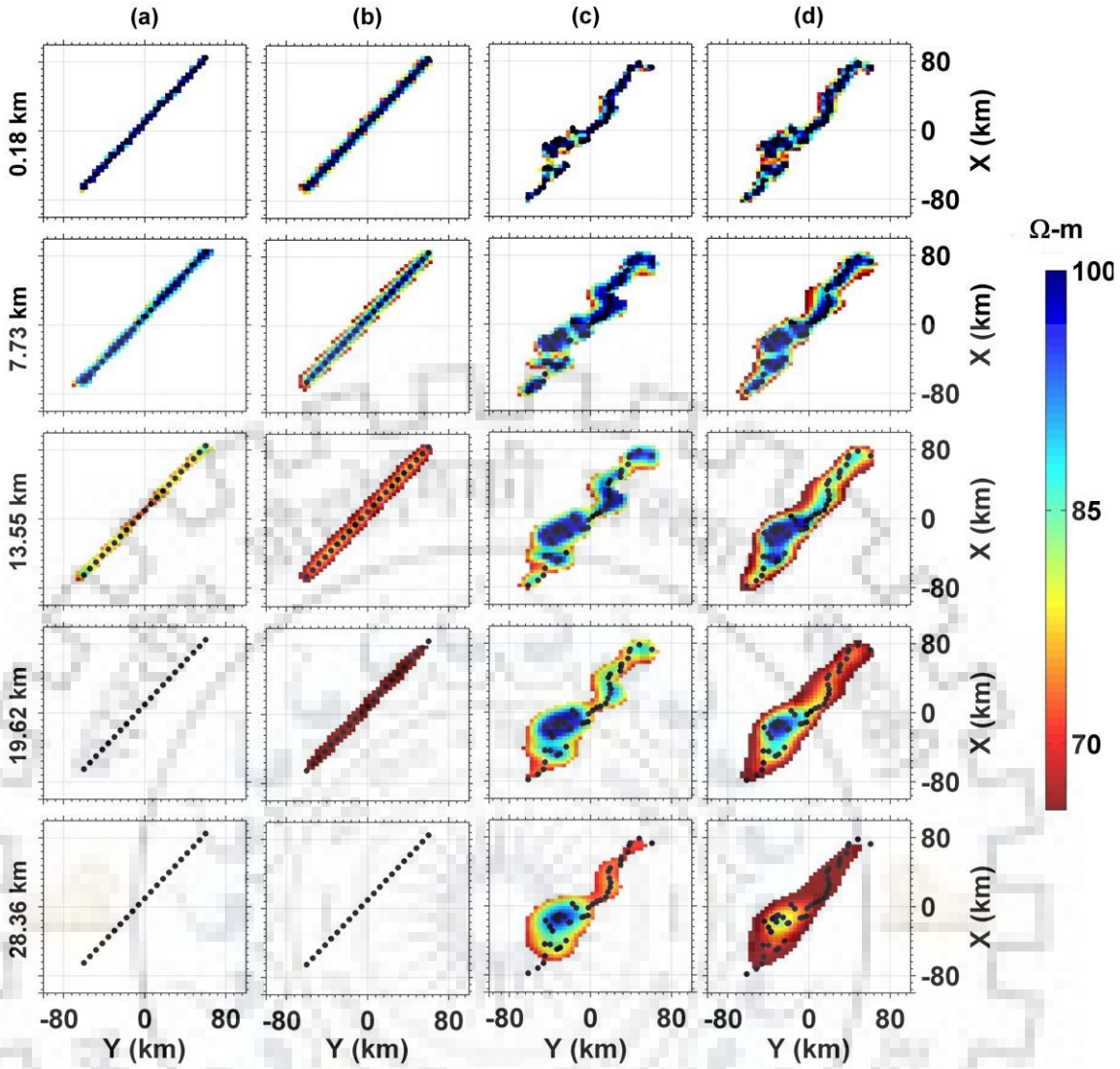

Figure 3.4: Vertical columns showing depth slices of 3D inverted model depicting effect of resistivity of initial guess model for model generated with 100 Ωm as true model inverted using guess model of (a) guess model of 10 Ωm for profile (i), (b) guess model of 50 Ωm for profile (i), (c) guess model of 10 Ωm for profile (ii) and (d) guess model of 50 Ωm for profile (ii).

Table 3.2: The inversion and convergence parameters of synthetic experiments for studying the effect of resistivity of the homogeneous half-space guess model.

Profile	Resistivity of initial half-space (Ωm)	Starting nRMS	Final nRMS	No. of iterations
(i)	1000	50.83	1.11	62
	500	29.00	1.03	9
	50	6.90	1.00	3
	10	16.05	1.00	13
(ii)	1000	50.09	1.05	23
	500	29.05	1.02	14
	50	6.88	1.00	8
	10	16.04	1.03	40

Table 3.3: Resistivity used in defining the zone of influence for various initial guess models and zone of influence for profile (i).

True Resistivity of half-space (Ωm)	Resistivity of initial half-space (Ωm)	Arithmetic Mean Resistivity (Ωm)	Geometric Mean Resistivity (Ωm)	Width of Zone of influence (km)
100	1	50	**10**	**4**
100	10	55	**32**	**4**
100	50	75	**71**	**12**
100	200	**150**	141	**32**
100	500	**300**	224	**32**
100	1000	**550**	316	**20**
100	2000	**2550**	700	**20**

3.4.1.2 Effect of Range and Density of Time Periods

To study the effect of range and density of time periods 3D inversions were performed for both the profiles mentioned in first experiment. Dataset (a) was generated for 25 periods logarithmically distributed in the range 0.01-1000 s with 5 periods per decade. Dataset (b) was generated for 50 periods logarithmically distributed in the range 0.01-1000 s with 10 periods per decade. Dataset (c) was generated for 30 periods logarithmically distributed in

the range 0.01-10000 s with 5 periods per decade. For each profile the initial half-space guess models of resistivity 1000 Ωm was used. The starting and final normalized Root Mean Square (nRMS) error values along with the number of inversion iterations it took for convergence in each case is given in Table 3.4. The depth slices (x-y plane) of the three inverted 3D models corresponding to datasets (a) to (c) for profile (i) are plotted in columns 'a' to 'c'of Fig. 3.5. Similarly, the depth slices for profile (ii) are shown in Fig. 3.6.

Table 3.4: The inversion and convergence parameters of synthetic experiments performed for studying the effect of range and density of time periods.

Profile	**Time Period range (sec)**	**Starting nRMS**	**Final nRMS**	**No. of iterations**
(i)	0.01-1000 (25)	50.83	1.11	62
	0.01-1000 (50)	51.52	1.01	31
	0.01-10000 (30)	51.6	1.04	58
(ii)	0.01-1000 (25)	50.09	1.05	23
	0.01-1000 (50)	50.97	1.00	26
	0.01-10000 (30)	51.70	1.03	37

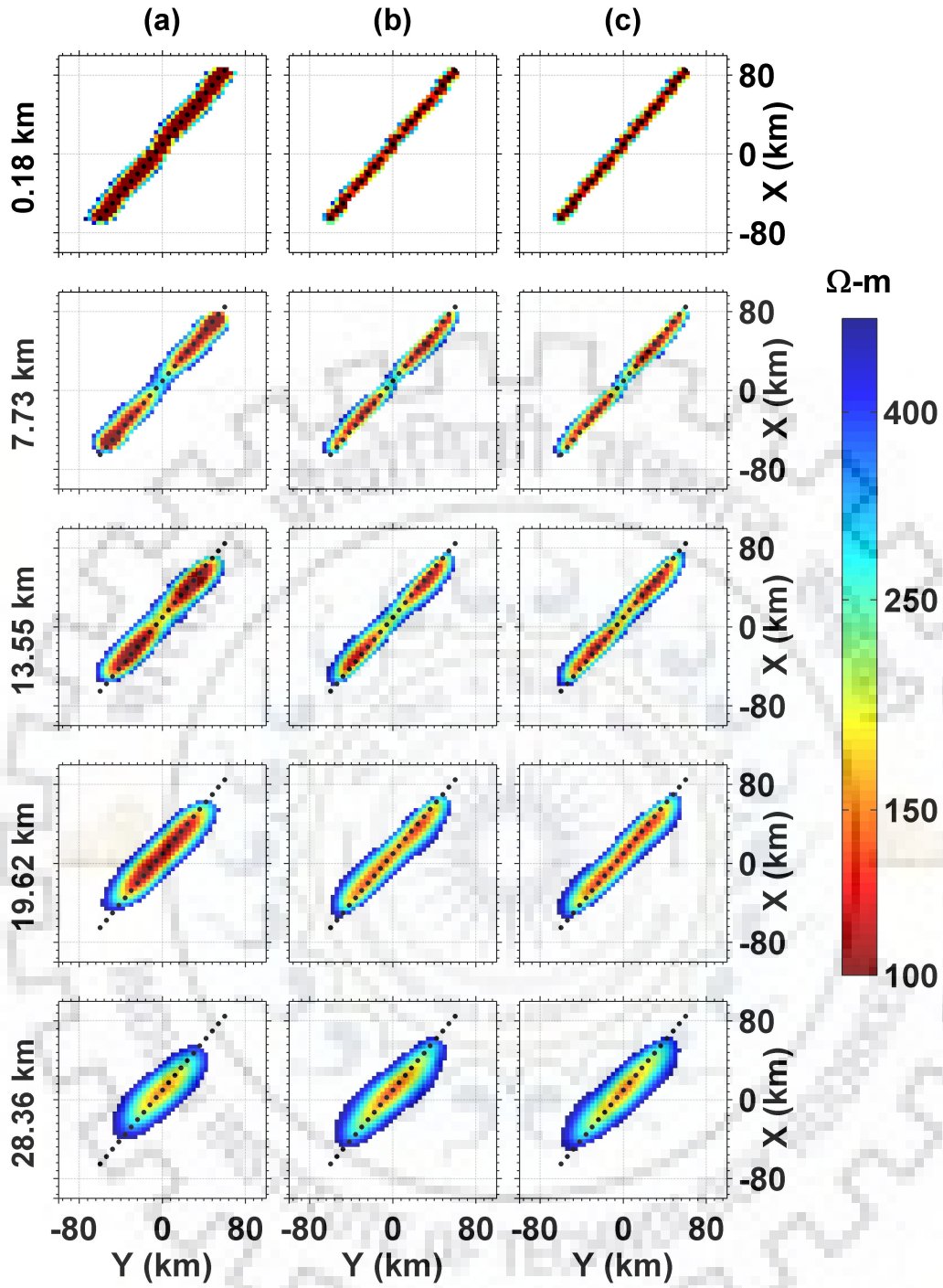

Figure 3.5: Vertical columns showing depth slices of 3D inverted model depicting effect of range and density of time period for data generated on profile (i): (a) for 25 periods logarithmically distributed in the range 0.01-1000 s with 5 periods per decade, (b) for 50 periods logarithmically distributed in the range 0.01-1000 s with 10 periods per decade and (c) for 30 periods logarithmically distributed in the range 0.01-10000 s with 5 periods per decade.

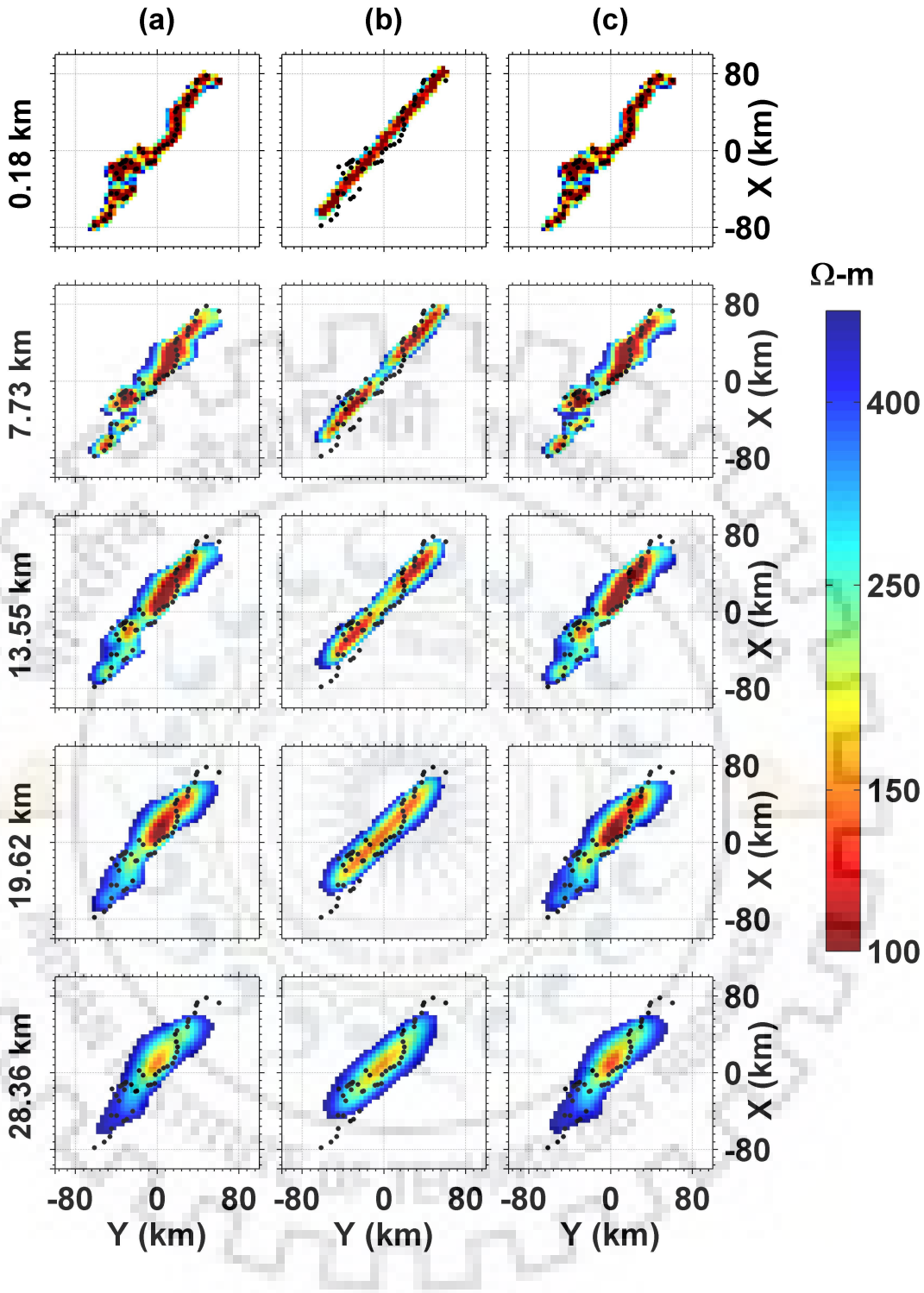

Figure 3.6: Vertical columns showing depth slices of 3D inverted model depicting effect of range and density of time period for data generated on profile (ii): (a) for 25 periods logarithmically distributed in the range 0.01-1000 s with 5 periods per decade, (b) for 50 periods logarithmically distributed in the range 0.01-1000 s with 10 periods per decade and (c) for 30 periods logarithmically distributed in the range 0.01-10000 s with 5 periods per decade.

In first column of Fig. 3.5, at deeper depths the resolution of profile in the extreme ends decreases. However, from second and third columns of Fig. 3.5, it was observed that at deeper depths (> than 19.62 km) the resolution of along the profile features gets better as the number of periods per decade was increased. The effect of increased density of time periods, in column two of Fig. 3.6, is not visible greatly on the profile (ii). However, in column three of Fig. 3.6, for deeper depths the resolution of profile gets better as the period range is increased.

3.4.1.3 Effect of Density of Sites

To study the effect of density of sites 3D inversion was performed on above mentioned two profiles with varying site density and spacing. For profile (i) variations used were: (a) 21 sites placed diagonally in a straight line, with a constant 9 km spacing, (b) 41 sites placed diagonally in a straight line, with a constant 5 km spacing, (c) 25 sites placed diagonally in a straight line, with constant site spacing of 5 km at the center of the profile and 9 km elsewhere and (d) 25 sites placed diagonally in a straight line, with spacing of 9 km, here the profile length was increased by adding two sites on both ends of the profile. For profile (ii) variations used were (a) 39 sites at the actual field locations along RG profile and (b) 54 sites with increased site density near the southern end of profile.

The data were computed at 25 periods distributed logarithmically in the time range 0.01-1000 s. The initial half-space guess models of resistivity 1000 Ωm was used for each case. The starting and final normalized Root Mean Square (nRMS) error values along with the number of inversion iterations needed for convergence in each case are given in Table 3.5.

The depth slices (x-y plane) of the three inverted 3D models for profile (i) corresponding to cases (a) to (d) are plotted in columns ‘a’ to ‘d’ of Fig. 3.7.

Table 3.5: The inversion and convergence parameters of synthetic experiments performed for studying the effect of density of sites.

Profile	**Number of sites and site spacing (km)**	**Starting nRMS**	**Final nRMS**	**No. of iterations**
(i)	21 (9)	50.83	1.11	62
	41 (5)	50.94	1.00	18
	25 (5 and 9)	50.84	1.00	22
	25 (9)	50.93	1.00	17
(ii)	39 (Nonuniform)	50.09	1.05	23
	54 (Nonuniform)	50.95	1.00	26

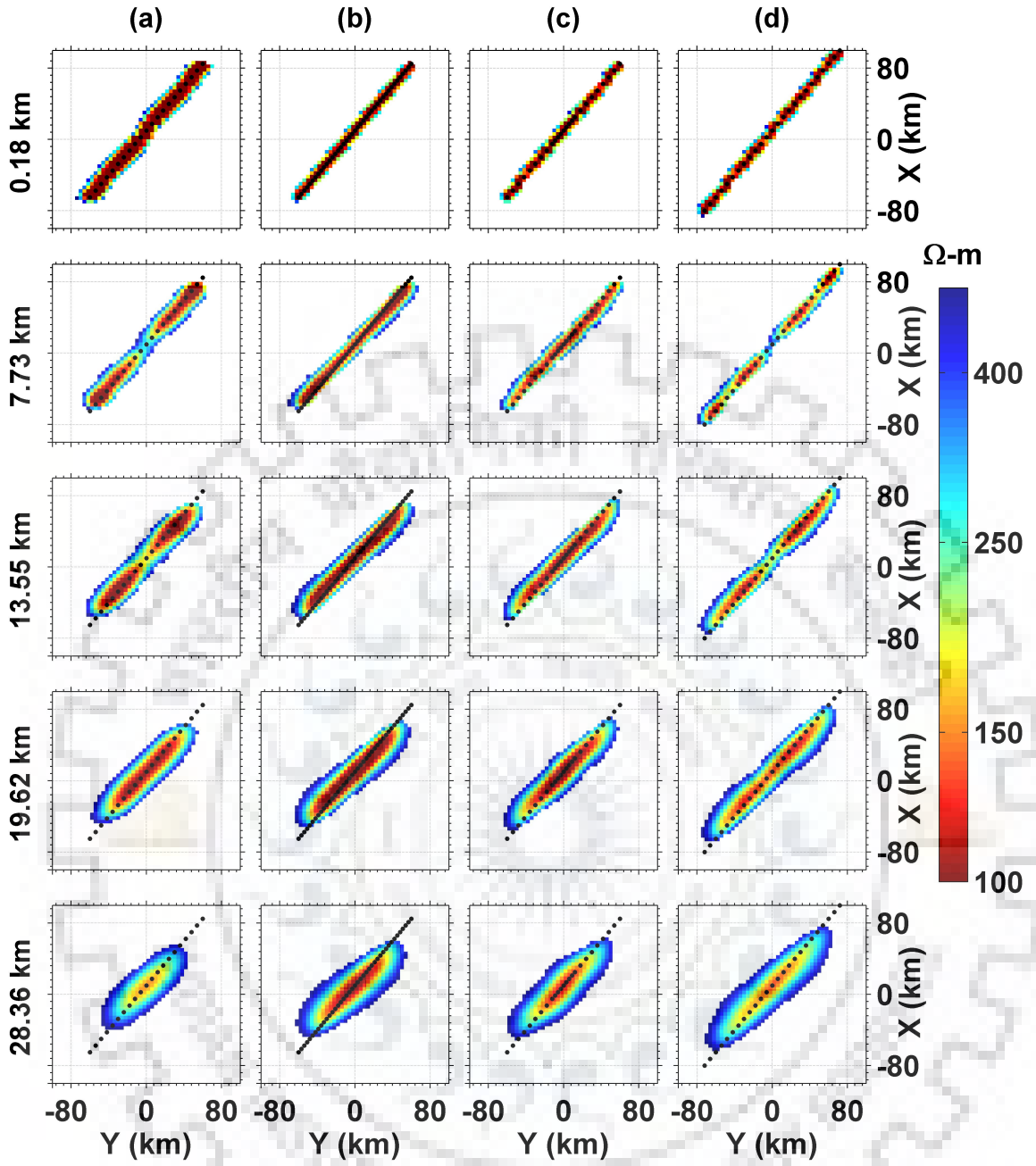

Figure 3.7: Vertical columns showing depth slices of 3D inverted model depicting effect of density of sites for data generated on profile (i) for cases: (a) 21 sites placed diagonally in a straight line, with a constant 9 km spacing, (b) 41 sites with a 5 km constant site spacing, (c) 25 sites with site spacing of 5 km at the center of the profile and 9 km elsewhere and (d) 25 sites with site spacing of 9 km, with profile length increased by adding two sites on both ends of profile.

It was observed from the Fig. 3.7(a), that for profile (i), case (a), the true resistivity of 100 Ωm was not recovered correctly at depths 7.73 and 13.55 km. However, it was recovered at these depths when the site density was increased in case (b) (Fig. 3.7(b)). Further, for case

(a) at a depth of 19.62 km the resolution of resistivity was limited to sites within the profile and not towards the edges (Fig. 3.7(a)). This effect was analogous to the corresponding end effect in any interpolation problem. The true resistivity at depths 7.73 and 13.55 km was also recovered correctly for case (c), when the site density was increased in the central region only (Fig. 3.7(c)). However, the low resolution persists at a depth of 19.62 km for the sites near the edges of the profile, as in (Fig. 3.7(a)). This lack of resolution was overcome by increasing the length of profile by adding two sites at each end. Fig. 3.7(d) shows the inverted model of extended profile where the end effect has shifted further outward in the extended profile. The zone of influence for straight profile was found to be 20 km wide and this width increases with depth.

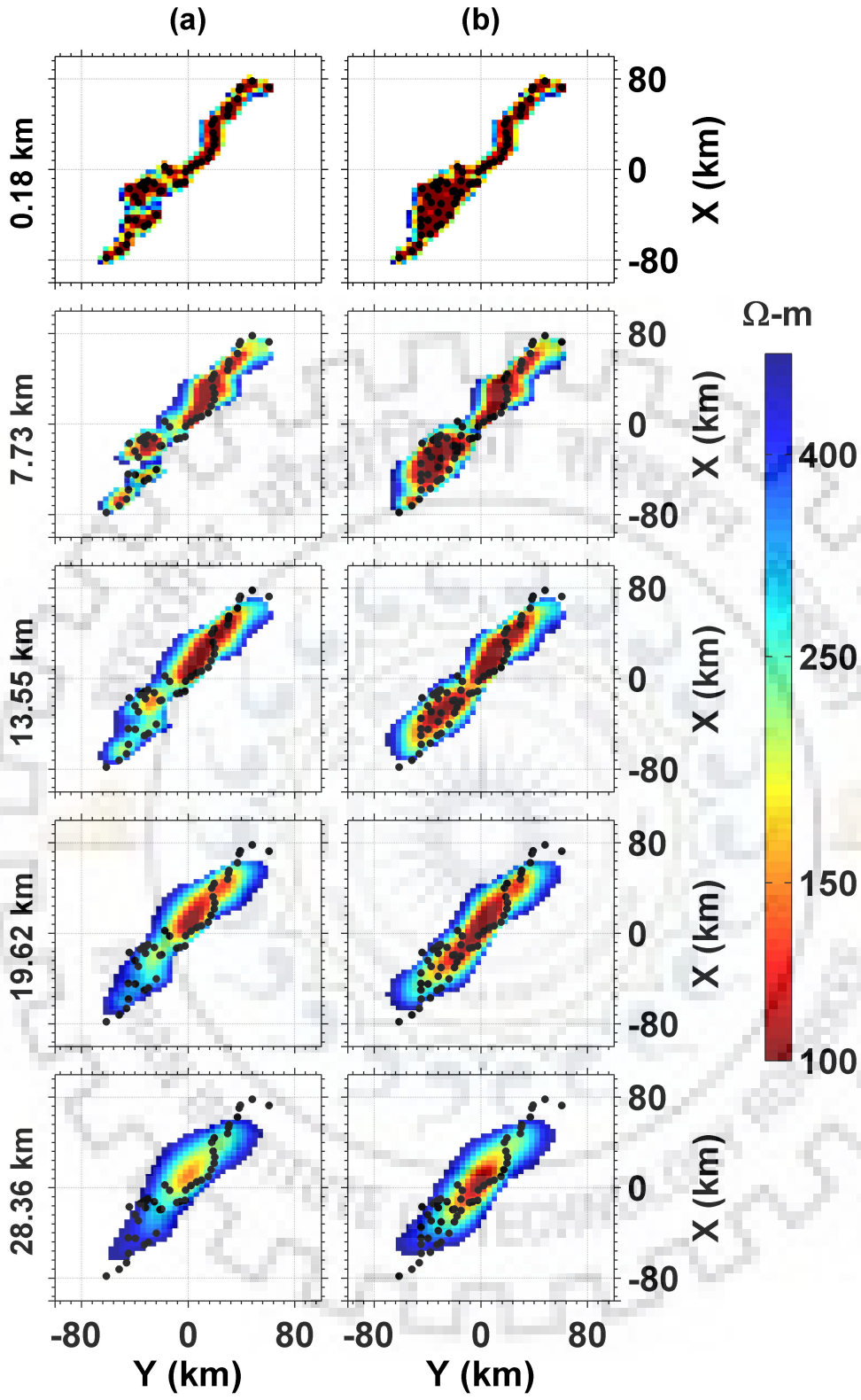

Figure 3.8: Vertical columns showing depth slices of 3D inverted model depicting effect of density of sites for data generated at (a) 39 MT sites at the actual field locations along RG profile i.e. profile (ii) and (b) 54 MT sites with increased density of sites in the south of RG profile.

For the RG profile, when all sites were placed on actual recording locations, the width of the zone of influence increases to about 40 km (Fig. 3.8(a)) due to wider scatter of sites. In Fig. 3.8(a) it can be seen that near the southern end the true value of 100 Ωm is not recovered closely. So the site density was increased between X = 0 km to X = 70 km in Fig. 3.8(b) and it was found that the true value of resistivity was recovered reasonably well at 7.73 km, 13.55 km and 19.62 km. This experiment suggests that an off-profile nearby resistivity feature can be sensed by the data to a varying degree of resolution. This sensitivity of data reduce as one moves away from the profile.

The above three experiments suggest that the zone of influence varies with resistivity, time periods and site spacing. The optimal values of all these parameters must be explored and fixed prior to field data inversion.

3.4.2 Inversion of Field Data

3D inversions were performed on recorded MT data using various data sets comprising different combinations of VTF, PT and Z. VTF and PT data are primarily sensitive to resistivity contrast across a surface rather than to the two resistivity values. Hence, the initial guess model has a significant effect on the resistivity structure produced by VTF and PT data. 3D inversion experiments were done with four resistivity values (10, 100, 1000 and 10000 Ωm) of the half-space initial guess model. On the basis of nRMS error values and convergence level, it was concluded that the 100 Ωm half-space was the optimum one and it was used for all subsequent inversion experiments on RG profile data. The model discretization and grid characteristics were same as used in the synthetic experiment discussed in previous section (3.4.1). To study the impact of smoothing matrix, we performed one inversion with a constant isotropic smoothing of 0.3 in all three directions. Two more inversions were performed with anisotropic smoothing having higher value in geoelectric strike direction. The smoothing parameters in these two cases, in x-, y- and z-directions, were (0.3, 0.5 and 0.1) and (0.1, 0.7 and 0.1) respectively. Based on the experiments on smoothing factor and in view of general Himalayan tectonic configuration along the main Himalayan arc, the model smoothing was set as (0.3, 0.5 and 0.1) in x-, y- and z-directions respectively for subsequent inversions. Higher smoothing factor in strike direction has been used in literature by other workers [108, 234]. With these choices of control parameters all the inversion experiments carried out on real data are described next.

In the first inversion experiment, the VTF data were inverted at 40 periods lying in the period range 1.19-1000 s using a constant error floor of 0.03. The nRMS error value reduced from a starting value of 4.74 to 1.54 in 24 inversion iterations. The inverted model, in the form of depth slices extracted at five depths, is shown in the first column of Fig. 3.9.

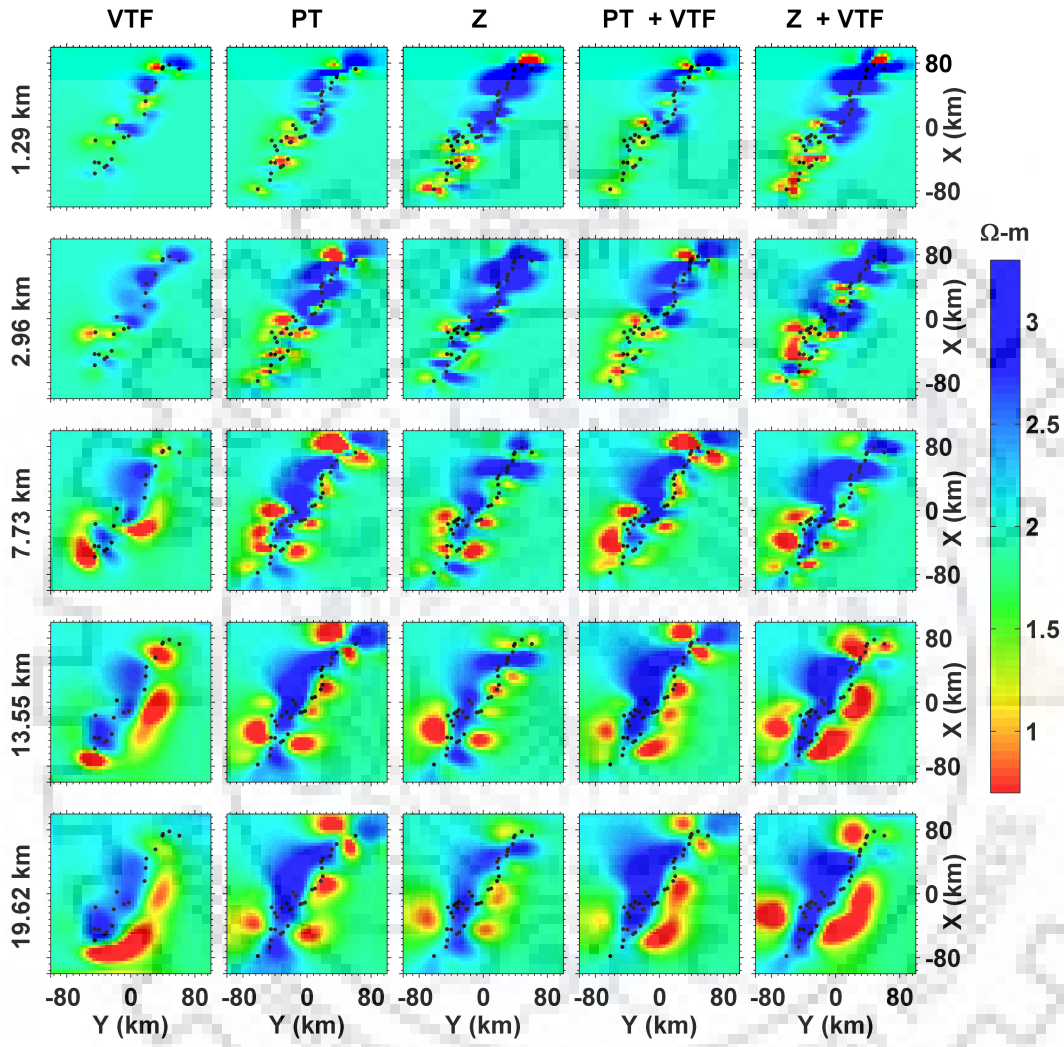

Figure 3.9: Depth slices of 3D inverted model obtained from models presented in the form of columns from left to right as VTF, PT, Z, VTF + PT and VTF + Z.

In the second inversion run, the Phase Tensor (PT) data were inverted at 34 sites for 41 periods in the range 0.01-1000 s. The error floor value used was 5% of absolute value of phase tensor component, $\Phi|_{ij}|$, along with the threshold error floor of 0.05. The nRMS error value reduced from a starting value of 9.31 to 4.7 in 68 inversion iterations. The inverted model, in the form of depth slices, is shown in second column of Fig. 3.9.

In the third inversion run, the full impedance tensor data were inverted at 39 sites for 41 periods in the range 0.01-1000 s. The data error floor used was 10% of $|Z_{ij}|$ along with the

threshold error floor of 10% of $\sqrt{|Z_{xy} * Z_{yx}|}$ for the diagonal elements. The nRMS error value reduced from a starting value 27.9 to 2.05 in 91 inversion iterations. The inverted model, in the form of depth slices, is shown in third column of Fig. 3.9. The observed and fitted VTF data are compared in Fig. 3.10. At selected sites, the observed and the computed apparent resistivity and phase curves are shown in Fig. 3.11. It is evident from Fig. 3.11 that the fit between the observed and computed responses is, better for the off-diagonal components of impedance tensor than it is for the diagonal components of impedance tensor. This is due to the fact that the 3D distortion matrix elements are not included as unknown in the inversion scheme [11].

In the fourth and fifth runs we carried out joint inversion of (i) PT and VTF and (ii) Z and VTF data. The nRMS error value reduced from 7.99 to 4.63 in 73 inversion iterations for fourth run and from 25.13 to 1.97 in 90 inversion iterations for the fifth run. These two inverted models, in the form of depth slices, are shown in fourth and fifth columns of Fig. 3.9.

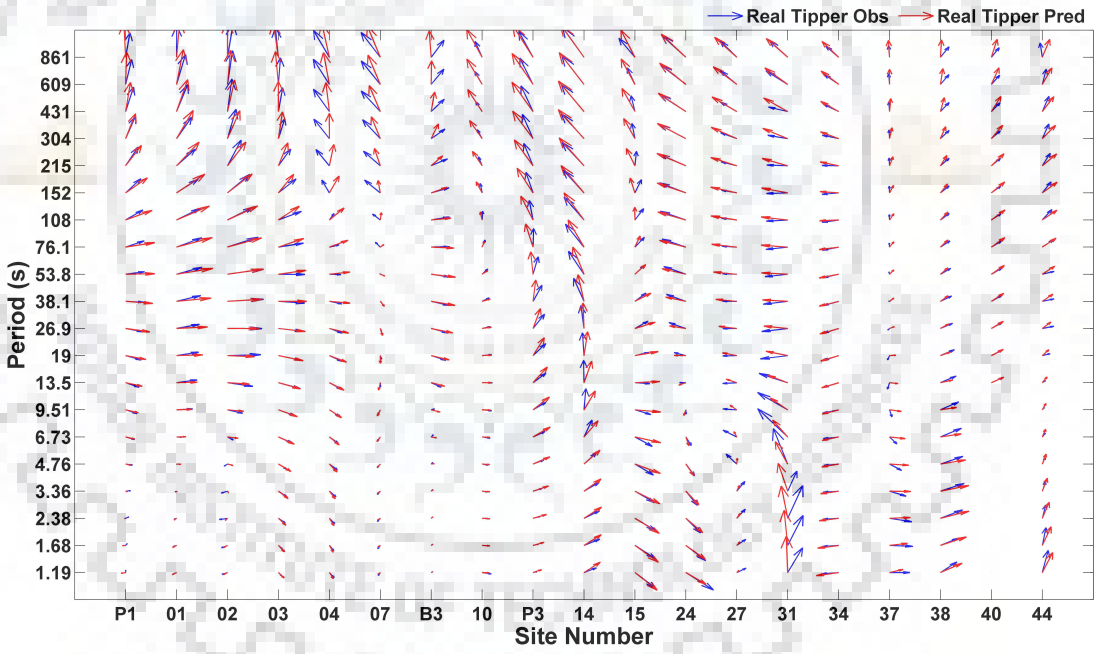

Figure 3.10: Observed and computed VTF response.

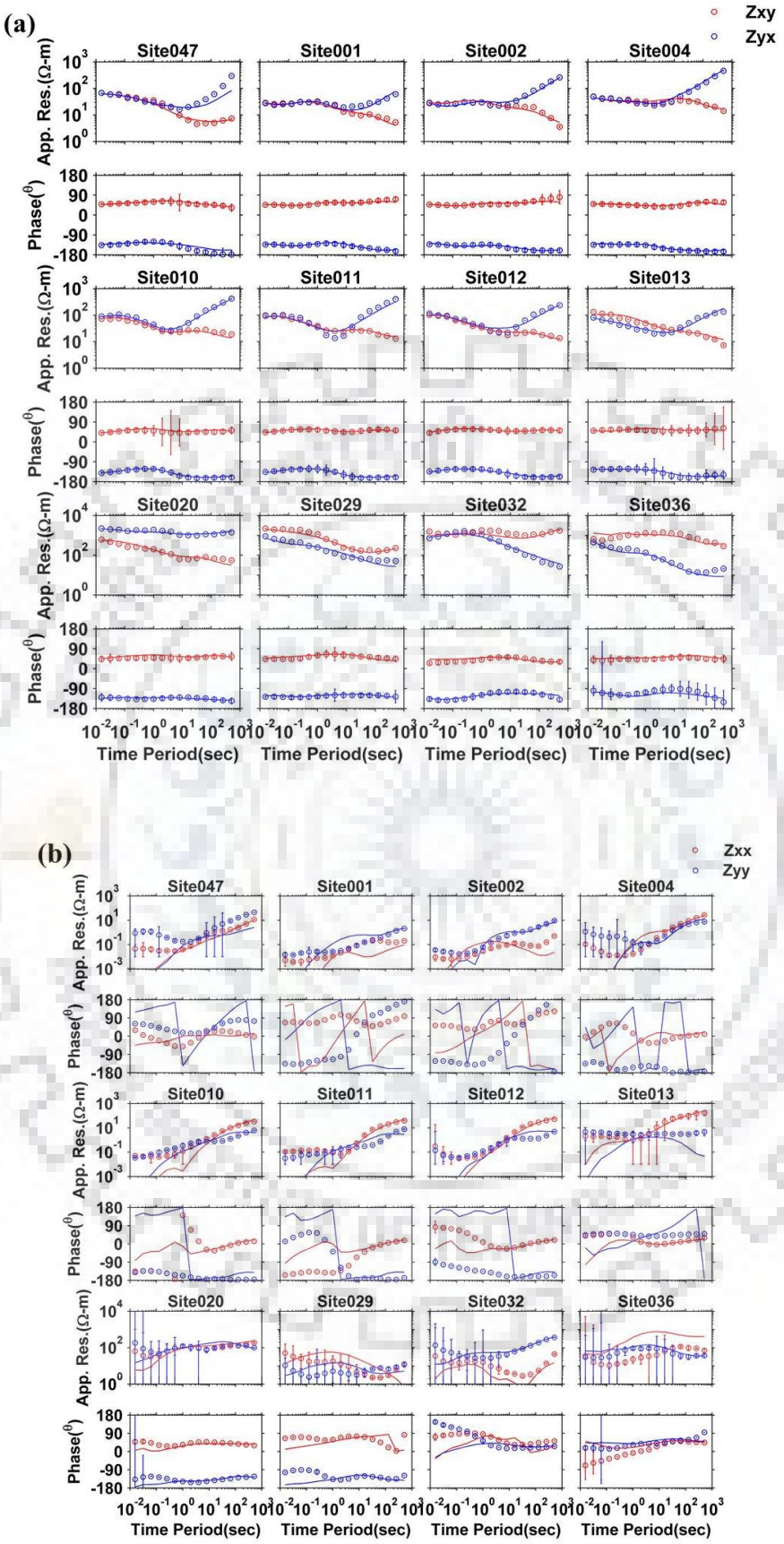

Figure 3.11: Misfit plot of apparent resistivity and phase derived from full impedance tensor for selected sites, (a) off-diagonal components and (b) diagonal components.

3.4.3 Results and Interpretation

To highlight the differences in the quality of inverted models, in Fig. 3.12 are presented the stacked y-z plane slices of the two 3D models that were obtained from Z data inversion and from the joint inversion of Z and VTF data. Three low resistivity (conductive) features ('C', 'F' and 'G') and one high resistive feature ('B') are marked in Fig. 3.12. Out of these, the feature, 'C', is an on-profile feature while 'F' and 'G' are the off-profile features. These features are more prominent in the joint inversion model. To select the final model a comparison of nRMS error values in Z and VTF data, is presented in Table 3.6, for the three inverted models obtained after inversions of only VTF, only Z and Z+VTF data. The errors in Z and VTF for the joint inversion are of the same order as the corresponding errors in individual data inversion. Further, the misfit (17.52) in Z data for the inverted model of VTF data is enormously high in comparison to the corresponding misfit value of joint inversion. Similarly, the misfit (4.40) in VTF data for the inverted model of Z data is high in comparison to the corresponding misfit value of joint inversion. This implies that in joint inversion the ill-effects of each data subset get constrained by the other data subset. Therefore, the model obtained from joint inversion is selected as the final model to be used for subsequent experiment and further discussion.

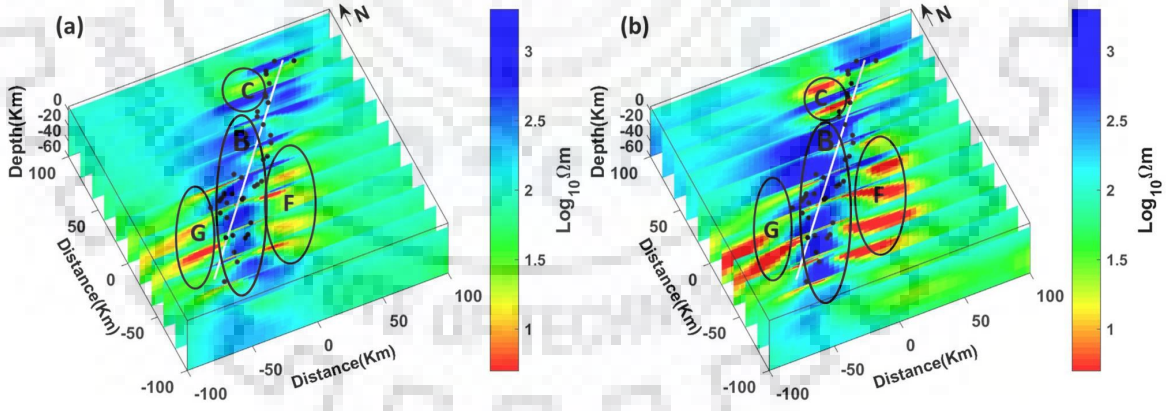

Figure 3.12: 3D model yz-plane slices of the inverted model obtained after inversion of (a) full impedance data with 100 Ωm half-space as initial guess model and (b) full impedance data and the VTF data with 100 Ωm half-space as initial guess model.

Table 3.6: The comparison of nRMS error values in Z and VTF data for three inverted models.

Data set used for inversion	**nRMS in Z**	**nRMS in VTF**
Z+VTF	2.04	1.67
only VTF	17.52	1.54
only Z	2.05	4.40

In Fig. 3.13, the final model is plotted in the form of the depth slices (x-y plane) at different depth intervals. It shows several other conductive and resistivity features superimposed on various thrust geometries and tectonic boundaries on near surface slices. In Fig. 3.14 are given three inverted models: (a) the profile section, extracted from our 3D inverted model, (b) the 2D inverted model of the RG profile obtained by Miglani et al. [144] and (c) the 2D inverted model of another parallel profile, Bijnaur-Malari (BM) profile, located about 100 km east of RG profile obtained by Rawat et al. [183]. In these models seven major features are identified and labeled as characters 'A' to 'G'. These labels are same as in Fig. 3.12. The sensitivity tests were performed to validate each of these features and the outcomes of sensitivity tests are discussed next.

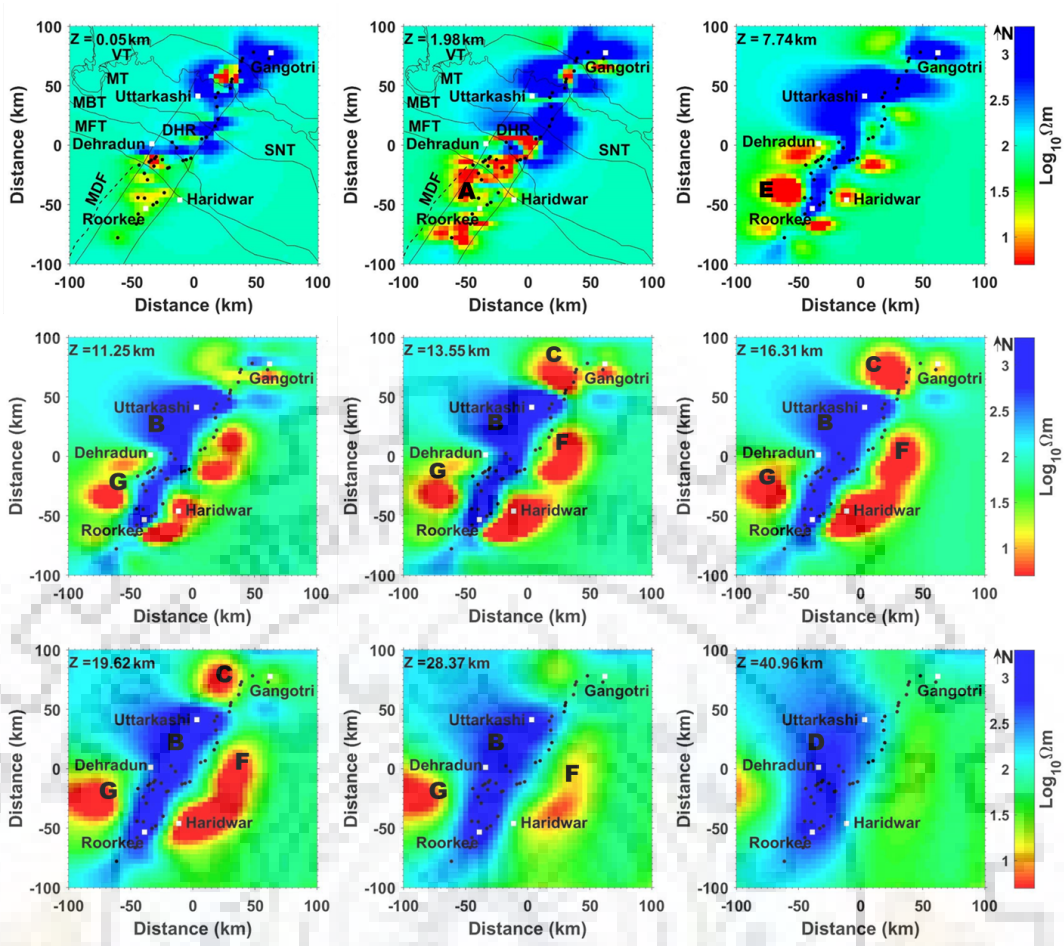

Figure 3.13: Depth slices of 3D inverted model estimated through joint inversion of full impedance tensor and VTF data. The depth level (Z) is shown in each slice panel. Major resistivity features are marked by character 'A' to 'G' in the respective depth slice.

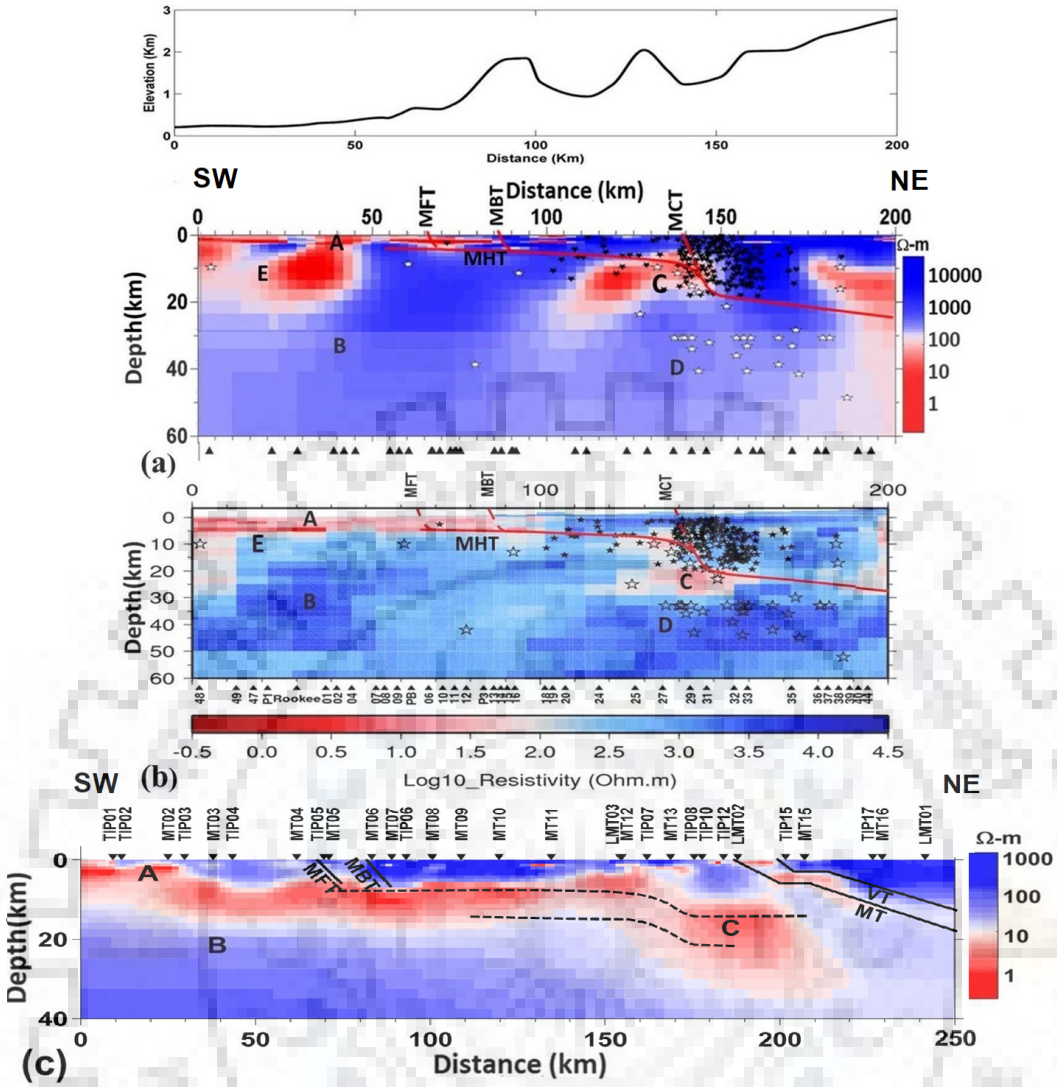

Figure 3.14: (a) Profile section extracted from 3D model obtained from full impedance tensor and VTF joint inversion with 100 Ωm half-space as initial guess model, along with the elevation section of profile. Also, the earthquake hypocenters are shown as stars with different colors: white ($M_b > 3$) and black ($M_b < 3$). (b) 2D inverted model along the profile from Miglani et al. [144], (c) Inverted 2D model of MT profile adapted from Rawat et al. [183], in 100 km east of RG profile.

3.4.3.1 Sensitivity Test

The sensitivities of various features of the final model were tested, one by one, for their robustness. This has been done by first replacing the resistivity of a particular feature by the background resistivity value (100 Ωm) and then computing the forward response. The nRMS error value was computed between the inverted model response and the response of the model obtained after removing the feature. It has been found that the nRMS error values increases

if any one of the features was removed. The nRMS error values for the sensitivity tests for 'A', 'B', 'C', 'D', 'E', 'F' and 'G' features increased from 1.977 to 6.62, 2.7, 4.16, 2.5, 2.7, 2.4 and 2.5 respectively. It was observed that each feature contributes to the model response at certain sites and for a certain period band. For clear demonstration, bar diagrams showing the site wise changes in nRMS error value with and without the two off-profile features, 'F' and 'G', are shown in Fig. 3.15 and Fig. 3.16 respectively. This analysis establishes that the conductive and resistive features in the model were not inversion artifacts.

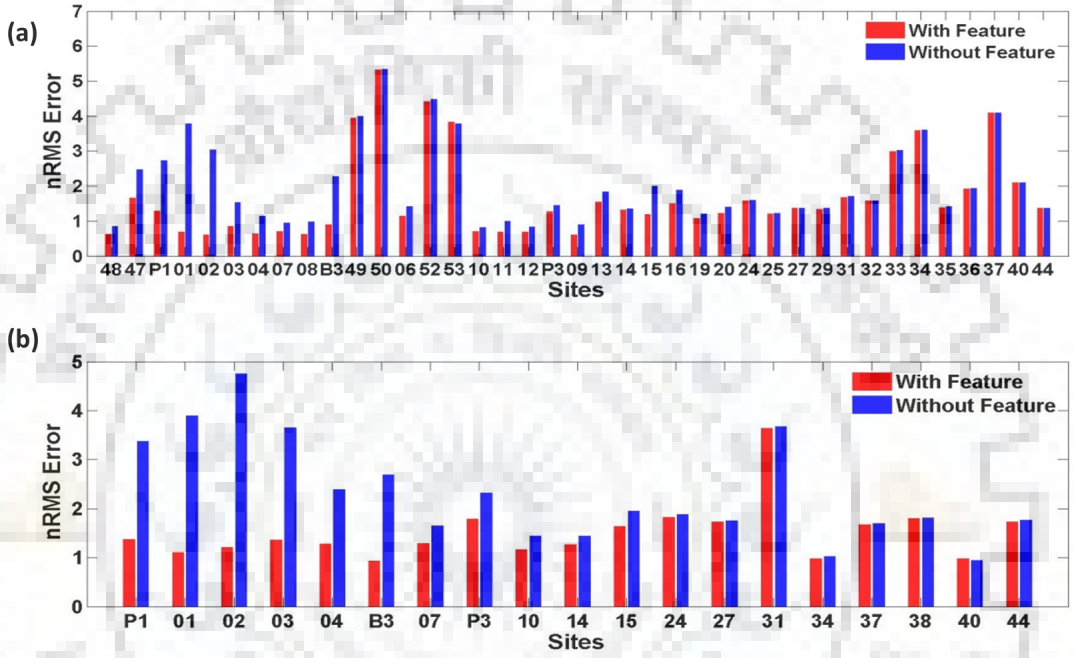

Figure 3.15: Sensitivity test for off-profile feature, 'F' showing site wise nRMS error value comparison with and without feature for (a) Full Impedance Tensor and (b) VTF.

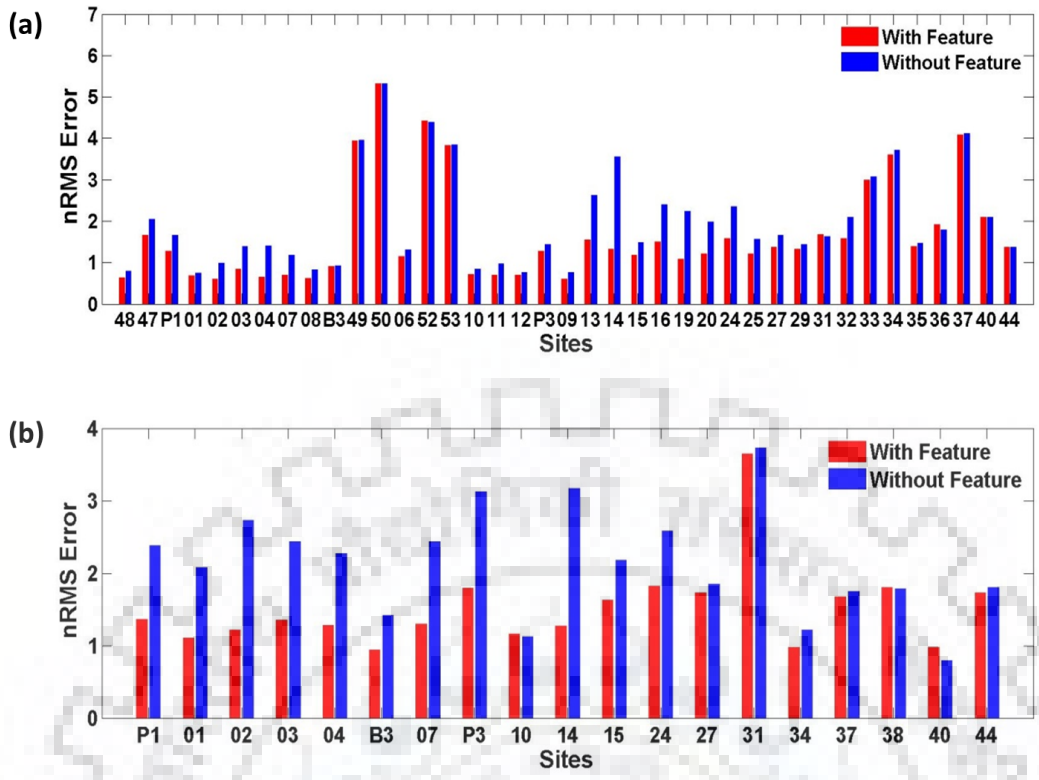

Figure 3.16: Sensitivity test for off-profile feature 'G' showing site wise nRMS error value comparison with and without feature for (a) Full Impedance Tensor and (b) VTF.

3.4.3.2 Geological Interpretation of the Geoelectrical Model

The five panels (a-e) of Fig. 3.9 present various x-y planes of the five resistivity models that were obtained by respectively performing 3D inversion of VTF, PT, Z, VTF+PT and VTF+Z data. Since the different components of MT data have different degrees of sensitivity to the model features, the geometry and resolution of these different features of the models vary. For example, VTF and PT data are primarily sensitive to the resistivity contrast and a reasonably good initial guess model is needed to substantiate the information about the resistivity of subsurface features. A conductive off-profile feature was deciphered on the basis of VTF based 3D forward modeling [88]. This feature is present in almost all the inverted models shown in Fig. 3.9. However, it is more prominent in the models obtained using VTF data (Fig. 3.12).

In the final model, seven significant resistive and conductive features are clearly identifiable and these are labeled as 'A' to 'G'. Five of these features ('A' to 'E') are located along the profile section while the other two ('F' and 'G') are off-profile features. We now investigate the tectonic and geological significance of these features and their relationships

with models of the region obtained from other geophysical methods.

In Fig. 3.14, each of the three models has all the major features ('A' to 'E') albeit with different degree of spatial and vertical resolution. The variations in the dimension and location of different common features (Fig. 3.14) are due to the fact that the models are obtained using different data sets (RG profile data for Fig. 3.14(a-b) and BM data for Fig. 3.14(c)) and different algorithms (Singh et al. [204] and Rodi and Mackie [186]).

Geologically, the feature 'A' is interpreted as the conductive sediments deposited by the southerly-flowing river system of the Himalaya. It defines the Indo-Gangetic Plain (IGP) sediments. It has a low resistivity (< 50 Ω m) and it is mainly confined to the southern part of the profile between the IGP and SH regions. The thickness of this feature is 6 km in the southern part of the profile. It may be added that various workers have estimated the thickness of IGP sediments of the order of 5 km. Based on 1D inversion of MT data, Gupta et al. [78] estimated a sediment thickness of 5-6 km in the SH region. Rawat et al. [183] estimated a similar zone (IGP sediments) having a thickness of 3-5 km. In Nepal Himalayan region, Lemonnier et al. [118] proposed the Gangetic foreland as a low resistivity (30 Ωm) feature with a thickness of 5 km. In Sikkim Himalaya, Kumar et al. [112] delineated the foreland basin having a low resistivity (< 50 Ωm) layer of thickness 4–6 km.

The feature 'B' corresponds to the highly resistive (> 1000 Ωm) Indian basement that runs nearly transverse to the average geoelectric strike, N71°W which is also the strike direction of MBT. This resistive feature was interpreted as an electrical image of DHR beneath the IGP that continued up to MCT-I. [88] estimated its geoelectric strike as N13°E. This feature lies beneath the IGP and SH and it continues into the LH with a low angle dip. The horizontal and vertical geometry of this feature can be seen in x-y plane as a highly resistive feature along the profile section (Fig. 3.13). This resistive feature was explained by Caldwell et al. [38] through receiver function technique as a positive impedance contrast. [95] performed 3D velocity inversion of five independent subsets of data and generated a consistent 3D velocity map of Garhwal Himalayan region. They also interpreted the high velocity structure in their velocity model as a continuation of DHR up to the MCT zone.

The feature 'C' is a conductive (low resistivity) (< 10 Ωm) region beneath the MCT zone. It extends vertically from 6 to 25 km and horizontally to the south of the MCT zone. The feature 'C' is a typical example of a mid-crustal conductor commonly observed in the Himalayan region. This feature is present in two other models, obtained by 2D inversion of

MT data of RG profile (Fig. 3.14(b)) and nearly parallel BM profile of Rawat et al. [183] (Fig. 3.14(c)). In Fig. 3.14(c), the conductive feature 'C' is located in the depth range 13-25 km and it is lying beneath the MCT zone and extended southward [183]. A similar conductive feature, in the MCT zone, is also observed in Sikkim Himalaya [112] and in Nepal Himalayan [118]. However, lateral and vertical extension of this conductive feature varies slightly in different models within the MCT zone. This feature is supporting the *flat ramp flat* geometry (Fig. 3.14(a)) of MHT, with ramp in the MCT zone. The ramp dips down MHT from 10 km to about 20 km depth in the MCT zone. This conductive feature was also seen as a low velocity anomaly in the 3D velocity model of Kanaujia et al. [95]. They interpreted it as a saturated fractured zone that resulted from the compressional tectonics between DHR and MCT-I. The zone is seismically active and is linked with the ramp where the upper brittle portion of MHT is marked by seismic activities and lower portion shows the presence of fluids and temperature increase. Caldwell et al. [38] predicted this zone with a negative impedance contrast. The tectonic lines drawn in Fig. 3.14(a) inferred the *flat ramp flat* geometry of MHT, a feature also present in the 2D MT model of Miglani et al. [144] and in the model derived through the receiver function technique of Caldwell et al. [38].

The feature 'D' is a resistive ($>$ 1000 Ωm) feature, visible at a depth below 30 km in the northern part of RG profile. This resistive feature is common in three models shown in Fig. 3.14(a). This feature is interpreted as an resistivity image of the subducting Indian Plate beneath the MCT zone.

The feature 'E', is located in the RG profile section as a deep conductive feature ($<$ 10 Ωm) in southern most zone of the profile. It appears to be associated with the Delhi-Mahendragarh fault zone, related to the shallow focus earthquake.

Apart from the five along the profile features, the inverted model has two off-profile conductive features, 'F' and 'G', which are running nearly parallel to DHR on the eastern and western side of DHR. These features support the hypothesis that DHR is bounded by the faults. The sixth feature, 'F', is an elongated conductive feature having a resistivity value $<$ 10 Ωm. It is interpreted as a highly fractured zone saturated with fluids. The top of this zone lies at a depth of 8 km in the eastern side of RG profile and it is dipping in northeast direction. A similar conductive feature was also observed in the resistivity model obtained from the profile of Rawat et al. [183]. They defined this feature as an intra-crustal high conducting layer (IC-HCL). Since the profile of Rawat et al. [183] is located far away

from the zone of influence of our data, it can't be established that our feature 'F' is similar to their conductive feature IC-HCL. The minor variations in these two geoelectric models can be validated through the hypothesis of along strike segmentation of main Himalayan arc [68]. The conductive feature, 'F', is consistent with the conductor delineated on the basis of an earlier regional magnetovariational study [6]. In their 3D velocity model, Kanaujia et al. [95] have also presented this feature as a low velocity zone/anomaly running nearly parallel to the high-velocity DHR. They interpreted it as a highly fractured sedimentary rock deposited at the southeastern boundary of DHR.

Finally the seventh feature, 'G', is also a conductive ($<$ 10 Ωm) feature. This feature extends vertically from 13 km to 30 km. The feature is confined in the IGP and SH region and is located in western side of the profile. This feature appears to be associated with the seismicity of Mahendragarh-Dehradun fault (MDF). Bansal and Verma [18] suggested that MDF is seismically active and generates moderate seismicity. They suggested that the earthquake of March 05, 2012, which was assigned a focal depth of 14 km and a magnitude 4.9, was related to MDF. The, off-profile conductive features, 'F' and 'G', and resistive feature, DHR, are parallel and transverse to the main Himalayan arc. Therefore, on the basis of resistivity feature discussed above we conclude that this investigation supports the idea of existence of transverse tectonics structure in Garhwal Himalayan region.

3.4.3.3 Seismicity Relationship

To understand the relationship between seismicity and resistivity features in the 3D model, in Fig. 3.17, the hypocenters of about 300 small, moderate and large earthquakes (0.5$\geq$ Mb $\leq$ 6.8) taken from Arup et al. [8], Shandilya and Shandilya [198], Wason et al. [248] and https://earthquake.usgs.gov/earthquakes/search/ are projected on respective depth planes. The same is also shown in 2D model Fig. 3.14(a). The largest magnitude earthquake recorded in the region, in recent past, was the Uttarkashi earthquake on October 19, 1991. The majority ($\geq$ 60%) of these earthquake hypocenters are located within the upper 20 km of the crust. The fault plane solutions indicated that majority of these earthquakes were associated with the thrust faults with their planes dipping towards north or northeast direction, perpendicular to the main Himalayan arc. However, a few earthquakes also show strike slip or normal fault plane solution [130, 175, 259]. Occurrence of earthquakes in the Himalayan region is generally explained on the basis of thrust tectonics. Under-thrusting of

Indian plate beneath the Eurasian plate causes the northern end of Indian plate to be strained and fractured from time to time giving rise to the earthquake belt. A significant aspect of the seismicity is that a belt of high rate of earthquakes occurrence follows the arcuate belt that lies in the MCT zone and in Lesser Himalaya close to the MCT zone [259]. It has been observed that the earthquakes are generally located in the resistive zone of the crust with a few exceptions where they are near or in the conductive zone. Seismicity is clustered in MCT zone at depths of 1.9 km, 7.74 km and 11.25 km (Fig. 3.17). The cluster at 11.25 km is located in the resistive feature between the two conductive features. The conductive feature represents the fluid filled zone in the active compression regime of the Himalaya. The mechanical weakening effect could counteract the normal stresses and lower the strain threshold for a brittle failure [35, 82]. The fluid at high pore pressure acts as lubricant, facilitating the occurrence of earthquakes. Thus the resistive zones adjacent to the conductive zone become seismically active.

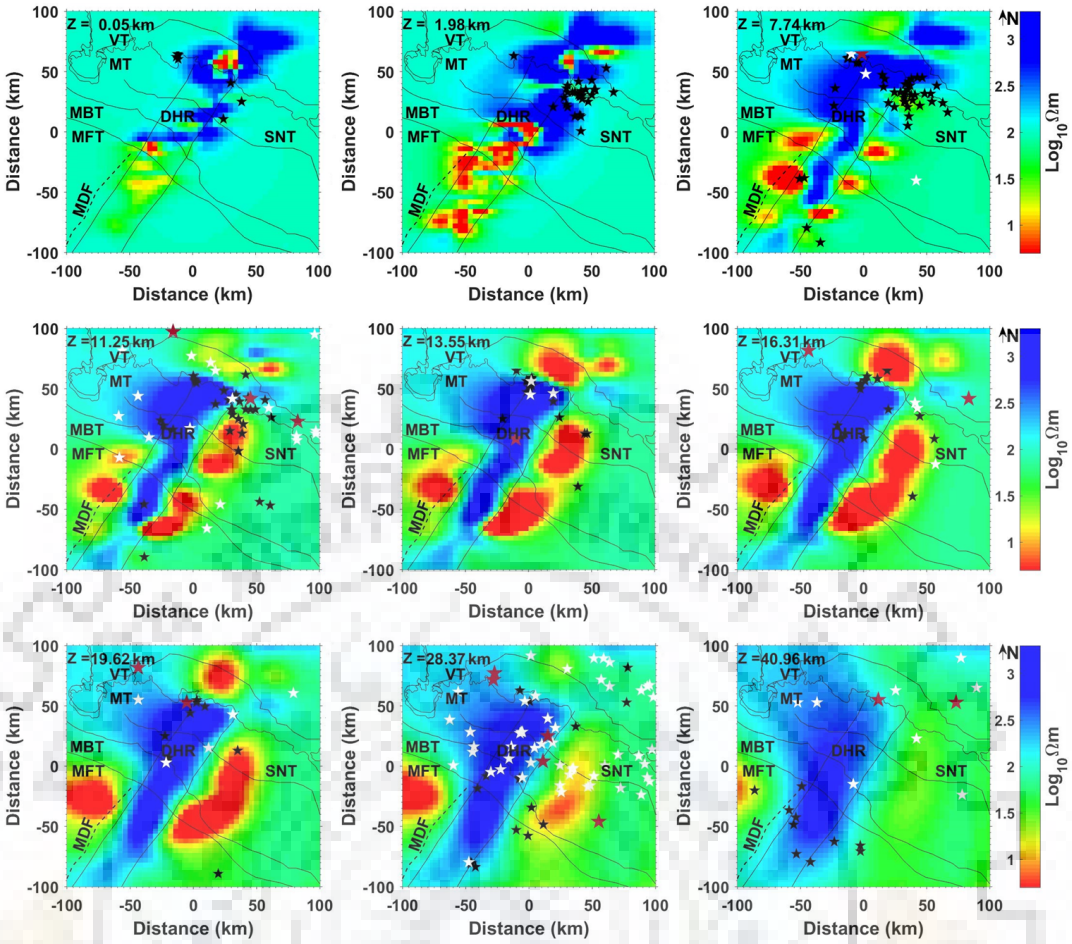

Figure 3.17: Depth slices of 3D inverted model estimated through joint inversion of full impedance tensor and VTF data. Earthquakes hypocenter are shown by star of different color and size according to magnitude: black (Mb $<$ 3), white (3 $\leq$ Mb $\leq$ 5), red (Mb $>$5). The depth level (z) is shown in each slice panel.

3.5 Summary of Results

The resistivity model, derived from 3D inversion of MT profile data recorded in Garhwal Himalayan Corridor, yields detailed 3D model with two off-profile new features in comparison to the feature present in earlier resistivity model obtained by 2D inversion of same data. The new off-profile features are aligned transverse to the main Himalayan arc and are, therefore, referred here as the transverse tectonic features. The new features delineated in 3D model are robust, geologically meaningful and consistent with the regional tectonic and 3D velocity model recently presented for the region. The model defines the geometry of DHR beneath the IGP, SH and LH in Garhwal Himalayan region. The model also suggests that DHR is a fault bounded structure. The fault structures related to DHR are reflected in

the model as conductive features running nearly parallel to DHR. The model also supports the *flat ramp flat* geometry of MHT, consistent with the seismological and other geophysical models of the region. The model presented here could be further refined by adding more densely acquired MT data in the vicinity.

In the next chapter the main focus is given to the seismically active MCT zone. A 3D MT study done on this zone near and around Chamoli region is described.

Chapter 4

3D INVERSION OF MT DATA FROM CHAMOLI REGION

4.1 Preamble

The second case study was carried out in the seismically active Main Central Thrust (MCT) zone in Northwest Himalaya. The MCT zone falls in the Main Himalayan Seismic belt which has experienced several large earthquakes in past and most of these occurred at shallow depth (10 to 20 km). Considering the seismological importance of the MCT region Magnetotelluric (MT) data were recorded at 28 sites in and around Chamoli region of Uttarakhand, India. This dataset was processed and inverted to image the subsurface electrical resistivity of the region and to study its correlation with the seismic velocity model. The dimensionality analysis of MT data reveals complex variation in strike direction implying the general 3D nature of impedance tensor data. The 3D inversion of MT data was performed using the code *AP3DMT*, discussed earlier. The final 3D resistivity model was obtained after several 3D inversion experiments. The inverted model shows a broad intra-crustal conductive (low resistivity) ($<$ 10 m) feature distributed in the depth range 3.60-19.62 km. Width of this feature varies with depth and it is maximum in the depth range 7.73-16.31 km. This feature is interpreted to be a result of the fluids generated by metamorphic dehydration in deeper depths and getting pushed upward through the fractured zones. The deeper part of conductive feature is associated with the source area of the main shock of Chamoli earthquake of March 29, 1999 (Mb 6.3). Further, there are few high resistive blocks intervening the broad conductive feature. The resistivity model corroborates the existence of thermal springs and of a high geothermal gradient. In the shallow depth

range 1.92-11.25 km there are some conductive features and these are interpreted as the fluid saturated fracture zones associated with swarms of aftershocks of the Chamoli 1999 earthquake. The resistivity features visible in the 3D inverted resistivity model are correlated with seismicity and geological tectonics. At shallow depths, hypocenters of the swarms of aftershocks are mainly concentrated in the high resistivity feature adjacent to the conductive features. However, at deeper depths hypocenters of the main shock and its aftershocks are in the conductive feature itself and coincide with the seismogenic source area of Chamoli Earthquake. The conductive fluid-filled feature is also consistent with the low velocity zone deciphered through earthquake tomography studies of the region. Further, the resistivity model was correlated with the seismic velocity structure of the region and distribution of earthquake hypocenters there in.

4.2 Tectonics and Geothermal Systems of the Region

The study area is located in and around the MCT zone, in Chamoli region of Northwest Himalaya. The rock types available in this region are mainly quartzites, schist and phyllites which suggest occurrence of inverted metamorphism. The MCT zone, lying within the Himalayan Seismic belt (HSB) [162], is bounded by two thrusts, Munsiari Thrust in south and Vaikrita Thrust in north. These thrusts are also referred as MCT-I and MCT-II, respectively [129, 232]. The HSB is a seismic gap in Himalaya with a total length of approximately 700 km. In the study area HSB is approximately 50km wide. Various authors have related HSB to MCT. Seeber and Armbruster [193] considered HSB to be down dip of the MCT while Khattri et al. [104] and Ni and Barazangi [162] argued that HSB lies between MBT and MCT, closer to MCT. Near MCT, the earthquakes in HSB occur above the detachment plane at shallow depth range 10-23 km. The detachment plane is also known as Main Himalayan Thrust (MHT) [193]. Ni and Barazangi [162] estimated the depth of MHT to be about 17-20 km near the MCT. Along the detachment plane the Indian plate is underthrusting the Eurasian Plate [151, 162, 193]. Thus, the major thrusts (MFT, MBT, MCT) and earthquakes in the main Himalayan arc are a result of rupturing of the detachment plane. Khattri [103] gave the depth range of 15-20 km for earthquake foci in MCT zone. In recent past, the central seismic gap around the study region has encountered two large earthquakes, the 1991 Uttarakashi earthquake (M_b 6.3) and the 1999 Chamoli earthquake

(M_b 6.4). The Chamoli earthquake occurred on south of MCT-I at the Basement Thrust and it was succeeded by large number of aftershocks (more than 300). More than 40 of these aftershocks range between magnitude of 4 and 6. Swarms of aftershocks of Chamoli earthquake include two moderate earthquakes of 2005 (M_b 5.3) and 2011(M_b 4.6).

National Geophysical Research Institute (NGRI) and Indian Meterological Department (IMD) installed numerous temporary and permanent sesimic stations [87, 129, 130] to record the earthquakes occurrences in the region. For earthquake precursory research a Multi-Parametric Geophysical Observatory (MPGO), is established in Ghuttu, Garhwal Himalaya [113]. It continuously records the various time-varying geophysical fields. A study of fault plane solutions by Ni and Barazangi [162] indicates that most of the earthquakes in the region are associated with thrust faults with their fault planes dipping gently ($< 30^\circ$) towards north or N-E and their strike being perpendicular to the main Himalayan arc. For a few moderate magnitude earthquakes there may exist strike slip and normal fault planes [104, 129, 175, 259].

The south of MCT-I in Garhwal Himalaya is characterized by anticline structure. The anticline is a part of schuppen zone formed by folding of southward moving thrusts. It is delimited on the two sides by (i) an E-W trending, Alakananda Fault (AF), a dextral wrench fault, in south and (ii) a N-S trending Nandprayag Fault (NF), a vertical fault, in east [242]. After the 1999 Chamoli Earthquake Kayal et al. [96] represented the region around AF with isoseismal VII and a trend of E-W direction. They describe this region with generation of landslides, ground fissures, and emergence of new springs and drying of some old springs.

The Northwest Himalaya also contains many known and unknown geothermal systems [76, 179] characterized by tertiary magmatism, metamorphic events and quaternary orogenic activity. A majority of thermal springs, as shown in Fig. 4.1, are located between MCT-I and Central Himalayan axis. The thermal springs are confined within to a region having N-S extension of 45 km (30 km to north of and 15 km to south of MCT-II). In E-W direction the width of the region is in a range of 10-40 km, starting from Alakananda valley and going upto Tons valley. The hot springs of the Alakananda Valley have temperature gradient of $60\pm20^\circ$C/km and the heat flow of 130 ± 30mW/m^2 [76]. The hot springs of central crystallines show a temperature range of 55°C to 94°C. Most of the thermal springs emerge through joints and are controlled by interface of lithological units. Across the MCT, in Lesser Himalaya the metamorphic pressure and temperature are 5 kbar and 550°C respectively,

while in the Higher Himalaya these are 14 kbar and 850°C respectively [217]. Most of the thermal springs emerge through joints and are controlled by the interface of lithological units. The Mid- Tertiary granites are known in the area, so conduction by such younger acid magmatic bodies (<10 Ma) and the geothermal gradient may be a contributing factor of fluid heats.

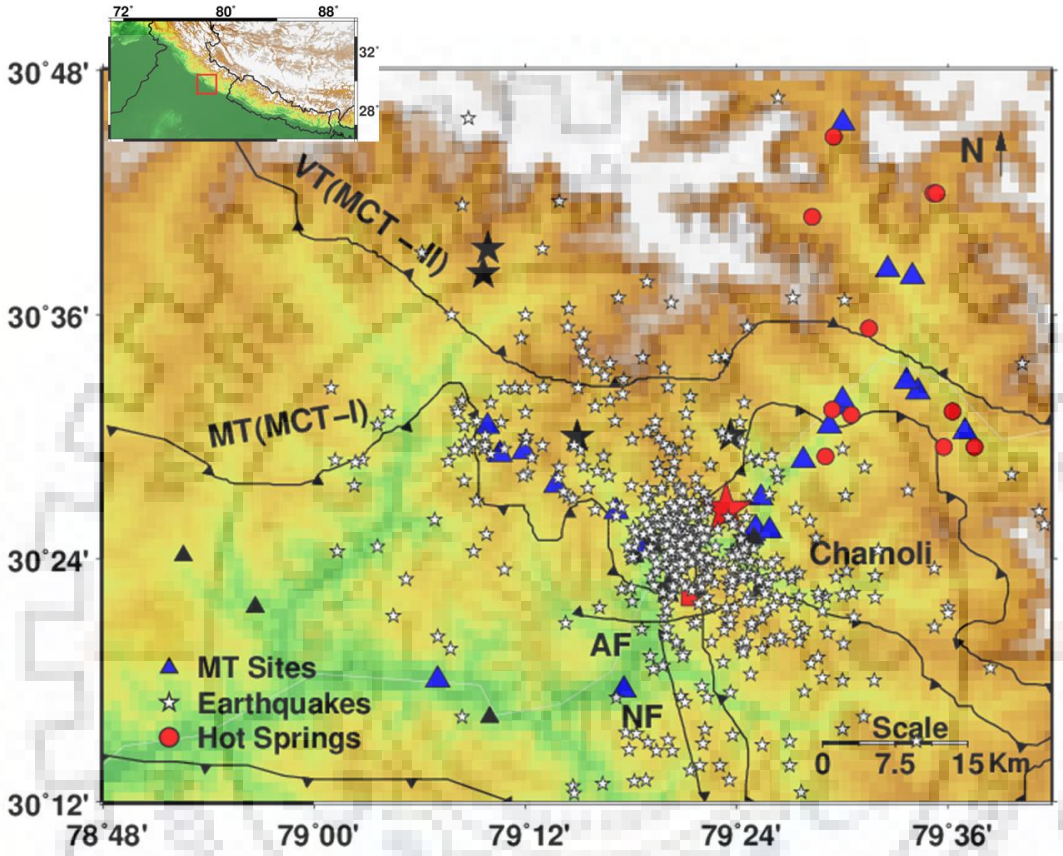

Figure 4.1: A simplified map, showing Garhwal Himalayan thrusts: MT (MCT-I): Munsiari thrust; VT (MCT-II: Vaikrita thrust; AF: Alakananada Fault; NF :Nandaprayag Fault (complied from [96, 129]). MT sites are shown by upward facing triangle. Red circles represent the location of thermal springs. White stars are earthquake epicenters with magnitude less than 5. Black stars are earthquake epicenters with magnitude greater than 5. And red star is the 1999 Chamoli Earthquake. Map was created with gmt software version 5 (http://gmt.soest.hawaii.edu/).

4.3 Description of Data

MT data were acquired in and around Chamoli Region, covering the MCT zone, between 30° to 31°N and 78° to 80°E. The total area covered by MT sites is approximately 3850 km^2. The area is located in tough Himalayan terrain where it was not possible to maintain a

constant site spacing and a regular grid. It was difficult to find electrically noise free sites as there are several small and large hydro-power projects and more are in progress. Site density was kept high in the MCT zone with a site spacing of 2-5 km while it was 10-15 km outside the MCT zone. The MT time series data were acquired at 28 sites using Metronix ADU06 system. The recorded time series were processed using MAPROS [67] processing software and impedance tensor components were estimated in a period range 0.001-1000 s. Location of these sites is shown in Fig. 4.2.

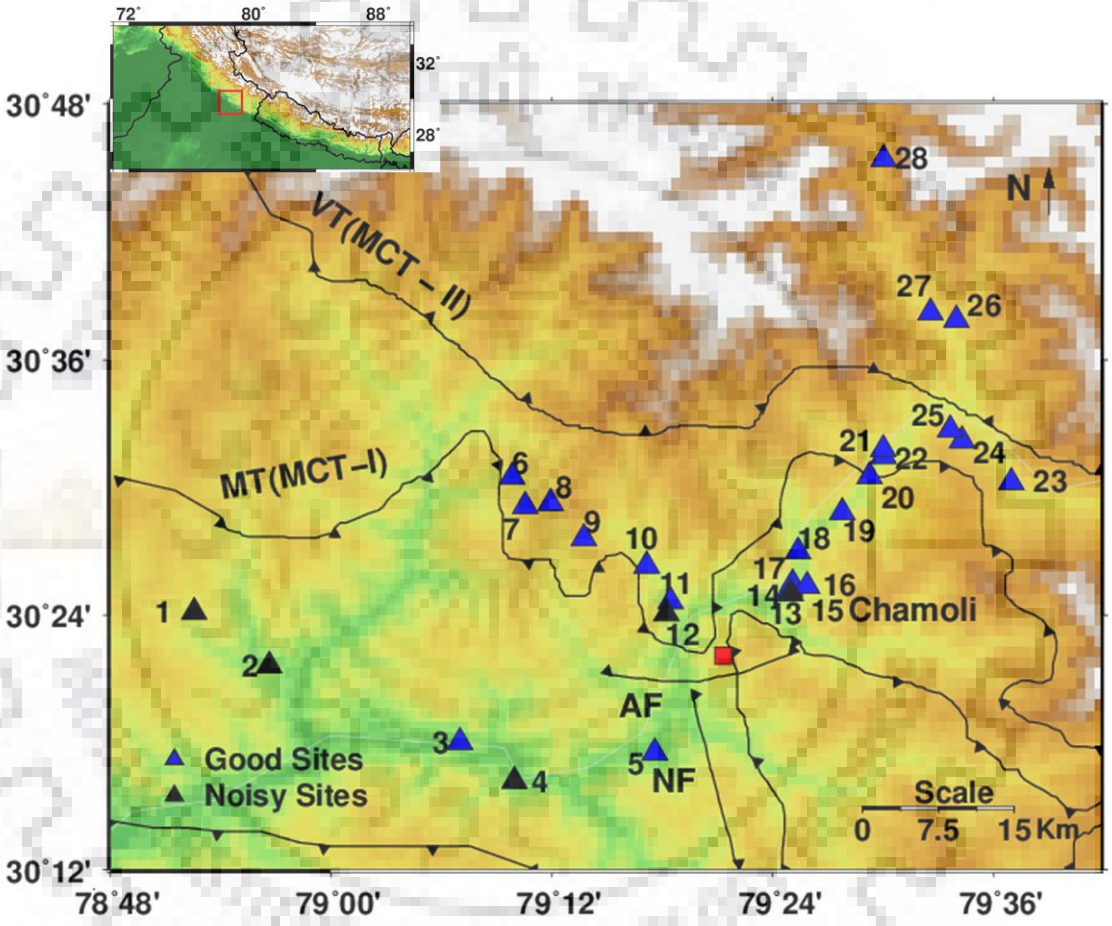

Figure 4.2: A simplified map, showing Garhwal Himalayan thrusts: MCT-I: Munsiari thrust; MCT-II: Vaikrita thrust; AF: Alakananada Fault; NF: Nandaprayag Fault (complied from [96, 129]) and location of MT sites are shown by triangle. Other acronyms are SH is Sub-Himalaya; HH is Higher Himalaya and MCT zone is Main Central Thrust Zone. Map was created with gmt software version 5 (http://gmt.soest.hawaii.edu/).

4.4 Dimensionality Analysis

Dimensionality analysis of this data set was performed using Bahr's phase sensitive skew method [16], magnetotelluric phase tensor analysis [37] and WAL rotational invariants

method [137]. Bahr and phase tensor analysis methods also provide directionality and geoelectric strike direction. It was found that the strike direction of the region varies both with time period and location of sites.

Based on the Bahr's phase sensitive skew criteria, Table 2.1, the data set in different regions and for different time periods can be characterized as 1D, 2D and 3D. The Fig. 4.3 reveals that a majority of MT sites in the region are 3D in nature while few sites, in the central zone, are 2D in nature. The Bahr sensitive strike(θ) direction in Fig. 4.4 also varies in a wide range between N6° E to N81° E again emphasizing the 3D nature of the region.

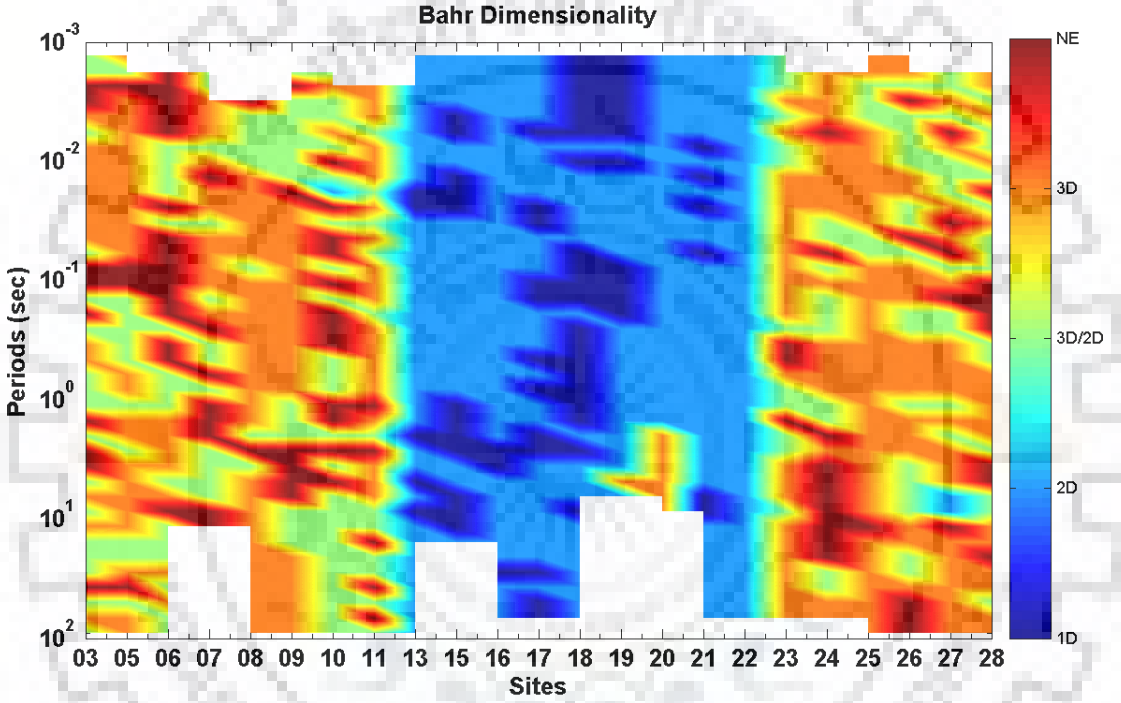

Figure 4.3: Pseudo-section representing the geoelectric dimensionality for 23 sites using Bahr's Dimensionality criteria.

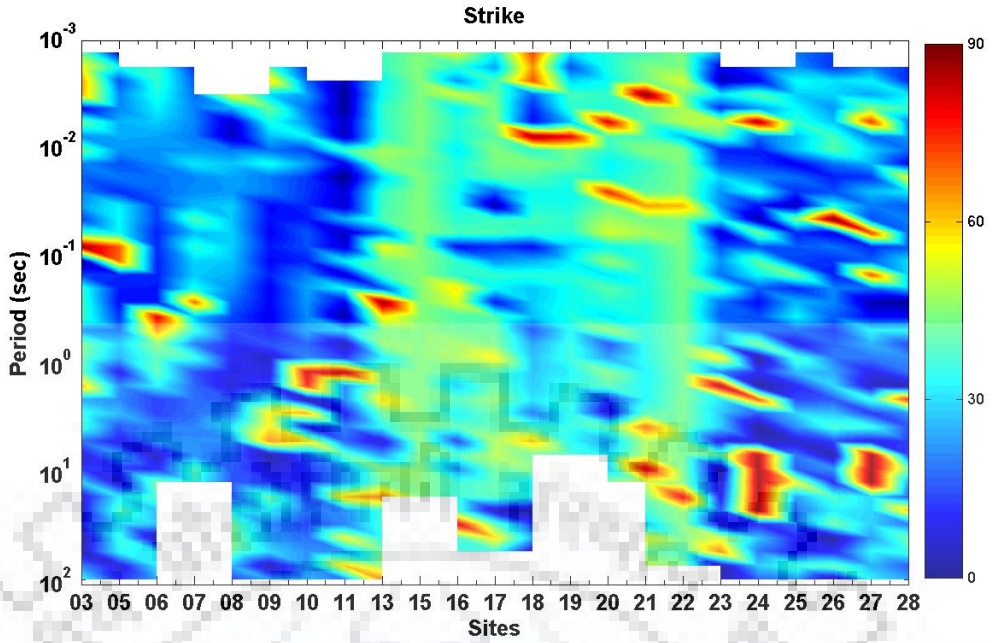

Figure 4.4: Pseudo-section of estimated strike for 23 sites using Bahr's Dimensionality criteria.

In dimensionality analysis method by [37], the structure is considered to be 3D when skew angle, β, is greater than or equal to 3. For 23 sites, Fig. 4.5 shows the variation of β using Caldwell phase tensor method. From the phase tensor plots and the strike directions, it was concluded whether the data corresponds to different sites and time periods are 1D, 2D or 3D in nature. Most of the sites in Fig. 4.5 show ,skew angle, $\beta > 3^{\circ}$, indicating dominance of a 3D structure in the region. The phase tensor ellipses along with the strike directions in the form of rose diagrams are plotted in Fig. 4.6. The colorbar in Fig. 4.6 shows the β values. A phase tensor ellipse is a circle for 1D structures and is an ellipse with its major axis aligned along the geoelectric strike direction for regional 2D structures. For 3D structure the ellipse parameters have larger values. The phase tensor strikes tend to rotate to higher angles (in the N-E direction) at larger depths. The strike direction for this data set in the Caldwell phase tensor method also varies over a wide range between N13° E to N88° E, again indicating 3D nature of data.

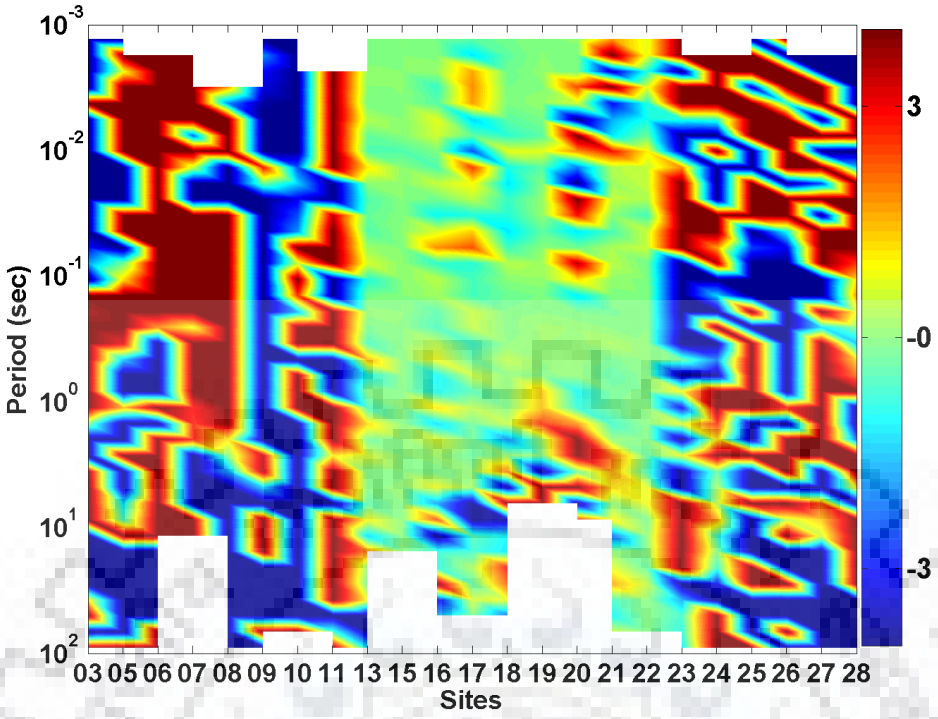

Figure 4.5: Dimensionality analysis pseudo-section of β (Skew) for 23 sites obtained using Caldwell's phase tensor criteria.

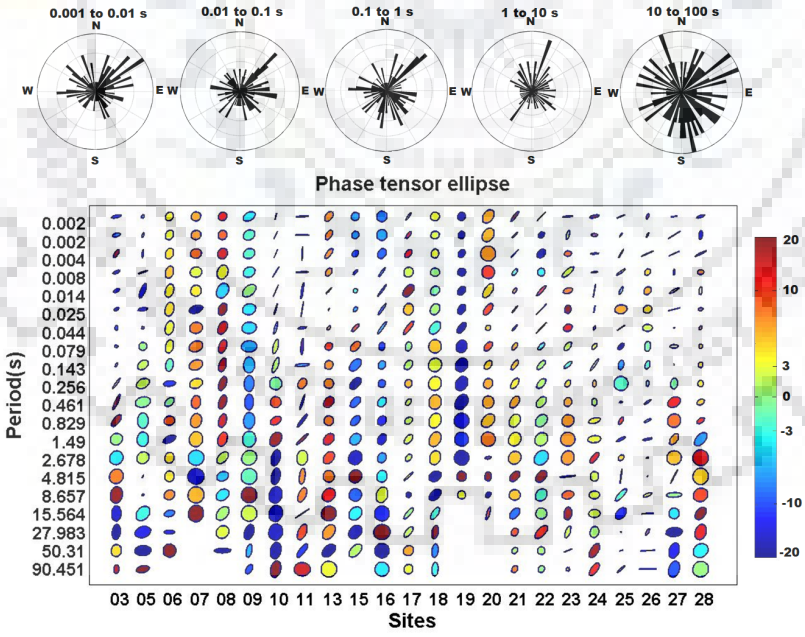

Figure 4.6: The rose strike showing the strike directions (Top Panel) along with the phase tensor ellipse at all the sites obtained using Cadwell's phase tensor method [37] (Bottom Panel).

The dimensionality of the region was also studied using the WAL rotational invariants

method [137]. Fig. 4.7 again reveals that 3D nature is dominant in the region. For sites 15 and 18-20, only at few time periods, the 2D structure was observed. As majority of the sites depict 3D structure, the strike analysis was not possible using WAL method.

Since, all the impedance tensor analysis methods establish 3D nature of the region, 3D inversion of the data was performed using the code, *AP3DMT* [204].

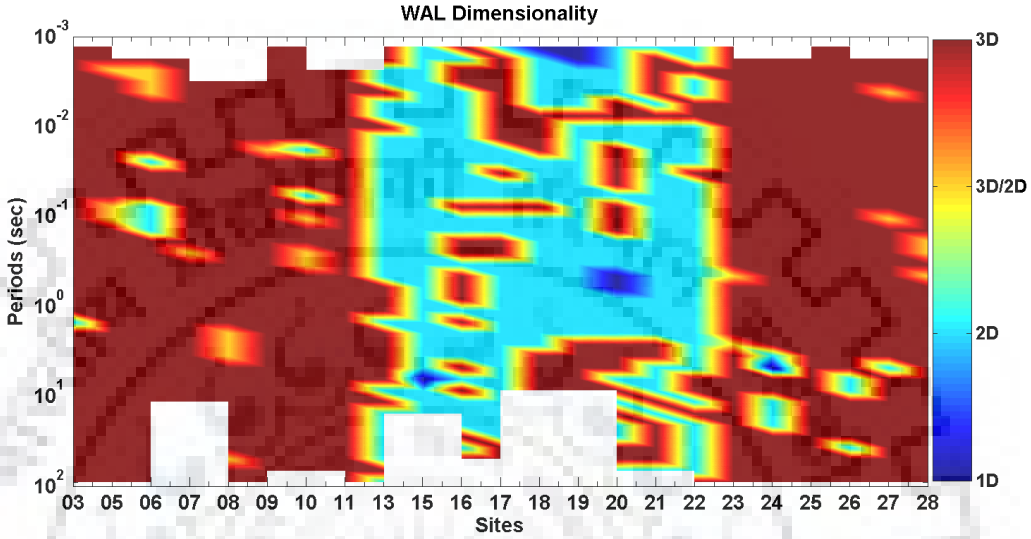

Figure 4.7: Dimensionality analysis pseudo-section for 23 sites obtained using WAL rotational invariants criteria.

4.5 Data and Control Parameters Selection

3D inversion experiments were performed with both only the off-diagonal elements of the impedance tensor ($\mathbf{Z}$) and with all elements of $\mathbf{Z}$. The MT responses were used for 39 periods in the range 0.001-100s, distributed logarithmically with 8 periods per decade. To design an optimal grid, two experiments were carried out: (i) to identify the optimal coarseness parameters for the grid and (ii) to estimate the optimal distance of the first grid line from the surface. Based upon these experiments, in the final optimal grid the model domain was discretized with $50 \times 56 \times 40$ cells (with 7 layers in air). The distance of the first grid line from surface was 50 m. The spacing between subsequent grid lines was increased by a factor of 1.2 extending up to a depth of 370 km. The grid size for the central region of the model, defined by the scatter of the sites, was 1.7 km for both x- and y- directions. Hence, in the central region there were $38 \times 46 \times 40$ cells in x-, y- and z- directions respectively. A total of 24 cells were padded around the central region of the model, six in each horizontal direction

with the grid line spacing increasing by a factor of 1.8. With this grid, the dimension of the model domain becomes $320 \times 330 \times 370$ km in x-, y- and z- directions respectively. In order to account for the large errors in some data values, the inversion was performed with two data error floor values, 10 % and 15 %, of absolute value of each of the components of full impedance tensor (Z). However, when the diagonal components have large errors, the threshold error floor values for the diagonal components were 10 % or 15 % of $\sqrt{|Z_{xy} * Z_{yx}|}$. In all the inversion runs, an isotropic smoothness (0.3 0.3 0.3) was used. However, to accommodate Himalayan tectonic thrust orientations (MCT-I and MCT-II), anisotropic smoothness was also tested. The starting value of Marquardt regularization parameters (λ) was set to 10, the iteration process terminates if regularization parameter reaches a value of 10^{-8}. To determine the suitable half-space initial model the data set was inverted with different initial half-space models of resistivities 1, 10, 100, 1000 and 10000 Ωm. Based on the initial and final nRMS (Normalized Root Mean Square) error values (Table 4.1) and on the final model resolution, the 100 Ωm half-space model was found to be the most suitable initial guess model for this dataset.

Table 4.1: The inversion and convergence parameters for different resistivities of the homogeneous half-space guess model.

Resistivity of initial half-space (Ωm)	**Starting nRMS**	**Final nRMS**	**No. of iterations**
1	9.89	6.87	49
10	12.57	6.67	64
100	31.64	5.25	100
1000	100.08	6.90	91

4.6 Inversion Results

3D inversion of Chamoli data set was initiated by first inverting the full impedance tensor data at 28 sites for 39 periods distributed logarithmically in the period range 0.001-100s. A data error floor of 10 % of absolute value of Z in combination with the threshold error floor of 10 % of $\sqrt{|Z_{xy} * Z_{yx}|}$ for the diagonal elements. The inversion process did not converge even in 109 iterations. The iteration process could only reduce nRMS error value from a

starting value of 62.48 to 26.2 and the inversion terminated due to the regularization threshold criteria. A study of site wise nRMS error values reveal that 5 out of the 28 sites, exhibit abnormally high value of nRMS (>10). The high value of nRMS error value was due to the large errors in data. Hence, for further inversion experiments these five sites were removed from the dataset and only 23 sites were used.

The off-diagonal impedance tensor data were also inverted for these 23 sites. The data error floor of 10% of $|Zxy|$ and $|Zyx|$ was used. In this case the nRMS error value reduced from 10.36 to 3.42 in 117 inversion iterations. We still felt that large errors in the data were responsible for the high nRMS error value. So, in the next inversion run, the data error floor was increased from 10 % to 15 %. In addition to this, the inverted model of previous inversion run was used as the initial guess model and the nRMS error value reduced from 3.06 to 1.85 in 20 inversion iterations.

In the next two inversion runs, the full impedance tensor (Z) data were inverted for the reduced dataset of 23 sites, keeping all the inversion control parameters same and using the two data error floors values. The nRMS error value reduced from 31.64 to 5.25 in 100 inversion iterations for the error floor of 10 % and from 26.71 to 2.23 in 64 inversion iterations for error floor of 15 %. These two inverted models, in the form of depth slices are shown in the first and second columns of Fig. 4.8. Although, the increase in error floor from 10 to 15 % reduced the nRMS error value, yet it did not lead to any significant differences in the two inverted models. Therefore, the model obtained from 15 % error floor was taken as the final inverted model for further discussion. For the final inverted model, the misfit of the off-diagonal apparent resistivity and phase is presented in Fig. 4.9. In Fig. 4.10, the evolution of the final model, in the form of depth slices, for the iteration numbers 15, 30, 40, 50, 64 is given in columns (1-5). The final inverted model was further studied for stability, robustness and sensitivity.

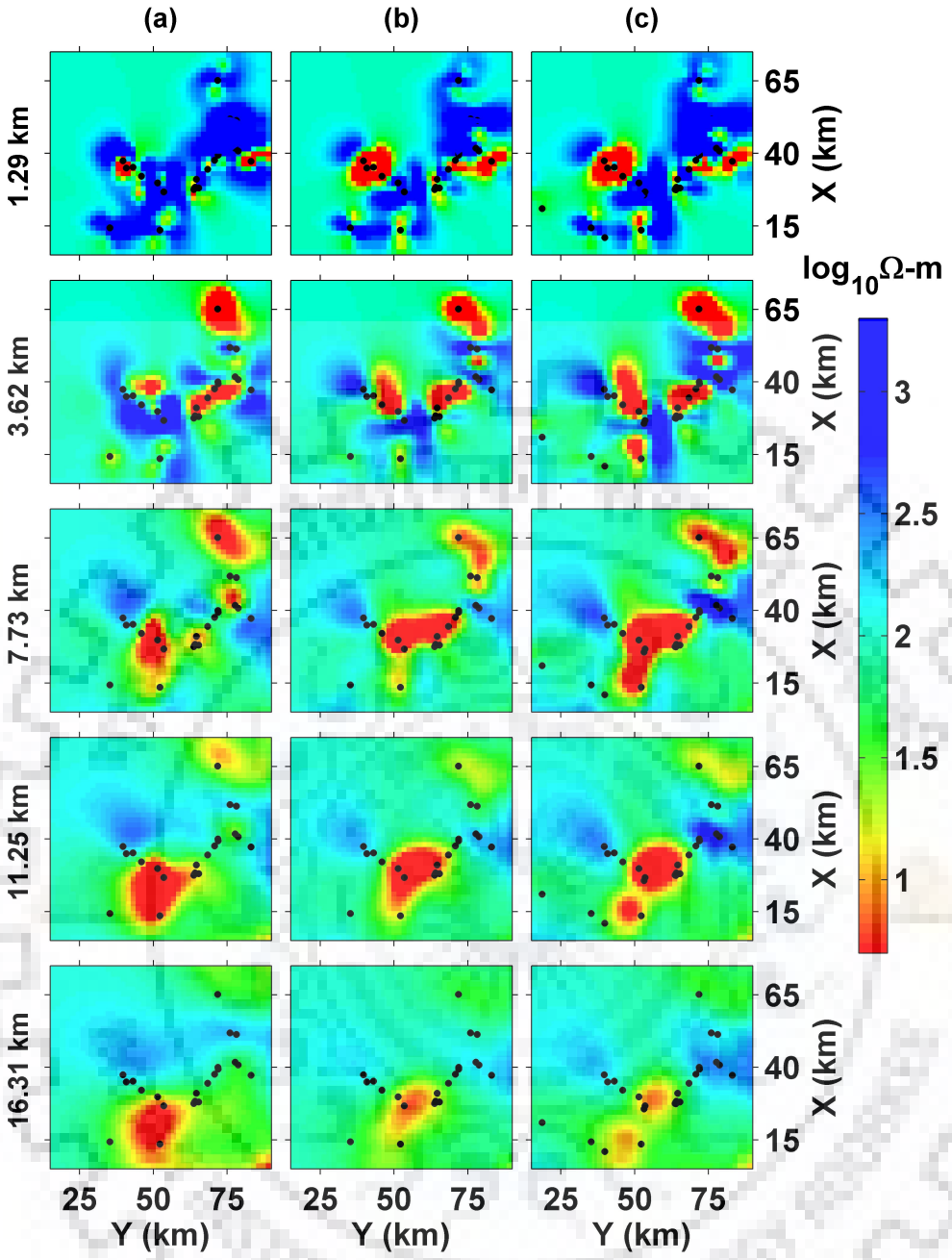

Figure 4.8: Depth slices of 3D inverted models for: a) Full impedance 23 sites with 10 % error floor and initial guess model of 100 Ωm, (b) Full impedance 23 sites with 15 % error floor and initial guess model of 100 Ωm, (c) Full impedance 28 sites with 15 % error floor and initial guess model is the inverted model of (b).

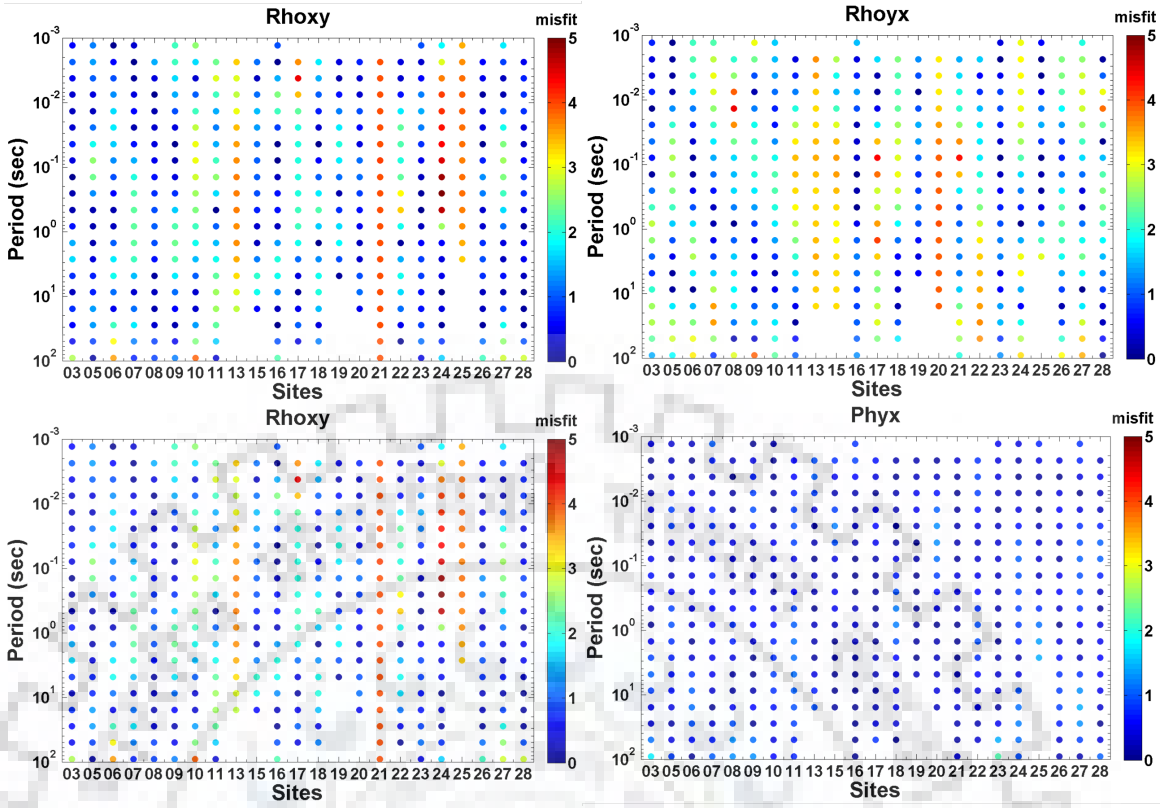

Figure 4.9: Misfit plot of apparent resistivity and phase for off-diagonal impedance tensor at all the sites for final inverted model.

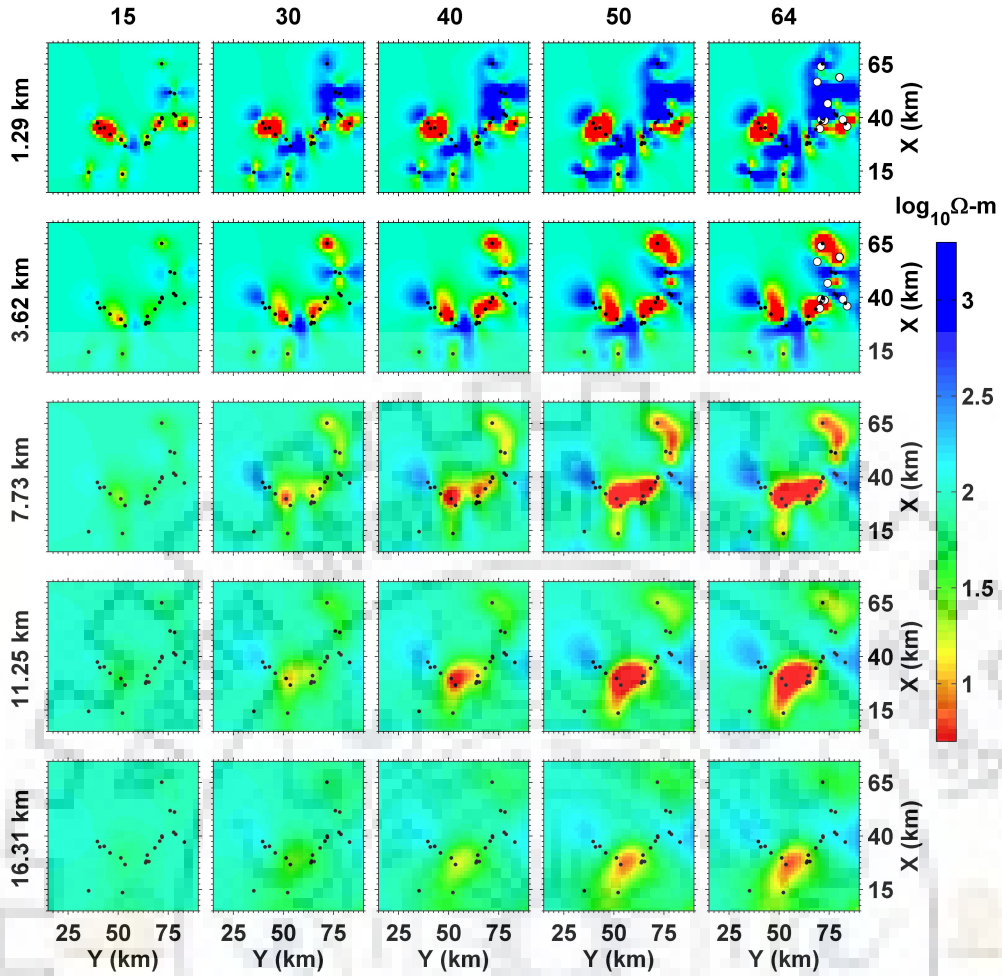

Figure 4.10: Depth slices showing the final inverted model development with iterations (15, 30, 40, 50, and 64). Locations of thermal springs at first two depth slices of final model (iteration 64) are shown by white circles.

In order to see whether the final model is consistent with the data of all the 28 MT sites, an inversion of complete data set was done with the final inverted model as the initial guess model. The nRMS error value decreased from 62.48 to 3.84 in 58 inversion iterations. This inverted model, in the form of depth slices, is shown in the third column of Fig. 4.8. It is important to note that, unlike the first inversion run where the convergence was not achieved and no model features were recovered, the general model features recovered now are similar as in the final inverted model. This experiment suggests that the data of all the 28 sites is consistent with the final inverted model and that the high nRMS error value in the first run was indeed due to the large errors in the data of few sites.

Since, in some regions outside the MCT zone the density of MT sites is sparse (Fig. 4.2), the validity of resistivity features in these zones needs to be established. So, a synthetic experiment was performed by computing the forward response of the final inverted model

for (i) the original site locations and (ii) a larger set of sites obtained by increasing the site density in the regions where site density was sparse. After adding 5 % Gaussian noise to the synthetic responses, the inversion was performed on these two sets of synthetic data. It was found that the nRMS error value reduced from 63.70 to 1.11 in 103 inversion iterations in the first case while it reduced from 57.00 to 1.10 in 51 inversion iterations for the second case. To visualize the similarity of these two models, the ratio of cell resistivities is presented, along with the two inverted models, in Fig. 4.11. It is evident that the ratio is close to one for most of the cells. This experiment indicates that the features in the final inverted model are significant and are not artifacts of sparsity of sites.

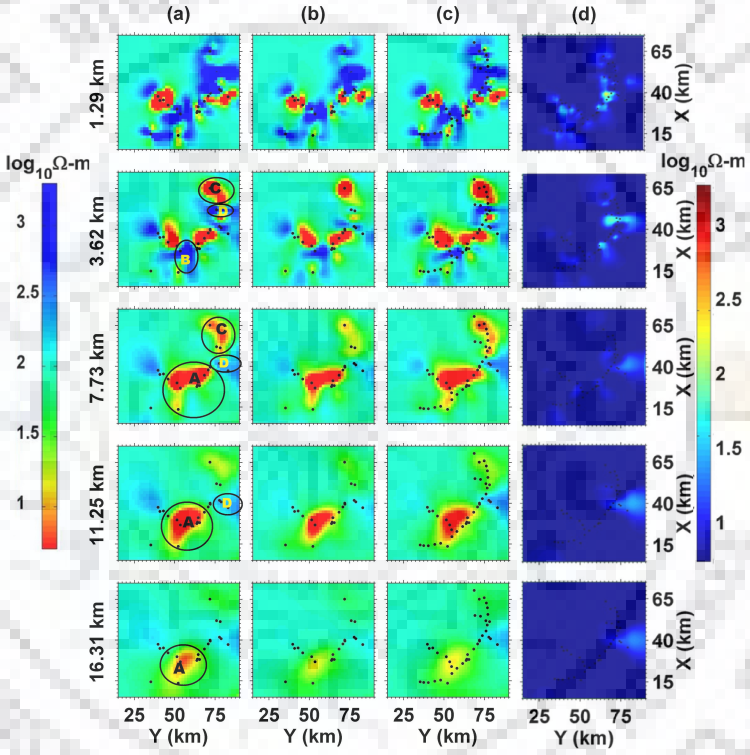

Figure 4.11: Depth slices of 3D models, (a) final inverted model, (b) inverted model for synthetic data at recorded sites spacing, (c) inverted model for synthetic data with dense site spacing and (d) ratio of cell resistivities of two models (b and c).

4.6.1 Depth of Investigation

In another experiment, the reliable depth of investigation upto which the model is valid, was estimated through a synthetic test suggested by Parker (1982). Accordingly, to determine the deepest depth of investigation for the recorded MT response, a half-space of perfect conductor and resistor was inserted at the bottom of the grid. The depth of investigation of

the model was given by the depth at which the nRMS error value starts increasing when the conductor/resistor was inserted. In the final inverted model a perfect conductor/resistor was inserted, one by one, at depths corresponding to the different horizontal grid planes, starting from the 49.20 km to 19.62 km. First, the forward response for each case was obtained and then the nRMS error value was computed between this response and the response of final inverted model. The change in nRMS error value was not observed when conductor/resistor was added at grid planes in the depth range 50 to 28 km. The increase in nRMS error value was perceptible for the grid planes at 23 km and shallower depths (Fig. 4.12). From this experiment it was inferred that the depth of investigation of present MT dataset is 23.60 km.

In next section various resistivity features present in the final inverted model are validated through sensitivity tests.

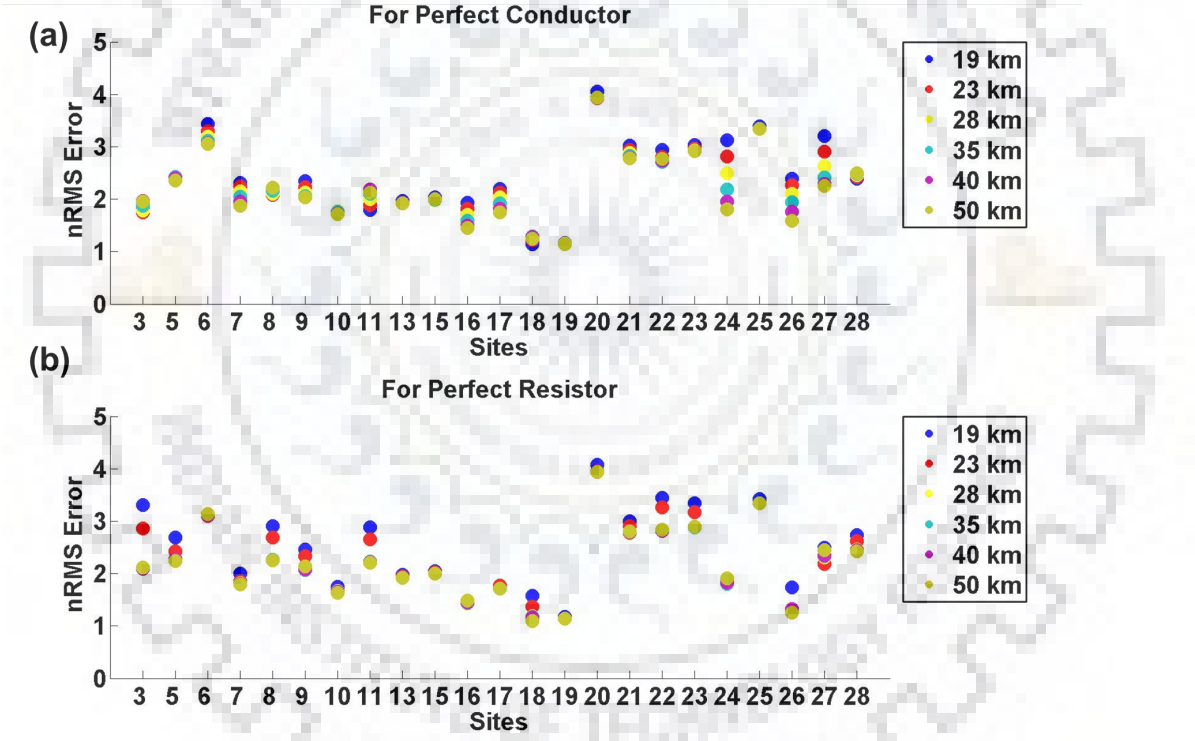

Figure 4.12: Scatters showing the nRMS error values at different depths when grid planes are replaced by (a) a perfect conductor and (b) a perfect resistor.

4.6.2 Sensitivity Tests

To test the robustness of various resistivity features present in the final inverted model, the sensitivity tests were performed for the four major features identified in Fig. 4.11(a) and labeled by the characters 'A' to 'D'. This has been done by replacing the resistivity of a

particular feature by the background value (100 Ωm) and, thereafter, computing the forward response again. The nRMS error value was the computed between this response and the response of final inverted model. It was found that the nRMS error value increases whenever a feature was replaced by the background resistivity value. For conductive features 'A' and 'C', the nRMS error values increased from 2.23 to 3.16 and 2.5 respectively. For the resistive features, 'B' and 'D', the nRMS error value increased from 2.23 to 4.40 in both cases. The nRMS error value increase was higher in the off-diagonal components of impedance. The bar diagram, Fig. 4.13, shows site wise changes in nRMS error values of the responses with and without features. From this figure, it is clear that each of the four major features significantly contributes to the responses at the sites above the features and at the neighboring sites. Thus, it was concluded that in the final model, the conductive and resistive features were not the inversion artifacts but were indeed contributing to the data and the final inverted model was stable and consistent with data. Geological and tectonic interpretation of the model is discussed in the following section.

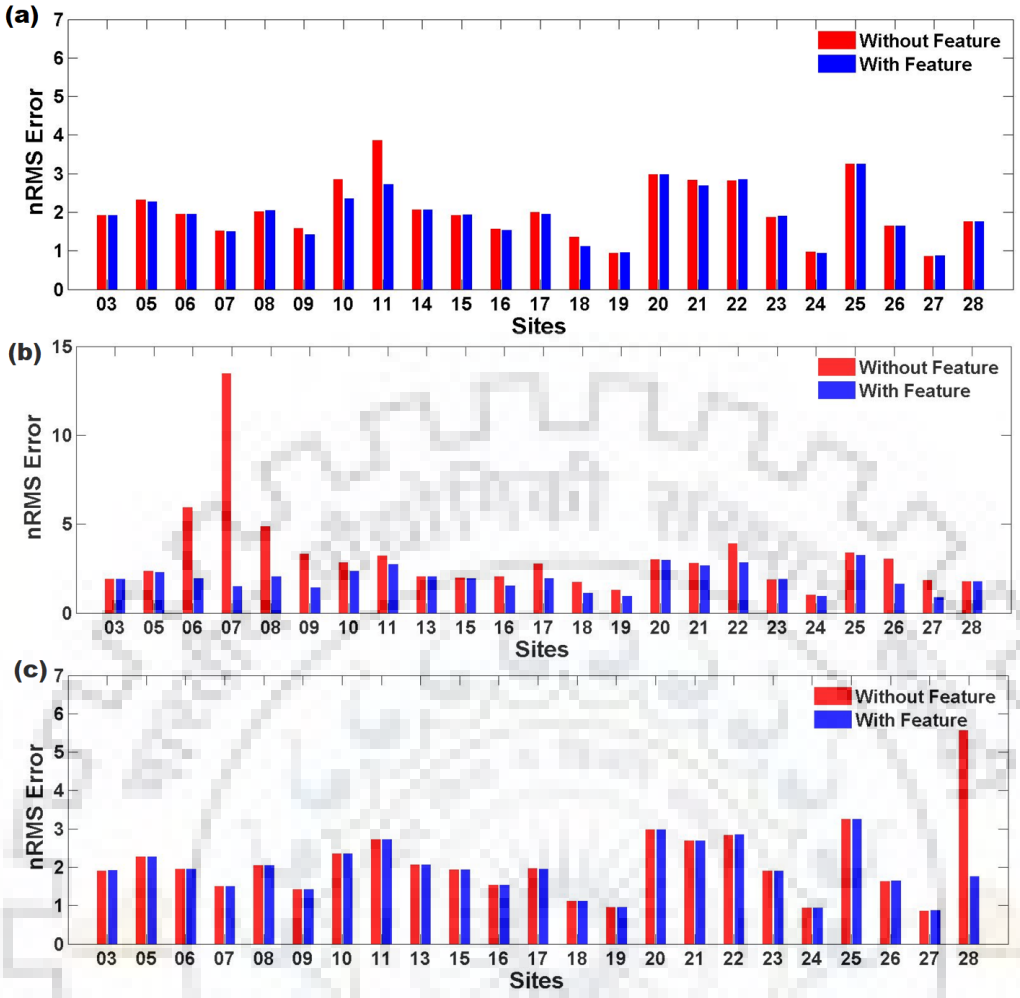

Figure 4.13: Sensitivity test for feature (a) 'A', (b) 'B' and 'D', and (c) 'C,' showing site wise nRMS value comparison with and without the features of final inverted model.

4.6.3 Discussion of Results

A comprehensive view of different features of the final inverted model is shown in Fig. 4.14 in the form of stacked x-y and y-z planes. The electrical resistivity image of the model reveals a complex resistivity structure under Chamoli region. Fig. 4.14(a) suggests that a conductive feature (<10 Ωm) in the central zone is originating at a depth of 16.31 km and is extending upwards upto a depth of 3.60 km. At the depth of origin (16.31 km) this feature is oriented in the N-E direction and has a width of about 10 km. The feature broadens upward having a maximum width of about 20 km at a depth of 11.25 km. Further upward (above 11.25 km depth), the northern end of this conductive feature is merging with another conductive feature which is oriented in the N-W direction. The merged feature then splits into narrow conductive channels which, in turn, are moving further upward upto a depth of about 3.60

km. These narrow conductive channels are not visible at depths shallower than 1.29 km.

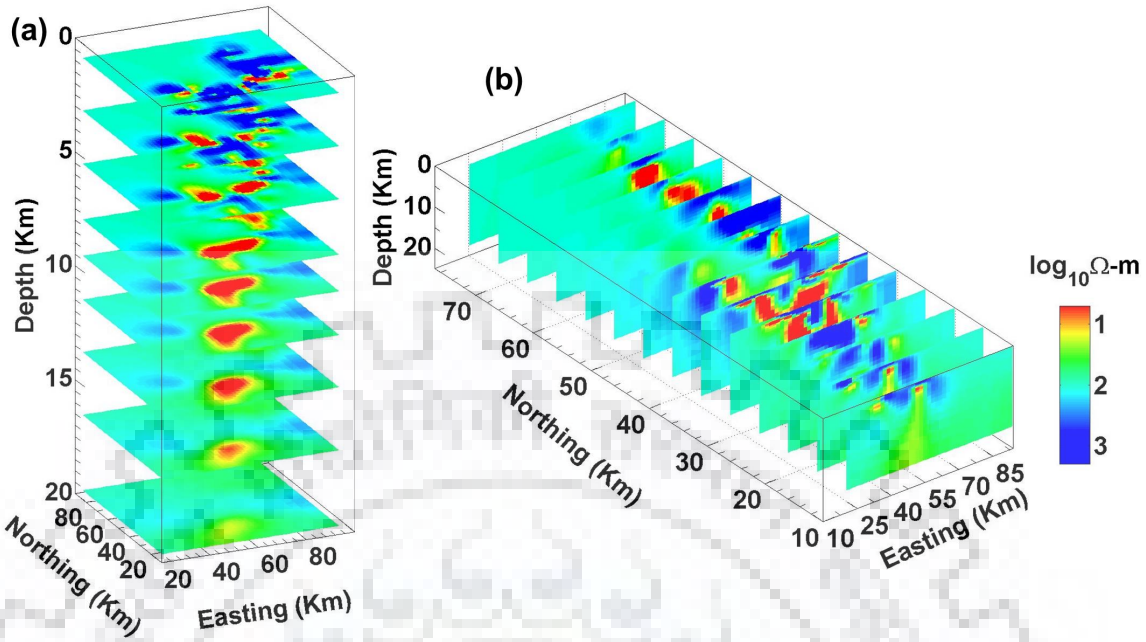

Figure 4.14: Stacked plane slices for final inverted model (a) X-Y planes (b) Y-Z planes.

The four resistivity features (‘A’ to ‘D’), identified and marked in Fig. 4.15(a), are classified into two doublets (pair of low and high resistivity features), first one (‘AB’) comprising features ‘A’ (low resistivity / conductive) and ‘B’ (high resistivity) is located in MCT zone and Inner Lesser Himalaya and the second one (‘CD’) comprising the features ‘C’ (low resistivity / conductive) and ‘D’ (high resistivity) is located in Higher Himalayan region. The conductive features (‘A’ and ‘C’) are related to the change in porosity, fluid content, pore distribution and possibly high heat flow and these can be explained in terms of the fluid saturated sediments adjacent to the resistive rigid rock matrix (‘B’ and ‘D’). A metamorphic dehydration reaction takes place in the under thrusting Indian crust and the released fluid percolates upwards through the interconnected pores into the brittle portion of the crust making these zones conductive features. The presence of fluids reduces the frictional force, increases the stress and triggers the medium and large size earthquakes [96, 129]. Thus, the activity of fault system is influenced by the conductive features resulting from the fluid saturated fractured zone and lying adjacent to the high resistivity brittle features.

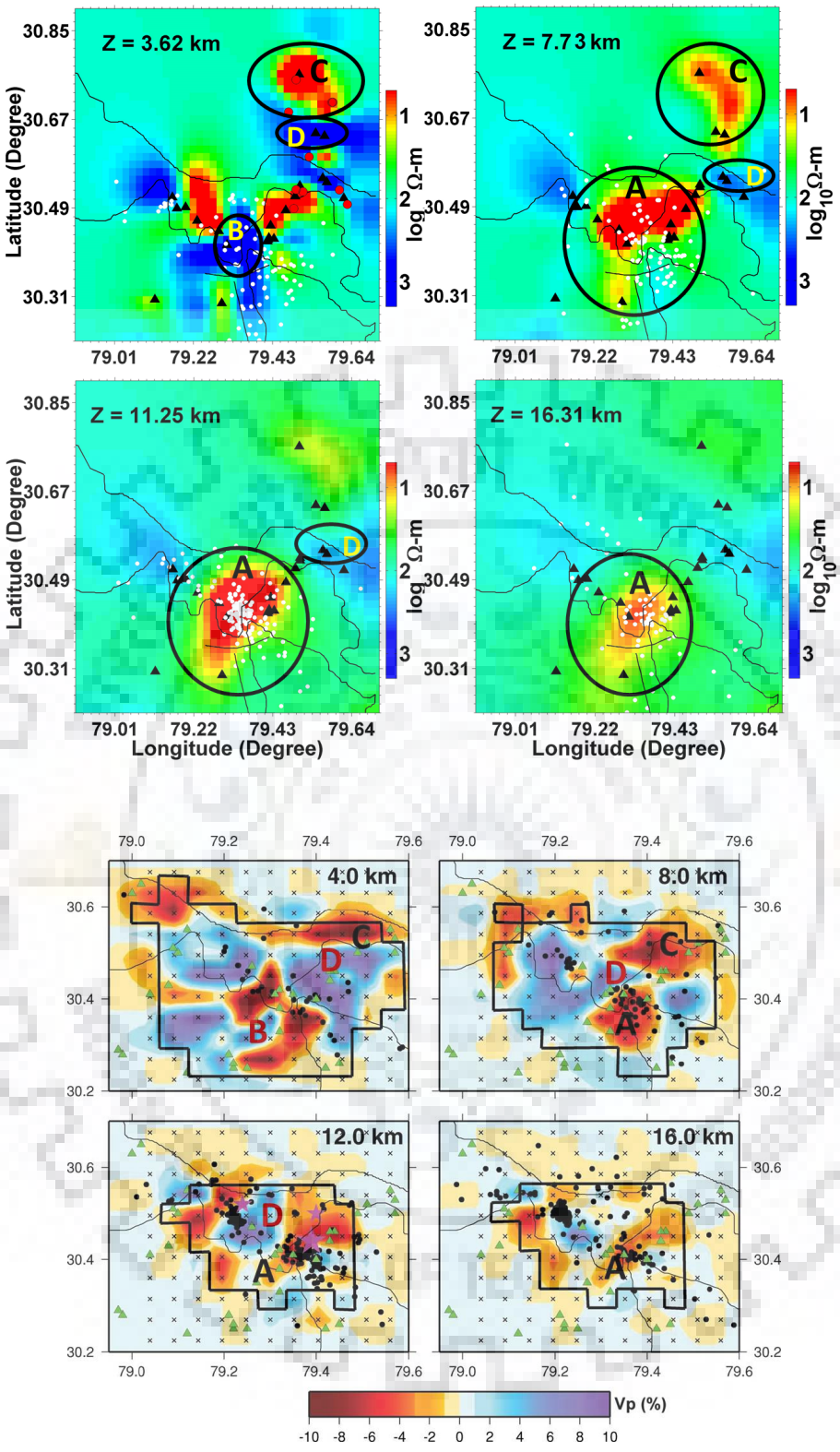

Figure 4.15: (a) Hypocenter of earthquakes that occurred within ±2 km of each depth slice are plotted on the respective depth slice by white circles. Locations of thermal springs [76] are shown by red circles at depth plane 3.60 km. And MT sites are shown by black triangles. Character 'A' to 'D' is the major resistivity at respective depth slice and (b) Plan view of P-wave velocity images from tomography model of same region by Mahesh et al. [129]

Further, the inverted resistivity model supports the hypothesis that explains the role of fluid in triggering the earthquakes in the region [129]. A seismic tomography study in the region [154] identifies a low velocity zone in the depth range of 12-15 km. The authors have interpreted this feature as a fluid filled rock matrix. This low velocity zone is consistent with the conductive feature 'A' (Fig. 4.15(a)). The doublet, 'AB', is similar to the low and high velocity converter defined in the seismic tomography study by Mahesh et al. [129] and given in Fig. 4.15(b). These velocity converters are confined to the depth range 10-20 km. The conductive feature 'A', originating at 16.31 km depth, is also consistent with the low velocity zone trending nearly E-W and interpreted as the source area of Chamoli earthquake [154].

It may be added that the conductive features could result from a high temperature gradient of $60\pm20^{\circ}$C/km and a heat flow of 130 ± 30mW/m^2 [76]. Many thermal springs with temperatures between 55° to 94° are observed in the study region. These thermal springs appear as emerging through the joints and are controlled by the interfaces of lithological units [76]. We have plotted locations of thermal springs in Fig. 4.15(a). These thermal springs have a good correlation with the near surface conductive features.

The conductive feature 'C', in Higher Himalayan region, is located in the depth range 1.29-11.25 km. The resistive feature 'D', adjacent to the conductive feature 'C' corresponds to the high-grade metamorphic rocks of upper crustal layer in Higher Himalayan region. This high resistive feature is common in Higher Himalayan region and is also seen in other models e.g. in the 2D resistivity model of Rawat et al. [183].

In order to study the correlation between the resistivity and seismicity of the region, in Fig. 4.15(a) the hypocenters of about 400 earthquakes [87, 96, 129], mainly comprising Chamoli earthquake and its aftershocks, are also plotted. On each depth slice, the hypocenters of earthquakes within ±2 km of its depth are projected. It is evident from Fig. 4.15(a) that, at shallow depths (3.60-7.73 km), the hypocenters are mostly located on the resistive side of the boundary between the low and high resistivity features. However, in depth range 11.25-16.31 km, the earthquakes are also clustered in the conductive feature which is interpreted as seismogenic source area for 1999 Chamoli earthquake [154]. The conductive feature, representing the fluid-filled saturated zone, was interpreted as a low velocity zone in approximately same depth range(12-15 km) in the velocity tomography model by Mukhopadhyay and Kayal [154].

4.7 Summary of Results

The MT data recorded in the Chamoli region, covering the MCT zone, were inverted in the period range 0.001-100 s using our own 3D inversion code *AP3DMT*. A series of inversion experiments were carried out to arrive at the final 3D resistivity model of the region. The inverted model is found to be consistent with the data and is validated. The main features of the resistivity model are the presence of two doublets of low-high resistivity features. The low resistivity/conductive feature of the doublet represents the fluid saturated fracture zone while the high resistivity feature represents the brittle rigid rocks. The conductive features are interpreted to be a result of the fluids present in deeper depths. These fluids were generated by metamorphic dehydration and pushed upward through the fractured zones. The model correlates well with the velocity model obtained from seismic tomography studies. The doublet view point is consistent with the low-high velocity converters defined in the seismic tomography study. The resistivity model also explains the role of fluid in triggering the medium and large size earthquakes in the region. The resistivity model explains the high heat flow and the presence of thermal springs in the area.

Next case study was not using MT data, rather it used Direct Current Resisitvity (DCR) method for a geotechnical study of the Tehri region.

Chapter 5

DCR STUDY IN TEHRI REGION

5.1 Preamble

In this chapter, a geotechnical case study at a bridge site in Tehri region is discussed. The subsurface soil characterization is important for the foundation design of civil engineering structures, bridges and for the determination of depth to the bed rock. The conventional direct methods, such as excavation and borehole drilling, are costly and time consuming. Therefore, the indirect non-destructive geophysical methods, such as electrical resistivity and seismic refraction, are increasingly being used in combination with the borehole and geotechnical investigations like pressure probe and Standard Penetration Test (SPT) [1, 84, 107, 227]. In this work, the 2D and 3D inversion of the six Electrical Resistivity Tomography (ERT) profiles, recorded on both East and West banks of a river, were interpreted to determine an electrical resistivity image with depth. The 2D inversion was done using the software *Res2Dinv* while 3D inversion was carried out using a MATLAB based code *AP3DMT-DC*. The borehole data and the geological inputs were used for lithological correlation and calibration of the resistivity values with subsurface formation. Finally, a correlation study of resistivity and Standard Penetration Test (SPT) data (N-values) was performed. A linear relationship between N-values and resistivity was inferred and used for determining the soil strength parameters from ERT. Many researchers have used different combinations of ERT and SPT data for soil characterization and have presented different forms of relationship between the electrical parameters and the N-values. It was found that no universal relationship exists between the two data types. Both, weak and strong correlation between the resistivity and N-values have been reported by various workers. The 3D ERT

methodology provides a subsurface image showing variation of electrical resistivity in more detail.

5.2 Study Area and Data Description

The study area is located in the vicinity of 260.5 m high Tehri dam in Tehri town, Uttarakhand, India. The Tehri town lies in Inner Lesser Himalayan region. The major lithological units of the area are Inner Lesser Himalaya, Almora-Nappe and Krol Nappe. The Inner Lesser Himalaya comprises mainly granite-gneisses and mica schist, whereas, the Krol-Almora-Nappe have exposed phyllites, quartzites, limestone and slates. The dam is built in downstream of the Bhagirathi River in a narrow gorge with steep slope within the Lesser Himalayan region. The region falls in Zone-IV of the seismic zoning map of India [29]. The region has witnessed several moderate size earthquakes in recent past. The famous Uttarakashi 1991, M_b 6.3 and Chamoli 1999, M_b 6.4 earthquakes [79] fall in Uttarakhand. A bridge is proposed in Bhagirathi River valley on the Tehri dam reservoir site (Fig. 5.1). At the site, the river has a general southerly flow in a V-shaped valley. Geologically, Chandpur Formation of Garhwal Himalaya group is well preserved along the bridge location. The exposed rock consists of Quartzitic phyllites with minor bands of phyllitic quartzite having developed foliation.

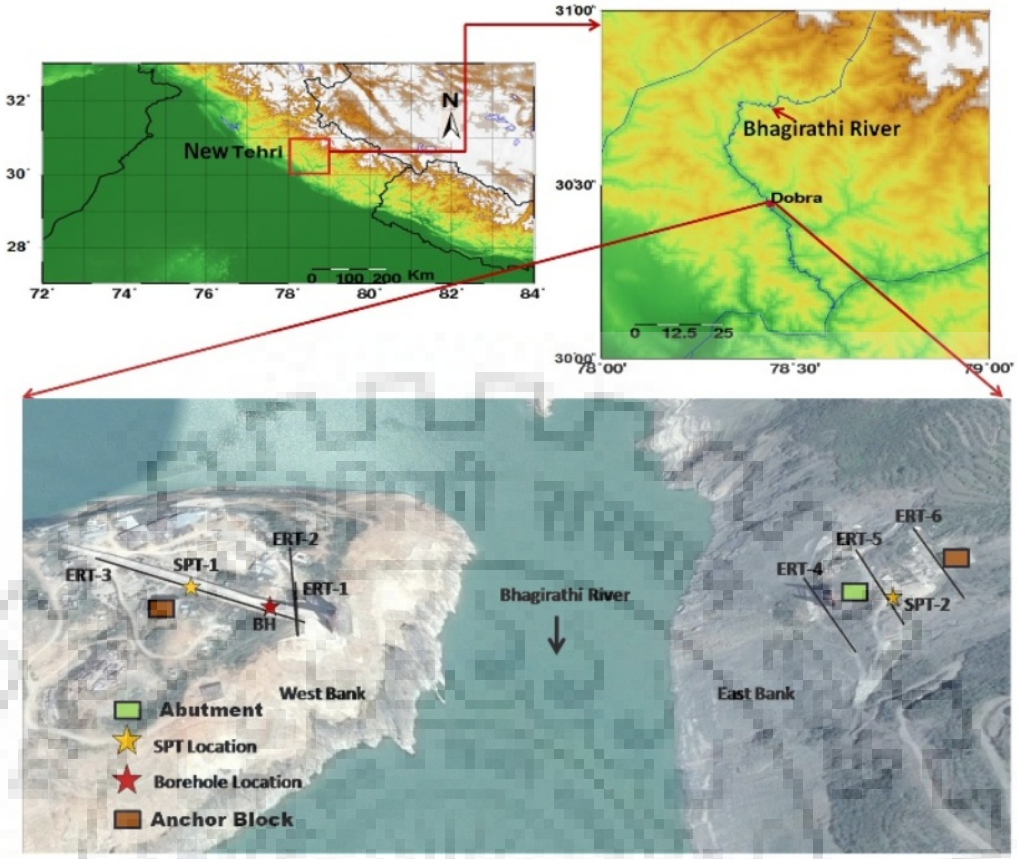

Figure 5.1: Study area, showing the locations of Electrical Resistivity Tomography (ERT) and Standard Penetration Test (SPT) at the investigated sites. Map was created with gmt software version 5 (`http://gmt.soest.hawaii.edu/`) and `http://earth.google.com/web/`.

At the investigated site, the West bank of the Bhagirathi River has a fairly steep slope of the order of 75°-85° towards N90°-N95°. The exposed rocks are present on the slopes of the entire valley going upward from the river bed. River Borne Materials (RBM), representing the course of old river, are present near top of the valley. RBM consists of boulders of size greater than 10 cm and comprise quartz minerals with matrix of brown silt and clay. The rocks are visible on the valley face upto an elevation of 800 m Above Mean Sea Level (AMSL). The rock-RBM contact tends to move up on the upstream side, while the contact gradually goes down on the downstream side.

The East bank is extending above the proposed bridge level. Its slope is gentle with an inclination of 40°-45° towards N270°-N280°. Due to the thick dump materials of assorted size, no rock is seen exposed along the central line. The rocks are generally not exposed at the foundation level and further up. However, the rocks are visible above the anchor block site and at higher levels. At an elevation higher than 750 m (AMSL), the debris from

old landslides cover the rocks with a maximum thickness at the terrace level. Photographs showing the anchor block and the landslide debris on the East bank are given in Fig. 5.2. The rocks on this bank show large scale shearing with small scale folds. The details of data recorded are given in the next section.

Figure 5.2: Photographs showing (a) Anchor block and (b) Landslide debris.

Description of Data

Electrical Resistivity Tomography (ERT) measurements use the concept of standard four-electrode system. In ERT measurements, a large number of electrodes are deployed along a predefined profile line with fixed inter-electrode spacing. All the electrodes are connected to the resistivity meter through a multi-core cable. The use of multi-core cable, suggested by [19], improves the accuracy of results and reduces the time and manpower required. For each measurement, the resistivity meter automatically selects a particular set of four electrodes through a preloaded software (*Electre Pro*) designed sequence. Each measured apparent resistivity value can be considered as a weighted volume average of the true point resistivity of the region sensed by the equipment. The software used to design the measurement sequence allows the user to chose sequence parameters such as maximum number of electrodes used, inter-electrode spacing, particular electrode array configurations, current injection time, method to be used (Resistivity only or resistivity and induced polarization both), minimum and maximum stack etc.

5.2.1 DCR Data

Syscal Junior Switch-48 multi-electrodes resistivity imaging system was used for each ERT measurement and a maximum of 48 electrodes were used. It uses four multi-core cables with 12 electrode takeouts having a maximum of 10 m inter-electrode spacing. However, the inter-electrode spacing can be reduced as per the availability of space. This spacing will also be controlled by the desired depth of investigation. A total of six ERT profiles were recorded. Out of these one ERT was recorded with a 2 m inter-electrode spacing while the remaining five were recorded with a 4 m spacing. Details of data acquisition parameters, measurement sequence, inter-electrode spacing for each profile is given in Table 5.1. In the present investigation, in view of its higher sensitivity, the Dipole-Dipole (Dp-Dp) array which determines more effectively the true geometry of subsurface electrical resistivity model in comparison to other arrays [224] was used. Fig. 5.1 shows the locations of these ERT profiles. 2D and 3D inversion of the ERT data are discussed in the following sections.

Table 5.1: Data acquisition parameters and (Normalized Root Mean Square) nRMS error value after convergence in ERT inversion

ERT No.	Electrode Array	Inter-electrode Spacing(m)	Profile Length(m)	Error in 2D ERT inversion	Error in 3D ERT inversion
1	Dipole-Dipole	2	94	3.7	
2	Dipole-Dipole	4	188	7.1	2.40
3	Dipole-Dipole	4	188	8.7	2.52
4	Dipole-Dipole	4	188	3.5	
5	Dipole-Dipole	4	188	5.7	1.77
6	Dipole-Dipole	4	188	7.0	

5.2.2 Geotechnical Data

In addition to the geophysical methods, such as electrical resistivity and seismic refraction, geotechnical investigations such as Standard Penetration Test (SPT) were used by various authors in combination with borehole and pressure probe method. [1, 84, 107, 227]. Following the procedure of IS 6403-(1981) code, in SPT test the soil strength is defined in terms of number of blows (N-values). The N-values are defined as the number of blows per

30 cm of penetration into the soil [222]. The N-values are directly related to the soil strength and its compactness. However, in the soils containing coarse gravels, cobbles or boulders, the sampler can get obstructed, resulting in unreliable and inconsistent N-values [111]. Thus, to understand the relationship between the electrical parameters and the N-values, one has to study the controlling factors responsible for variations in electrical resistivity and in soil strength. The electrical resistivity variation in subsurface soil is controlled by the soil properties such as grain size distribution, compactness, porosity and electrical properties of the fluid present in the pore spaces [4]. Thus, in view of the common factors responsible for the variation in resistivity and in soil strength, a relationship need be found between the resistivity and N-values. For this purpose, the SPT data, in the form of N-values, [191] recorded on the West bank near ERT-3 and on the East bank near ERT-5 was used. The locations of these SPT sites along with one borehole location are shown in Fig. 5.1. The resistivity values of these sites from ERT method was then correlated with corresponding N-values.

The present study is based on the premise that the rock remains same and only its weathering changes. A weathering decreasing downwards leads to a decreasing porosity but increasing compactness. This, in turn, results in an increase in resistivity as well as N-value. In such a situation a good correlation may exist, provided the salinity of formation water remains constant with depth.

5.3 Inversion of DCR Data

Inversion of ERT data was done in two stages. First, the 2D inversion was done using the *Res2dinv* software [123] and then the 3D inversion was done using the code *AP3DMT-DC* [203].

For 2D inversion, the data set was visually examined to filter out the spikes and the outlier data points. A damped least-square constrained robust inversion, as implemented in *Res2dinv* software, was performed on data for each ERT profile. In forward modeling, the model cells with widths equal to half the inter-electrode spacing were used. The diagonal filter option, available in the software, was used for generating the subsurface resistivity image with depth along the entire profile line. The diagonal filter option is a modification to the smoothness-constrained least-square inversion method and it is used to reduce the artifacts

in the inversion model. The artifacts are reduced by modifying the horizontal roughness filter so that it has components in the diagonal directions also [64, 123]. Further, the inverted depth slices with same color scale were regenerated, using MATLAB. The depth slices, of inverted model obtained by 2D inversion, for the profile data recorded at the West and East banks are shown in Fig. 5.3 and 5.4 respectively. The horizontal distance, along the surface of each profile is shown w.r.t. the first electrode at the origin. The elevation data recorded by handheld GPS at each electrode location were used to add topographic information in each inverted model. The quality of inverted models was monitored by the Root Mean Square error between the measured and computed model response which is expressed as [221],

$$RMS = \sqrt{\frac{1}{N}\sum_{i=1}^{N}\left(\frac{d_i - f_i}{d_i}\right)^2}, \tag{5.3.1}$$

where d_i and f_i are the measured and the calculated responses for the i^{th} data point and N is the total number of data points.

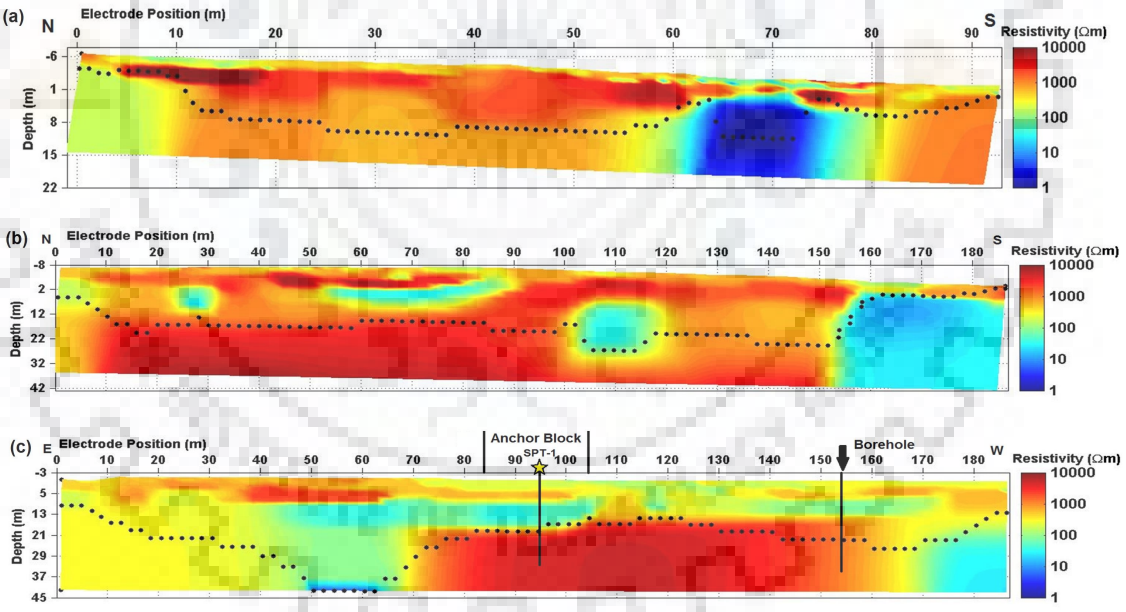

Figure 5.3: Inverted models at West bank showing resistivity variation with depth obtained by 2D inversion of ERT-1, 2 and 3 in (a), (b) and (c) respectively and the dotted lines represent the Depth of investigation (DOI). Locations of anchor block, SPT-1 and borehole are projected on bottom panel.

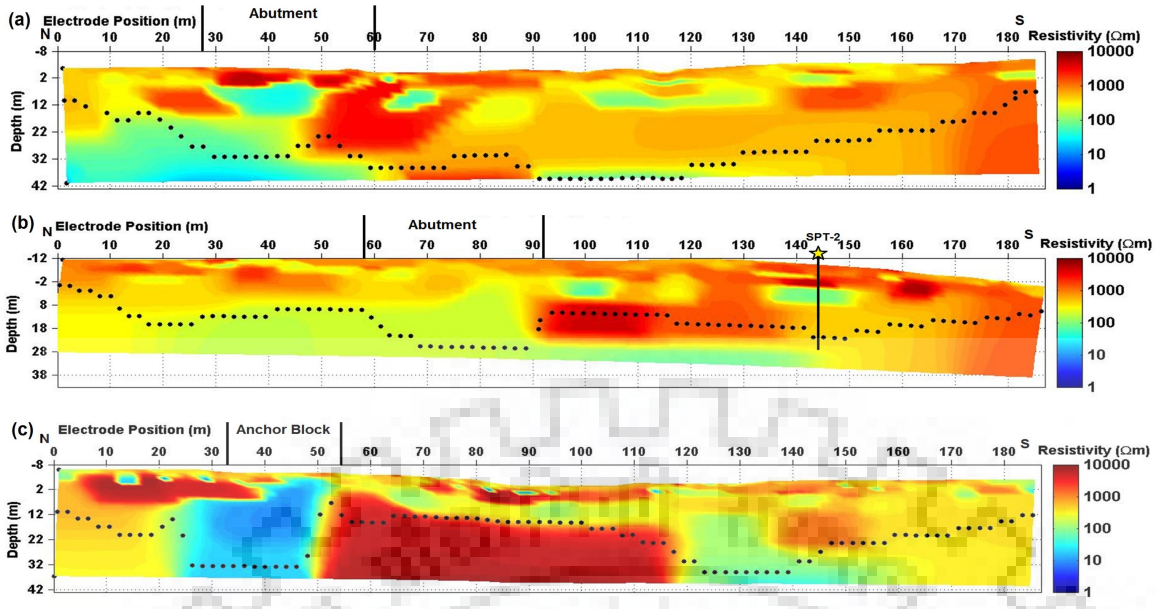

Figure 5.4: Inverted models at East bank showing resistivity variation with depth obtained by 2D inversion of ERT-4, 5 and 6 in (a), (b) and (c) respectively and the dotted lines represent the Depth of investigation (DOI). Locations of abutment are projected on (a) and (b). Projection of anchor block is shown on (c). Location of SPT-2 is also shown on middle panel(b).

Lithological correlation of the resistivity values, extracted from the inverted depth slice of ERT-3 (Fig. 5.3(c)), at the borehole location on West bank is shown in Fig. 5.5. The formation is mainly dominated by RBM consisting of gravels/boulders of different sizes and of clayey material. Accordingly, the average resistivity of different lithological units are: top unsaturated dry soil layer-416 Ωm, sand with gravels-550 Ωm, saturated sand with pebbles and cobbles-122 Ωm, coarse sand and boulders-650 Ωm and phyllite basement-917 Ωm. This correlation has been used as a guide to infer the lithology from the resistivity values for all resistivity depth slices. This also gives the depth of groundwater table at 6.7 m below the surface as a conductive feature (122 Ωm).

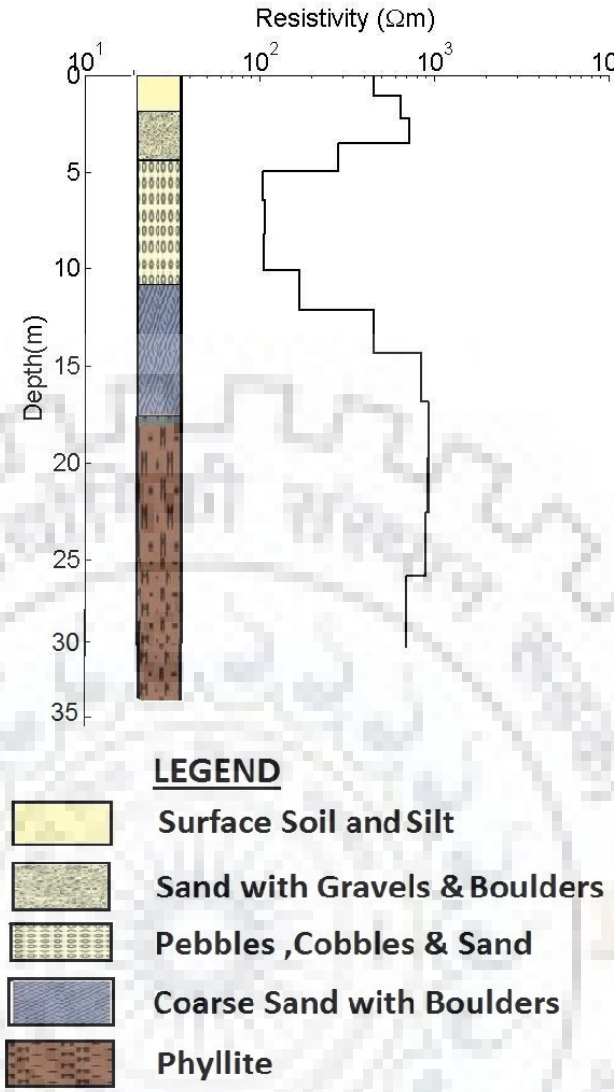

Figure 5.5: lithological correlation of resistivity variation at the borehole site near ERT-3.

For performing the 3D inversion using the MATLAB code *AP3DMT-DC* [203] the filtered data, used for 2D inversion, was collated in a 3D format. In case of West Bank, the 3D inversion of the collated ERT profiles was not feasible as the two profiles are almost perpendicular to each other and it would have required a large grid (minimum $105 \times 105 \times 20$). So the 3D inversion for ERT-2 and 3 was performed separately and the two inverted depth slices are shown in Fig. 5.6. Both the models were discretized into $31 \times 112 \times 38$ cells. With this grid, the dimension of the model domain becomes $1000 \times 2000 \times 1000$ m in x-, y- and z- directions respectively. A total of 32 cells were padded around the central region of the model, eight in each horizontal direction with the spacing increasing by a factor of 1.8. Two grid lines were placed between the consecutive electrodes in the profile direction. The grid spacing in the central region of the model was

2 m and 4 m in x- and y- directions respectively. Hence, in the central region there were $15 \times 96 \times 38$ cells in x-, y- and z- directions respectively. Below the surface, the distance of the first grid line was at 0.2 m and the spacing of each subsequent grid line was increased by a factor of 1.2, extending up to 1 km. For inversion, the error floor was set at 5 % of apparent resistivity value. The initial guess model was a homogeneous half space of 1000 Ωm, the average value of the observed apparent resistivities. The nRMS value reduced from 46.10 to 2.40 in 52 inversion iterations for ERT-2 and from 58.3 to 2.52 in 35 inversion iterations for ERT-3. For West bank the inverted models for both these profile are shown, in the form of depth slices, in Fig. 5.6.

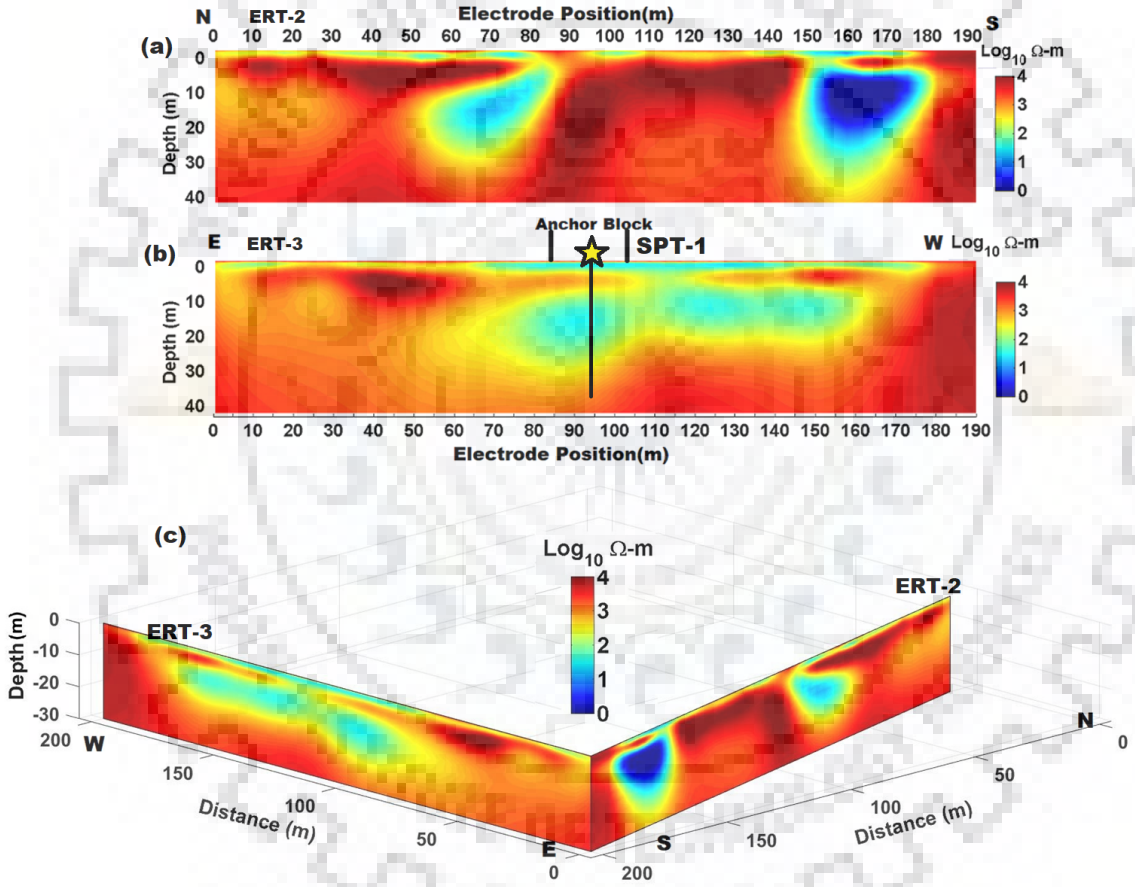

Figure 5.6: Inverted models showing resistivity variation with depth obtained by 3D inversion of ERT data from *AP3DMT-DC* code at West bank.

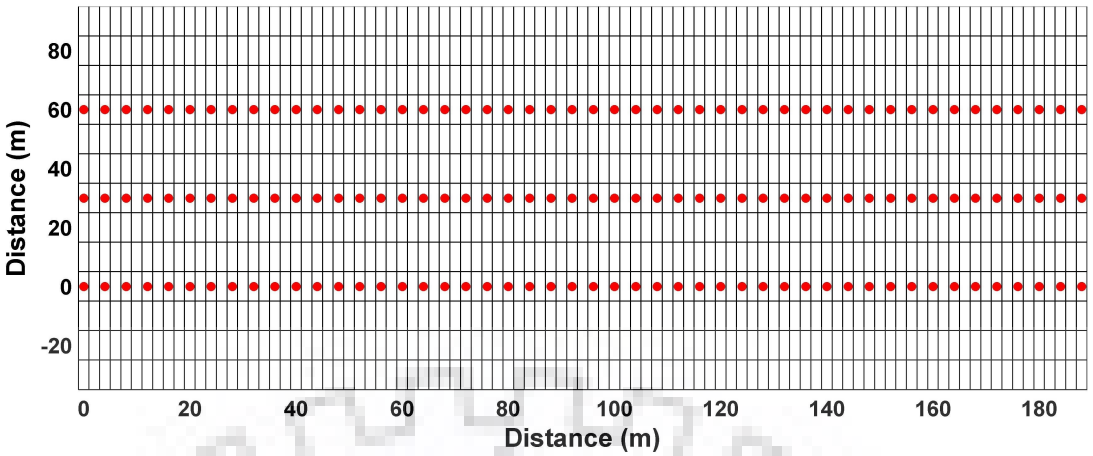

Figure 5.7: Location of grid and electrodes as taken for 3D inversion of East Bank.

For 3D inversion of East bank ERT profiles with *AP3DMT-DC* code, the model was discretized into $25 \times 107 \times 28$ cells. With this grid, the dimension of the model domain becomes $2600 \times 700 \times 1000$ m in x-, y- and z- directions respectively. A total of 24 cells were padded around the central region of the model, six in each horizontal direction with the spacing increasing by a factor of 1.8. Two grid lines were present between the consecutive electrodes in the profile direction. The grid line spacing in the central region of the model was 10 m and 2 m for the x- and y- directions respectively. Hence, in the central region there were $13 \times 95 \times 28$ cells in x-, y- and z- directions respectively. Below the surface, the distance of the first grid line was 1.2 m and the subsequent grid line spacing was increased by a factor of 1.2, extending up to 1 km. For the East bank the location of grids and profile positions are shown in Fig. 5.7. For inversion, the error floor was set at 5 % of the apparent resistivity value. The initial guess model was a homogeneous half space of 447 Ωm, average value of the observed apparent resistivities. In 148 iterations the nRMS value reduced from 32.57 to 1.77. For East bank, the three depth slices for each of the profiles, ERT-4, 5 and 6, are shown, from top to bottom, in Fig. 5.8. The complete inverted model corresponding to depth slices for each x- value is shown in Fig. 5.9.

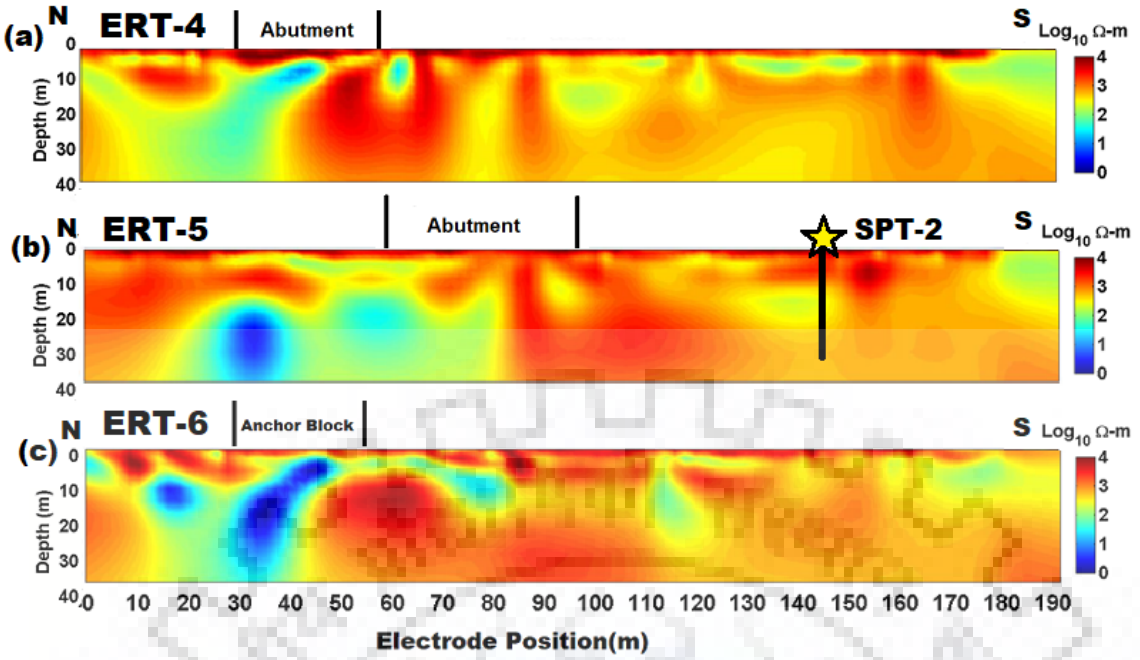

Figure 5.8: Inverted models showing resistivity variation with depth obtained by 3D inversion of ERT data at East bank from *AP3DMT-DC* code. Depth planes correspond to ERT-4, 5 and 6 from top to bottom.

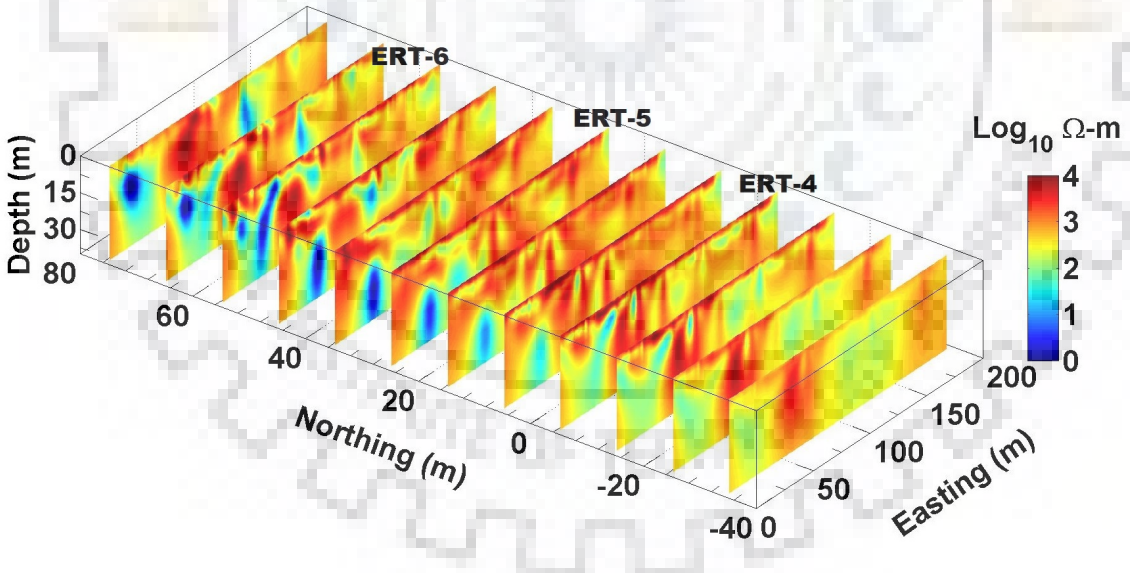

Figure 5.9: Y-Z Slice planes of 3D inverted model from *AP3DMT-DC* code at East bank and showing locations of ERT-4, 5 and 6

The 3D inversion of the three ERT proflies on the East Bank was also performed with the software *Res3Dinv* [122]. In *Res3dinv* a '*.dat' file with collated data of three ERT's (ERT-4, 5 and 6) was provided as an input. Along with this, the grid type (uniform, nonuniform, arbitrary, trapezoidal), the number and location of grids in x-, y- and z- direction, the array

type, the type of data (resistivity or resistance) and the number of electrodes used were also given in the input file. *Res3dinv* uses smoothness-constrained 'Standard Gauss-Newton' or Incomplete Gauss-Newton least-squares method for inversion. In addition to this, one can modify values of the initial and minimum damping factor, flatness filter weight, type of reference resistivity (average or first iteration), number of iterations, minimum change in RMS error (0.2), the methodology to be used in forward modeling (Finite difference or Finite element) etc. In *Res3dinv* there is a limit on the number of nodes to be used between the two electrode positions in finite-difference method (at least 2 nodes). The number of inversion iteration are also limited to 40 only.

For 3D inversion of ERT's on the East Bank with *Res3dinv* software Finite difference method was used for mesh designing. The padding was not used in model discretization, as it was not available in the software. So, the model was discretized into $13 \times 96 \times 17$ cells. With this grid, the dimension of the model domain becomes $60 \times 190 \times 45$ m in x-, y- and z- directions respectively. Two nodes were taken between the consecutive electrodes in profile direction. The grid spacing for the model was 2 m and 5 m in x- and y- directions respectively. Below the surface, the distance of first grid line was 0.35 m and the spacing of each subsequent grid increased by a factor of 1.15, extending up to 45 m. For inversion, the standard deviation of error distribution was 0.1045. The initial guess model used was a homogeneous half space of resistivity computed on the basis of the average of observed apparent resistivities. The nRMS error value reduced from 22.29 to 5.39 in 40 inversion iterations. The inverted model, in form of depth slices, is shown in Fig. 5.10.

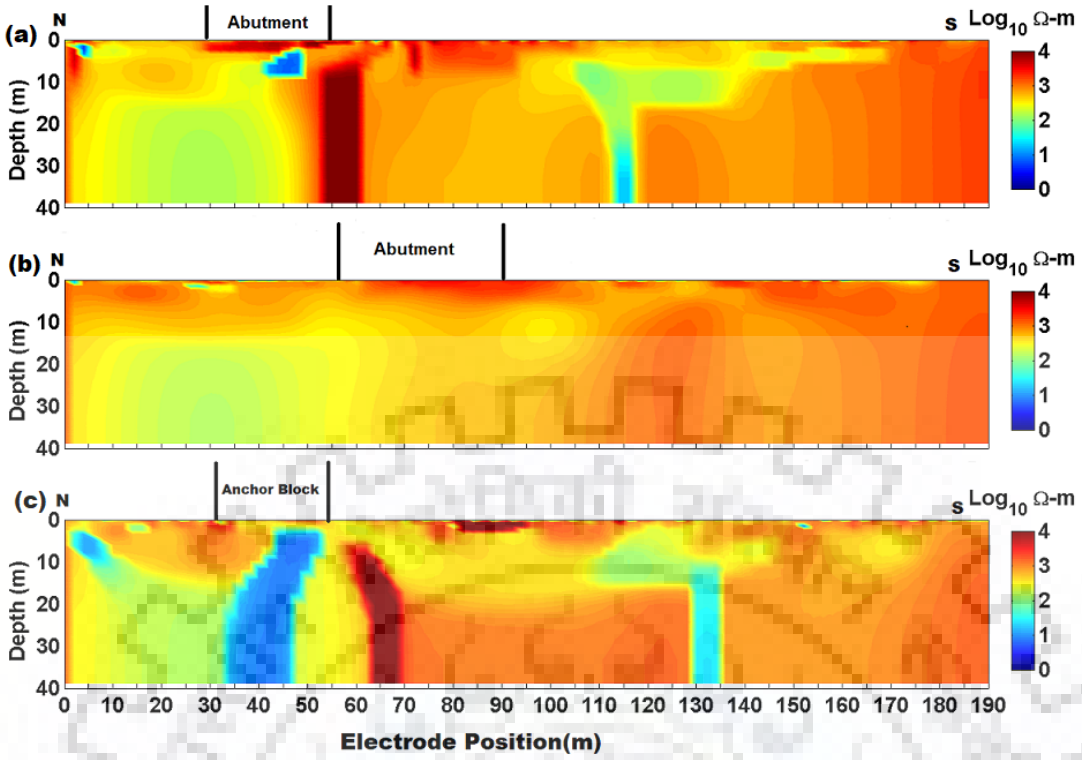

Figure 5.10: Inverted models showing resistivity variation with depth obtained by 3D inversion of ERT data using *Res3Dinv* at East bank.

The 3D inversion of ERT profiles on West bank was not possible with *Res3dinv* as the software limits the number of nodes to 16000 during the forward computations.

Next, the results of inverted models obtained from 2D and 3D inversion are correlated with the lithology of the area.

5.4 Lithological Correlation of Resistivity Models

The formation zones in the resistivity depth slices of Fig. 5.3 to 5.10 are identified by the horizontal position as *'surface mark'* (with respect to the first electrode) and vertical position as *depth* (in vertical scale).

The resistivity distribution as observed from the 2D and 3D inversion of the ERT profiles in the West bank is shown in Fig. 5.3 (ERT-1, 2 and 3) and Fig. 5.6 (ERT-2 and 3) respectively. In the West bank, the local geology indicates that the subsurface formation mainly consists of RBM which is underlain by weathered Phyllites rock. A significant variation was observed in resistivity of subsurface material at different depths. It was as low as 1.07 Ωm for the saturated clayey/silty soil matrix and it reaches to more than 5000

Ωm for the bedrock. ERT-1 and 2 were recorded along the same line but with different inter-electrodes spacing along the bank oriented in the N-S direction with the first electrode located in the North. So, the 3D inversion was done only for ERT-2 and 3. The resistivity variation in RBM is related to the grain size distribution, clay/silt contents and the amount of water present in pore spaces. The resistivity decreases with decreasing particle size distribution and also with the water saturation, while it increases with increase in particle size (gravels/pebbles and boulders). The bedrock was characterized by high resistivity.

The geoelectrical section shown in Fig. 5.3(a) is also included in Fig. 5.3(b) in its quarter space southern part. Therefore, the focus is on electrical structure for ERT-2, presented in Fig. 5.3(b) (2D inversion) and Fig. 5.6(a) (3D inversion with *AP3DMT-DC*). In Fig. 5.3(b) the saturated clayey/silty RBM zones were visible as conductive ($<$ 120 Ωm) features, (i) between the *'surface mark'* of 104-118 m in the *depth* range 8-27 m and (ii) between the *'surface mark'* of 154-184 m in the *depth* range 4-42 m. However for Fig. 5.6(a) it was visible only between the *'surface mark'* of 154 and 184 m in the *depth* range 4-36 m. The bedrock was visible in both the inverted models as a resistive feature ($>$ 2000 Ωm). The position of bedrock was between the *'surface mark'* of 16-150 m and the *depth* range of 17-30 m.

The third profile, ERT-3, is aligned nearly perpendicular to the ERT-2. This profile is oriented along N115°-N295° with its first electrode in the river bank side. The geoelectrical images showing resistivity variation, in the form of depth slices, along the profile are shown, in the form of depth slices, in Fig. 5.3(c) and Fig. 5.6(b) for 2D inversion with software *Res2Dinv* and 3D inversion with code *AP3DMT-DC* respectively. Along this profile, the top surface of bedrock varies between *depth* 17 to 22 m. The bedrock is weathered and less saturated near middle of the profile and becomes softer and more saturated towards East as reflected in the resistivity depth slices. The resistivity of bedrock varies from 258-964 Ωm. The RBM also shows variation in saturation and gravels/boulders size. The saturated silt corresponds to resistivity values $<$25 Ωm, while the gravel and coarse material corresponds to resistivity between 25-258 Ωm. The inverted slice in Fig. 5.6(c) shows that the saturated silt is present only near the reservoir and as we move away from it the resistivity increases. The extent of bedrock is visible more clearly in 3D inverted depth slices (Fig. 5.6).

The formation on the East bank is characterized by fairly steep slopes and weathered Phyllites in different water saturation conditions. Phyllite rock is sheared and highly

weathered as observed at higher elevation above the investigated site. A huge thickness of past landslide debris was visible on the surface. The loose debris and weathered rock have different water saturation conditions which are reflected in the resistivity variation in electrical models derived from the three sets of inversions (i) 2D inversion (Fig. 5.4), (ii) 3D inversion with *AP3DMT-DC* code (Fig. 5.8 and 5.9) and (iii) 3D inversion with *Res3Dinv* (Fig. 5.10). All the ERT profiles on East Bank were recorded with a 4 m inter-electrode spacing and these are generally aligned in NW-SE direction located at different elevations.

The three resistivity depth slices of ERT-4, Fig. 5.4(a), 5.8(a) and 5.10(a), obtained by different inversion algorithms, show local resistive and conductive features in the northern part of the profile. It was visible in all the three depth slices, but with a variation in horizontal and vertical extent. The depth slice of resistivity model obtained from 3D inversion (Fig. 5.8(a)) shows that the conductive feature in North is limited upto the *'surface mark'* of 35 m and corresponds to boulders and debris in saturated conditions. In the South of the profile, the bedrock appears at the *depth* of 15 m from the surface as a resistive (> 2000 Ωm) feature. A local resistive feature was related to the reinforced concrete foundation structure and extends upto the *depth* of 25 m. The position of the *'surface mark'* of concrete structure in horizontal direction varies in all the three inverted models: and is (i) 28 to 60 m in Fig. 5.4(a), (ii) 35 to 70 m in Fig. 5.8(a) and (iii) only between 50 to 65 m in Fig. 5.10(a). A conductive feature below the 8 m *depth* corresponds to a silty sand and was underlain by the weathered rock upto the *depth* of more than 40 m.

Similarly, the resistivity depth slices for ERT-5, Fig. 5.4(b), 5.8(b) and 5.10(b), obtained by different inversion algorithms, show resistive and conductive blocks. These blocks represent the boulders and weathered rock/debris in partial saturation (low resistivity). In Fig. 5.4(b) no basement rock was observed on the northern side of profile upto the *depth* of 30 m. However, it was visible in Fig. 5.8(b) between the *'surface mark'* of 0 to 20 m and upto the *depth* of 40 m. In the southern side of this profile, bedrock was encountered at the *depth* of 25 m in all the three inverted models.

ERT-6 is located on a still higher elevation. Above the profile, rocks are seen on eastern side. The profile lies between the anchor block and the reservoir. Geoelectrical sections showing resistivity variation, in the form of depth slices, and location of anchor block are shown in Fig. 5.4(c) (2D inversion), 5.8(c) (3D inversion with *AP3DMT-DC*) and 5.10(c) (3D inversion with *Res3Dinv*). The reinforced foundation of anchor block, with resistivity

ranging from 2000-4500 Ωm, is clearly seen in Fig. 5.10(c). The *'surface mark'* of reinforced foundation is between 34 to 54 m in *depth* range 2-10 m. Some localized blocks with low resistivity values were also visible. The water saturated fine debris material with resistivity of 9-50 Ωm was extended upto the *depth* greater than 40 m. Bedrock was visible in the middle of the profile in all the three inverted models, as highly resistive (7600 Ωm) feature, from the surface to the *depth* of 15 m.

The relationship between resistivity and the soil strength parameter (N-values) is discussed in the next section.

5.5 Correlation of Geotechnical and Resistivity Data

We now analyze the electrical resistivity and the N-values, derived from Standard Penetration Test (SPT), together to identify their possible correlation. For this purpose, the N-values [191] recorded on the West bank near ERT-3 and on the East bank near ERT-5 were used. The N-values give the point information about the soil strength. The variation of N-values with depth at the two banks are shown in Fig. 5.11. The N-values in Fig. 5.11(a) increases with depth due to the presence of weathered rock. The decrease in N-values in Fig. 5.11(b) is caused by the saturated silty soil matrix.

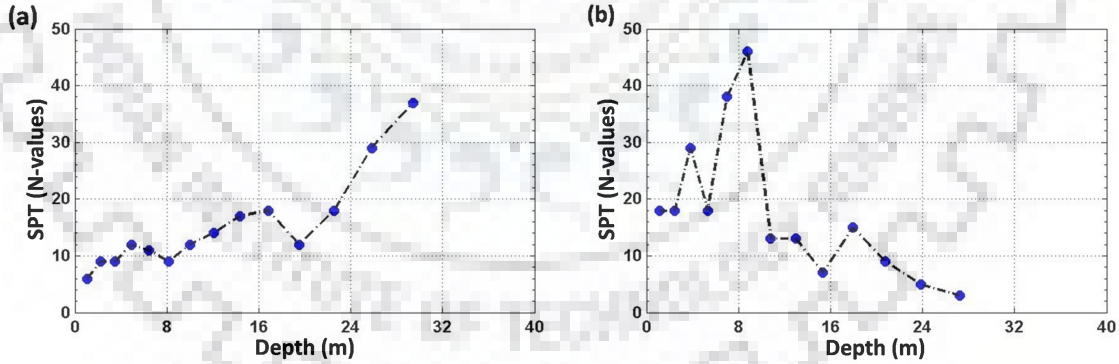

Figure 5.11: Variation of N-values with depth at (a) SPT-1 (ERT-3) and (b) SPT-2(ERT-5).

The five resistivity values, around the point of observation of the N-values, extracted from the 2D inverted models of profiles ERT-3 and 5 are shown in Fig. 5.12(a and b). To obtain a statistically representative value of the resistivity, the average and standard deviation of the resistivity values around each point of observation were computed. In addition to the five points averaging window, the three and seven points averaging windows were also tested. It was found that the general nature of the resistivity variation with depth remains

same. Average resistivity variation with depth using three, five and seven points averaging windows, extracted from the 2D inverted models of profiles ERT-3 and ERT-5, are shown in Fig. 5.12(c and d). Similarly, the five resistivity values, around the point of observation of the N-values, were also extracted from the 3D inverted models of profiles ERT-3 and 5.

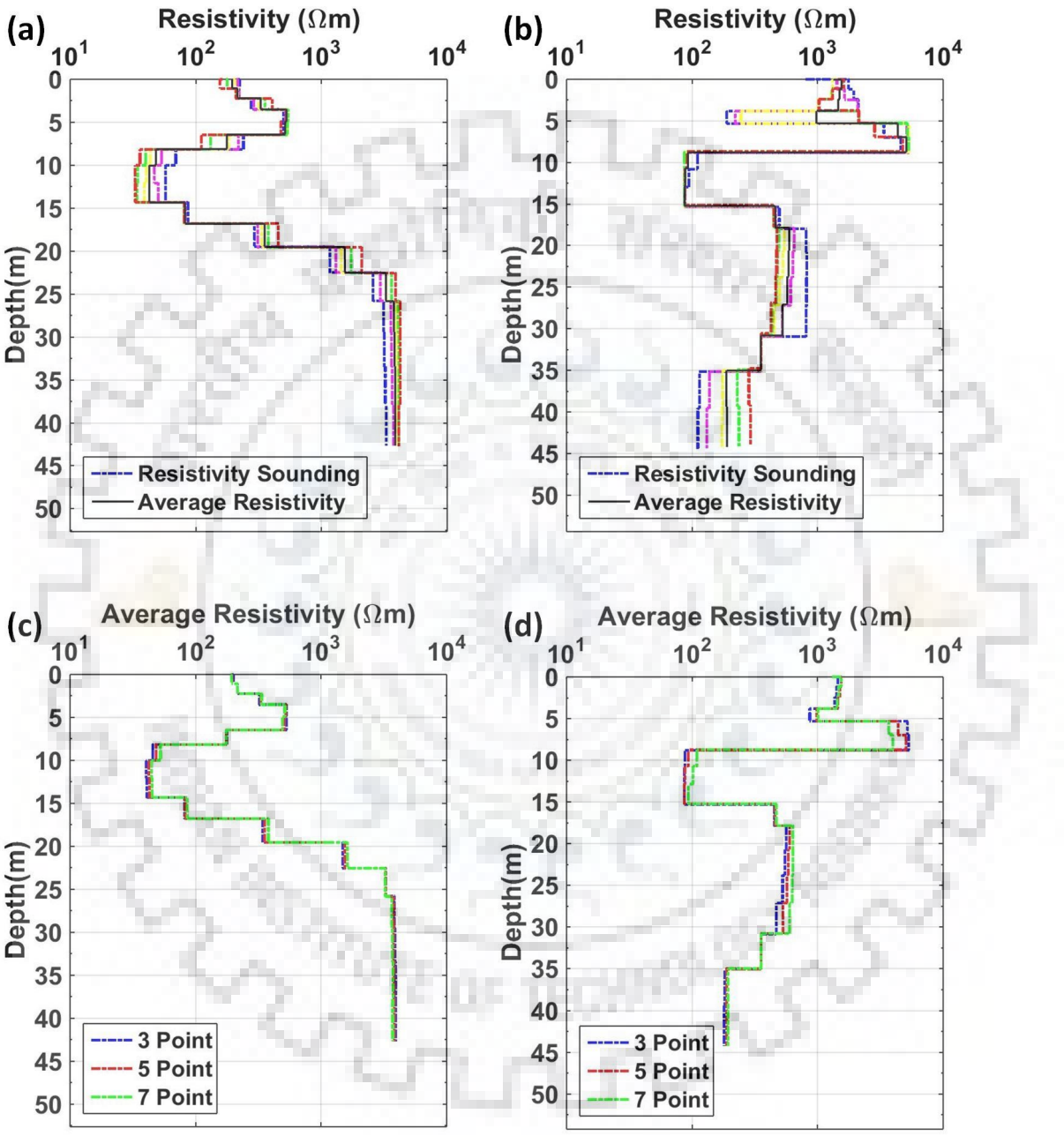

Figure 5.12: Variation of resistivity values with depth at each ERT along with the average resistivity (estimated for five sounding points) (a) ERT-3 and (b) ERT-5. Average resistivity variation with depth using 3, 5 and 7 points are given in (c) and (d) for ERT-3 and ERT-5 respectively.

The resistivity vs N-values plots are given in Fig. 5.13(a and b) for West and East banks

respectively. Following Hatta et al. [84] and Braga et al. [31] the relationship between resistivity (ρ) and N-values (N) was studied. It can be seen that, for N $<$ 16, the N-values are not consistent and the corresponding resistivity values are nearly constant. This is due to the fact that the N-values are unreliable in coarse gravel and boulders [111]. Therefore, any relationship between resistivity and N-values for N $<$ 16 will be meaningless. For N $>$ 16, the fitted N-values with resistivity are given in Fig. 5.13(c and d) and 5.14(c and d) for 2D and 3D inversion respectively. The relationship was linear and the coefficients of correlation for West bank were 0.85 (2D inversion) and 0.87 (3D inversion with *AP3DMT-DC*). The coefficients of correlation for East bank were 0.87 and 0.96 for 2D and 3D inversion cases respectively. The correlation was good when resistivity values from 3D inversion were used. The generalized linear relationship for the study area can be written as,

$$\rho = \mathbf{aN} + \mathbf{b}, \tag{5.5.1}$$

where, the coefficients, a and b, in case of 2D inversion are 181.14 and -2572.02 for West and 136.19 and -1304.83 for East bank respectively. The coefficients, a and b, in case of 3D inversion are 25.87 and -439.58 for West and 108.3 and -1091.33 for East bank respectively.

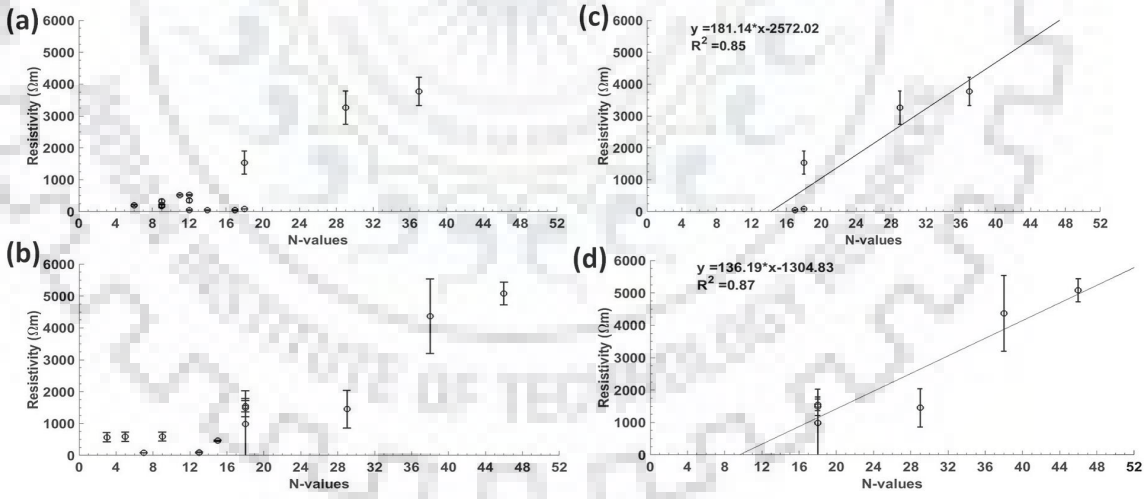

Figure 5.13: Plot of Resistivity from 2D inversion and number of blow counts (N-values) for (a) ERT-3 and (b) ERT-5. Linear relationship between resistivity and number of blow counts (N-values) for (N $>$ 16) at (c) ERT-3 and (d) ERT-5.

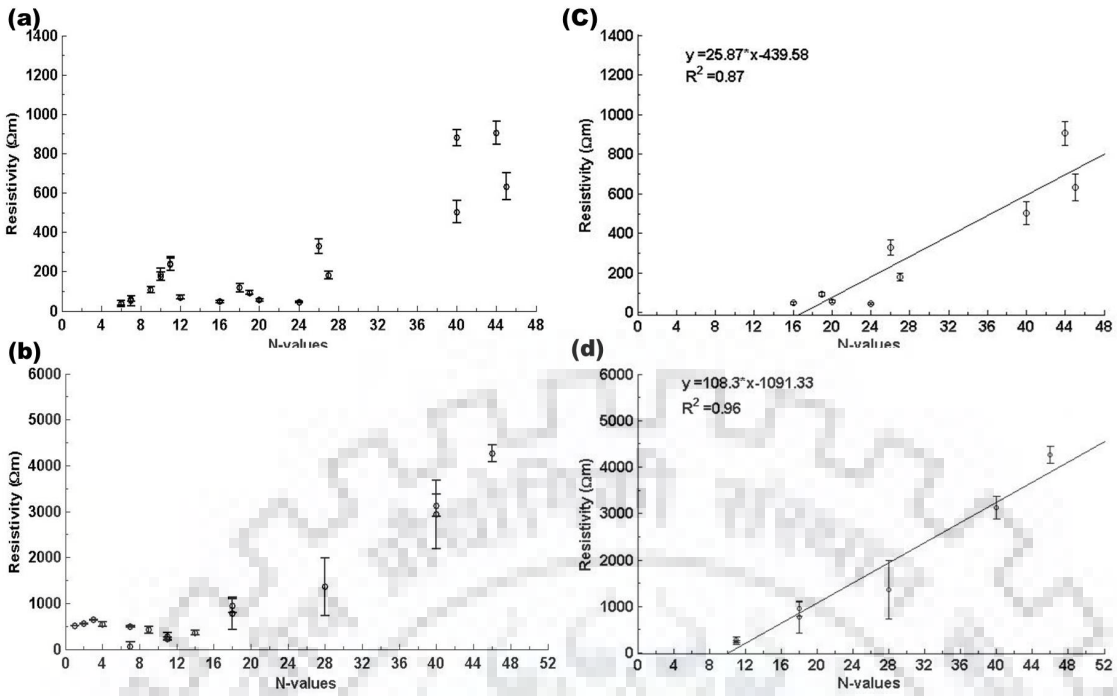

Figure 5.14: Plot of Resistivity values extracted from 3D inversion and number of blow counts (N-values) with *AP3DMT-DC* for (a) ERT-3 and (b) ERT-5. Linear relationship between resistivity and number of blow counts (N-values) for (N $>$ 16) at (c) ERT-3 and (d) ERT-5.

Variation in numerical values of the coefficients is a reflection on lithological variations at the two banks. Higher *a* value on the West bank and East banks for 2D inversion indicates that the resistivity was more sensitive to the N-values and it reflects a low content of clay/silt in West bank in comparison to that on the East bank. A negative resistivity has no physical interpretation. However, it indicates that the relationship was not useful for the N-values smaller than 14 and 10 on the West and East bank respectively. Still, the ERT data provide information about the soil strength even in areas where the N-values were unreliable and inconsistent. The relationship can be employed for geotechnical investigations in the Himalayan region where undertaking a destructive test is prohibited. The linear relationship may also be applicable to the places other than Himalayan region for the same rock formation having different degree of weathering and constant salinity of saturating water.

5.6 Summary of Results

Electrical Resistivity Tomography (ERT) method has been used for subsurface formation characterization at a proposed bridge site on Bhagirathi River in Uttarakhand, Himalayan region. This characterization of near surface formation has been done through 2D and 3D inversion of ERT data, recorded on both the banks of the river. The borehole and geological inputs have been used for lithological correlation and for reducing non-uniqueness and ambiguity in geophysical inversion. Based on the 2D and 3D inversions the resistivities of different lithological units have been defined for the investigated sites. The basement depth has been found on the basis of resistivity variation. The correlation study shows that the resistivity is linearly correlated with the N-values. The coefficient of correlation at the two locations is greater than 0.85 indicating that it is good and consistent. The ERT data provide information about the soil strength even in zones where the N-values are unreliable and inconsistent. The linear relationship is applicable to places other than Himalayan region if the rock/soil formation and its water saturation are same. Once such a correlation is established for a particular region, it can be used for geotechnical investigations economically and efficiently.

The next case study deals with the 3D individual and joint inversions of Direct Current Resistivity (DCR) and Radio Magnetotelluric (RMT) data with a view to study the contamination of groundwater due to a waste disposal site in Roorkee region.

Chapter 6

DCR STUDY IN ROORKEE REGION

6.1 Preamble

The last case study was carried out to examine the impact of untreated sewage irrigation and waste disposal practices on groundwater in Roorkee region. For this, the field measurements were carried out near a waste disposal site which was irrigated with untreated sewage water. The two techniques used were the Direct Current Resistivity (DCR) and the Radio Magnetotelluric (RMT) methods. The DCR method was used in Electrical Resistivity Tomography (ERT) mode. The two methods are widely used to study various hydro-geophysical problems, such as groundwater contamination, aquifer delineation, sewage leakage, leakage pathways in earth-filled dam [86, 174, 223, 258]. The data were acquired along six ERT and 10 RMT profiles. These data have been analyzed earlier using the 2D individual and joint inversion techniques [258]. However, in order to interpret the data in 2D, strong assumptions are required with respect to the geological strike direction and the direction of RMT source signals. Since, the structure of the problem is 3D and the data were recorded in 3D mode, 3D inversion of the recorded data was performed, both independently and jointly, using the code *AP3DMT-DC* [203]. The validation of the algorithm capabilities was demonstrated through a synthetic study. This study demonstrates that the two methods, DCR and RMT, complement each other and that the inverted model obtained through joint 3D inversion is better resolved than the individual 3D inversions. The 3D inverted resistivity model of the recorded data shows an unconfined aquifer of low resistivity overlain by a slightly resistive near surface unsaturated formation. Moving away from the waste disposal site, an increase was observed in resistivity of the shallow unconfined aquifer indicating an

undisturbed geology. The flow direction of contaminated water is nearly parallel to Solani River. The profile sections of the 3D model were correlated with the corresponding 2D inverted models and were found to be consistent. In comparison to the inverted results of an uncontaminated reference site, the inverted results of the contaminated region show a decrease in resistivity of the aquifer layer establishing the influence of contamination.

6.2 Geohydrology of the Study Area

The study area (Fig. 6.1) is around the waste disposal site in Saliyar Village located between 29°53′N to 29°54′N and 77°51′E to 77∘52′E. The area lies in the lower piedmont zone, also known as Tarai zone, of Himalayan foothill region, around Roorkee, Uttarakhand. The area comprises mostly unconsolidated alluvial sediments of Quaternary period. The sediments of the area consist of alternating layers of clay, sand, pebble and gravel in some places. The general lithology of the top soil layer of thickness 3-6 m is sandy loam having roughly equal distribution of soil, sand, silt, and clay [206]. Below this lies the shallow unconfined aquifer of thickness 3-27 m which, in turn, is underlain by a second aquifer (aquiclude) of thickness 14 m. The two aquifers are separated by a clayey layer intermixed with gravel.

The southeasterly flowing Solani River is located at a distance of approximately 500m from the waste disposal site in Northwest direction (Fig. 6.1). The groundwater flow is controlled by a gentle elevation and slope in the southeast direction and it is almost parallel to the Solani River [25, 206].

The contamination in groundwater, due to waste disposal and untreated sewage irrigation practices in the region, has been studied by many workers using the physio-chemical parameters of groundwater [25, 94, 206]. All of these workers found that the upper aquifer near the Saliyar village is contaminated due to the sewage water irrigation. Bhatnagar et al. [25] investigated that the heavy metal concentration is high in the plots irrigated with untreated sewage water. Moderate to severe water contamination is observed in some parts. Singhal et al. [206] indicated that the value of total dissolved solids is high in groundwater of the upper unconfined aquifer of Saliyar Village. ERT and RMT data were acquired in this region to image the different zones of contamination.

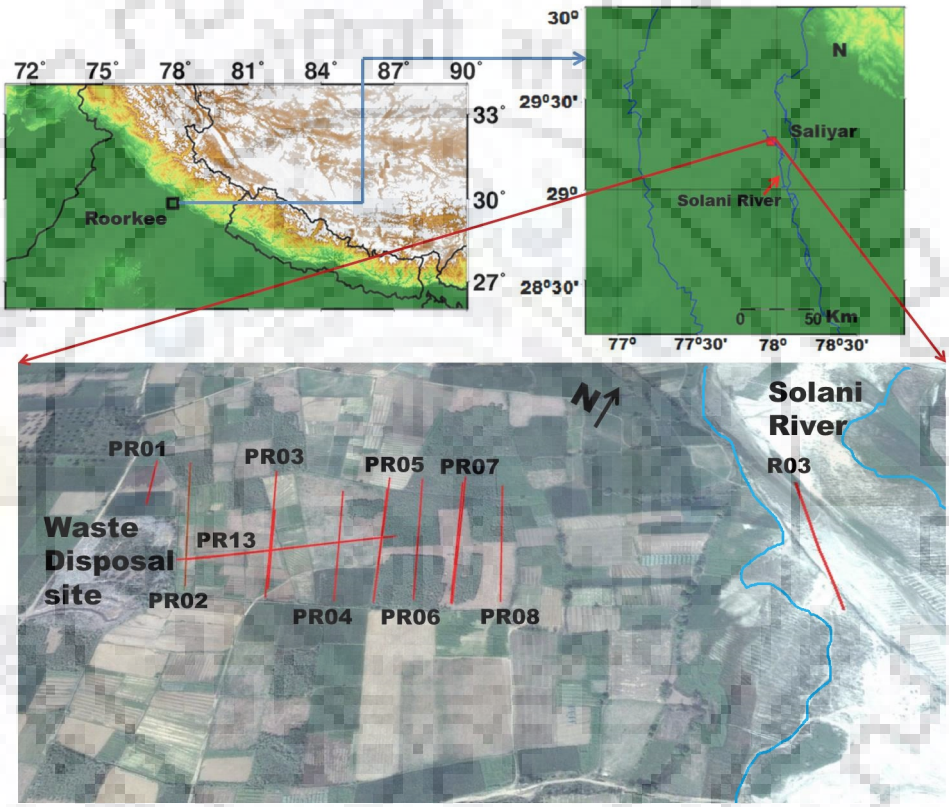

Figure 6.1: Study area, showing the locations of ERT and RMT measurements around the waste disposal site, Saliyar, Roorkee.Map was created with gmt software version 5 (`http://gmt.soest.hawaii.edu/`) and `http://earth.google.com/web/`.

6.3 RMT Data Acquisition and processing

The RMT Data measuring instrument is a four channel system that can be used for tensor measurements. The system consists of a receiver unit, an electrical antenna to observe the electric field and magnetic coils for the measurement of the horizontal components of the magnetic field. The magnetic field measurements are performed with a magnetic coil – a cylinder with a high permeability core of about 30 cm length and a multi-section coil. The electric antenna is represented by a symmetrical dipole with two arms. The electrical line can be grounded or ungrounded. The length of this line can vary from 4 to 20 m. The cable used for the ungrounded lines should have a significant weight. The magnetic field can be measured for selected frequencies by a coil and the electric field by two grounded electrodes or by an electrical antenna yielding information about the conductivity distribution up to several hundred metres depending on the conductivity distribution beneath the investigated area.

Time series of the electric and magnetic fields are recorded in two frequency bands: one from 10 kHz to 100 kHz with a sampling frequency of 312.5 kHz and the other from 100 kHz to 1 MHz with a sampling frequency of 2.5 MHz. Time series are saved in the receiver unit and transferred to a field PC via an ethernet connection in the field. The measured time series contain all the frequencies from 10 kHz to 1 MHz associated with powerful radio stations. The user can select the gain factor, frequency range and segment length of the time series by using the acquisition software installed in the receiver. The acquisition software also makes it possible to use the so-called spectral mode in which the user can predefine the frequencies to be observed and the system then measures only transfer functions of those frequencies. In the spectral mode, the data is not transferred to the PC; they are processed entirely in the receiver unit. In addition to the software installed in the receiver used to control and carry out measurements, data processing software was developed. This software was installed on a laptop and was used for displaying and processing the observed RMT time-series. These time series can be transferred in the field via an ethernet cable to the laptop so that they can be visualized, auto and cross-spectra can be calculated and displayed quickly. In this way, the quality of the data can be examined in the field. Radio transmitters are easily identified in the power spectra as strong signals over narrow frequency intervals. The entire system, including the magnetic and electric sensors, was calibrated in the laboratory.

The calibration files were saved and included in the processing software. They are used to calibrate the cross- and power spectra in order to avoid instrumental effects and to calculate the transfer functions in real physical units. The correct determination of the azimuth of radio transmitters is very important for a radiomagnetotelluric survey. All the azimuths of the radio transmitters available in the survey area can be viewed by the software in the frequency band 10 kHz–100 kHz or in the frequency band 100 kHz–1 MHz. The azimuth is calculated relative to the magnetic field in the north direction and the user can define an azimuth range in which to select the available transmitters. The user can define an azimuth range. The coherency level, typically with a value of 0.8, can also be selected by the user. Thus, the transfer functions only need to be calculated for the frequencies with coherencies greater than the selected coherency level and for radio transmitters located within the azimuth range defined by the user. After having calculated the power and cross-spectra and after having determined the coherencies and azimuth angles, transfer functions (apparent resistivity and phase) are derived for each frequency from the power and cross-spectra. Presently, this is done in the scalar mode, i.e., calculations of the apparent resistivity and phase are based on the impedance tensor elements Zxy and Zyx. Although the new RMT instrument is a broadband system and is capable of recording time series in a broad frequency range from 10 kHz to 1 MHz our presentation does not use the full information of the data. It is assumed beforehand that the profile direction is perpendicular to the geoelectric strike direction. Under this assumption it is then possible to calculate TE and TM responses by simply combining orthogonal components of the horizontal electric and magnetic fields for the estimation of the corresponding impedances.

6.4 ERT and RMT Data Description

Yogeshwar et al. [258] recorded 13 RMT and eight ERT profiles in and around Roorkee. Out of these, only 10 RMT and six ERT profiles located between the waste disposal site and the Solani River (Fig. 6.1) were inverted. It may be mentioned that profile, ‘R03’, on the right Bank of Solani River, is far away from the waste disposal site, and is treated as a reference profile from uncontaminated region. The profiles, as shown in Fig. 6.1 are mainly oriented in the southeast direction and are parallel to each other except for the profile PR13 which is perpendicular to all the remaining profiles and was not used in 2D inversion. The profiles

are labeled PR01 to PR13 as shown in Fig. 6.1. The distance between the two consecutive profiles is about 50 m. The total area covered is approximately 200 $\times$ 650 m^2. The area above the waste disposal site was not accessible for measurements.

The ERT measurements were carried out utilizing an ABEM Terrameter SAS 1000 (ABEM, 2004). Wenner and Schlumberger short and long configurations were used for ERT data acquisition, with a profile length of 200 m (excluding profile PR03, which is 120 m long). The inter-electrode spacing of 5 m and 2.5 m was used for the outer and middle part of the profile. The short configuration leads to a better resolution of the near surface structures for the middle part of the profile.

The RMT measurements were carried out using the RMT-F instrument of the University of Cologne [230]. In order to carry the RMT measurements the important factor is the direction of radio-transmitter and its frequency. The sensors are needed to be placed in the orthogonal directions. The RMT profile length is 200 m for most of the profiles with an inter-station spacing of 10 m for most of the stations. For profiles PR01 and PR03 the length is approximately 100m. Five to six frequencies, in the range 10 kHz to 1 MHz, were used for both E-polarization (TE-mode) and B-polarization (TM-mode). The acquisition parameters of RMT data are shown in Table 6.1.

Table 6.1: Data acquisition parameters of RMT data

Profile Name	Number of Stations	Profile Length(m)
PR01	9	80
PR02	21	200
PR03	10	100
PR04	18	170
PR05	18	170
PR06	20	190
PR07	20	190
PR08	19	180
PR13	21	200
R03	21	200

The contamination problem due to untreated sewage water irrigation is, in general, 3D in nature. The ERT and RMT data were acquired in a field configuration which makes it amenable to a 3D study and hence, its 3D inversion was performed.

6.5 3D Inversion of Data

The 3D inversion of ERT and RMT datasets was done using the inversion code *AP3DMT-DC* [203]. *AP3DMT-DC* is an extended version of the 3D Magnetotelluric (MT) inversion code, *AP3DMT* [204]. For the convergence and accuracy of the iterative inversion procedure optimal values of few inversion parameters are required, (i) Marquardt Regularization parameter, (ii) Number of iterations and tolerance for Bi-Conjugate Gradient Stabilized (Bi-CGSTAB) matrix solver [243], (iii) data weighting matrix, (iv) 3D forward and inverse modeling grid parameterization and (v) starting model resistivity. The control parameters used in the inversion are discussed in the following section.

6.5.1 3D Inversion Control Parameters

Average apparent resistivity of ERT data was used as the resistivity of half-space initial guess model for both individual and joint inversion runs. To account for different depths of investigation and different boundary conditions in the two methods, the spacing of grid lines in the inner domain (Fig. 6.2) was governed by the ERT method while that in the outer domain was governed by the RMT method. For inner domain, the grid lines spacing in the horizontal direction was such that there were minimum two grids lines between any pair of electrodes. Larger grid spacing was used in the outer domain to satisfy the boundary conditions for the RMT problem (Fig. 6.2). With respect to the vertical direction, the first grid spacing below the surface was fixed at approximately one-fourth of the minimum electrode spacing and subsequent spacings were increased by a factor of 1.2.

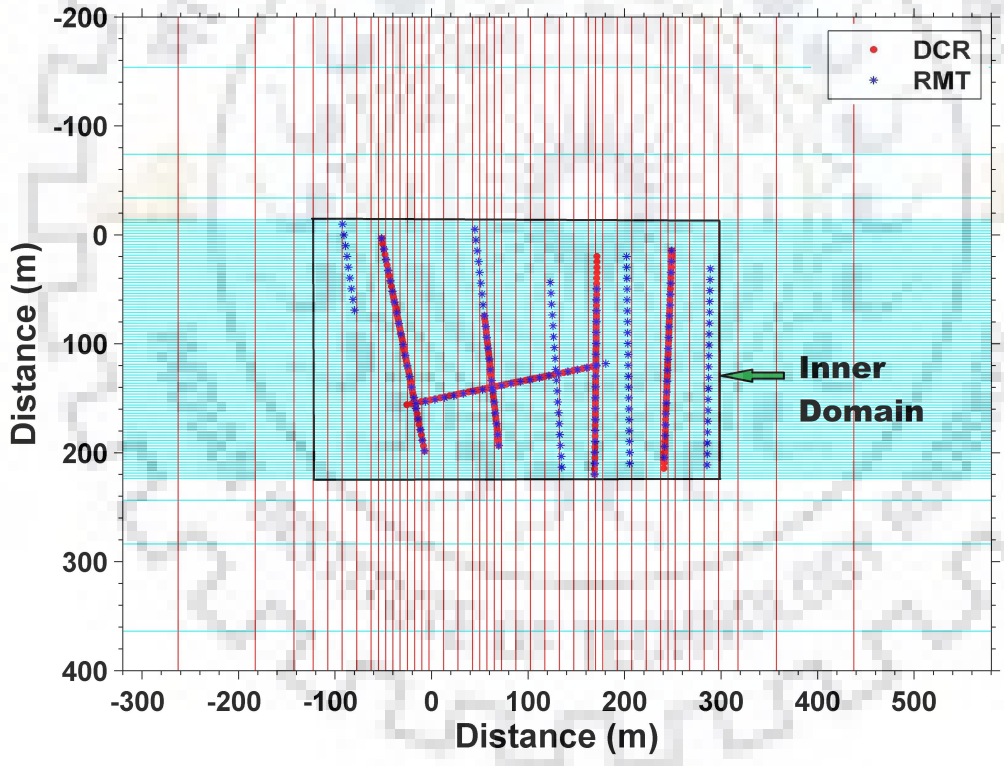

Figure 6.2: Profiles orientation and electrodes position (red color) along six ERT profiles, station locations (blue color) along 10 RMT profiles and grid lines and inner domain boundaries used in 3D inversion.

The initial value of Marquardt regularization parameter (λ) was chosen to be 10 on the basis of L-curve analysis [142]. BiCGSTAB scheme [243] belongs to a class of Krylov subspace techniques and was efficiently used to solve iteratively the sparse linear system. It

may also be mentioned here that the Finite Difference equations for all nodes resulted in a highly sparse coefficient matrix. The tolerance parameter of BiCGSTAB was chosen to be 10^{-10} for RMT forward problem. For ERT a direct matrix solver was used.

For 3D joint inversion of ERT and RMT data, there are two built in features in the code, *AP3DMT-DC* which improve the quality of inversion results. The first crucial aspect was the data scaling matrix which normalizes the two datasets and the second one was the revision of target Normalized Root Mean Square (nRMS) error value during the inversion process.

The weighting factors (data scaling matrix) were chosen on the basis of the units, magnitudes of the data and the errors in the data. The data set with more number of independent data points can have significant influence on the imaging. To resolve this issue following Commer and Newman [46], a data scaling matrix was chosen using the norms of the gradients of data misfit of the two data sets. With such a gradient based scheme, equal speed of convergence can be achieved for both the methods. Let us consider ERT and RMT dataset and call them as data set-1 and -2 respectively. If the number of data points in data set-1 is greater than that in data set-2, the up-weighting factor g_w for the data set-2 is computed as,

$$g_w = \sqrt{\frac{\|\nabla\phi_1\|}{\|\nabla\phi_2\|}}. \tag{6.5.1}$$

where, $\phi 1$ and $\phi 2$ is the data misfit for each ERT and RMT datasets respectively. This scheme incorporates both the number of data points and the resolution capacity of each method in the joint inversion.

If the data error, in the data covariance diagonal matrices, $\mathbf{C_d}^{RMT}$ and $\mathbf{C_d}^{ERT}$, are close to the true ones, there is a certain danger of obtaining either a badly resolved model or an unstable model, when iterating to an nRMS value of one for the re-weighted system. Hence, the desired nRMS error value should be adopted according to the chosen weighting factors [93].

Let total number of data be $N_d = N_{RMT} + N_{ERT}$, where $N_{RMT}$is the number of the data points in RMT and N_{ERT} is the number of the data points in ERT. The weights of ERT data are re-weighted by a constant factor, g_w, while that of RMT data are unity. The desired $nRMS^{opt}$ was chosen as,

$$nRMS^{opt} = \sqrt{\frac{1}{N_{RMT} + N_{ERT}} \left\{ N_{RMT} + g_w^2 N_{ERT} \right\}}. \tag{6.5.2}$$

After re-weighting the error bars in data values change and the desired nRMS error value gets modified automatically. To define the optimal set of parameters for the field data experiment 3D inversion of synthetic data from a canonical synthetic model was performed using the algorithm *AP3DMT-DC*.

6.6 3D Synthetic Experiment

The canonical model used for generating synthetic data consists of two blocks, of resistivities 10 Ωm and 1000 Ωm (Fig. 6.3). The background half-space resistivity was 100 Ωm. Such a canonical model is optimal to investigate the resolution and convergence of ERT and RMT in a joint inversion scheme. Each block had a dimension 60 × 30 × 15.4 m. These blocks were placed at a distance of 20 m from each other in y- direction. The tops of both the blocks were 5.4 m below the surface. The model was discretized into 36 × 36 × 20 cells with horizontal cell dimensions being 5 m each. For vertical discretization, the first grid line was at a distance of 1 m from surface. Each subsequent spacing was increased by a factor of 1.2, extending up to 1 km. A total of 24 cells were padded around the central region, six in each horizontal direction with increasing width. With this grid, the dimension of the model domain became 2 × 2 × 1 km in x-, y- and z- directions respectively. The true model, in the form of depth slices, is shown in the first column of Fig. 6.3.

The synthetic responses of ERT and RMT data were computed using the codes *Res3DMod* Loke [123] and *ModEM* Kelbert et al. [99] respectively. For inversion, a homogeneous model of 100 Ωm was used as an initial guess model.

For ERT data the apparent resistivity response was generated. The inter-electrode spacing was 5 m in the profile direction and the spacing between two profiles was 10 m, same as in case of RMT data. 5 % Gaussian noise was added to the computed response. These noisy data were inverted and the nRMS error value reduced, in 26 iterations, from 9.90 to 1.03. The inverted model, in the form of depth slices, is shown in the second column of Fig. 6.3.

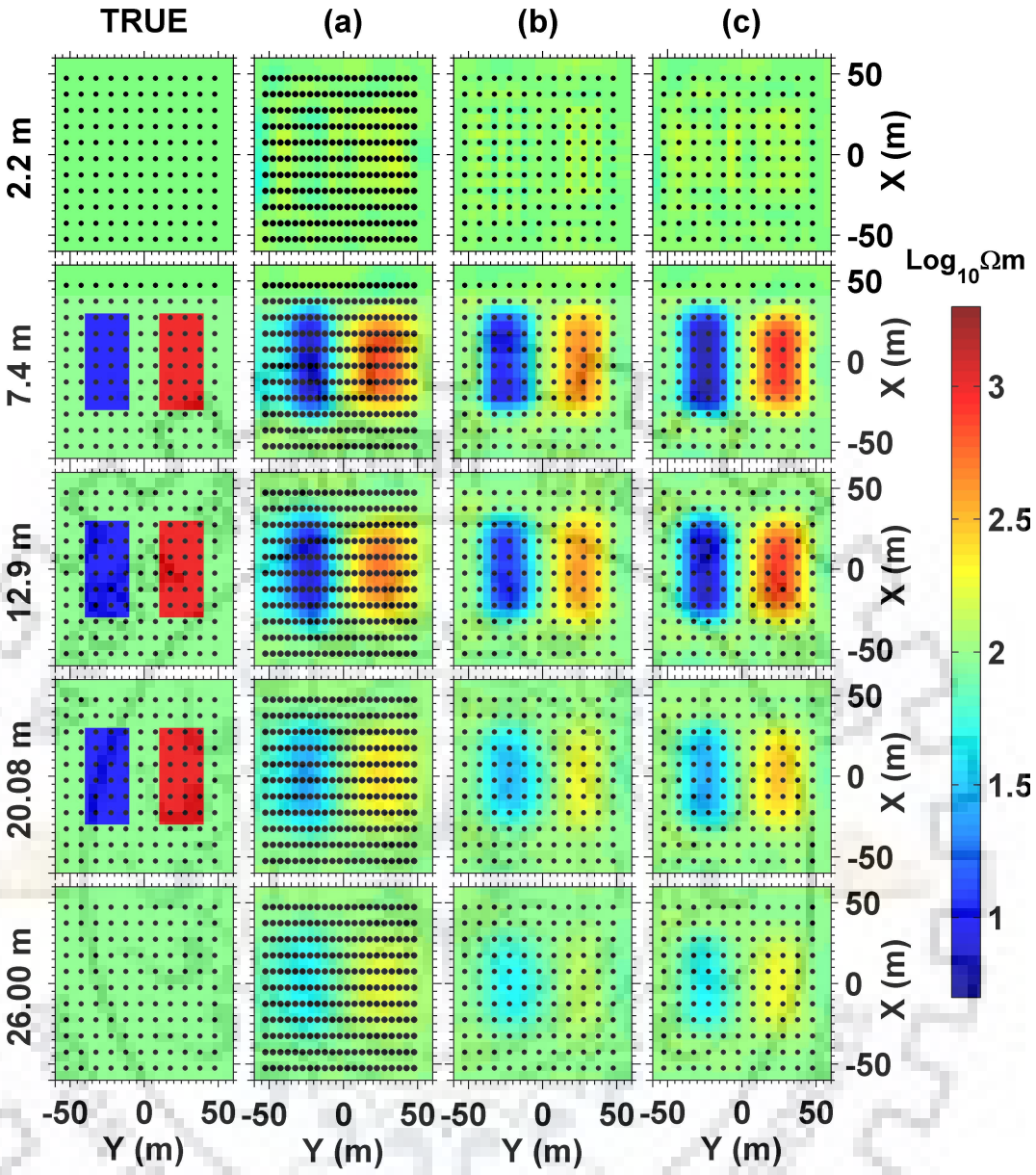

Figure 6.3: Depth sections of 3D inverted resistivity model from data generated from synthetic 3D model. True model depth section is shown in first column along with inverted models from, (a) RMT data, (b) ERT data and (c) model from joint inversion of ERT and RMT data.

For RMT data, the off-diagonal resistivity and phase responses were generated for 12 time periods spaced logarithmically in the range 10^{-6}-10^{-4} s. The RMT stations were placed on 11 profiles with 11 stations in each profile and with an inter-station spacing of 10 m Fig. 6.3. 5 % Gaussian noise was added to the computed response. These noisy data were inverted and the nRMS error value reduced, in 46 iterations, from 9.84 to 1.10. The inverted model, in the form of depth slices, is shown in the third column of Fig. 6.3. From the second

and third columns of Fig. 6.3, it can be seen that the depth to the bottom of conductive block was better resolved by RMT inversion while the resistivity of the resistive block was better resolved in ERT data inversion.

Lastly, the joint inversion of the ERT and RMT datasets was performed using the same data and model parameters as in the individual inversions. Since, norm of the gradient of RMT data was larger, up-weighting was done for ERT data by a factor of 3.40 (using eq 6.5.1). The new target nRMS error value was found to be 1.1613 (using eq 6.5.1). In the joint inversion, the nRMS error value reduced, in 56 iterations, from 15.73 to 1.68. The inverted model, in the form of depth slices, is shown in the fourth column of Fig. 6.3. Fig. 6.4 shows the misfit plot of the off-diagonal components of apparent resistivity and phase for selected stations of RMT data. The misfit plot for ERT data, in the form of a pseudosection, for the profile at x = -2.50 m, is shown in Fig. 6.5.

The joint inversion of ERT and RMT data resolved correctly both the resistivity and geometry of the two blocks. This study clearly shows the advantage of performing 3D joint inversions of ERT and RMT data.

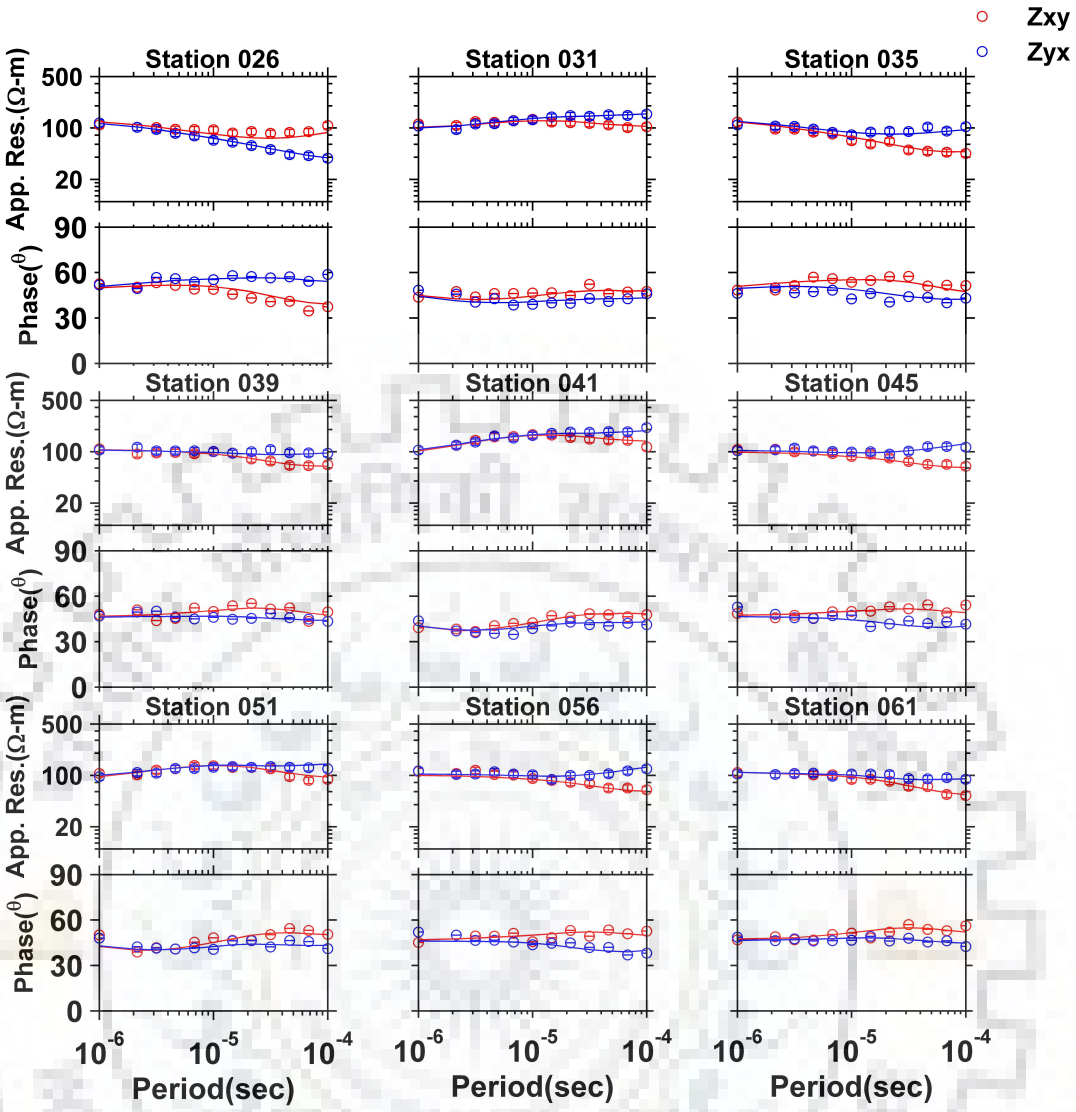

Figure 6.4: Misfit plot of off-diagonal components of apparent resistivity and phase. Red and blue circles represent the observed data whereas red and blue lines represent computed data for the inverse model.

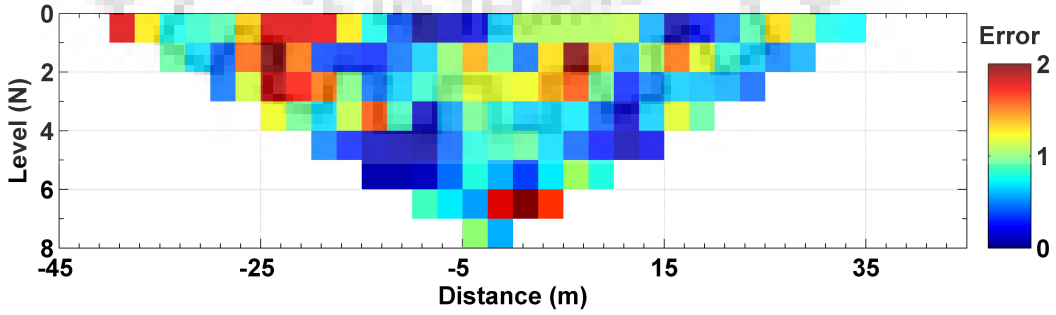

Figure 6.5: Misfit plot of apparent resistivity of ERT data, in the form of pseudosection, for profile at x = -2.50 m.

6.7 Field Data Inversion

The field ERT and RMT data, acquired on various profiles, were inverted individually and jointly for the contaminated region as well as for the uncontaminated reference profile, 'R03'.

The data for five ERT profiles (PR02-PR08), recorded near the waste disposal site in Saliyar village were inverted using the 3D inversion code *AP3DMT-DC*. Location of these profiles is shown in Fig. 6.2. Model grids were designed on the basis of inter-electrode spacing, profile length and electrode configuration used for measurements. Accordingly, the dimension of the model domain becomes 2755 $\times$ 2880 $\times$ 400 m in x-, y- and z- directions respectively. A total of 24 cells were padded around the central region of the model, six in each horizontal direction with the distance increasing by a factor of two. Care was taken to ensure that at least two grid lines exist between the consecutive electrodes. The grid line spacing used in the central region of the model was 2.5 m for x- direction (profile direction). For y- direction (perpendicular to profiles), the grid line spacing was 7.5 m around the profiles while it was enhanced to 15 m in the middle of two consecutive profiles. Thus, in the central region there were 95 $\times$ 36 $\times$ 17 cells in x-, y- and z- directions respectively. Below the surface, the first grid line spacing was 1.0 m and the spacing of each subsequent grid line was increased by a factor of 1.15. The initial guess model was chosen to be a homogeneous half space of 34 Ωm (average of the observed apparent resistivity values). The total number of data points in Wenner and Schlumberger array configurations were 1413 and 3044 respectively. Data type and convergence parameters for all the inversion runs are given in Table 6.2. The inverted resistivity models for Wenner and Schlumberger configurations, in the form of X-Y profile depth sections, showing depth wise resistivity variation, are shown in Fig. 6.6 and 6.7 respectively. Similarly, 3D inversion was performed for the ERT data of reference profile, 'R03'. The models obtained from Wenner and Schlumberger array configurations for this profile are shown at surface location 600 m in Fig. 6.6 and 6.7 respectively. This 2D depth section for Wenner array along with the corresponding depth section obtained by Yogeshwar et al. [258] are shown in Fig. 6.9(b) and 6.9(a) respectively.

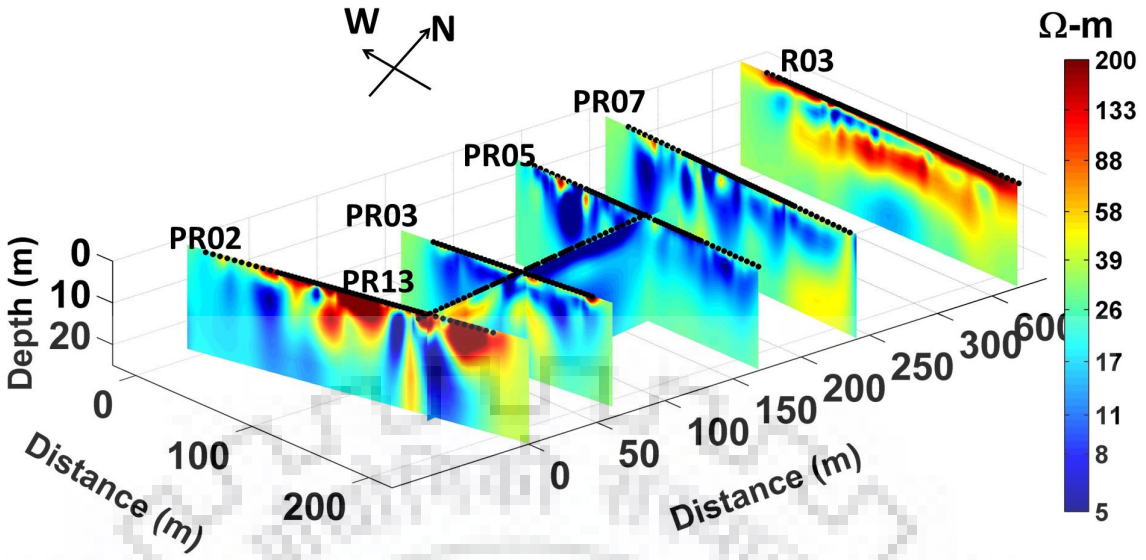

Figure 6.6: Depth sections of resistivity model obtained from 3D inversion of Wenner array configuration, ERT data, for five profiles in contaminated zone and one reference profile, 'R03'.

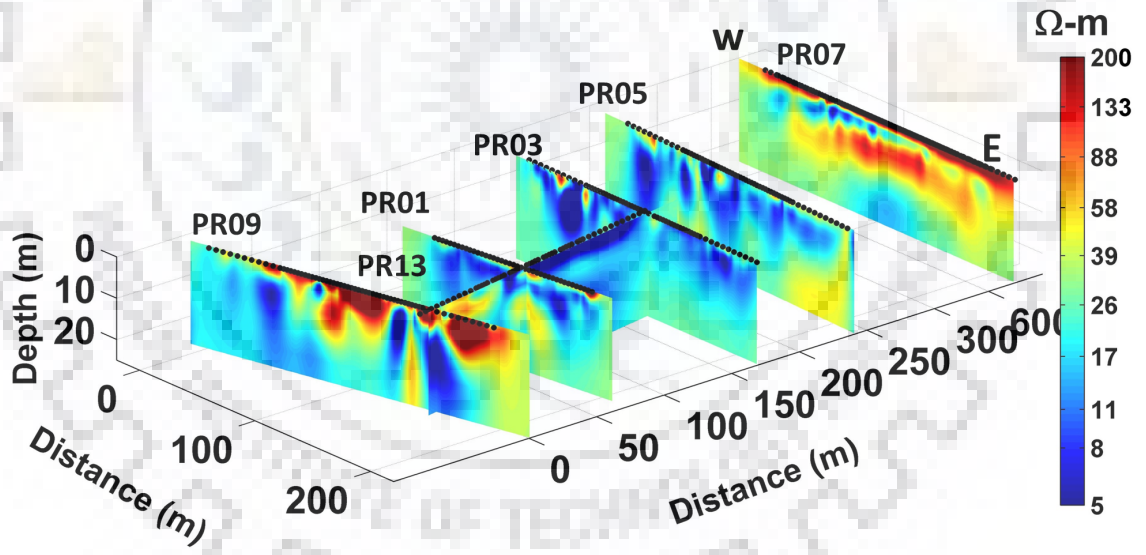

Figure 6.7: Depth sections of resistivity model obtained 3D inversion of Schlumberger array configuration for five profiles in contaminated zone and one reference profile, 'R03'.

Table 6.2: Data type, error floor and convergence parameters for all the 3D inversion runs on recorded data.

Data Type	Error Floor (%)		Starting	Final	No. of
	Apparent	Phase	nRMS	nRMS	iterations
ERT(5 profiles) Wenner array	5	-	14.67	1.89	64
ERT(5 profiles) Schlumberger array	5	-	40.00	2.67	51
ERT(R03 profile) Wenner array	5	-	4.67	1.45	55
ERT(R03 profile) Schlumberger array	5	-	4.29	1.55	56
RMT (9 profiles)	5	2.5	35.73	3.03	59
RMT (9 profiles)	10	10	17.76	1.19	73
RMT (R03 profile)	5	2.5	18.60	2.26	69
ERT+RMT (5+9 profiles)	5	2.5	20.05	2.46	109
ERT+RMT (R03 profile)	5	2.5	21.20	2.49	103

The RMT data, recorded on nine profiles with inter-station spacing of 10 m and inter profile spacing of 35 m, were inverted. The RMT data comprise off-diagonal components of resistivity and phase for 20 time periods in the period range $1.05\text{x}10^{-6}$-8.33x^{-5} s. The number of periods varies at each station due to the limitations in availability of transmitter frequency during the recording. However, 5 to 6 periods were used for inversion at each station. The initial guess model was a homogeneous half space of 34 Ωm, same as in the case of ERT data. The model parameters were also kept same as in the case of ERT data

inversion. The inverted model, in the form of X-Y profile depth sections, showing depth wise subsurface resistivity variations, is shown in Fig. 6.8. Similarly, the 3D inversion was performed on the RMT data for the reference profile 'R03' and the depth section for its inverted model is shown at surface location 600 m in Fig. 6.8. This 2D depth section along with the corresponding 2D depth section obtained by Yogeshwar et al. [258] are shown in Fig. 6.9(d) and 6.9(c) respectively.

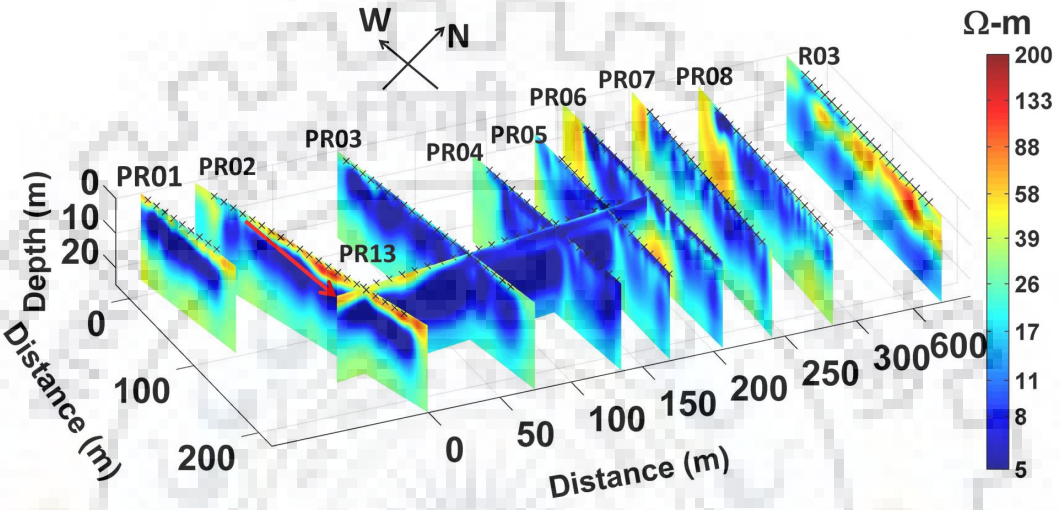

Figure 6.8: Depth sections of 3D inverted resistivity model obtained from RMT data for nine profiles in contaminated zone and one reference profile.

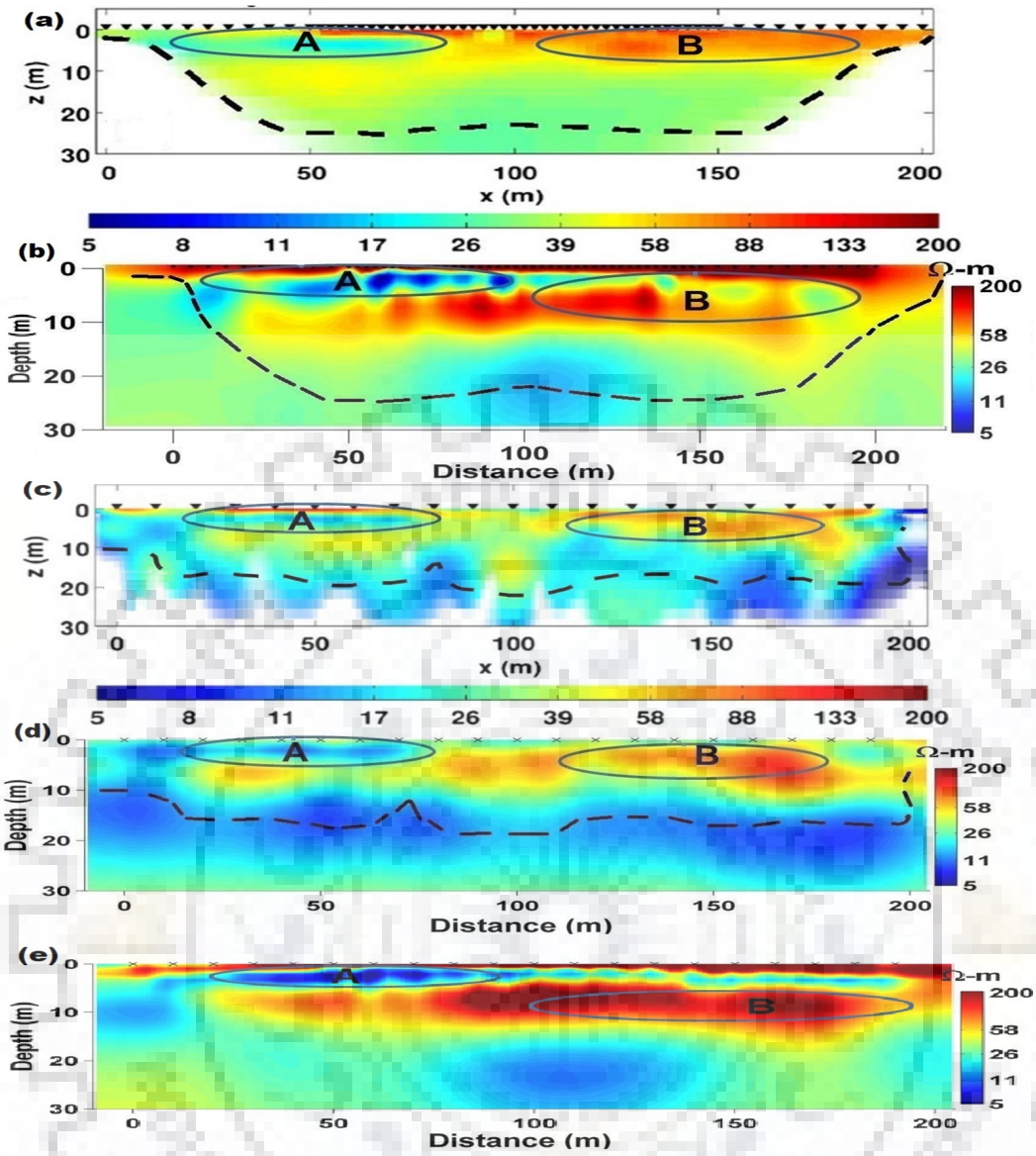

Figure 6.9: A comparison of 3D inverted model with the corresponding 2D inversion for reference profile 'R03' as from, (a) 2D inversion of ERT data by Yogeshwar et al. [258],(b) 3D inversion of ERT data using *AP3DMT-DC*, (c) 2D inversion of TM mode of RMT data by Yogeshwar et al. [258], (d) 3D inversion of RMT data using *AP3DMT-DC* and (e) 3D joint inversion of ERT and RMT data using *AP3DMT-DC*.

After performing 3D inversion of ERT and RMT data individually the joint inversion of ERT and RMT data was performed. The total data points for ERT and RMT methods were 1413 and 2823 respectively. The norm of the gradient of RMT data was found to be larger so an up-weighting was done for ERT data by a factor of 1.63. Accordingly, the target nRMS error value was also modified to 1.10. To maintain consistency, the inversion control parameters, model dimension and discretization were kept same as in the case of individual

data inversions. The inverted model, in the form of X-Y profile depth sections, showing depth wise subsurface resistivity variations, is shown in Fig. 6.10. Fig. 6.11 shows the misfit plot for apparent resistivity of ERT data for the profile PR05, in the form of pseudosection. Fig. 6.12 shows the misfit plot of the off-diagonal components of apparent resistivity and phase for a single station of each RMT profile.

The joint inversion of ERT and RMT data for the reference site was done using the same set of parameters as in case of individual inversion. However, in view of higher norm of the gradient of RMT data, the ERT data were up-weighted by a factor of 6.73. The depth section for the inverted model is shown at surface location 600m in Fig. 6.10 and in Fig. 6.9(e).

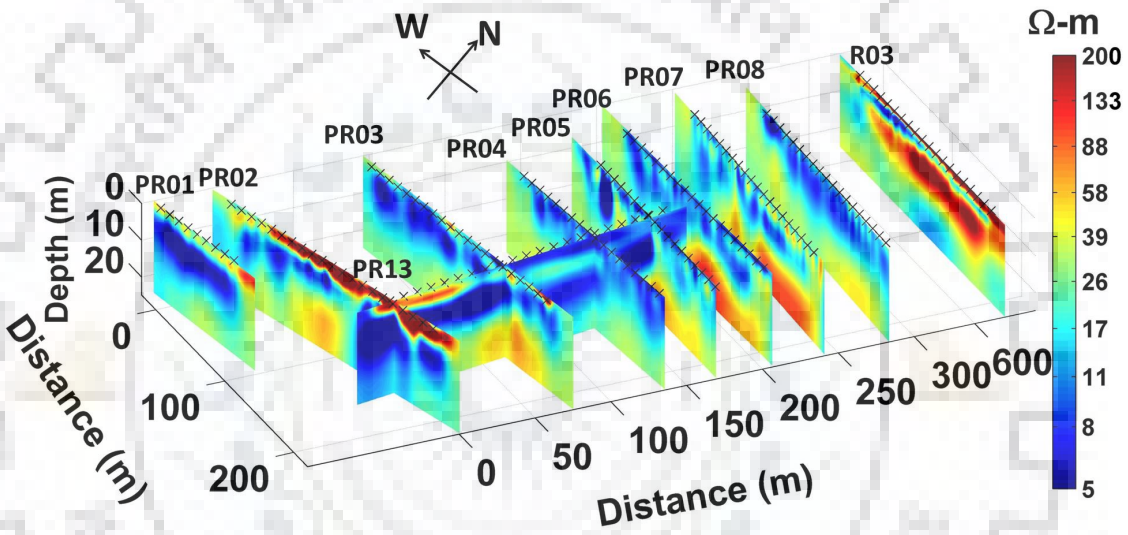

Figure 6.10: Depth sections of 3D inverted resistivity model obtained from joint inversion of ERT and RMT data for (5+9) profiles in contaminated zone and reference profile.

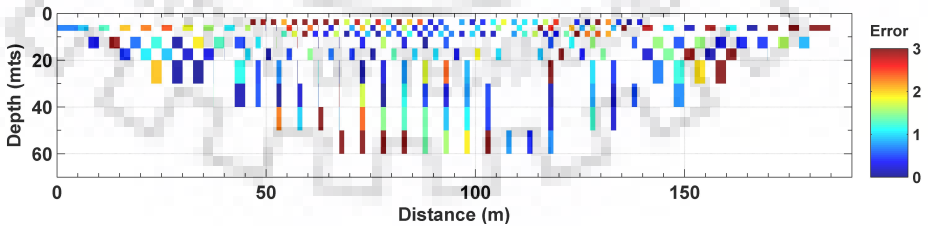

Figure 6.11: Misfit plot of apparent resistivity of ERT data, for profile PR05, shown in the form of pseudosection.

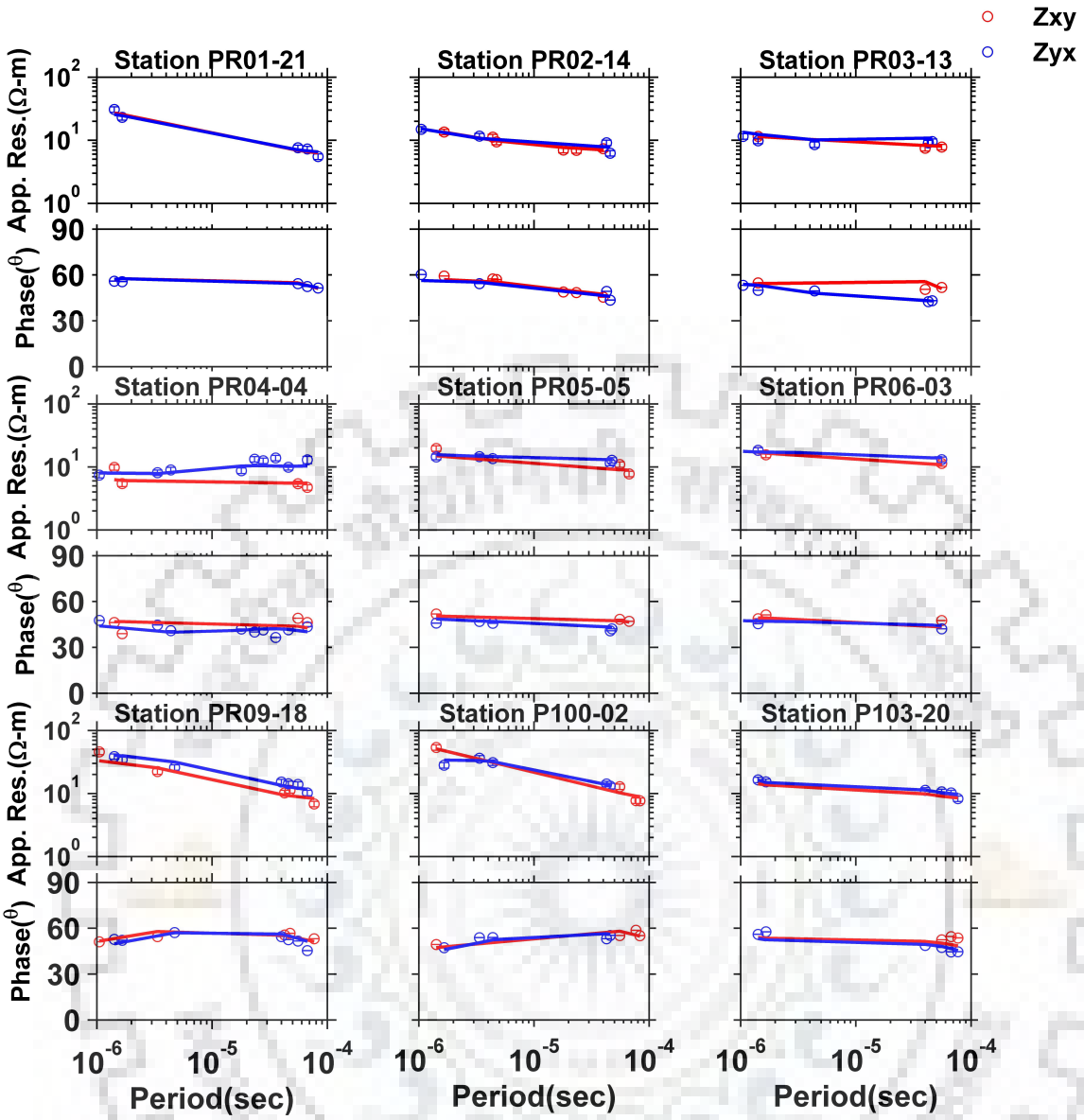

Figure 6.12: Misfit plot of off-diagonal components of apparent resistivity and phase for selected stations of field RMT data. Red and blue circles represent the observed data whereas red and blue lines represent computed data for the inverted model.

The significance of the features present in various inverted models is discussed below.

6.8 Discussion of Results

Geologically, the study area consists of alluvial sediments of recent age, deposited by the Himalayan Rivers. Solani River, a tributary of Ganga River, flows in southeast direction in the studied region. It is influencing the local geohydrology and groundwater flow. On the basis of groundwater table elevation contour maps, Singhal et al. [206] estimated that

the groundwater flow in studied region is also in southeast direction. The untreated sewage water from old Roorkee was pumped to the sewage farm in Saliyar village and it was being used for irrigation in agriculture.

The inverted model sections, obtained from ERT data recorded using Wenner configuration, are shown in Fig. 6.6. Of the six depth sections, five correspond to the region around the waste disposal site, while the sixth depth section corresponds to the uncontaminated reference profile. The inverted model for the reference profile, 'R03', shows a top thin (≈1m thick) resistive layer corresponding to the dry surface fine sand layer. It is underlain by a low resistivity/conductive layer, representing the upper unconfined aquifer zone. Resistivity depth sections, obtained from the data on profiles near the waste disposal site, have low resistivity values right from the surface. This indicates the presence of contamination in groundwater due to the sewage water irrigated agriculture field. In the depth section of profile PR02, high resistivity of the near surface zone is a result of artificial landfill unsaturated soil. Studies like, Bhatnagar et al. [25], Singhal et al. [206] and Kamboj et al. [94] did chemical analysis around the area and supports the contamination. These studies show high value of Total Dissolved Solids (TDS) (e.g. 847 mg/l), total solids (987.45 mg/l), Nitrogen, Bicarbonate and heavy metals (Cd, Cr, Mn and Pb), which indicates contamination in the study area. Table 6.3 shows the value of heavy metal concentration near the waste disposal sites and the WHO standards IS:10,500.

Table 6.3: Physiochemical and heavy metals analysis on untreated sewage water irrigated site by Bhatnagar et al. [25] and Singhal et al. [206].

Metal/ Researcher	**TDS** (mg/l)	**Ca $^{++}$** (mg/l)	**Mg** (mg/l)	**Cr** (mg/l)	**Fe** (mg/l)	**M** (mg/l)	**Pb** (mg/l)
Bhatnagar et al. [25]	1154	126	80.9	0.57	7.1	1.010	0.210
Singhal et al. [206]	1700	196.4	122.72	0.27	0.044	0.594	0.294
WHO standards	1000	100	50	0.50	1.00	0.100	0.100

The depth sections of the inverted model, obtained from inversion of RMT data recorded on the 10 profiles, are shown in Fig. 6.8. Of these 10 depth sections, nine correspond to the region around the waste disposal site, while the tenth depth section corresponds to the

uncontaminated reference profile, 'R03'. The depth sections for profiles PR01 and PR02 show a resistive ($>$ 100 Ωm) thin dry soil layer which is underlain by a conductive ($<$ 10 Ωm) thick zone corresponding to the contaminated upper unconfined aquifer. In the depth sections for profiles PR03-08, the conductive ($<$10 Ωm) layer is prominently visible right from the surface. The southeast direction of groundwater flow is indicated by an increase in the depth of water table elevation in southeast and it is shown by a red arrowhead line in the depth section for profile PR02 in Fig. 6.8.

Fig. 6.9 shows five inverted depth sections for the reference profile 'R03'. Three of these are obtained by 3D individual and joint inversions of ERT and RMT data (Fig. 6.9(b, d & e)). The remaining two depth sections are obtained from individual 2D inversion of ERT and RMT data performed by Yogeshwar et al. [258] (Fig. 6.9(a & c). In all these depth sections, near the surface ($<$ 10 m), there exists a low resistivity (15-25 Ωm) zone labeled by character 'A' and a high resistivity (60 -200 Ωm) zone labeled by character 'B'. These two zones vary, to some extent, in their geometry and resistivity value in the different depth sections. The low resistivity zone, 'A', represents a water saturated region comprising upper unconfined aquifer layer. Whereas, the high resistivity feature, 'B', represents the presence of unsaturated coarser material with gravels. Below a depth of 10 m lies the saturated layer (resistivity 12-40 Ωm) of unconfined aquifer. This zone is visible more clearly in the inverted model obtained from RMT data (Fig. 6.9(d)).

Results from synthetic example (Fig. 6.3) suggest that the resistivity values and geometry of the low and high resistivity features are together best revealed by the joint inversion of ERT and RMT data. Therefore, the inverted model obtained from joint inversion of ERT and RMT recorded data was preferred model.

The 3D inverted model obtained after joint inversion of the five ERT and nine RMT profiles and one reference profile is shown in Fig. 6.10. In this resistivity model a thin resistive (100-200 Ωm) layer, representing the unsaturated top soil, is clearly visible in depth sections of profiles PR01 and PR02. Whereas, the resistive layer in the depth section under profile R03 represents the fine dry sand. The depth sections for profiles in sewage irrigated agriculture field show a conductive ($<$10 Ωm) layer right from the surface. There are some localized high resistivity pockets in depth sections of profiles PR03 and PR07 and these correspond to large size boulders or dry zone. The entire unconfined aquifer in the area seems to be affected by contamination due to the untreated sewage water irrigation.

The horizontal (X-Y) slices, extracted at five different depths from the 3D models obtained from the two individual and the joint inversion of ERT, RMT data, are shown in Fig. 6.13. For the joint inversion, the X-Y slices show an absence of low resistivity at deeper depths ($>$ 16 m), indicating that the contaminated water is not reaching beyond a depth of 16 m. It is due to the presence of non-permeable layer below the unconfined-aquifer. The high resistivity below the unconfined layer is due to the presence of gravel and coarser material in clay.

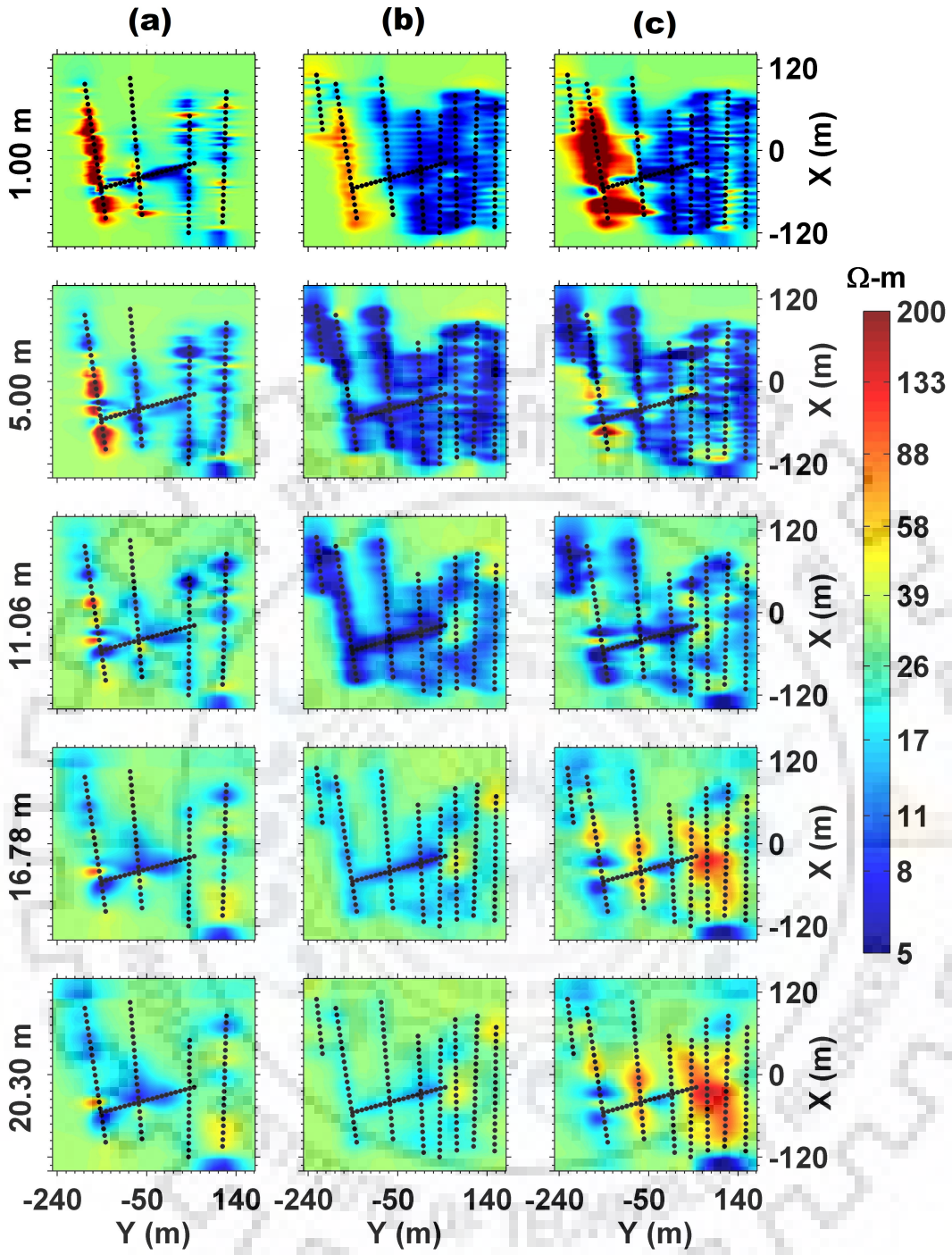

Figure 6.13: Depth sections of 3D inverted resistivity model from (a) ERT data, (b) RMT data and (c) for joint inversion of ERT and RMT data from contaminated zone.

6.9 Summary of Results

The ERT and RMT data recorded near the waste disposal site in Saliyar village, Roorkee were interpreted using a 3D inversion technique. For this purpose, the recently developed 3D joint inversion code, *AP3DMT-DC*, was used for individual and joint inversion of ERT and RMT field data. To define the optimal values of inversion control parameters the code was used on a canonical synthetic model. The 3D joint inversion reconstructs the synthetic model most accurately in terms of geometry and resistivity. Both, the individual and joint 3D inversion of the field data converge to an almost optimal fit at a rather similar speed for both the methods. The 3D inverted depth sections are consistent within themselves and also with the corresponding 2D inversion results. The derived models are compatible with the general hydrogeological understanding of the area. The 3D resistivity depth sections from joint inversion show a low resistivity, upto a depth of 16 m, representing an upper unconfined aquifer which is very likely affected by the groundwater contamination. The resistivity increases after a depth of 16 m indicating that the contamination is not penetrating beyond this depth. The 3D resistivity model obtained by the joint inversion of ERT and RMT data better explains the resistivity variation and geometry of all the features than the models obtained by individual inversions.

Chapter 7

CONCLUSIONS

The Magnetotelluric (MT), Radio Magnetotelluric (RMT), and Direct Current Resistivity (DCR) data were interpreted using a recently developed 3D inversion algorithm *AP3DMT-DC*. For this purpose, the data recorded by our group (MT group at IIT Roorkee) prior to the onset of this study were integrated with the data recorded during the present study. Based on the nature of problem studied, the entire dataset is divided into four subsets, (i) MT data recorded at 39 sites in Garhwal Himalayan Corridor (GHC), Roorkee to Gangotri (RG) profile, (ii) MT data recorded at 28 sites in and around MCT zone in Chamoli region, (iii) DCR data recorded at six profiles near a proposed bridge site in Tehri region and (iv) Data along 10 DCR and six RMT profiles recorded around Roorkee region. All the four studied regions are located in Uttarakhand, India. This is the first study in which 3D inversion is implemented on the MT data recorded from Uttarakhand, India.

Extensive 3D inversion experiments were carried out to validate the inverted models obtained from these datasets. In first two MT studies, the geoelectrical models were interpreted in terms of geological tectonics and seismological information available in the studied regions. In the third study the geoelectrical model was interpreted for geotechnical characterization of the region. In the fourth study, the shallow subsurface model obtained from DCR and RMT data was interpreted, in terms of hydrogeological characteristics of the region, to evaluated groundwater contamination due to waste disposal and untreated sewage water irrigation. Major conclusions of these studies are listed below.

7.1 Conclusions of MT Studies

Resistivity depth model obtained from 3D inversion of RG profile reveals new off-profile resistivity structures, aligned transverse to the main Himalayan arc and are termed as the transverse tectonic features. The new features, delineated in the 3D resistivity model [57], are robust, geologically meaningful and consistent with the regional tectonics and 3D velocity model Kanaujia et al. [95] of the region. The model defines the geometry of Delhi Haridwar Ridge (DHR) beneath Indo-Gangetic Plain (IGP), Sub Himalaya (SH) and Lesser Himalaya (LH) in Garhwal Himalayan region. The model also suggests that DHR is a fault bounded structure. The faults bounding DHR are reflected in the model as low-resistivity zones running nearly parallel to DHR. The model also supports the *flat ramp flat* geometry of Main Himalayan Thrust (MHT) and is consistent with the seismological and other geophysical models of the region.

The inverted 3D resistivity depth model from Chamoli region delineated two doublets each comprising a low and high resistivity regions. The low resistivity ($<$10 Ωm) region in the doublet represents a fluid saturated fracture zone while the high resistivity ($>$500 Ωm) region represents the brittle rigid rocks. The low resistivity features are interpreted to be a result of the fluids present in deeper depths. These fluids were generated by metamorphic dehydration and pushed upward through the fractured zones. The model correlates well with the velocity model obtained from the seismic tomography studies [129, 154]. The doublet view point is consistent with the low-high velocity converters defined in the seismic tomography study by Mahesh et al. [129]. The resistivity model also explains the role of fluid in triggering the medium and large size earthquakes in the region. The resistivity model explains the high heat flow and the presence of thermal springs in the area.

7.2 Conclusions of DCR Studies

The Direct Current Resistivity (DCR) investigations at a bridge site in Tehri region are used for electrical characterization of the near surface soil. Electrical Resistivity Tomography (ERT) profiles were correlated with borehole and Soil Penetration Test (SPT) data. A linear correlation between electrical resistivity and N-values, derived from SPT data, has been inferred. This relationship will be very useful, especially in Himalayan region, for future

geotechnical investigations.

The three resistivity depth models, obtained from 3D inversion of DCR and RMT data individually and jointly, were consistent. Of the three models, the joint model was found to be the most revealing one. It reveals the shallow subsurface electrical nature of soil, water saturation and the extent of groundwater contamination in Roorkee region of Uttarakhand, India. It shows an unconfined aquifer of low resistivity overlain by a slightly resistive near surface unsaturated formation. Moving away from the waste disposal site, an increase is observed in resistivity of the shallow unconfined aquifer indicating an undisturbed geology. The flow direction of contaminated water is nearly parallel to Solani River.

7.3 Scope for Future Research

The present study opens-up the scope of a detailed 3D MT studies in Himalayan region with dense data coverage in potentially hazardous zones. Following 3D MT investigations can be initiated in near future.

(i) 3D MT investigations in Garhwal Himalayan region by adding more MT sites in lateral direction. MT sites may be added between two profiles (Roorkee-Gangotri and Bijnaur-Malari) and full 3D inversion of the entire dataset is recommended. The dense data coverage will be helpful in understanding the electrical variability along and perpendicular to Himalayan arc.

(ii) Topography correction feature may be added in the existing 3D inversion code. Using this updated code, the present dataset may be re-inverted to study the 3D topography effect.

(iv) DCR and RMT studies can be used more frequently for geotechnical studies and for monitoring the flow of groundwater in potentially hazardous zones.

BIBLIOGRAPHY

[1] Akinlabi, I. and Adeyemi, G. (2014). Determination of Empirical Relations between Geoelectrical Data and Geotechnical Parameters in Foundation Studies for a proposed Earth Dam. *The Pacific Journal of Science and Technology*, 15(2):279–287.

[2] Amatyakul, P., Boonchaisuk, S., Rung-Arunwan, T., Vachiratienchai, C., Wood, S. H., Pirarai, K., Fuangswasdi, A., and Siripunvaraporn, W. (2016). Exploring the shallow geothermal fluid reservoir of fang geothermal system, Thailand via a 3-D magnetotelluric survey. *Geothermics*, 64:516–526.

[3] Amatyakul, P., Vachiratienchai, C., and Siripunvaraporn, W. (2017). WSJointInv2D-MT-DCR: an efficient joint two-dimensional magnetotelluric and direct current resistivity inversion. *Computers & Geosciences*, 102:100–108.

[4] Archie, G. E. (1942). The electrical resistivity log as an aid in determining some reservoir characteristics. *Transactions of the AIME*, 146(01):54–62.

[5] Argote-Espino, D. L., López-García, P. A., and Tejero-Andrade, A. (2016). 3D-ERT geophysical prospecting for the investigation of two terraces of an archaeological site northeast of Tlaxcala state, Mexico. *Journal of Archaeological Science: Reports*, 8:406–415.

[6] Arora, B. and Adam, A. (1992). Anomalous directional behaviour of induction arrows above elongated conductive structures and its possible causes. *Physics of the earth and planetary interiors*, 74(3-4):183–190.

[7] Arora, B., Gahalaut, V., and Kumar, N. (2012). Structural control on along-strike variation in the seismicity of the northwest Himalaya. *Journal of Asian Earth Sciences*, 57:15–24.

[8] Arup, S., Ashwani, K., Gupta, S., and Arjun, K. (2014). Spectral Analysis of the Earthquake Sources around Roorkee (India) Region and its surrounding Indo-Gangetic Plains. *Disaster Advances*, 7(6):1–11.

[9] Auden, J. (1935). Transverses in the Himalaya. *Rec. Geol. Surv. India*, 69(2):123–167.

[10] Avdeev, D. and Avdeeva, A. (2009). 3D Magnetotelluric inversion using a limited-memory quasi-Newton optimization. *Geophysics*, 74:F45–F57.

[11] Avdeeva, A., Moorkamp, M., Avdeev, D., Jegen, M., and Miensopust, M. (2015). Three-dimensional inversion of magnetotelluric impedance tensor data and full distortion matrix. *Geophysical Journal International*, 202(1):464–481.

[12] Azeez, K. A. (2016). Magnetotelluric Constraints on the Occurrence of Lower Crustal Earthquakes in the Intra-plate Setting of Central Indian Tectonic Zone. *Acta Geologica Sinica-English Edition*, 90(3):884–899.

[13] Azeez, K. A., Mohan, K., Veeraswamy, K., Rastogi, B., Gupta, A. K., and Harinarayana, T. (2018). 3D crustal resistivity structure beneath the Wagad aftershock zone of the 2001 Bhuj earthquake, Kutch, India: heterogeneous resistivity structure controlled by widespread fluid infiltration and clues to aftershocks pattern. *Tectonophysics*, 747:54–67.

[14] Azeez, K. A., Patro, P. K., Harinarayana, T., and Sarma, S. (2017). Magnetotelluric imaging across the tectonic structures in the eastern segment of the Central Indian Tectonic Zone: preserved imprints of polyphase tectonics and evidence for suture status of the Tan Shear. *Precambrian Research*, 298:325–340.

[15] Bahr, K. (1988). Interpretation of the magnetotelluric impedance tensor: regional induction and local telluric distortion. *J. Geophys*, 62(2):119–127.

[16] Bahr, K. (1991). Geological noise in Magnetotelluric data: a classification of distortion types. *Physics of the Earth and Planetary Interiors*, 66:24–38.

[17] Bai, D., Unsworth, M. J., Meju, M. A., Ma, X., Teng, J., Kong, X., Sun, Y., Sun, J., Wang, L., Jiang, C., et al. (2010). Crustal deformation of the eastern Tibetan plateau revealed by magnetotelluric imaging. *Nature geoscience*, 3(5):358.

[18] Bansal, B. K. and Verma, M. (2012). The m 4.9 Delhi earthquake of 5 March 2012. *Curr Sci*, 102(12):1704–1708.

[19] Barker, R. (1981). The offset system of electrical resistivity sounding and its use with a multicore cable. *Geophysical prospecting*, 29(1):128–143.

[20] Becken, M. and Ritter, O. (2012). Magnetotelluric studies at the San Andreas Fault Zone: implications for the role of fluids. *Surveys in Geophysics*, 33(1):65–105.

[21] Becken, M., Ritter, O., Park, S. K., Bedrosian, P. A., Weckmann, U., and Weber, M. (2008b). A deep crustal fluid channel into the San Andreas fault system near Parkfield, California. *Geophysical Journal International*, 173:718–732.

[22] Begum, S. K. and Harinarayana, T. (2016). Basement Configuration from Magnetotelluric Studies in Bhuj Earthquake Epicentral Zone, Gujarat, India. *Open Journal of Earthquake Research*, 5(03):177.

[23] Beka, T. I., Smirnov, M., Birkelund, Y., Senger, K., and Bergh, S. G. (2016). Analysis and 3D inversion of magnetotelluric crooked profile data from central Svalbard for geothermal application. *Tectonophysics*, 686:98–115.

[24] Berdichevsky, M. N. and Dmitriev, V. I. (2010). *Models and methods of magnetotellurics*. Springer Science & Business Media.

[25] Bhatnagar, R., Joshi, H., and Singhal, D. (2004). Environmental evaluation of sewage irrigation system, Roorkee, India. *Journal of Environmental Hydrology*, 12.

[26] Bhattacharya, B. and Shalivahan, S. (2016). *Geoelectric Methods: Theory and Application*. New Delhi, India: McGraw Hill Education (India) Pvt. Ltd.

[27] Bhattacharya, B. B. and Shalivahan (2002). The electric moho underneath Eastern Indian Craton. *Geophysical Research Letters*, 29(10):14–1.

[28] Bing, Z. and Greenhalgh, S. A. (2001). Finite element three dimensional direct current resistivity modelling: accuracy and efficiency considerations. *Geophysical Journal International*, 145(3):679–688.

[29] BIS (2002). The Bureau of Indian Standards Criteria for Earthquake Resistant Design of Structures: Part 1 – General Provisions and Buildings,Fifth Revision (BIS Publication No. IS: 1893 (part 1):200), New Delhi, 2002.

[30] Borah, U. K., Patro, P. K., and Suresh, V. (2015). Processing of noisy magnetotelluric time series from Koyna-Warna seismic region, India: a systematic approach. *Annals of Geophysics*, 58(2):0222.

[31] Braga, A. C., Malagutti F° _, W., Dourado, J. C., and Chang, H. K. (1999). Correlation of electrical resistivity and induced polarization data with geotechnical survey standard penetration test measurements. *Journal of Environmental and Engineering Geophysics*, 4(2):123–130.

[32] Brasse, H. and Eydam, D. (2008). Electrical conductivity beneath the Bolivian Orocline and its relation to subduction processes at the South American continental margin. *Journal of Geophysical Research: Solid Earth*, 113(B7).

[33] Brasse, H., Schäfer, A., Díaz, D., Alvarado, G. E., Muñoz, A., and Mütschard, L. (2015). Deep-crustal magma reservoirs beneath the Nicaraguan volcanic arc, revealed by 2-D and semi 3-D inversion of magnetotelluric data. *Physics of the Earth and Planetary Interiors*, 248:55–62.

[34] Brasse, H. and Soyer, W. (2001). A magnetotelluric study in the Southern Chilean Andes. *Geophysical Research Letters*, 28(19):3757–3760.

[35] Byerlee, J. (1990). Friction, overpressure and fault normal compression. *Geophysical Research Letters*, 17(12):2109–2112.

[36] Cagniard, L. (1953). Basic theory of the magnetotelluric method of geophysical prospecting. *Geophysics*, 18.

[37] Caldwell, T. G., Bibby, H., and Brown, C. (2004). The magnetotelluric phase tensor. *Geophysical Journal International*, 158:457–469.

[38] Caldwell, W. B., Klemperer, S. L., Lawrence, J. F., Rai, S. S., et al. (2013). Characterizing the Main Himalayan Thrust in the Garhwal Himalaya, India with receiver function CCP stacking. *Earth and Planetary Science Letters*, 367:15–27.

[39] Candansayar, M. E. and Tezkan, B. (2008). Two-dimensional joint inversion of radiomagnetotelluric and direct current resistivity data. *Geophysical Prospecting*, 56(5):737–749.

[40] Cantwell, T. (1960). *Detection and Analysis of Low Frequency Magnetotelluric Signals*. PhD thesis, Massachusetts Institute of Technology.

[41] Chambers, J. E., Kuras, O., Meldrum, P. I., Ogilvy, R. D., and Hollands, J. (2006). Electrical resistivity tomography applied to geologic, hydrogeologic, and engineering investigations at a former waste-disposal site. *Geophysics*, 71(6):B231–B239.

[42] Chandrasekhar, E., Ramesh, D., and Biswal, T. (2018). Magnetotelluric evidence on the southward extension of the Eastern Ghats mobile belt from Ongole, India. *Journal of Asian Earth Sciences*, 164:23–32.

[43] Chave, A. D. and Jones, A. G. (2012). *The magnetotelluric method: Theory and practice*. Cambridge University Press.

[44] Chave, A. D. and Smith, J. T. (1994). On electric and magnetic galvanic distortion tensor decompositions. *Journal of Geophysical Research*, 99:4669–4682.

[45] Coggon, J. H. (1971). Electromagnetic and electrical modeling by the finite element method. *Geophysics*, 36(1):132–155.

[46] Commer, M. and Newman, G. A. (2009). Three-dimensional controlled-source electromagnetic and Magnetotelluric joint inversion. *Geophysical Journal International*.

[47] Constable, C. S., Parker, R. L., and Constable, C. G. (1987). Occam's inversion: a practical algorithm for generating smooth models from electromagnetic sounding data. *Geophysics*, 52:289–300.

[48] Coscia, I., Greenhalgh, S. A., Linde, N., Doetsch, J., Marescot, L., Günther, T., Vogt, T., and Green, A. G. (2011). 3D crosshole ERT for aquifer characterization and monitoring of infiltrating river water. *Geophysics*, 76(2):G49–G59.

[49] Cumming, W. and Mackie, R. (2010). Resistivity imaging of geothermal resources using 1D, 2D and 3D MT inversion and TDEM static shift correction illustrated by a Glass Mountain case history. In *Proceedings world geothermal congress*, Bali, Indonesia.

[50] Danda, N. and Rao, C. (2019). Magnetotelluric study to characterize sediment thickness across Kachchh and Cambay rift basins, western India. *CURRENT SCIENCE*, 116(2):299.

[51] Danda, N., Rao, C., and Kumar, A. (2017). Geoelectric structure of northern Cambay rift basin from magnetotelluric data. *Earth, Planets and Space*, 69(1):140.

[52] De Giorgi, L. and Leucci, G. (2018). The archaeological site of Sagalassos (Turkey): exploring the mysteries of the invisible layers using geophysical methods. *Exploration Geophysics*, 49(5):751–761.

[53] Degroot-Hedlin, C. and Constable, S. (1990). Occam's inversion to generate smooth, two-dimensional models from magnetotelluric data. *Geophysics*, 55(12):1613–1624.

[54] Dehiya, R., Singh, A., Gupta, P. K., and Israil, M. (2017a). 3-D CSEM data inversion algorithm based on simultaneously active multiple transmitters concept. *Geophysical Journal International*, 209(2):1004–1017.

[55] Dehiya, R., Singh, A., Gupta, P. K., and Israil, M. (2017b). Optimization of computations for adjoint field and Jacobian needed in 3D CSEM inversion. *Journal of Applied Geophysics*, 136:444–454.

[56] Devi, A., Israil, M., Anbalagan, R., and Gupta, P. K. (2017). Subsurface soil characterization using geoelectrical and geotechnical investigations at a bridge site in uttarakhand himalayan region. *Journal of Applied Geophysics*, 144:78–85.

[57] Devi, A., Israil, M., Gupta, P. K., Varshney, S. K., and Meqbel, N. (2019). Transverse tectonics structures in the Garhwal Himalaya Corridor inferred from 3D inversion of magnetotelluric profile data. *(Pure and Applied Geophysics)*.

[58] Dey, A. and Morrison, H. F. (1979). Resistivity modeling for arbitrarily shaped three-dimensional structures. *Geophysics*, 44(4):753–780.

[59] Di Maio, R., Fabbrocino, S., Forte, G., and Piegari, E. (2014). A three-dimensional hydrogeological–geophysical model of a multi-layered aquifer in the coastal alluvial plain of Sarno River (southern Italy). *Hydrogeology journal*, 22(3):691–703.

[60] Dieter, K., Paterson, N. R., and Grant, F. S. (1969). IP and resistivity type curves for three-dimensional bodies. *Geophysics*, 34(4):615–632.

[61] Egbert, G. D. (2006). Efficient Inversion of Multi-frequency and Multi-Source Electromagnetic Data. In *Final Project Report. College of Oceanic and Atmospheric Sciences,*, Oregon State University, College of Oceanic and Atmospheric Sciences, Oregon State University.

[62] Egbert, G. D. and Kelbert, A. (2012). Computational recipes for electromagnetic inverse problems. *Geophysical Journal International*, 188:251–267.

[63] Eissa, R., Cassidy, N., Pringle, J., and Stimpson, I. (2019). Electrical resistivity tomography array comparisons to detect cleared-wall foundations in brownfield sites. *Quarterly Journal of Engineering Geology and Hydrogeology*, pages qjegh2018–192.

[64] Farquharson, C. G. (2007). Constructing piecewise-constant models in multidimensional minimum-structure inversions. *Geophysics*, 73(1):K1–K9.

[65] Farquharson, C. G. and Miensopust, M. P. (2011). Three-dimensional finite-element modelling of magnetotelluric data with a divergence correction. *Journal of Applied Geophysics*, 75(4):699–710.

[66] Fomenko, E. Y. and Mogi, T. (2002). A new computation method for a staggered grid of 3D EM field conservative modeling. *Earth Planets Space*, 54:499–509.

[67] Friedrichs, B. (2003). Mapros: magnetotelluric data processing software. *Metronix GmbH, Braunschweig, Germany*.

[68] Gahalaut, V. and Arora, B. (2012). Segmentation of seismicity along the Himalayan Arc due to structural heterogeneities in the under-thrusting Indian plate and overriding Himalayan wedge. *Episodes*, 35(4):493–500.

[69] Godin, L. and Harris, L. B. (2014). Tracking basement cross-strike discontinuities in the Indian crust beneath the Himalayan orogen using gravity data–relationship to upper crustal faults. *Geophysical Journal International*, 198(1):198–215.

[70] Gokarn, S., Gupta, G., and Rao, C. (2004). Geoelectric structure of the Dharwar craton from magnetotelluric studies: Archean suture identified along the Chitradurga-Gadag schist belt. *Geophysical Journal International*, 158(2):712–728.

[71] Gokarn, S., Rao, C., Selvaraj, C., Gupta, G., and Singh, B. (2013). Crustal evolution and tectonics of the Archean Bundelkhand craton, Central India. *Journal of the Geological Society of India*, 82(5):455–460.

[72] Gokarn, S. G., Rao, C. K., and Gupta, G. (2002). Crustal structure in the Siwalik Himalayas using magnetotelluric studies. *Earth, planets and space*, 54(1):19–13.

[73] Gomez-Trevino, E. and Edwards, R. (1983). Electromagnetic soundings in the sedimentary basin of southern Ontario-a case history. *Geophysics*, 48(3):311–330.

[74] Gribenko, A., Green, M., Cuma, M., and Zhdanov, M. S. (2010). Efficient 3D inversion of MT data using integral equations method and the receiver footprint approach: application to the large-scale inversion of the EarthScope MT data. In *Expanded Abstracts of the SEG meeting*, page 644–649, Denver, Colorado.

[75] Groom, R. W. and Bailey, R. (1989). Decomposition of magnetotelluric impedance tensors in the presence of local three-dimensional galvanic distortion. *Journal of Geophysical Research*, 94:1913–1925.

[76] GSI (1991). Geothermal Atlas of India.

[77] Günther, T., Rücker, C., and Spitzer, K. (2006). Three-dimensional modelling and inversion of DC resistivity data incorporating topography-II. Inversion. *Geophysical Journal International*, 166(2):506–517.

[78] Gupta, G., Gokarn, S., and Singh, B. (1994). Thickness of the Siwalik sediments in the Mohand-Ramnagar region using magnetotelluric studies. *Physics of the earth and planetary interiors*, 83(3-4):217–224.

[79] Gupta, S., Mahesh, P., Sivaram, K., and Rai, S. (2012). Active fault beneath the Tehri dam, Garhwal Himalaya- seismological evidence. *Current Science*, 103(11):1343–1347.

[80] Haber, E. (2005). Quasi-Newton methods for large scale electromagnetic inverse problem. *Inverse Problem*, 21:305–317.

[81] Haber, E., Ascher, U. M., Aruliah, D. A., and Oldenburg, D. W. (2000). Fast Simulation of 3D Electromagnetic Problems Using Potentials. *Journal of Computational Physics.*, 163:150–171.

[82] Harris, R. A. (1998). Introduction to special section: Stress triggers, stress shadows, and implications for seismic hazard. *Journal of Geophysical Research: Solid Earth*, 103(B10):24347–24358.

[83] Hasan, M., Shang, Y.-j., Jin, W.-j., and Akhter, G. (2019). Investigation of fractured rock aquifer in South China using electrical resistivity tomography and self-potential methods. *Journal of Mountain Science*, 16(4):850–869.

[84] Hatta, K. A., Azahar, S. B., and Osman, S. (2015). Correlation of Electrical Resistivity and SPT-N value from Standard Penetration Test (SPT) of Sandy Soil. In *Applied Mechanics and Materials*, volume 785, pages 702–706. Trans Tech Publ.

[85] Heise, W., Caldwell, T. G., Bibby, H. M., and Bennie, S. L. (2010). Three-dimensional electrical resistivity image of magma beneath an active continental rift, Taupo Volcanic Zone, New Zealand. *Geophysical Research Letters*, 37 (10):art. no. L10301.

[86] Høyer, A.-S., Klint, K., Fiandaca, G., Maurya, P., Christiansen, A., Balbarini, N., Bjerg, P., Hansen, T., and Møller, I. (2019). Development of a high-resolution 3D geological model for landfill leachate risk assessment. *Engineering Geology*, 249:45–59.

[87] IMD (2000). Chamoli Earthquake of March 29, 1999 and its Aftershocks: a Consolidated Document. *Meteorol. Monograph Seism.*, 2:70.

[88] Israil, M., Mamoriya, P., Gupta, P. K., and Varshney, S. (2016). Transverse tectonics feature delineated by modelling of magnetotelluric data from Garhwal Himalaya corridor, India. *Current Science (00113891)*, 111(5).

[89] Israil, M., Tyagi, D., Gupta, P., and Niwas, S. (2008). Magnetotelluric investigations for imaging electrical structure of Garhwal Himalayan corridor, Uttarakhand, India. *Journal of Earth System Science*, 117(3):189.

[90] Jain, A., S, S., and Manickavasagam, R. (2002). Himalayan Collision Tectonics. *Gondwana Res. Group Mem.*, 7(5):114.

[91] Jamal, N. and Singh, N. (2018). Identification of fracture zones for groundwater exploration using very low frequency electromagnetic (VLF-EM) and electrical resistivity (ER) methods in hard rock area of Sangod Block, Kota District, Rajasthan, India. *Groundwater for Sustainable Development*, 7:195–203.

[92] Jones, K. A., Ingham, M. R., and Bibby, H. M. (2008). The hydrothermal vent system of Mount Ruapehu, New Zealand– a high frequency MT survey of the summit plateau. *Journal of Volcanology and Geothermal Research*, 176:591–600.

[93] Kalscheuer, T., De los Ángeles García Juanatey, M., Meqbel, N., and Pedersen, L. B. (2010). Non-linear model error and resolution properties from two-dimensional single and

joint inversions of direct current resistivity and radiomagnetotelluric data. *Geophysical Journal International*, 182(3):1174–1188.

[94] Kamboj, N., Chaubey, A., Kumar, S., and Parasher, C. (2015). Assessment of Physico-Chemical Parameter of Solani River at Roorkee, Uttarakhand, India. *International journal of current research*, 7(6):16670–16673.

[95] Kanaujia, J., Kumar, A., and Gupta, S. (2016). Three-dimensional velocity structure around Tehri region of the Garhwal Lesser Himalaya: constraints on geometry of the underthrusting Indian plate. *Geophysical Journal International*, 205(2):900–914.

[96] Kayal, J., Ram, S., Singh, O., Chakraborty, P., and Karunakar, G. (2003a). Aftershocks of the March 1999 Chamoli earthquake and seismotectonic structure of the Garhwal Himalaya. *Bulletin of the Seismological Society of America*, 93(1):109–117.

[97] Kayal, J., Ram, S., Singh, O., Chakraborty, P., and Karunakar, G. (2003b). The March 1999 Chamoli earthquake in the Garhwal Himalaya: Aftershock characteristics and tectonic structure. *Geological Society of India*, 62(5):558–580.

[98] Kelbert, A., Egbert, G. D., and Schultz, A. (2008). Non-linear conjugate gradient inversion for global EM induction: resolution studies. *Geophysical Journal International*, 173:365–381.

[99] Kelbert, A., Meqbel, N., Egbert, G. D., and Tandon, K. (2014). ModEM: a modular system for inversion of electromagnetic geophysical data. *Computers and Geosciences*, 66:40–53.

[100] Keller, G. V. and Frischknecht, F. C. (1966). *Electrical methods in geophysical prospecting*. Pergamon Press.

[101] Keller, G. V. and Kaufman, A. A. (2000). *The magnetotelluric sounding method*. Elsevier.

[102] Khattri, K. (1987). Great earthquakes, seismicity gaps and potential for earthquake disaster along the Himalaya plate boundary. *Tectonophysics*, 138(1):79–92.

[103] Khattri, K. (1999). Probabilities of occurrence of great earthquakes in the Himalaya. *Proceedings of the Indian Academy of Sciences-Earth and Planetary Sciences*, 108(2):87–92.

[104] Khattri, K., Chander, R., Gaur, V., Sarkar, I., et al. (1989). New seismological results on the tectonics of the Garhwal Himalaya. *Proceedings of the Indian Academy of Sciences-Earth and Planetary Sciences*, 98(1):91–109.

[105] Khattri, K. and Tyagi, A. (1983a). Seismicity patterns in the Himalayan plate boundary and identification of the areas of high seismic potential. *Tectonophysics*, 96(3-4):281–297.

[106] Khattri, K. and Tyagi, A. (1983b). The transverse tectonic features in the Himalaya. *Tectonophysics*, 96(1-2):19–29.

[107] Kirar, B., Maheshwari, B., and Muley, P. (2016). Correlation Between Shear Wave Velocity (Vs) and SPT Resistance (N) for Roorkee Region. *International Journal of Geosynthetics and Ground Engineering*, 2(1):1–11.

[108] Kiyan, D., Jones, A. G., and Vozar, J. (2013). The inability of magnetotelluric off-diagonal impedance tensor elements to sense oblique conductors in three-Dimensional inversion. *Geophysical Journal International*, 196(3):1351–1364.

[109] Komori, S., Kagiyama, T., Takakura, S., Ohsawa, S., Mimura, M., and Mogi, T. (2013). Effect of the hydrothermal alteration on the surface conductivity of rock matrix: comparative study between relatively-high and low temperature hydrothermal systems. *Journal of Volcanology and Geothermal Research*, 264:164–171.

[110] Konda, S., Patro, P. K., and Rao, C. (2015). Geoelectric signatures of Palnad sub basin and Nallamalai Fold Belt, Cuddapah Basin, India. *Journal of the Geological Society of India*, 86(4):377–382.

[111] Kulhawy, F. H. and Mayne, P. W. (1990). Manual on estimating soil properties for foundation design. Technical report, Electric Power Research Inst., Palo Alto, CA (USA); Cornell Univ., Ithaca, NY (USA). Geotechnical Engineering Group.

[112] Kumar, G. P., Manglik, A., and Thiagarajan, S. (2014). Crustal geoelectric structure of the Sikkim Himalaya and adjoining Gangetic foreland basin. *Tectonophysics*, 637:238–250.

[113] Kumar, N., Rawat, G., Choubey, V. M., and Hazarika, D. (2013). Earthquake precursory research in western Himalaya based on the multi-parametric geophysical observatory data. *Acta Geophysica*, 61(4):977–999.

[114] Kumar, S., Patro, P. K., and Chaudhary, B. (2018). Three dimensional topography correction applied to magnetotelluric data from Sikkim Himalayas. *Physics of the Earth and Planetary Interiors*, 279:33–46.

[115] Kumar Tiwari, A., Singh, N., and Maurya, S. (2018). Conductivity-depth Imaging of Large Loop TEM Sounding Data Acquired using Central loop Configuration. *International Journal of Engineering Research and*, V7.

[116] Ledo, J. (2006). 2-D versus 3-D magnetotelluric data interpretation. *Surveys in Geophysics*, 27:111–148.

[117] Lee, T. (1975). An integral equation and its solution for some two-and three-dimensional problems in resistivity and induced polarization. *Geophysical Journal International*, 42(1):81–95.

[118] Lemonnier, C., Marquis, G., Perrier, F., Avouac, J.-P., Chitrakar, G., Kafle, B., Sapkota, S., Gautam, U., Tiwari, D., and Bano, M. (1999). Electrical structure of the Himalaya of central Nepal: High conductivity around the mid-crustal ramp along the MHT. *Geophysical Research Letters*, 26(21):3261–3264.

[119] Li, Y. and Oldenburg, D. W. (1992). Approximate inverse mappings in DC resistivity problems. *Geophysical Journal International*, 109(2):343–362.

[120] Lilley, F. (1993). Magnetotelluric analysis using Mohr circles. *Geophysics*, 58(10):1498–1506.

[121] Loke, M. (2004). Tutorial: 2-d and 3-d electrical imaging surveys.

[122] Loke, M. (2013a). Manual for RES3DINV. rapid 3-D resistivity & IP inversion using the least-squares method (For 3-D surveys using the pole–pole, pole–dipole, dipole–dipole, rectangular, Wenner, Wenner-Schlumberger and non-conventional arrays). *On land, aquatic and cross-borehole surveys. Geoelectrical Imaging*.

[123] Loke, M. H. (2013b). RES2DINV version 3.71. Geotom Software Sdn Bsd.

[124] Loke, M. H. and Barker, R. D. (1996). Rapid least-squares inversion of apparent resistivity pseudosections by a quasi-Newton method. *Geophysical prospecting*, 44(1):131–152.

[125] Lowry, T., Allen, M. B., and Shive, P. N. (1989). Singularity removal: A refinement of resistivity modeling techniques. *Geophysics*, 54(6):766–774.

[126] Mackie, R. L. and Madden, T. R. (1993). Three-dimensional magnetotelluric inversion using conjugate gradients. *Geophysical Journal International*, 115:215–229.

[127] Mackie, R. L., Madden, T. R., and Wannamaker, P. E. (1993). Three-dimensional magnetotelluric imodeling using difference equations: Theory and comparison to integral equation solutions. *Geophysics*, 58:215–226.

[128] Mackie, R. L., Smith, J. T., and Madden, T. R. (1994). Three-dimensional electromagnetic modeling using finite difference equations: The magnetotelluric example. *Radio Science*, 29:923–935.

[129] Mahesh, P., Gupta, S., Rai, S., and Sarma, P. R. (2012). Fluid driven earthquakes in the Chamoli Region, Garhwal Himalaya: evidence from local earthquake tomography. *Geophysical Journal International*, 191(3):1295–1304.

[130] Mahesh, P., Rai, S., Sivaram, K., Paul, A., Gupta, S., Sarma, R., and Gaur, V. (2013). One-dimensional reference velocity model and precise locations of earthquake hypocenters in the Kumaon–Garhwal himalaya. *Bulletin of the Seismological Society of America*, 103(1):328–339.

[131] Malleswari, D., Veeraswamy, K., Azeez, K. A., Gupta, A., Babu, N., Patro, P. K., and Harinarayana, T. (2019). Magnetotelluric investigation of lithospheric electrical structure beneath the Dharwar Craton in south India: Evidence for mantle suture and plume-continental interaction. *Geoscience Frontiers*.

[132] Manglik, A., Adilakshmi, L., Suresh, M., and Thiagarajan, S. (2015). Thick sedimentary sequence around Bahraich in the northern part of the central Ganga foreland basin. *Tectonophysics*, 653:33–40.

[133] Manglik, A., Kumar, G. P., and Thiagarajan, S. (2013). Transverse tectonics in the Sikkim Himalaya: A magnetotelluric study. *Tectonophysics*, 589:142–150.

[134] Manglik, A. and Verma, S. K. (1998). Delineation of sediments below flood basalts by joint inversion of seismic and magnetotelluric data. *Geophysical Research Letters*, 25(21):4015–4018.

[135] Manglik, A., Verma, S. K., Sain, K., Arayana, T., and Rao, V. V. (2011). Joint Inversion of Seismic and MT Data–An Example from Southern Granulite Terrain, India. In *The Earth's Magnetic Interior*, pages 83–90.

[136] Marquardt, D. W. (1963). An algorithm for least-squares estimation of nonlinear parameters. *Journal of the Society for Industrial and Applied Mathematics*, 11:431–441.

[137] Marti, A., Queralt, P., and Ledo, J. (2009). WALDIM: A code for the dimensionality analysis of Magnetotelluric data using the rotational invariants of the Magnetotelluric tensor. *Radio Science*, 35:2295–2303.

[138] Maurya, P. K., Balbarini, N., Møller, I., Rønde, V., Christiansen, A. V., Bjerg, P. L., Auken, E., and Fiandaca, G. (2018a). Subsurface imaging of water electrical conductivity, hydraulic permeability and lithology at contaminated sites by induced polarization. *Geophysical Journal International*, 213(2):770–785.

[139] Maurya, V. P., Bhattacharya, B., Adhikari, P., Das, L., et al. (2015). Preliminary magnetotelluric results across Dalma volcanics, Eastern India: Inferences on metallogeny. *Journal of Applied Geophysics*, 115:171–182.

[140] Maurya, V. P., Singh, R. K., Bhattacharya, B. B., et al. (2018b). Magnetotelluric exploration of a deposit scale prospecting over a proterozoic volcanics, Eastern India. *Journal of Applied Geophysics*, 159:666–677.

[141] McNeice, G. and Jones, A. G. (2001). Multisite, multifrequency tensor decomposition of magnetotelluric data. *Geophysics*, 66:158–173.

[142] Meqbel, N. (2009). *The Electrical Conductivity Structure of the Dead Sea Basin Derived from 2D and 3D Inversion of Magnetotelluric Data*. PhD thesis, Free University of Berlin, Berlin, Germany.

[143] Miensopust, M. and Jones, A. G. 3D MT Inversion Workshop. `https://www.dias.ie/mt3dinv/3D_forward_model.html`.

[144] Miglani, R., Shahrukh, M., Israil, M., Gupta, P. K., Varshney, S., and Sokolova, E. (2014). Geoelectric structure estimated from magnetotelluric data from the Uttarakhand Himalaya, India. *Journal of earth system science*, 123(8):1907–1918.

[145] Mitsuhata, Y. and Uchida, T. (2004). 3D magnetotelluric modeling using the T-ω finite-element method. *Geophysics*, 69(1):108–119.

[146] Mohan, K., Chaudhary, P., Kumar, G. P., Kothyari, G. C., Choudhary, V., Nagar, M., Patel, P., Gandhi, D., Kushwaha, D., and Rastogi, B. (2018a). Magnetotelluric Investigations in Tuwa-Godhra Region, Gujarat (India). *Pure and Applied Geophysics*, 175(10):3569–3589.

[147] Mohan, K., Chaudhary, P., Kumar, G. P., and Rastogi, B. (2019). Magnetotelluric investigations in the southern end of the Cambay basin (near coast), Gujarat, India. *Journal of Applied Geophysics*, 162:80–92.

[148] Mohan, K., Chaudhary, P., Patel, P., Chaudhary, B., and Chopra, S. (2018b). Magnetotelluric study to characterize Kachchh Mainland Fault (KMF) and Katrol Hill Fault (KHF) in the western part of Kachchh region of Gujarat, India. *Tectonophysics*, 726:43–61.

[149] Mohan, K., Kumar, G. P., Chaudhary, P., Choudhary, V. K., Nagar, M., Khuswaha, D., Patel, P., Gandhi, D., and Rastogi, B. (2017). Magnetotelluric investigations to identify geothermal source zone near Chabsar hotwater spring site, Ahmedabad, Gujarat, Northwest India. *Geothermics*, 65:198–209.

[150] Mohan, K., Rastogi, B., and Chaudhary, P. (2015). Magnetotelluric studies in the epicenter zone of 2001, Bhuj earthquake. *Journal of Asian Earth Sciences*, 98:75–84.

[151] Molnar, P., Chen, W.-P., Fitch, T., Tapponnier, P., Warsi, W., and Wu, F. (1977). Structure and tectonics of the Himalaya: a brief summary of relevant geophysical observations. *Himalaya: Sciences de la Terre*, 268:269–294.

[152] Moorkamp, M., Fishwick, S., Walker, R. J., and Jones, A. G. (2019). Geophysical evidence for crustal and mantle weak zones controlling intra-plate seismicity–the 2017 Botswana earthquake sequence. *Earth and Planetary Science Letters*, 506:175–183.

[153] Moorkamp, M., Heincke, B., Jegen, M., Roberts, A. W., and Hobbs, R. W. (2011). A framework for 3-D joint inversion of MT, gravity and seismic refraction data. *Geophysical Journal International*, 184(1):477–493.

[154] Mukhopadhyay, S. and Kayal, J. (2003). Seismic tomography structure of the 1999 Chamoli earthquake source area in the Garhwal Himalaya. *Bulletin of the Seismological Society of America*, 93(4):1854–1861.

[155] Nabighian, M. N., editor (1988). *Electromagnetic methods in applied geophysics: Theory*, volume 1. SEG Books.

[156] Nam, M. J., Kim, H. J., Song, Y., Lee, T. J., Son, J.-S., and Suh, J. H. (2007). 3D magnetotelluric modelling including surface topography. *Geophysical Prospecting*, 55(2):277–287.

[157] Negri, S., Leucci, G., and Mazzone, F. (2008). High resolution 3D ERT to help GPR data interpretation for researching archaeological items in a geologically complex subsurface. *Journal of Applied Geophysics*, 65(3-4):111–120.

[158] Newman, G. A. and Alumbaugh, D. L. (1997). Three-dimensional massively parallel electromagnetic inversion-I Theory. *Geophysical Journal International*, 128:345–354.

[159] Newman, G. A. and Alumbaugh, D. L. (2000). Three-dimensional magnetotelluric inversion using non-linear conjugate gradients. *Geophysical Journal International*, 140:410–424.

[160] Newman, G. A. and Boggs, P. T. (2004). Solution accelerators for large-scale three-dimensional electromagnetic inverse problems. *Inverse Problem*, 20:S151–S170.

[161] Newman, G. A., Recher, S., Tezkan, B., and Neubauer, F. M. (2003). Case History 3D inversion of a scalar radio Magnetotelluric field data set. *Geophysics*, 68:791–802.

[162] Ni, J. and Barazangi, M. (1984). Seismotectonics of the Himalayan collision zone: Geometry of the underthrusting Indian plate beneath the Himalaya. *Journal of Geophysical Research: Solid Earth*, 89(B2):1147–1163.

[163] Ogawa, Y. (2002). On two-dimensional modeling of magnetotelluric field data. *Surveys in Geophysics*, 23:251–272.

[164] Ogilvy, R., Meldrum, P., Kuras, O., Wilkinson, P., Chambers, J., Sen, M., Pulido-Bosch, A., Gisbert, J., Jorreto, S., Frances, I., et al. (2009). Automated monitoring of coastal aquifers with electrical resistivity tomography. *Near Surface Geophysics*, 7(5-6):367–376.

[165] Okabe, M. (1981). Boundary element method for the arbitrary inhomogeneities problem in electrical prospecting. *Geophysical Prospecting*, 29(1):39–59.

[166] Park, S. K. and Van, G. P. (1991). Inversion of pole-pole data for 3-D resistivity structure beneath arrays of electrodes. *Geophysics*, 56(7):951–960.

[167] Parker, R. L. (1983). The magnetotelluric inverse problem. *Geophysical surveys*, 6(1-2):5–25.

[168] Parker, R. L. (1994). *Geophysical inverse theory*. Princeton University Press, Princeton.

[169] Patro, P. K., Borah, U. K., Babu, G. A., Veeraiah, B., and Sarma, S. (2017). Ground electrical and electromagnetic studies in Koyna-Warna region, India. *Journal of the Geological Society of India*, 90(6):711–719.

[170] Patro, P. K. and Harinarayana, T. (2009). Deep geoelectric structure of the Sikkim Himalayas (NE India) using magnetotelluric studies. *Physics of the Earth and Planetary Interiors*, 173(1):171–176.

[171] Patro, P. K., Raju, K., and Sarma, S. (2018). Some Insights into the Lithospheric Electrical Structure in the Western Ghat Region from Magnetotelluric Studies. *Journal of the Geological Society of India*, 92(5):529–532.

[172] Patro, P. K. and Sarma, S. (2016). Evidence for an extensive intrusive component of the Deccan Large Igneous Province in the Narmada Son Lineament region, India from three dimensional magnetotelluric studies. *Earth and Planetary Science Letters*, 451:168–176.

[173] Petrick Jr, W. R., Sill, W. R., and Wards, S. (1981). Three-dimensional resistivity inversion using alpha centers. *Geophysics*, 46(8):1148–1162.

[174] Pidlisecky, A., Moran, T., Hansen, B., and Knight, R. (2016). Electrical resistivity imaging of seawater intrusion into the monterey bay aquifer system. *Groundwater*, 54(2):255–261.

[175] Prasath, R. A., Paul, A., and Singh, S. (2017). Upper crustal stress and seismotectonics of the Garhwal Himalaya using small-to-moderate earthquakes: Implications to the local structures and free fluids. *Journal of Asian Earth Sciences*, 135:198–211.

[176] Pratap, A., Naick, B. P., Naganjaneyulu, K., et al. (2018a). A magnetotelluric study from over Dharwar cratonic nucleus into Billigiri Rangan charnockitic massif, India. *Physics of the Earth and Planetary Interiors*, 280:32–39.

[177] Pratap, A., Naick, B. P., Naganjaneyulu, K., et al. (2018b). Lithospheric architecture in the Archaean Dharwar craton, India: A magnetotelluric model. *Journal of Asian Earth Sciences*, 163:43–53.

[178] Qureshy, M. (1969). Thickening of a basalt layer as a possible cause for the uplift of the Himalayas—A suggestion based on gravity data. *Tectonophysics*, 7(2):137–157.

[179] Rai, S. K., Tiwari, S. K., Bartarya, S., and Gupta, A. K. (2015). Geothermal systems in the Northwest Himalaya. *Current Science*, pages 1597–1599.

[180] Raiche, A. P., Jupp, D., Rutter, H., and Vozoff, K. (1985). The joint use of coincident loop transient electromagnetic and schlumberger sounding to resolve layered structures. *Geophysics*, 50(10):1618–1627.

[181] Ramirez, A., Daily, W., Binley, A., LaBrecque, D., and Roelant, D. (1996). Detection of leaks in underground storage tanks using electrical resistance methods. *Journal of Environmental and Engineering Geophysics*, 1(3):189–203.

[182] Rao, C. K., Ogawa, Y., and Gupta, G. (2004). Electromagnetic imaging of magma across the Narmada Son lineament, central India. *Earth, planets and space*, 56(2):229–238.

[183] Rawat, G., Arora, B., and Gupta, P. (2014). Electrical resistivity cross-section across the Garhwal Himalaya: Proxy to fluid-seismicity linkage. *Tectonophysics*, 637:68–79.

[184] Reddy, I. K., Phillips, R. J., and Rankin, D. (1977). Three-dimensional modelling in magnetotelluric and magnetic variational sounding. *Geophysical Journal*, 51:313–325.

[185] Rijo, L. (1984). Inversion of three-dimensional resistivity and induced-polarization data. In *SEG Technical Program Expanded Abstracts 1984*, pages 113–117. Society of Exploration Geophysicists.

[186] Rodi, W. L. and Mackie, R. L. (2001). Nonlinear conjugate gradients algorithm for 2-D magnetotelluric inversion. *Geophysics*, 66:174–187.

[187] Sasaki, Y. (1989). Two-dimensional joint inversion of magnetotelluric and dipole-dipole resistivity data. *Geophysics*, 54:254–262.

[188] Sasaki, Y. (1994). 3-D resistivity inversion using the finite-element method. *Geophysics*, 59(12):1839–1848.

[189] Sasaki, Y. (2001). Full 3D inversion of electromagnetic data on PC. *Journal of Applied Geophysics*, 46:45–54.

[190] Sasaki, Y. (2004). Three-dimensional inversion of static-shifted magnetotelluric data. *Earth Planets Space*, 56:239–248.

[191] Sastry, R. G., Singh, V. N., Saran, S., and Mittal, S. (2006). Geophysical Site Testing for Dobra - Chnati Bridge. Technical report. Unpublished.

[192] Sati, D. and Nautiyal, S. (1994). Possible role of Delhi–Haridwar subsurface ridge in generation of Uttarkashi earthquake, Garhwal Himalaya, India. *Current Science*, pages 39–44.

[193] Seeber, L. and Armbruster, J. G. (1981). Great detachment earthquakes along the Himalayan arc and long-term forecasting. *Earthquake prediction*, pages 259–277.

[194] Seeber, L. and Armbruster, J. G. (1982). *Continental Subduction Along the Northwestern and Central Portions of the Himalaya Arc*. Lamont-Doherty Geological Observatory of Columbia University.

[195] Seher, T. and Tezkan, B. (2007). Radiomagnetotelluric and direct current resistivity measurements for the characterization of conducting soils. *Journal of Applied Geophysics*, 63(1):35–45.

[196] Shalivahan and Bhattacharya, B. B. (2002). Implications of novel results about Moho from magnetotelluric studies. *Current Science*, 83(10):1259–1264.

[197] Shalivahan and Bhattacharya, B. B. (2005). Electrical anisotropy of asthenosphere in a region of window to mantle underneath Eastern Indian Craton. *Physics of the Earth and Planetary Interiors*, 152(1):43–61.

[198] Shandilya, A. K. and Shandilya, A. (2016). Studies on the Seismicity in Garhwal Himalaya, India. In *Geostatistical and Geospatial Approaches for the Characterization of Natural Resources in the Environment*, pages 503–512. Springer.

[199] Sharma, S., Prácser, E., and Roy, K. (2005). Joint inversion of seismic refraction and magnetotelluric data for resolving deeper subsurface structure. *Acta Geodaetica et Geophysica Hungarica*, 40(2):241–258.

[200] Shima, H. (1992). 2-D and 3-D resistivity image reconstruction using crosshole data. *Geophysics*, 57(10):1270–1281.

[201] Shukla, A., Prakash, R., Singh, R., Mishra, P., and Bhatnagar, A. (2007). Seismotectonic implications of Delhi region through fault plane solutions of some recent earthquakes. *Current Science*, pages 1848–1853.

[202] Simpson, F. and Bahr, K. *Practical magnetotellurics*. Cambridge University Press.

[203] Singh, A. (2018). *Development of MATLAB based 3D inversion algorithm for MT and DCR data*. PhD thesis, Indian Institute of Technology Roorkee, Roorkee, India.

[204] Singh, A., Dehiya, R., Gupta, P. K., and Israil, M. (2017). A MATLAB based 3D modeling and inversion code for MT data. *Computers & Geosciences*, 104:1–11.

[205] Singh, N. P. and Mogi, T. (2005). Electromagnetic response of a large circular loop source on a layered earth: A new computation method. *Pure and Applied Geophysics*, 162(1):181–200.

[206] Singhal, D., Roy, T., Joshi, H., and Seth, A. (2003). Evaluation of Groundwater Pollution in Roorkee Town, Uttaranchal. *Journal of the Geological Society of India*, 62:465–477.

[207] Sinharay, R. K., Srivastava, S., and Bhattacharya, B. B. (2010). Audiomagnetotelluric studies to trace the hydrological system of thermal fluid flow of Bakreswar Hot Spring, Eastern India: A case history. *Geophysics*, 75(5):B187–B195.

[208] Siripunvaraporn, W. (2012). Three-Dimensional Magnetotelluric Inversion: An Introductory Guide for Developers and Users. *Surveys in Geophysics*, 33:5–27.

[209] Siripunvaraporn, W. and Egbert, G. (2000). An effcient data-subspace inversion method for 2D magnetotelluric data. *Geophysics*, 65(3):791–803.

[210] Siripunvaraporn, W. and Egbert, G. (2009). WSINV3DMT: vertical magnetic field transfer function inversion and parallel implementation. *Physics of the Earth and Planetary Interiors*, 173:317–329.

[211] Siripunvaraporn, W., Egbert, G., and Uyeshima, M. (2005b). Interpretation of two-dimensional magnetotelluric profile data with three-dimensional inversion: synthetic examples. *Geophysical Journal International*, 160:804–814.

[212] Smirnov, M. and Pedersen, L. B. (2009). Magnetotelluric measurements across the Sorgenfrei-Tornquist Zone in southern Sweden and Denmark. *Geophysical Journal International*, 176(2):443–456.

[213] Smirnov, M. Y. (2003). Magnetotelluric data processing with a robust statistical procedure having a high breakdown point. *Geophysical Journal International*, 152(1):1–7.

[214] Smith, J. T. (1996a). Conservative modeling of 3-D electromagnetic fields, Part I: properties and error analysis. *Geophysics*, 61:1308–1318.

[215] Smith, J. T. (1996b). Conservative modeling of 3-D electromagnetic fields, Part II: biconjugate gradient solution and an accelerator. *Geophysics*, 61:1319–1324.

[216] Sokolova, E. Y., Israil, M., Gupta, P., Koshurnikov, A., Smirnov, M. Y., and Cherevatova, M. (2016). Crustal electrical conductivity of the Indian continental subduction zone: New data from the profile in the Garhwal Himalaya. *Izvestiya, Physics of the Solid Earth*, 52(2):271–290.

[217] Spencer, C. J., Harris, R. A., and Dorais, M. J. (2012). The metamorphism and exhumation of the Himalayan metamorphic core, eastern Garhwal region, India. *Tectonics*, 31(1).

[218] Spitzer, K. (1995). A 3D finite-difference algorithm for DC resistivity modeling using conjugate gradient methods. *Geophysical Journal International*, 123:903–914.

[219] Spitzer, K., Wurmstich, B., Oristaglio, M., and Spies, B. (1999). Speed and accuracy in 3D resistivity modeling. *Three-Dimensional Electromagnetics*, 7:161–176.

[220] Spratt, J. E., Jones, A. G., Nelson, K. D., Unsworth, M. J., Team, I. M., et al. (2005). Crustal structure of the India–Asia collision zone, southern Tibet, from INDEPTH MT investigations. *Physics of the Earth and Planetary Interiors*, 150(1-3):227–237.

[221] Sudha, Tezkan, B., Israil, M., Singhal, D., and Rai, J. (2010a). Geoelectrical mapping of aquifer contamination: a case study from Roorkee, India. *Near Surface Geophysics*, 8(1):33–42.

[222] Sudha, K., Israil, M., Mittal, S., and Rai, J. (2009). Soil characterization using electrical resistivity tomography and geotechnical investigations. *Journal of Applied Geophysics*, 67(1):74–79.

[223] Sudha, K, T. B., Israil, M., Singhal, D., and Rai, J. (2010b). Geoelectrical mapping of aquifer contamination: a case study from Roorkee, India. *Near Surface Geophysics*, 8(1):33–42.

[224] Szalai, S., Koppán, A., Szokoli, K., and Szarka, L. C. (2013). Geoelectric imaging properties of traditional arrays and of the optimized Stummer configuration. *Near Surface Geophysics*, 11:51–62.

[225] Szalai, S., Szokoli, K., and Metwaly, M. (2014). Delineation of landslide endangered areas and mapping their fracture systems by the pressure probe method. *Landslides*, 11(5):923–932.

[226] Szalai, S., Szokoli, K., Metwaly, M., Gribovszki, Z., and Prácser, E. (2017). Prediction of the location of future rupture surfaces of a slowly moving loess landslide by electrical resistivity tomography. *Geophysical Prospecting*, 65(2):596–616.

[227] Szokoli, K., Szarka, L., Metwaly, M., Kalmár, J., Prácser, E., and Szalai, S. (2017). Characterisation of a landslide by its fracture system using Electric Resistivity Tomography and Pressure Probe methods. *Acta Geodaetica et Geophysica*, pages 1–16.

[228] Tezkan, B., Goldman, M., Greinwald, S., Hördt, A., Müller, I., Neubauer, F. M., and Zacher, G. (1996). A joint application of radiomagnetotellurics and transient electromagnetics to the investigation of a waste deposit in Cologne (Germany). *Journal of Applied Geophysics*, 34(3):199–212.

[229] Tezkan, B., Hördt, A., and Gobashy, M. (2000). Two dimensional inversion of radiomagnetotelluric data: selected case histories for waste site exploration. *Journal of Applied Geophysics*, 44:237–256.

[230] Tezkan, B. and Saraev, A. (2008). A new broadband radiomagnetotelluric instrument: applications to near surface investigations. *Near Surface Geophysics*, 6(4):245–252.

[231] Thakur, V. (2004). Active tectonics of Himalayan frontal thrust and seismic hazard to Ganga Plain. *Current science*, 86(11):1554–1560.

[232] Thakur, V. and Rawat, B. (1992). Geological Map of the Western Himalaya. Scale 1: 1,111,111.

[233] Tietze, K. and Ritter, O. (2013). Three-dimensional magnetotelluric inversion in practice—the electrical conductivity structure of the San Andreas Fault in Central California. *Geophysical Journal International*, 195(1):130–147.

[234] Tietze, K., Ritter, O., and Egbert, G. D. (2015). 3-D joint inversion of the magnetotelluric phase tensor and vertical magnetic transfer functions. *Geophysical Journal International*, 203(2):1128–1148.

[235] Ting, S. C. and Hohmann, G. W. (1981). Integral equation modeling of three-dimensional magnetotelluric response. *Geophysics,*, 46:182–197.

[236] Tsokas, G. N., Giannopoulos, A., Tsourlos, P., Vargemezis, G., Tealby, J., Sarris, A., Papazachos, C. B., and Savopoulou, T. (1994). A large scale geophysical survey in the archaeological site of Europos (northern Greece). *Journal of Applied Geophysics*, 32(1):85–98.

[237] Unsworth, M. (2010). Magnetotelluric studies of active continent–continent collisions. *Surveys in Geophysics*, 31(2):137–161.

[238] Unsworth, M. J., Jones, A. G., Wei, W., Marquis, G., Gokarn, S. G., Spratt, J. E., Bedrosian, P., Booker, J., Leshou, C., Clarke, G., et al. (2005). Crustal rheology of the Himalaya and Southern Tibet inferred from magnetotelluric data. *Nature*, 438(7064):78.

[239] Unsworth, M. J., Malin, P. E., Egbert, G. D., and Booker, J. R. (1997). Internal structure of the San Andreas fault at Parkfield, California. *Geology*, 25(4):359–362.

[240] Valdiya, K. (1976). Himalayan transverse faults and folds and their parallelism with subsurface structures of north Indian plains. *Tectonophysics*, 32(3-4):353–386.

[241] Valdiya, K. (2003). Reactivation of Himalayan frontal fault: implications. *Current Science*, pages 1031–1040.

[242] Valdiya, K. S. (1980). *Geology of Kumaun lesser Himalaya*. Wadia Institute of Himalayan Geology.

[243] Van der Vorst, H. A. (2003). *Iterative Krylov methods for large linear systems*, volume 13. Cambridge University Press.

[244] Varentsov, I. M., Sokolova, E. Y., and EMTESZ Working Group (2005). The magnetic control approach for the reliable estimation of transfer functions in the EMTESZ pomerania project. *Publications of the Institute of Geophysics, Polish Academy of Sciences*, C95(386):68–79.

[245] Vozoff, K. (1972). The magnetotelluric method in the exploration of sedimentary basins. *Computers & Geosciences*, 37:98–141.

[246] Vozoff, K. and Jupp, D. (1975). Joint inversion of geophysical data. *Geophysical Journal International*, 42(3):977–991.

[247] Wannamaker, P. E. (1991). Advances in three dimensional magnetotelluric modeling using integral equations. *Geophysics*, 56:1716–1728.

[248] Wason, H., Kumar, J., Walia, S., Jain, A., and Manickavasagam, R. (1999). Local seismicity of the Garhwal Himalaya subsequent of the Uttarkashi earthquake of 20 October 1991. *Geodynamics of the NW Himalaya*, 6:335–340.

[249] Weaver, J. T. (1994). *Mathematical methods for geo-electromagnetic induction*. Research Studies Press Ltd. John Wiley & Sons.

[250] Weaver, J. T., Agarwal, A. K., and Lilley, F. E. M. (2000). Characterization of the magnetotelluric impedance tensor. *Geophysical Journal International*, 129:133–142.

[251] Wei, W., Unsworth, M., Jones, A., Booker, J., Tan, H., Nelson, D., Chen, L., Li, S., Solon, K., Bedrosian, P., and others (2001). Detection of widespread fluids in the Tibetan crust by magnetotelluric studies. *Science*, 292(5517):716–719.

[252] Wiese, H. (1962). Geomagnetische tiefentellurik teil: ii. die streichrichtung der untergrundstrukturen des elektrischen widerstandes, erschlossen aus geomagnetischen variationen. *Geofis. Pura Appl.*, 52:83–103.

[253] Xiao, Q., Cai, X., Xu, X., Liang, G., and Zhang, B. (2010). Application of the 3D magnetotelluric inversion code in a geologically complex area. *Geophysical Prospecting*, 58(6):1177–1192.

[254] Xiong, Z. and Tripp, A. C. (1995). Electromagnetic scattering of large structures in layered earths using integral equations. *Radio Science*, 30:921–921.

[255] Xu, S.-z., Gao, Z., and Zhao, S.-k. (1988). An integral formulation for three-dimensional terrain modeling for resistivity surveys. *Geophysics*, 53(4):546–552.

[256] Yan, L. I., Xiang-Yun, H. U., Wen-Cai, Y. A. N. G., Wen-Bo, W. E. I., Hui, F. A. N. G., Bo, H. A. N., and Rong-Hua, P. E. N. G. (2013). A Study on Parallel Computation for 3D Magneto-Telluric Modeling Using the Staggered-Grid Finite Difference Method. *Chinese Journal of Geophysics*, 56(3):287–295.

[257] Yee, K. S. (1966). Numerical Solution of Initial Boundary Value Problems Involving Maxwell's Equations in Isotropic Media. *IEEE Transactions on Antennas and Propagation*, AP-14:302–307.

[258] Yogeshwar, P., Tezkan, B., Israil, M., and Candansayar, M. (2012). Groundwater contamination in the Roorkee area, India: 2D joint inversion of radiomagnetotelluric and direct current resistivity data. *Journal of Applied Geophysics*, 76:127–135.

[259] Yu, G., Khattri, K., Anderson, J., Brune, J., and Zeng, Y. (1995). Strong ground motion from the Uttarkashi, Himalaya, India, earthquake: comparison of observations with synthetics using the composite source model. *Bulletin of the Seismological Society of America*, 85(1):31–50.

[260] Yuguo, L. and Spitzer, K. (2002). Three-dimensional DC resistivity forward modelling using finite elements in comparison with finite-difference solutions. *Geophysical Journal International*, 151:924–934.

[261] Zhang, J., Mackie, R. L., and Madden, T. R. (1995). 3D resistivity forward modeling and inversion using conjugate gradients,. *Geophysics*, 60(5):1313–1325.

[262] Zhao, S. and Yedlin, M. J. (1996). Some refinements on the finite-difference method for 3-D DC resistivity modeling. *Geophysics*, 61(5):1301–1307.

[263] Zhdanov, M. S. (2009). Geophysical electromagnetic theory and methods. *Elsevier*.